VIABILITY AND CHARACTERIZATION OF A PLASMA WINDOW AS A FLOW LIMITER FOR AN ION BEAM GAS CHARGE STRIPPER

By

Andrew Leo LaJoie

A DISSERTATION

Submitted to
Michigan State University
in partial fulfillment of the requirements
for the degree of

Physics—Doctor of Philosophy

2020

ABSTRACT

VIABILITY AND CHARACTERIZATION OF A PLASMA WINDOW AS A FLOW LIMITER FOR AN ION BEAM GAS CHARGE STRIPPER

By

Andrew Leo LaJoie

Charge stripping is an increasingly necessary process in ion accelerators, particularly those which are used in accelerating high mass nuclei such as uranium. Generally in accelerator facilities, heavy ions are produced in the ion source with a relatively low charge state distribution. In the charge stripper, further removal of electrons from the ion beam enables greater energy gain in accelerating cavities downstream of the charge stripper, which can lower cost of attaining a desired energy. For this reason the charge stripper is typically located early in the accelerator. The ion acceleration community is met with an increasingly strong demand for higher particle counts in the ion beams because facility users almost always can benefit from higher statistics in their experiments. This means higher beam intensities. This need for higher intensity presents the challenge of preventing traditionally employed solid charge strippers, like diamond-like carbon (DLC) foils, from suffering overwhelming kinetic impact damage from the beam and reducing or eliminating their charge stripping function. These issues are even more critical when stripping heavy ions because of their much larger energy deposition per unit length compared with protons or low mass heavy ions. This high energy deposition results from a sharper Bragg peak for heavier ions.

Alternatively, gas charge strippers do not suffer from this kind of irreparable degradation, but do present a host of other unique challenges. Chief among these challenges is confining the gas to only a small segment of the beamline and preventing it from excessively leaking to other upstream and downstream components of the beamline whose performance can

be hindered or entirely prevented by pressures above 10^{-7} torr. The plasma window (PW) device is one which can limit the flow of gas from a high pressure gas charge stripping chamber (GCS) to the surrounding low pressure beamline - without the need for any solid interface, that would likely be damaged or destroyed by the ion beam. The PW is a direct current (DC) cascaded arc which heats and ionizes the gas flowing out of the GCS, thereby restricting the flow by greatly reducing the density of the gas flow. One would be located on both ends of the GCS. The degree to which this limits the gas flow depends on the temperature attained within the arc, which primarily depends upon the pressure maintained in the GCS and the arc current. These parameters are the operating conditions which can be user-controlled in a fixed-geometry PW to tune its utility. In addition, the PW performance depends on its geometry, both its channel radius and channel length. Both helium and argon are studied, each having pros and cons for potential gas charge stripper applications which will be summarized. Within the operating conditions and geometry studied in this thesis, the PW can reduce the gas flow escaping from the GCS by a factor of up to about 24 in argon and 15 in helium.

The goal of the work summarized in this thesis was to quantify the utility of the PW in reducing the gas leakage rate from the gas charge stripper in a variety of operating conditions, and to gain an understanding of the mechanisms involved in effecting the flow rate reduction. Design recommendations for a next generation PW are also given to address persisting challenges with employing it in tandem with a GCS for ion beams. This work shows that a PW-based gas charge stripper system may be effective for future high intensity ion accelerators. To get to that point, more work is necessary to extend the continuous, uninterrupted lifetime of the plasma window.

ACKNOWLEDGMENTS

There are a great many individuals without whose support this thesis would not be what it is now. Firstly thank you to Ady Hershcovitch and Peter Thieberger at Brookhaven National Laboratory for providing much of the components of the original plasma window used for this project, as well as insights into how to initiate and maintain the arc.

Thank you to my research advisor Felix Marti for your experience, patience, and encouragement throughout this project, helping to bring it from a device whose physical mechanisms for performance were rather nebulous and hidden to something that we now have a much better understanding of. I also thank Jian Gao for his contributions towards that same goal, especially in providing assistance in bringing the performance of the plasma window to bear. Thank you to Steve Lund for serving as my guidance committee chair and academic advisor, for providing valuable input and insights into improving publication and presentation quality, and for helping guide me towards promising employment prospects. I would also like to thank my other guidance committee members, John Verboncoeur, Tim Grotjohn, and Chong-Yu Ruan for their suggestions and constructive comments throughout my graduate career.

I also would like to thank the numerous friends - fellow graduate students I met at Michigan State University, as well as those I met earlier as an undergraduate - who've provided encouragement and support throughout my time at Michigan State University. Whether it was watching movies, playing games, sharing drinks, or just having conversations, I'm glad that you've been a part of my graduate school experience - the best part, in fact. Daine Smith, Brittany Lindstrom, Rachel Holt, Terri Poxon-Pearson, Roy Ready, Lisa Carpenter, Brandon Elman, Alice Mills, Bryan Isherwood and so many others that I regret

not being able to take up an entire page mentioning, you have all made the graduate school experience infinitely more endurable. My family members have also been a constant source of support, and I am incredibly grateful to you all!

Finally, I owe a huge thank you to my wife-to-be Nicki Larson. Your continuous encouragement has kept me going through even the toughest times, and you have helped pull me back to real life when I'd been spending too much time with my head buried in the world of the plasma window. You and Mars (our cat) have been great at providing much-needed distractions from work when it became overwhelming (or in the case of Mars, whenever he felt like it). Thank you so much for everything, you are the best!

TABLE OF CONTENTS

LIST OF TABLES

LIST OF FIGURES

KEY TO ABBREVIATIONS

BC	Boundary Condition
CCRF	Capacitively Coupled Radio Frequency
CR	Collisional Radiative
DC	Direct Current
DLC	Diamond-Like Carbon
DRC	Differential Rate Constant
EEDF	Electron Energy Distribution Function
FRIB	Facility for Rare Isotope Beams
GCS	Gas Charge Stripper
LOS	Line of Sight
LTE	Local Thermodynamic Equilibrium
MP	Matching Parameter
MSU	Michigan State University
NSCL	National Superconducting Cyclotron Laboratory
OES	Optical Emission Spectroscopy
PLTE	Partial Local Thermodynamic Equilibrium
PW	Plasma Window
WF	Work Function

Chapter 1

Introduction

1.1 Charge Stripping

Charge stripping is an increasingly necessary process in a high energy ion accelerator. Generally in accelerator facilities, heavy ions emerge from the ion source with a relatively low charge state distribution. Further stripping of electrons reduces total RF voltage required to accelerate to a given energy or enables higher attainable energies for a facility with a given total RF voltage [3, 16]. To understand the mechanism of charge stripping, consider that as the ion beam impinges upon the charge stripping media, the ions can capture or relinquish electrons to the target atoms. Cross sections for these processes depend upon the ion's properties: species, charge state, and energy. For a given beam energy, there exists some beam charge state such that the cross section for electron capture and electron loss are equivalent (or as close to equivalent as any integer charge state can allow). This charge state is therefore called the equilibrium charge state for that particular beam/stripper combination at that energy, with a charge state distribution forming about this equilibrium state [2, 16, 17]. An example of this is shown in Fig. 1.1, a reproduction of a figure published in Ref. [2], which illustrates electron loss and capture intersections as a function of charge state for several beam energies. The beam here is uranium with the stripper being helium gas. It should be noted that the charge stripper requires a material thickness sufficiently great for the beam

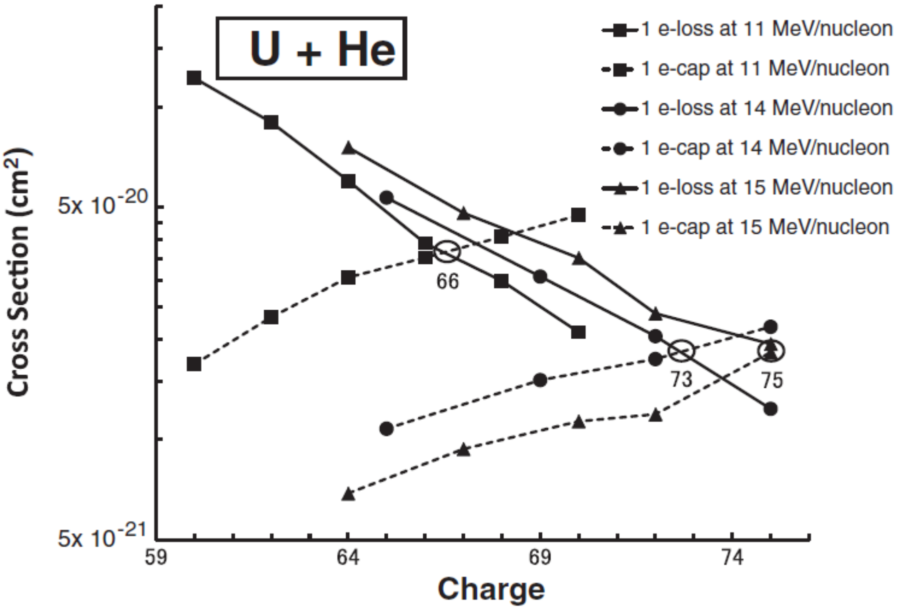

Figure 1.1: A figure published in Ref. [2], reproduced with permission. Cross sections of electron capture and loss are shown, with the intersection being the equilibrium charge state for the beam-stripper combination.

to attain this equilibrium charges state before exiting the charge stripper.

In the National Superconducting Cyclotron Laboratory (NSCL) where the research of this thesis was conducted, the primary application of the accelerator is for nuclear physicists and chemists to study the nature of nuclei, usually those that are short-lived, or “rare”. The accelerator facility is usually operated to produce a given ion beam of stable nuclei which then impinges on a low-Z target to produce the radioactive nuclei whose properties in terms of nuclear structure or subsequent reactions are investigated, in processes that are often rare and statistics-limited. Statistical limitations in these rare processes will be greatly relaxed in the successor Facility for Rare Isotope Beams (FRIB), which will nominally provide more than 2 orders of magnitude greater beam intensity, largely by increased particle count [18, 19]. This substantially higher ion beam intensity necessitates a charge stripper which can operate continuously on the timescale of the typical nuclear science experiment

- up to 2 weeks. Traditionally, solid charge strippers have been used, primarily diamond-like-carbon foils. However as accelerator facilities continue to push the intensity frontier, the lifetime of the foils diminishes substantially, and even for facilities currently in development such as the Facility for Rare Isotope Beams (FRIB), the kinetic impact damage sustained by these foils from the beam, also called radiation damage in the charge stripping community, would render them unusable in a matter of minutes to seconds. The foils suffer thinning from the energetic ion impingements, an effect called the "ion hammering effect" reducing the stripping efficiency. The foils furthermore suffer rapid and localized heating at the beam spot, resulting in sublimation which is the primary lifetime-limiting factor for beam current densities in excess of about 20 pA/cm^2 [3]. Much more detail describing the processes taking place particularly in beam-solid stripper material can be found in Refs. [3, 16]. For the purposes of nuclear physics and chemistry experiments that take place in the National Superconducting Cyclotron Laboratory (NSCL) and the upcoming successor facility FRIB, the beam is required to be utilized often for 1-2 weeks continuously. The charge stripper should be usable and stable over this entire duration.

As a result, the use of charge strippers that can be readily regenerated after beam interaction, such as gas or liquid, is rapidly becoming a necessity; indeed, for FRIB, it is already a necessity. More details on the topic of liquid charge strippers can be found in Refs. [20, 21] which discuss a liquid lithium charge stripper (the baseline for FRIB), and the review in Ref. [3] also details other liquid stripper possibilities. Gas charge strippers (GCS) face their own set of challenges which need to be addressed for them to be viable choices in high intensity heavy ion accelerators. Namely, gas charge strippers: yield lower charge state distributions than solid counterparts; can introduce substantial energy spread to the beam; necessarily require a more sophisticated system for containment; and can result in

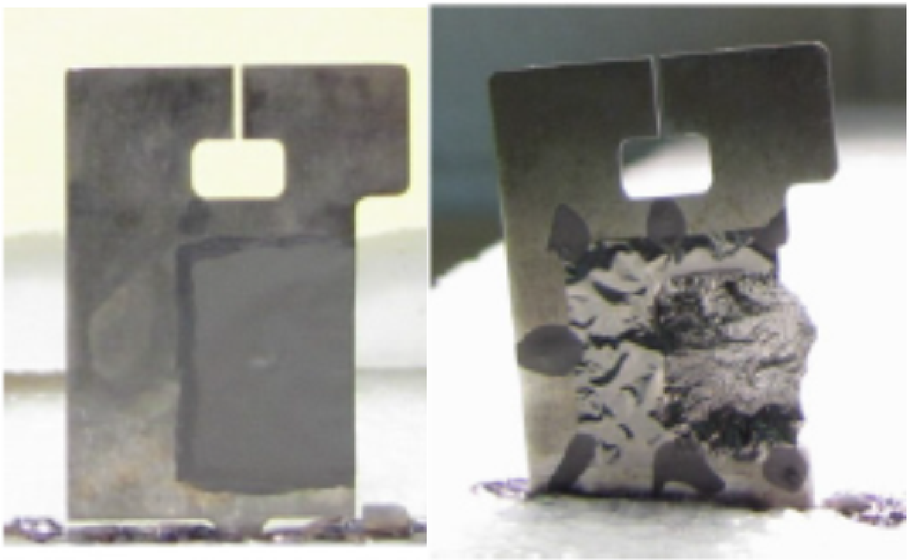

Figure 1.2: A figure published in Ref. [3], reproduced with permission. This illustrates the damage caused by an 8.1 MeV/u ^{208}Pb beam impinging on a DLC foil. The left frame is an unused foil and the right frame has accumulated a dose of 4-6x10^{14} ions of an approximately 2 mm diameter beam spot.

beam emittance growth attributed to the GCS having a long interaction region compared to a solid charge stripper. The charge stripping gas must be in a continuous flow, around 100 m/s, as a sort of curtain to remove stripper material that is heated by the gas so it can be cooled and recirculated.

A property of charge strippers with which they can be characterized is using the target thickness, defined as the target density multiplied by the interaction length, generally given in $\mu g/cm^2$ as:

$$\mu = \rho L = \frac{mP}{kT} L \, . \tag{1.1}$$

Here, ρ is the stripper density, m the gas mass, P the GCS pressure, k Boltzmann's constant, T the GCS temperature, and L the GCS length. For gases, this means that a given target thickness can be maintained by exchanging a shortening of GCS length L for an increase in GCS pressure P. The target thickness μ is what impacts the transiting beam's energy spread, but greater length will result in an undesired effect of increased beam size, due to angular dispersion induced from beam-stripper scatterings and space charge effects, and as a result, the beam's emittance will continually grow throughout. For this reason, achieving the desired target thickness μ is ideally achieved by having a large GCS pressure P and a short GCS length L. For an ion beam of a certain initial energy impinging on a gas charge stripper target, there is an optimum thickness for maximizing the outgoing mean charge state. Ideally this mean charge state would be the equilibrium charge state. This optimization exists because of a balance between competing effects: increasing thickness enables more interactions with the stripper, allowing the beam to achieve the equilibrium charge state distribution. However, further increases to the target thickness result in increased energy attenuation which decreases the equilibrium charge state distribution. This effect can be seen in Fig. 1.3. Selecting a single initial energy of ^{238}U beam to examine and comparing the mean charge state at different target thicknesses, it is clear the competing effects of increased charge-stripping interactions and greater energy attenuation result in an optimum GCS thickness for that particular initial beam energy. Target thicknesses both greater and lesser than this optimum value yield a lower mean charge. Additionally, this optimum thickness shifts to ever greater values as incident beam energy increases. For example the optimum thickness is about 2 mg/cm^2 at an energy of 14 MeV/u but about 4 mg/cm^2 at an energy of at 18 MeV/u.

Currently, the Radioactive Isotope Beam Factory, a facility of Japan's RIKEN uses a helium GCS maintained around 50 torr [2,4,22,23] and the FAIR facility at Germany's GSI has a pulsed GCS which provides peak pressure of around tens of torr which is sufficient for the low duty factor accelerator's needs [24–26]. For RIKEN, the beam energy at the charge

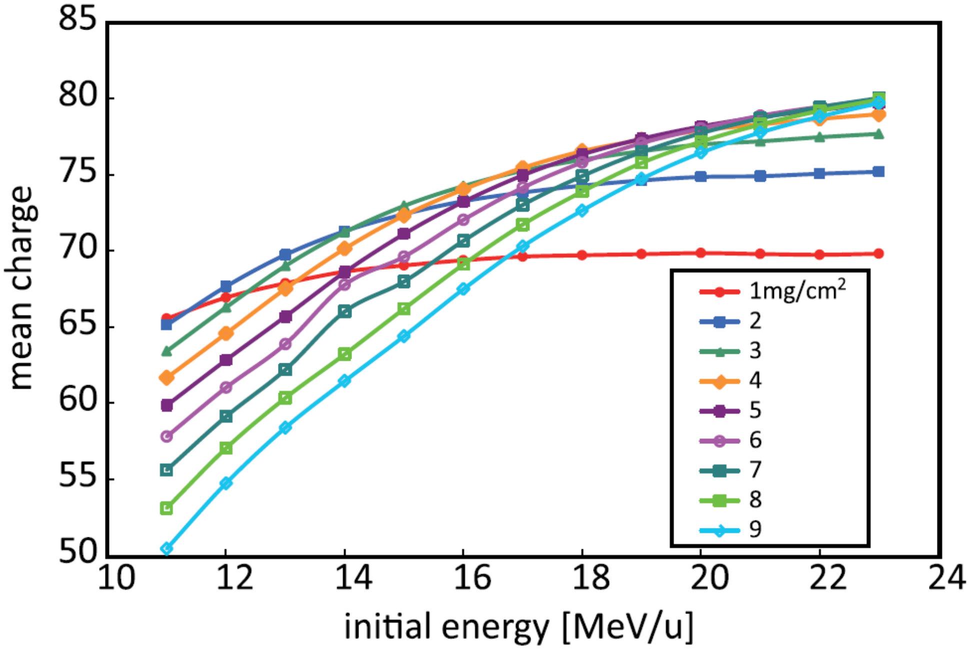

Figure 1.3: A figure published in Ref. [4], reproduced with permission. This shows calculations of mean (stripped) charge state of original $^{238}\text{U}^{35+}$ over a range of the beam's initial energy.

stripper is about 11 MeV/u, so based on Fig 1.3, the required target thickness for a 11 MeV/u U beam to achieve the equilibrium charge state is substantially lower than thickness required for achieving the equilibrium charge state for a 18 MeV/u U beam at FRIB.

The beam's interaction with the GCS also imposes a large power deposition, on the order of 1% of the beam power. Consider a beam that is 18 MeV/u ^{238}U, with current 350 eμA (hypothesized typical FRIB beam current for species O-U [27]) and transverse beam size of 1 mm diameter. For this beam impinging on a 300 torr, initially room temperature helium gas over a distance of 0.3 m, this corresponds to a power deposition of about 430 W and 1800 W/cm^3. An approximate calculation of the temperature rise of the helium gas in this beam-interacting column can be made by taking the specific heat of helium at standard temperature and pressure of 5.193 J/g*K, and supposing that the helium is flowing perpendicular to the beam trajectory at a rate of 100 m/s. With these conditions, the temperature increase of

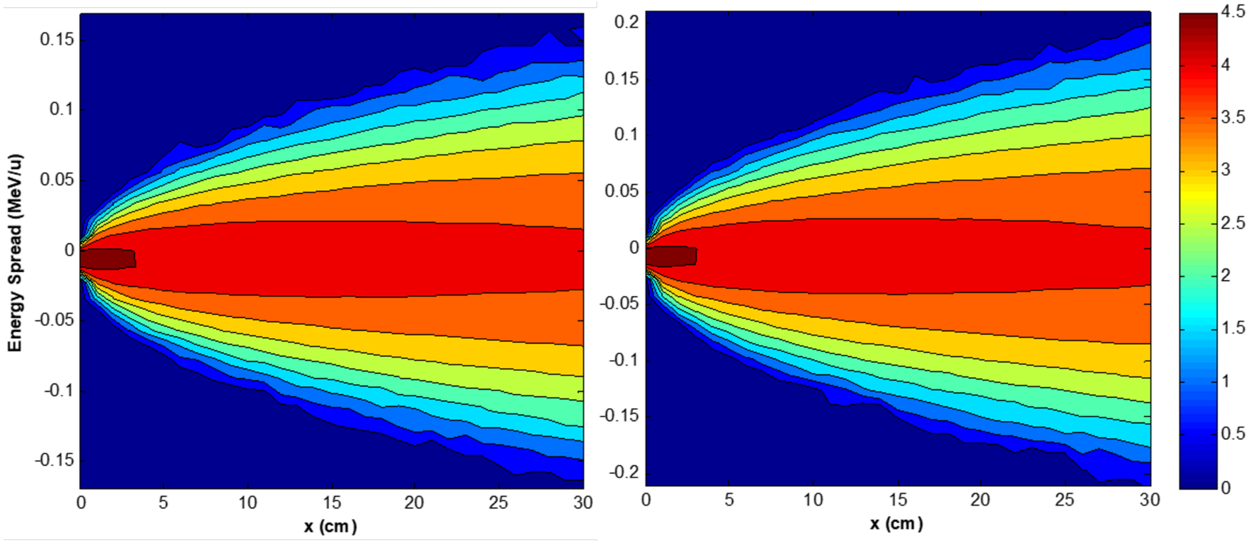

Figure 1.4: Energy spread calculations performed by F. Marti (left figure published in Ref. [3] and reproduced with permission, right figure unpublished). This indicates the growth of energy spread in a ^{238}U beam initially of charge state 33+ passing through a 225 torr (left) and 375 torr (right) He gas charge stripper that is 30 cm long. Note the change in ordinate scale.

the column of helium initially occupying the same volume as the beam is about 54 K.

Related to this is the issue of energy spread resulting from the ion beam's passage through the gas charge stripper. Simulations have been conducted by F. Marti [3] and P. Thieberger therein to assess the degree of energy spread the GCS introduces to the beam. In Fig. 1.4 an example of the energy spread evolution in 225 torr and 375 torr He gas charge strippers that are 30 cm long. The energy spread results from the beam heating the gas, which causes its density and therefore target thickness to change. In Fig. 1.5, another simulation published in Ref. [3] is shown, this one performed by P. Thieberger which illustrates the relative degree of energy spread in the outgoing beam after having transited a gas stripper with a single curtain of flowing stripper gas (as described above), as well as a gas stripper with two flowing curtains of opposing direction (red solid curve). This suggests that the differences in stripper heating can be mitigated by having multiple, direction-alternating curtain flows of stripper gas.

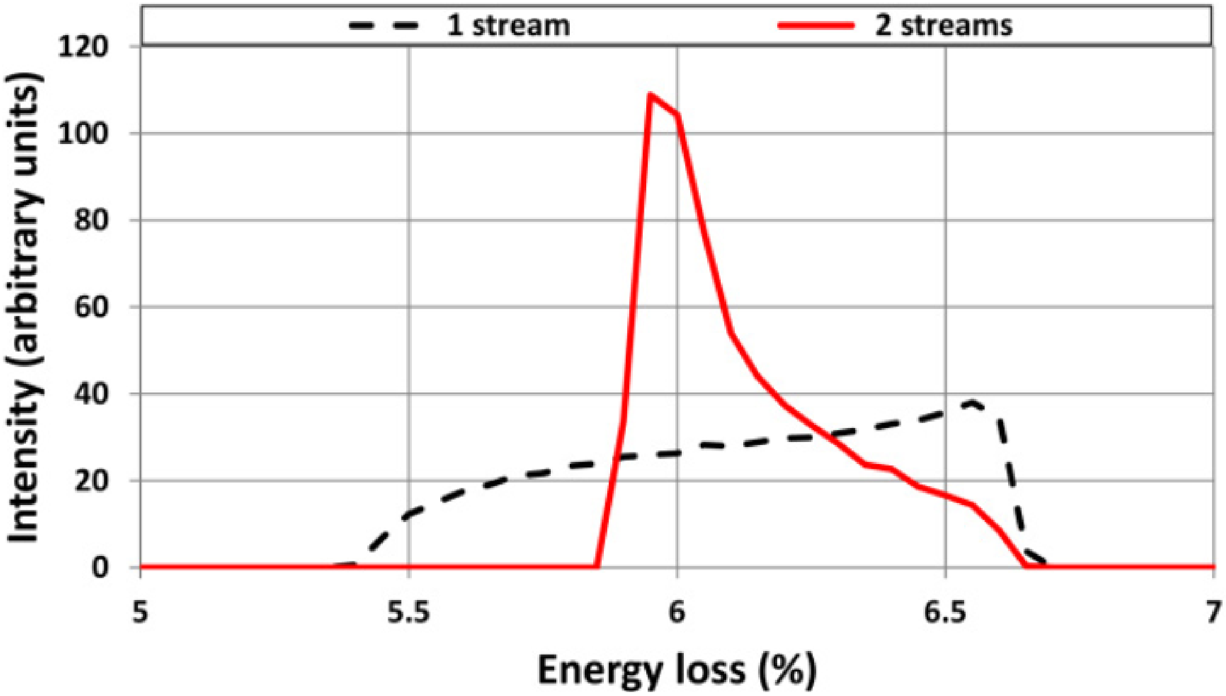

Figure 1.5: A figure published in Ref. [3], reproduced with permission. This is a calculation performed by P. Thieberger (Brookhaven National Lab). A greater spread in the beam energy loss means there will be a greater beam energy spread.

As mentioned above, the other challenge of gas charge strippers is that they require a system dedicated to containing the high pressure gas to prevent gas leakage to the upstream and downstream beamline. The GCS must be open-ended, since the ion beam would simply damage and ultimately bore through any solid walls containing the gas. This fact means that the contents of the GCS will leak out of the containing chamber at a rate related to the aperture size, since the conductance scales as the aperture area. To maintain constant pressure, the chamber must be constantly filled at the same rate that it leaks; this is accomplished differential pumping and recirculating the totality of the escaping gas. At beam energies between 10-20 MeV/u, helium gas yields the highest charge state distributions [2,22]. However its diffuses easily due to its low mass. This results in great difficulty in maintaining a chamber of sufficient pressure for charge stripping while simultaneously preventing the gas from flooding the rest of the beamline [23]. Maintaining low beamline pressure is a necessity to avoid unexpected interactions with background gas which would cause beam scattering and charge-exchange events, both of which would contribute to beam loss.

It is for this reason that a plasma window (PW) merits consideration, as it can greatly limit the gas leakage rate from a GCS operating at required pressures. This gas flow rate restriction is apparent when comparing the gas leakage rate through the PW channel from a given GCS pressure without arc to that when the arc is active, as illustrated in Fig. 1.6. A significant reduction in the rate of flow is observed, particularly for smaller diameter aperture channels, a fact that will be shown and explored in Chapter 4. The flow rate is restricted more with increasing current supplied to the arc. The conventional rationale for this behavior is that increasing temperature in the arc results in an increase in viscosity which inhibits the flow. It will be shown in Section 4.2.6 that this viscosity hypothesis isn't fully realizable under quantitative scrutiny, although the increasing temperature still plays a significant role.

In Fig. 1.6, the values included in parentheses next to the curves represent the flow rates corresponding to the respective GCS pressure without the presence of arc, merely a gas flow. It must be pointed out that these GCS pressures are actually not attainable with this PW test stand; the overall conductance is limited by the gas feed lines upstream of the PW and GCS, and is too small to allow most of these pressures to be achieved. Therefore, the values in parentheses are obtained by fitting to flow rates obtained at lower pressures and extrapolating to the higher ones. Measured flow rates through the PW channel without the presence of the arc are shown in Fig. 1.7. These flow rates are shown for several different PW channel configurations (or plate geometries), which are described in more detail along with an explanation of notation in Section 2.1.2. Note that by examining Figs. 1.6 and 1.7

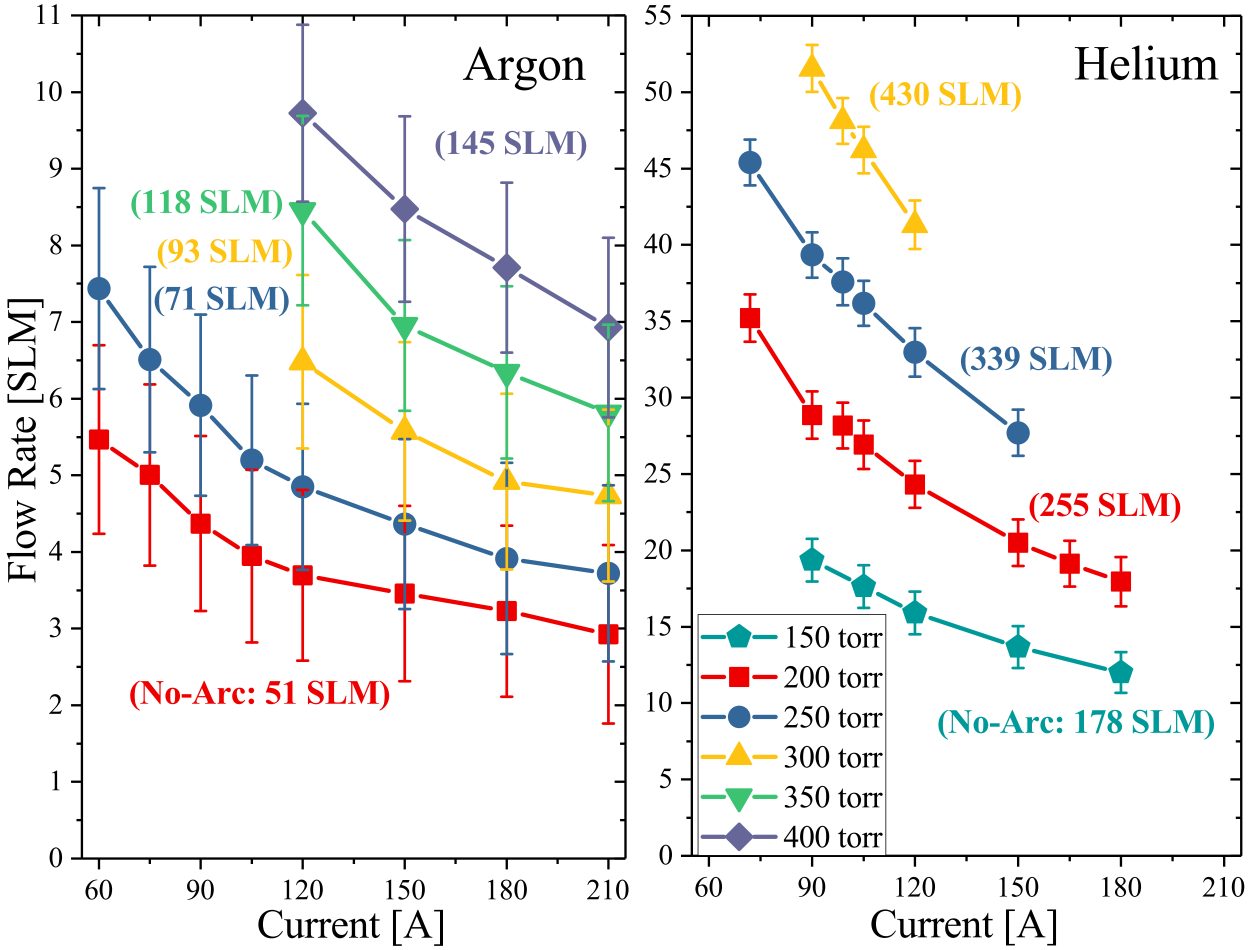

Figure 1.6: Flow rates in argon (left) and helium (right) gases for a PW consisting of six 6 mm aperture plates (6x6mm). Values in parentheses correspond to value obtained as the flow through the channel at the corresponding GCS pressure without the presence of the plasma arc.

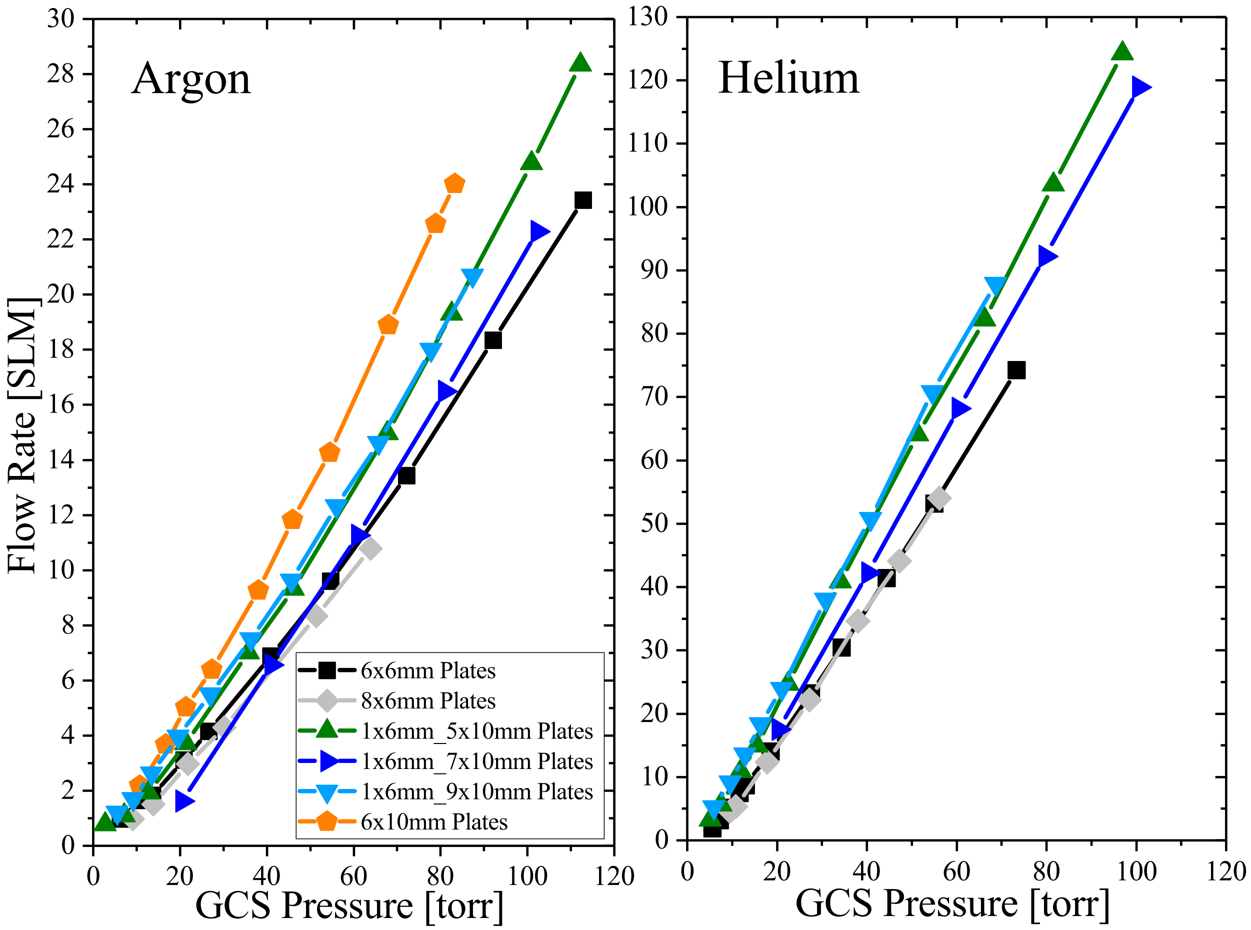

Figure 1.7: Flow rates in argon (left) and helium (right) gases through a variety of different PW channel configurations, all without presence of arc. Quadratic fits to this data are used to extrapolate no-arc flows to the GCS pressures studied in arc (100-400 torr).

that flow reduction rates for this geometry and these operating conditions are 10-24 for argon and 7-14 for helium. This significant flow reduction broadens the range of applicability of GCS applications.

1.2 Plasma

Plasmas span a vast array of conditions and regimes, as seen in Fig 1.8, but have some characteristics in common. Plasmas display behavior referred to as collective effects. This means that behavior of the entire plasma depends on the coupled behaviors of the individual constituents of the plasma (electrons, ions, and neutrals). An arc plasma is a class of plasma discharge that corresponds to currents in excess of about 1 amp and voltage drops of hundreds of volts across the arc [28].

Due to the high mobility of electrons in a plasma, the media is highly conductive and easily transmits current. Generally in plasmas, charge quasineutrality is assumed [5]. In this condition, the plasma is considered to be overall charge neutral and the plasma electron density n_e about equal to the ion density n_i in the bulk of the plasma, if only singly-ionized charge states of the gas species are present. The condition does not hold in certain locations such as near the cathodes, anode, and the enclosing walls. Here, "near" generally means several times a characteristic length called a Debye length. This is the length scale over which the electric field of any given plasma electron or ion is screened by oppositely charged neighbors by a factor $1/e$ ($e \simeq 2.72$) of what it would be without the presence of screening particles and is defined as [6]:

$$\lambda_D = \sqrt{\frac{\epsilon_0 k T_e}{e^2 n_e}}\,, \tag{1.2}$$

in which ϵ_0 is the perimittivity of free space, k the Boltzmann constant, T_e is the electron temperature, e the elementary charge, and n_e the electron density (which is also equal to ion density n_i in quasineutral regions as mentioned above).

1.2.1 Cascaded Arc Discharge

As mentioned above, An arc plasma is a class of plasma discharge that corresponds to currents on the order at least 1 A, across a voltage drop typically on the order of 100 V [28].

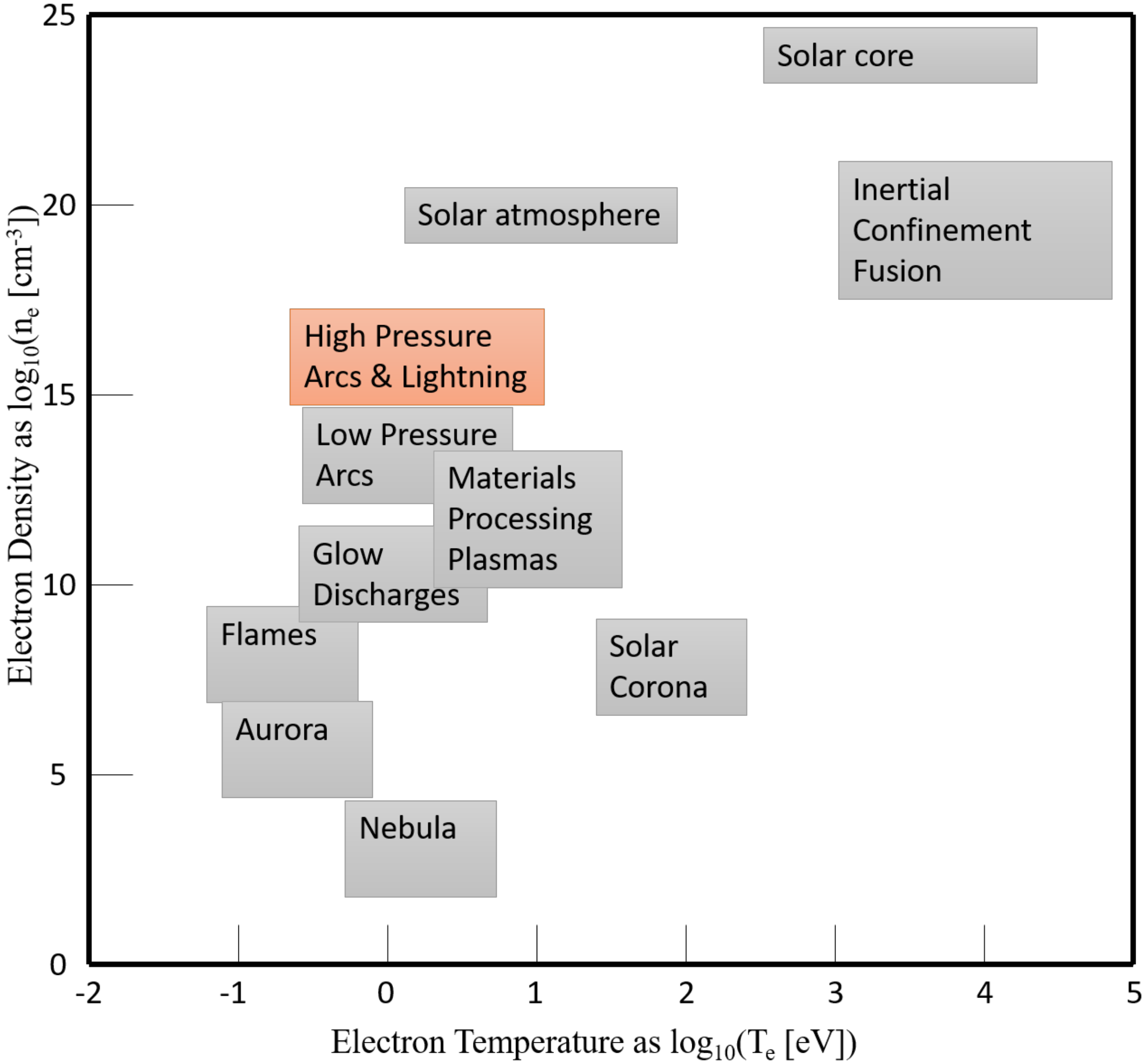

Figure 1.8: Plasma electron density vs. electron temperature, created after similar figures in Refs. [5,6]. The PW plasma characteristics would place it within the colored box ”High Pressure Arcs & Lightning”.

Plasmas generally need a continuous source of energy to sustain themselves, as otherwise the electrons and ions will tend to recombine back into neutral particles. In a star, this energy source is nuclear fusion. In a laboratory plasma arc such as the PW, the energy source is the electric field generated by the power supply in combination with the electrons expelled from the cathode(s) which initiate the process of ionizing the background gas, a process that propagates down the channel's length. If the local electric field is sufficient such that electrons may be emitted from the cathode surface and gain enough energy to ionize the local gas, electric breakdown will occur and an arc flow of current will be triggered [5]. In the PW, this high arc-initializing field is generated by means of a Tesla coil, which is only necessary to initiate the arc and is otherwise inactive. Subsequently, ions produced in the initial breakdown are heated through collisions with electrons, and are drawn to the cathode surface by the plasma electric field (separate from the Tesla coil field), whereby collisions heat up the cathode. The combination of the cathode's electric field and the heating by ion bombardment can allow electrons in the cathode to be elevated above the surface's work function and be ejected into the plasma. This is thermionic emission and distinguishes arc discharges from glow discharges, in which electrons are liberated from the cathodes by ions accelerated through a local potential drop, the cathode sheath [5, 28]. These electrons gain energy in the electric field that is established in the channel between cathode and anode, and share that energy with the heavy particles (ions and gas) through elastic and inelastic collisions [28].

It may spare some confusion to point out that in this thesis the descriptor "heavy" is applied in two distinct contexts: one referring to accelerated ion beam particles of relatively high nucleon count e.g. uranium; and a second referring to those particles within a plasma which aren't electrons (i.e. the neutral gas and singly-charged ion species). Generally these will be discussed as “heavy ion beam particles” or “heavy particles” for the two situations respectively, and the context of the discussion should be sufficient to deduce which is being referred to. The plasma heavy particles are also frequently simply called “heavies”.

An arc discharge is characterized by a moderately high current ($I > 1$ A) and low voltage (10s-100s of volts) [28], and a cascaded arc structure is a common means of enclosing this arc. The cascaded arc structure is a type of wall-stabilized arc discharge in which there are a series of individual metal plates insulated from one another along the channel with a floating potential dictated by the plasma within, in between the cathode and anode. This structure enables a gradual stepping down of voltage between the cathode and anode, granting greater stability to the arc than would otherwise be achievable over that same distance [29]. Additionally, this allows for the enclosing surfaces to be water cooled while not being a grounded surface that the arc would terminate at. Figure 1.9 shows a photo of such an arrangement, our cascaded arc that we refer to as the plasma window. The structure of the plasma window will be presented in detail in Section 2.1.

The arc is termed “wall-stabilized” because in order for the arc to be operated continuously, the high heat load (up to tens of kW) is transported via conduction to the walls [28]. This heat must then be removed to a void damage to the material structure, so all of these components need to be continuously cooled in order to prevent excessive heating, as they are all in contact with the heated gas of the arc. Pure water is usually the coolant of choice due to its low cost, ease of implementation, and high specific heat capacity. Furthermore, pure water (emphasizing that the water must be pure) has low conductivity so there will be very little electrical current through the coolant.

In Ref. [29] Maecker notes that for arc discharges that are arranged horizontally, as is the case in the present plasma window, there can be some nonuniformity in properties due

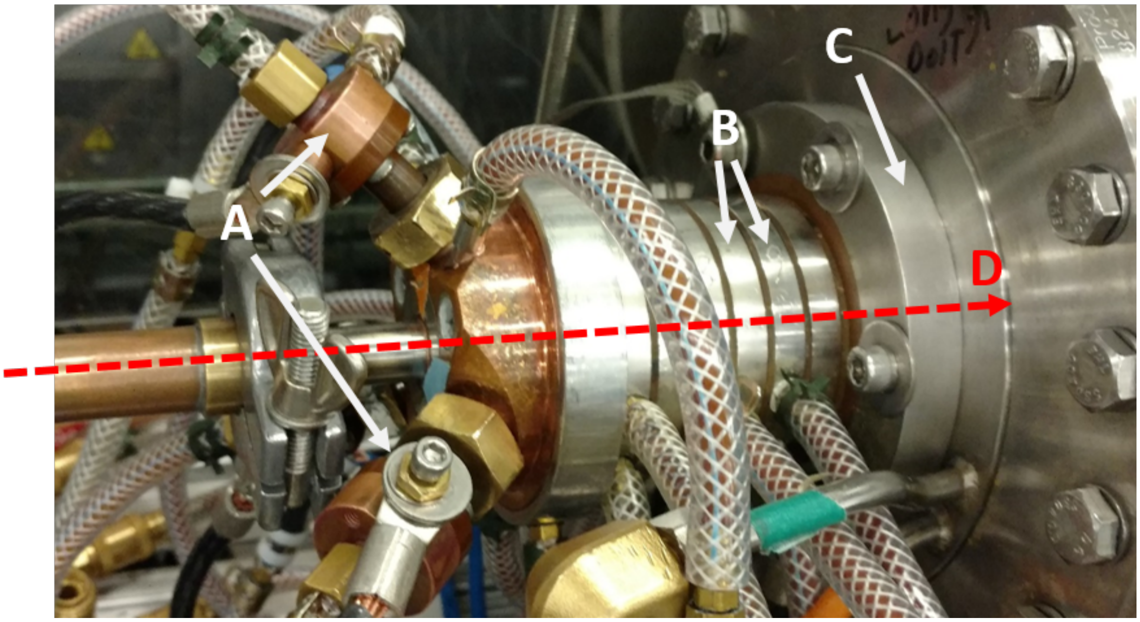

Figure 1.9: A photo of the plasma window. Labeled components are as follows: A. are the cathodes, B. are the cascaded plates (6 total in this image), C. is the anode plate attached to an expansion chamber connected to the vacuum pump assembly, and D. is the ion beam's trajectory through the plasma window, and the direction of gas flow. Outside of this image on the left side is the GCS chamber.

to natural convection. This effect is not considered in this work as the convective rate is insignificant compared to the plasma flow speed ranging from 100s to 1000s of m/s.

In the present application, the existence of the arc discharge in a channel connecting a chamber maintained at high pressure to a low pressure one under continuous evacuation is used to effect a reduction in the mass flow of gas through the channel from what it would be without any plasma arc in the region (just gas flow). The most commonly cited mechanism for being the root cause of this flow rate reduction is an increase in the channel's viscosity due to arc heating the gas throughout [30–32] and frequently the mass flow is reported to be described in terms of Poiseuille's equation [33–37], given by:

$$\dot{m}_P = \frac{\pi D^4 \bar{\rho} P'}{128\bar{\eta}} \, . \tag{1.3}$$

Here $\dot{m}_P$ is the Poiseuille mass flow rate, D is the channel diameter, ρ is the mean mass density of the gas throughout the channel, P' is the axial pressure derivative, and η is the mean viscosity throughout the channel. However, Poiseuille's equation, which is derived assuming a near-constant velocity through the channel, does not accurately model the characteristics of the flow. Viscosity in fact plays only a minor role in establishing the mass flow through the arc channel. The reasons for this are explored in detail in Section 4.2.6.

The degree of flow reduction achieved depends upon the operating conditions that a user can impose on the plasma window structure, namely the gas pressure upstream of the plasma, the arc current passing through the plasma, the geometry of the channel confining the arc, and the gas(es) flowing through the channel and being ionized. The influence of each of these properties on the flow rate will be investigated in this work. The limitations of the arc with reference to these properties will also be explored. Another phenomenon to note is the existence of a choked flow condition at the exit of the PW, where the gas expands into a larger chamber. Here the flow speed is supersonic and the pressure in this area can not have any impact on the behavior within the PW channel itself. Therefore, the flow rate through the channel for some given GCS pressure and arc current cannot be made any lower by changing outlet side characteristics.

There are operational limitations associated with each of these features of the arc which an operator sets. For a given arc current, gas pressure can only be reduced so much, until at some point there are insufficient ion collisions on the cathode to expel electrons to sustain the arc current. At this point, the arc collapses. The capabilities of the cooling system place upper limits on the gas pressure and arc currents, since the heat rate delivered by the arc to the electrodes increases with both quantities. Voltage drop over the arc increases with increasing cathode-anode distance (accomplished by employing either thicker plates or more of them). Plasma conductivity needs to be maintained over the entire channel to allow for electrons to transmit the current across the length, so the electric field must remain roughly unchanged over a longer distance, thus necessitating a greater total voltage drop with increasing arc length.

For the flow of any fluid through a region, one can obtain equations describing the balance of conserved kinetic properties by taking velocity moments of the Boltzmann equation [38–40]. The Boltzmann equation describes the statistical behavior of particles of species a whose velocities can be described by a distribution function $f_a(t, \mathbf{r}, \mathbf{v})$ over positions $\mathbf{r}$ and velocities $\mathbf{v}$. This Boltzmann equation is given by:

$$\frac{\partial f_a}{\partial t} + \frac{\partial}{\partial x_\beta}(v_\beta f_a) + \frac{\partial}{\partial v_\beta}\left(\frac{F_{a\beta}}{m_a} f_a\right) = C_a \, , \tag{1.4}$$

in which t is time, β are the spatial dimensions (there is an implicit sum over these in the above equation), m_a the mass of species a, $F_{a\beta}$ is the force exerted on a particle of species a and velocity $\mathbf{v}$, and C_a is called the collision term, which characterizes the effect of collisions between species and other species, either via elastic or inelastic scattering. We will consider this being applied to a plasma consisting in part of charged species which interact via the electromagnetic force involving a particle of charge e_a, so:

$$\mathbf{F}_a = e_a \mathbf{E} + e_a(\mathbf{v} \times \mathbf{B}) \, . \tag{1.5}$$

Balance equations for conserved properties (mass, momentum, and energy in particular) can be obtained in terms of macroscopic characteristics of the plasma by multiplying Eq. (1.4) by a power of velocity, and integrating over the distribution $f_a(\bar{x}, t)$ [39,41] over velocity.

Doing so with the $\mathbf{v}^0 = 1$, produces the particle continuity equation:

$$\frac{\partial n_a}{\partial t} + \nabla \cdot (n_a \mathbf{u}_a) = S_a\,, \tag{1.6}$$

where n_a is the number density of species a, u_a is the fluid flow velocity of species a, and S_a is the source term for volume production of species a.

Integrating over the distribution $f_a(\bar{x}, t)$ with $\mathbf{v}^1$, specifically multiplying (1.4) by $m_a\mathbf{v}$, produces the momentum balance equation:

$$\frac{\partial}{\partial t}(mn_a\mathbf{u}_a) + n_a m(\mathbf{u}_a \cdot \nabla)\mathbf{u}_a + \nabla P_a + \nabla \cdot \overset{\leftrightarrow}{\pi} - qn_a(\mathbf{E} + (\mathbf{u}_a \times \mathbf{B})) = S_m\,, \tag{1.7}$$

in which - in addition to the previously mentioned symbols - m_a is the mass, P_a is the partial pressure, q and is the electric charge, all of species a. Also, the electric field and magnetic field are given by E and B respectively, $\overset{\leftrightarrow}{\pi}$ is the stress tensor, and S_m is the source term for volume production of momentum for species a.

Integrating over the distribution with the velocity power being 2, specifically multiplying (1.4) by $m_a\frac{\mathbf{v}^2}{2}$ produces the energy balance equation:

$$\frac{\partial}{\partial t}\left(\frac{3}{2}n_a kT_a\right) + \nabla \cdot \left(\frac{3}{2}n_a kT_a\mathbf{u}_a\right) + n_a kT_a \nabla \cdot \mathbf{u}_a + \left(\overset{\leftrightarrow}{\pi} \cdot \nabla\right)\mathbf{u} + \nabla \cdot \mathbf{Q} = S_E\,, \tag{1.8}$$

in which T_a is the temperature of species a, Q is the thermal heat flux, and S_E is the source term for volume production of energy for species a.

Though these equations may appear daunting in these forms, some simplifying measures will be applied in Section 3.3 to make them more palatable and while still readily useful for analysis of the plasma window.

1.2.2 Collisions

Collisions in this work are always be treated as binary, between two particles which can either be the same type or different. If one of these collision participants is very slow relative to the other, we consider it stationary. Given that the thermal speeds of electrons and heavy particles are vastly different whenever $T_e \geq T_h$ (which is always the case in the plasmas investigated here). Due to the vast mass discrepancy, electrons can be considered as projectiles and heavies the stationary targets. The frequency with which a given binary collision occurs can be expressed as:

$$\nu_c = n_{tar} \langle v\sigma \rangle \,, \tag{1.9}$$

where the collision frequency is given by ν_c, the electron velocity is v, the target particle density is n_{tar}, and the process cross section is given by σ. The brackets signify that an average must be taken over the projectile energy distribution. We assume the velocity distribution is isotropic so we can substitute v for the kinetic energy $\sqrt{\frac{2E}{m_e}}$ of the electron projectile.

In general, the electron temperature can be, and frequently is, different from the temperature of the ions or gas. However, the ion temperature and gas temperature (that of the neutral particles) are frequently considered to be the same and don the moniker heavy particle temperature, T_h. This condition, also sometimes referred to as thermal nonequilibrium, is established when the electron-heavy energy exchange rate is close to or slower than the time scales for plasma transport [42,43]. The rate of energy exchange between two identical particles (electron-electron or heavy-heavy) is much more rapid than the exchange of energy between electrons and heavies [28,39,44] because binary collisions of like-massed particles results in greater energy exchanged than in collisions between particles with a large mass disparity. The associated self-thermalization times are quite rapid [41], as can be seen by the energy exchange rate Q_{ab} for species a and b:

$$Q_{ab} = 3\frac{m_a}{m_b} n_a \nu_{ab} k (T_a - T_b)\,, \tag{1.10}$$

where the species masses are given by m, temperatures are given by T, and the momentum-transfer collision frequency between the two is ν_{ab}. For particles of large mass disparity, e.g. if electrons colliding with gas atoms, the $\frac{m_a}{m_b}$ term will be smaller by a factor of at least 1/2000 than if the colliding species were both electrons or both gas atoms.

1.2.3 Emissions

Energetic electrons colliding with the heavier plasma constituents (ions and neutrals) can do so either elastically, or inelastically. With sufficient energy, electrons can ionize the heavy particle, removing one of its valence electrons in a reaction given by:

$$e + A_i \longleftrightarrow 2e + A_{i+1}\,, \tag{1.11}$$

where i is the initial ionization stage of atom species A. Note that this is a reversible reaction, with the reverse process being a three-body recombination. The atom can also undergo an excitation by the electron-impact collision, where one of the valence electrons is promoted to a higher energy level:

$$e + A_i(l) \longleftrightarrow e + A_i(u)\,, \tag{1.12}$$

where l and u denote lower and upper energy states of the reaction respectively. Note again that this is a reversible reaction.

Each possible reaction is governed by an interaction cross section, which, when coupled with the electron velocity distribution function, can be used to obtain that reaction's rate. Furthermore, if one assumes that the thermal electron velocites are much larger than any directional velocities, the three-dimensional Maxwell-Boltzmann distribution can be foregone in favor of a velocity-magnitude, or electron energy distribution function (EEDF) $f(E, T_e)$. Generally the heavy particles (neutrals and ions) are colder than the electrons, but even for equal temperatures, the heavies will have much lower thermal speeds due to their larger mass. As a result, for a given binary electron-impact reaction, the rate constant K of that reaction can then be obtained by:

$$K = \int_0^\infty f(E, T_e)\sqrt{2E/m_e}\,\sigma(E)dE\,. \tag{1.13}$$

Here, E is the electron kinetic energy, m_e the electron mass, $\sigma(E)$ is the process cross section as a function of energy, and $f(E, T_e)$ is the EEDF which is a function of energy E and the electron temperature T_e.

From here on, this section will refer to excited states as excitations of the neutral species, but it is worth emphasizing that so long as the heavy particle in question is not completely ionized (if that's the case, there are no more electrons to be excited or removed), all of the following can also apply to an ion's excited states as well. After being excited, the atom will remain in that state until it undergoes another process - either spontaneous emission to a lower state, or another collision with an electron that results in another excitation, de-excitation, or ionization.

In a spontaneous emission, the excited atom relaxes to a lower state by emitting a photon, which are typically in the infrared, visible, or UV range. This process naturally occurs in plasmas with predictable rates [7, 45] without any external influence, so utilizing these emissions for diagnostic purposes is convenient in that it is noninvasive and does not perturb the plasma [46], unlike other plasma diagnostic tools such as Langmuir probes which create a local perturbation. The photon energies of these emissions are equal to the difference between the upper (excited) and lower (relaxed) state. The characteristic energies of these excited states are linked to the the atom (or ion) in question. A Grotrian diagram indicates the energy levels of potential excited states of a given element and charge state and the allowed transitions between them. One example is provided in Fig. 1.10 for excited atomic helium (or He I) transitions. This diagram shows the emission lines observed in helium plasma using a spectrometer which will be described in Section 2.1.3.1

There are other sources of light from a plasma as well, which contribute to the spectrum's continuum emissions. These are, blackbody, free-bound transitions, and free-free transitions. In the visible wavelengths which are of concern in this thesis, the primary contributors are free-bound transitions and free-free transitions. These sources of continuum radiation originate from interactions of electrons with the heavies, i.e. the neutrals and ions. The free-bound radiation, also called recombination radiation, originates from a free electron recombining with an ion to form a bound state of an atom (or ion of a smaller charge state than originally), resulting in an emission of energy equivalent to the kinetic energy minus the difference between the ionization energy (corresponding to the original ion) and the

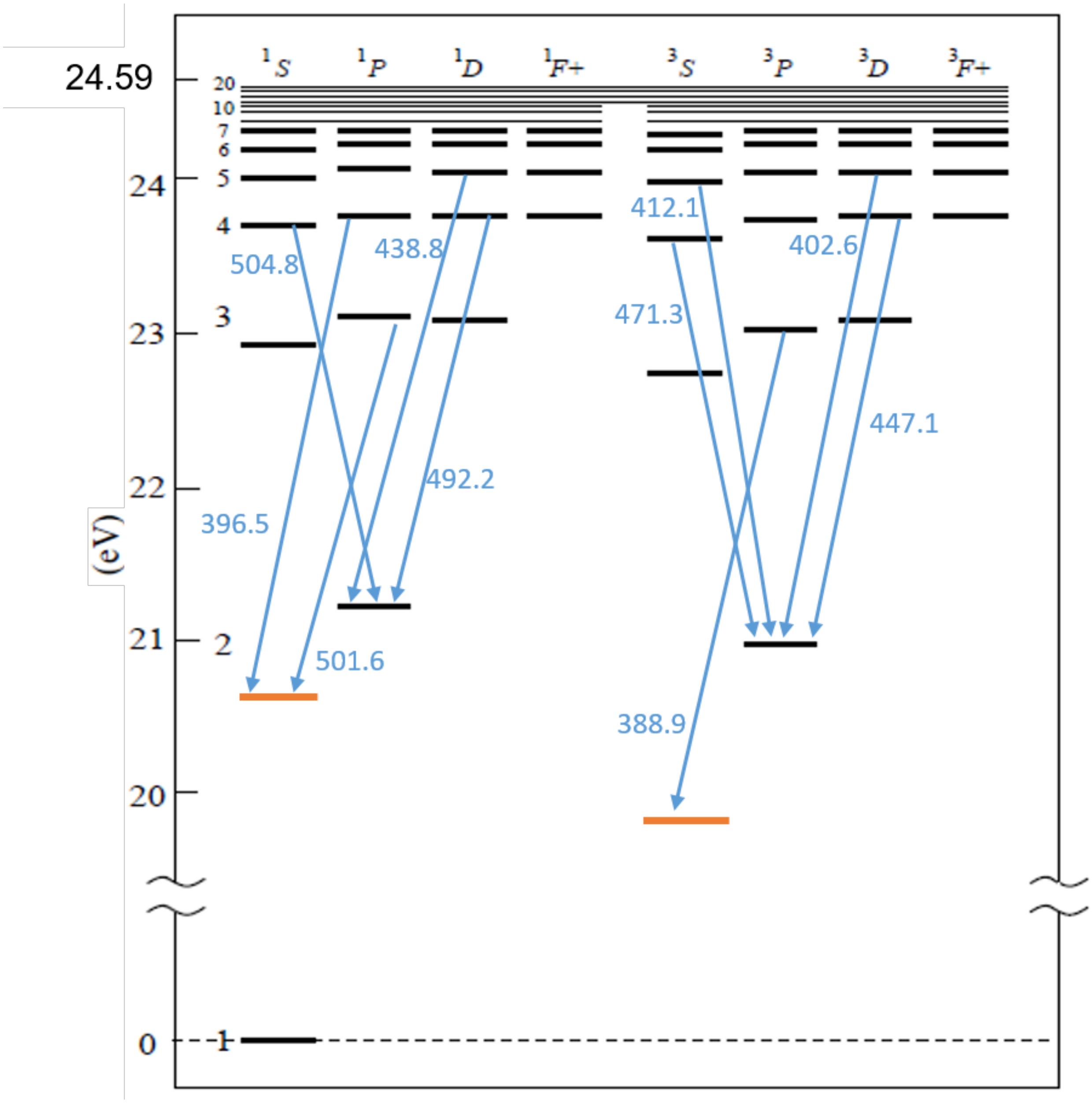

Figure 1.10: A Grotrian diagram illustrating the excitation level scheme of He I, with the levels in orange being the metastable levels. Blue lines indicate observed He I emissions that will be used to determine electron temperature T_e and electron density n_e. The labels are the emission wavelengths in nm.

bound state energy. Free-free radiation, also called Bremmsstrahlung radiation, results from acceleration of electrons colliding with an atom or ion, but without involving a recombination (the electron remains free after the interaction) [7,47,48].

1.2.4 Equilibrium Types

Often, the electrons within a plasma are assumed to follow a Maxwell-Boltzmann distribution, particularly at electron densities exceeding 10^{15} cm^{-3}, as is the case for the PW. This claim will be examined in more detail in Section 3.1, but for now we will take the electron energy distribution function (EEDF) as a Maxwellian, given by:

$$f(E,T_e) = 2\sqrt{\frac{E}{\pi}}\left(\frac{1}{kT_e}\right)^{3/2}\exp\left(\frac{-E}{kT_e}\right), \tag{1.14}$$

in which E is the electron energy and T_e is the electron effective temperature (an average quantity over the energy distribution function)

Practically, it is frequently of great importance to be able to calculate relative populations of the excited states of atoms or ions in a plasma of some temperature, pressure, and electron density, and doing so requires knowledge of the EEDF. All processes are in equilibrium with the inverse process, including emitted de-excitation radiation and its absorption. The populations of these excited states also depend upon the class of equilibrium the plasma exists in. Some relevant equilibria are briefly introduced below.

Thermal Equilibrium: This is a generally un-achievable condition in which particle densities can be calculated for all excited states, and are given by Boltzmann relation [43]:

$$\frac{n_k}{n_j} = \frac{g_k}{g_j}\exp\left(-\frac{E_k - E_j}{kT}\right), \tag{1.15}$$

in which, for states j and k, n are the state densities, g are state degeneracies, and E_u are the state energies.

Local Thermodynamic Equilibrium:

In the local thermodynamic equilibrium (LTE) regime, all kinetic temperatures are locally equal for each particle species, so $T_e = T_h = T$ [44,49]. Rates from collisional processes are much greater than rates from radiative processes , and all excited levels are in a thermodynamic equilibrium system of the same temperature T, so level densities are given by a Boltzmann distribution as in Eq. (1.15). This condition can sometimes be satisfied in laboratory plasmas, but requires relatively high densities, generally around 1×10^{17} cm^{-3} at least [47,50].

Partial Local Thermodynamic Equilibrium:

In this case, only populations of excited levels of sufficiently high state energy are related via Saha-Boltzmann relations to the next ionization stage's ground state. Equations and further discussion on the topic of partial local thermodynamic equilibrium (PLTE) are presented in Section 2.2.3.1.

1.3 Dissertation Organization

Chapter 2 — Experimental outlines, design, and instrumentation of the NSCL plasma window test stand will be described in this chapter.

Chapter 3 — Theory governing operation of the cascaded arc and flow characteristics in the plasma window as well as models with which to compare measurements with will be discussed.

Chapter 4 — Analysis results will be thoroughly detailed for the plasma window operating conditions that have been studied, and comparisons with other works will be presented.

Chapter 5 — Key findings will be summarized and discussion of the subsequent necessary steps for implementation with a gas charge stripper will be given.

Chapter 2

Experiment

2.1 Test Stand

Many of the components of the NSCL plasma window test stand have previously been described in Ref. [51]. The plasma window portion of the test stand is shown in Fig. 2.1, showing its position between the GCS chamber and the main chamber, also called the expansion chamber. The test stand acts as one side of the gas charge stripper assembly through which the ion beam would traverse. The system can be operated in either a fresh-gas mode in which the gas flow is sustained from a gas cylinder and is expelled directly to atmosphere, or in a recirculation-mode in which initially a large buffer chamber is pressurized with the gas from the cylinder and once full, a series of valves change the flow origin from the gas cylinder to this buffer chamber. In this mode, the gas is not expelled to atmosphere and instead continuously cycles through the test stand. Schematic diagrams for the fresh gas mode and recirculation mode are presented in Figs 2.2 and 2.3 respectively.

The gas flow is measured via an OMEGA FMA 1844A flowmeter calibrated for helium flows from 0 to 500 SLM. If the gas is argon, then a relative correction factor can be applied to convert between the measurement to equivalent argon flow according to instrument documentation. This relative correction factor, given in the respective device manuals, is expressed as:

Figure 2.1: A photo of the test stand, showing the section that includes the plasma window and associated diagnostics, the gas charge stripper chamber, and the main chamber.

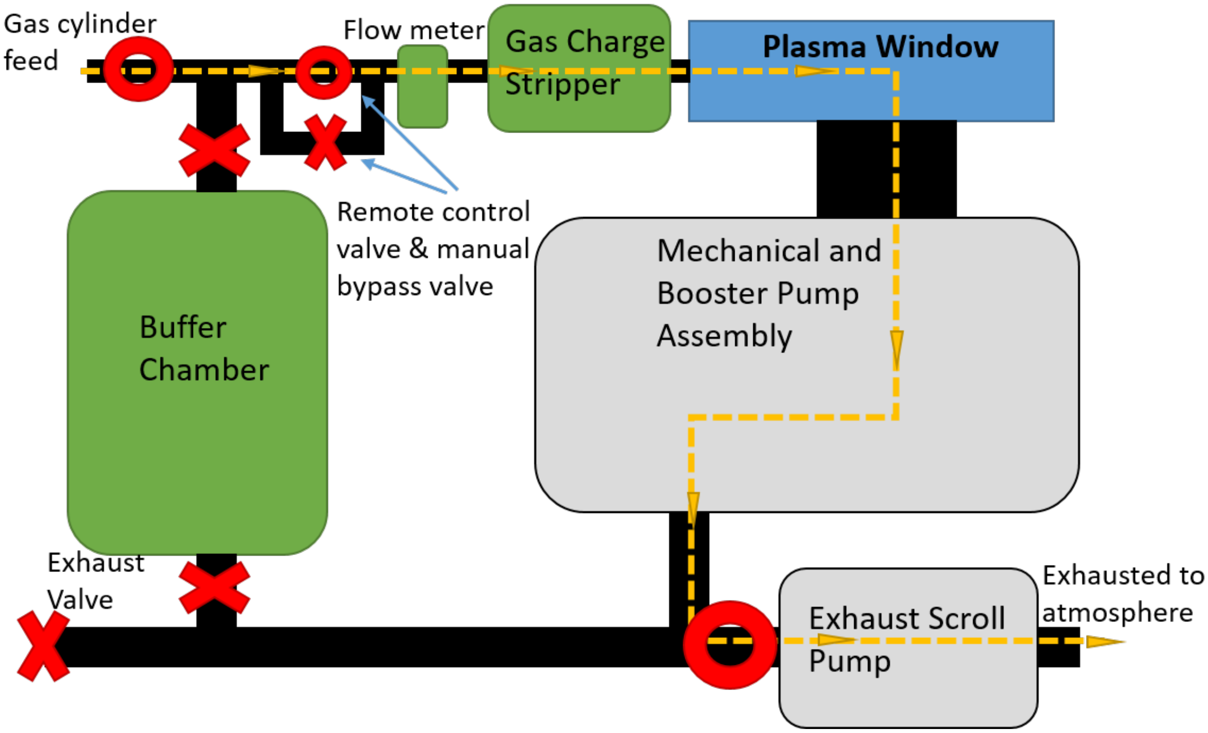

Figure 2.2: Plasma window test stand schematic in fresh gas flow mode. Either argon or helium is introduced via the gas cylinder feed.

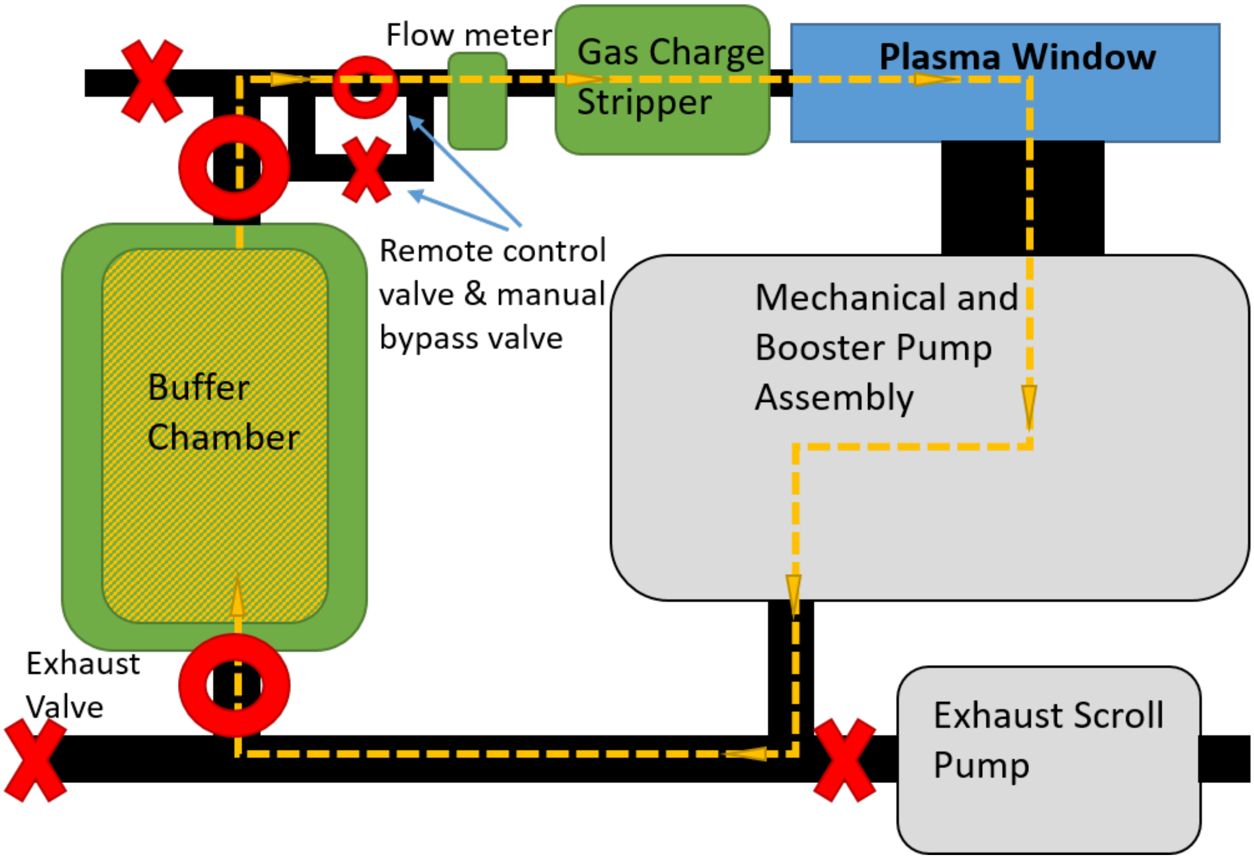

Figure 2.3: Plasma window test stand schematic in recirculation gas flow mode. Before operation, the buffer chamber is pressurized to around 12 PSI.

$$K_{rel} = \frac{K_a}{K_b}\,, \tag{2.1}$$

where K_a and K_b are the correction factors in translating from a nitrogen-calibrated instrument to flow in gas a and b respectively. The instrument documentation provides that $K_{Ar} = 1.205$ and $K_{He} = 2.43$.

2.1.1 Plasma Window

The gas that ionizes to plasma inside the plasma window is that which flows out of the GCS as a result of the pressure difference established between the GCS and the main chamber which is attached to the vacuum pumps. The high pressure GCS chamber is located upstream of the cathode-side of the plasma window, and the anode-side being attached to the low pressure main chamber. A voltage of -300 V is applied between the PW and the GCS, in a small region separated on either side by insulating breaks, in order to prevent stray electrons from creating an arc backwards to the grounded GCS, a scenario that can be highly damaging to the metal tubing in this region. This feature is illustrated in Fig. 2.4. The region then, going upstream to downstream, contains the following each separated by insulating breaks: grounded GCS, the anti-backwards-arcing voltage, and the cathode housing structure of the PW.

As indicated in Figs. 2.2 and 2.3, the gas flow from the either the pressurized gas cylinders or the buffer chamber (depending on operation mode) is adjusted either automatically with an MKS 250E pressure/flow controller or manually with a manual bypass valve so as to obtain the desired pressure in the GCS, monitored by an MKS Baratron 622B. A photo of the plasma window is shown in Fig. 1.9 as set up for a 6x6mm configuration. Another view,

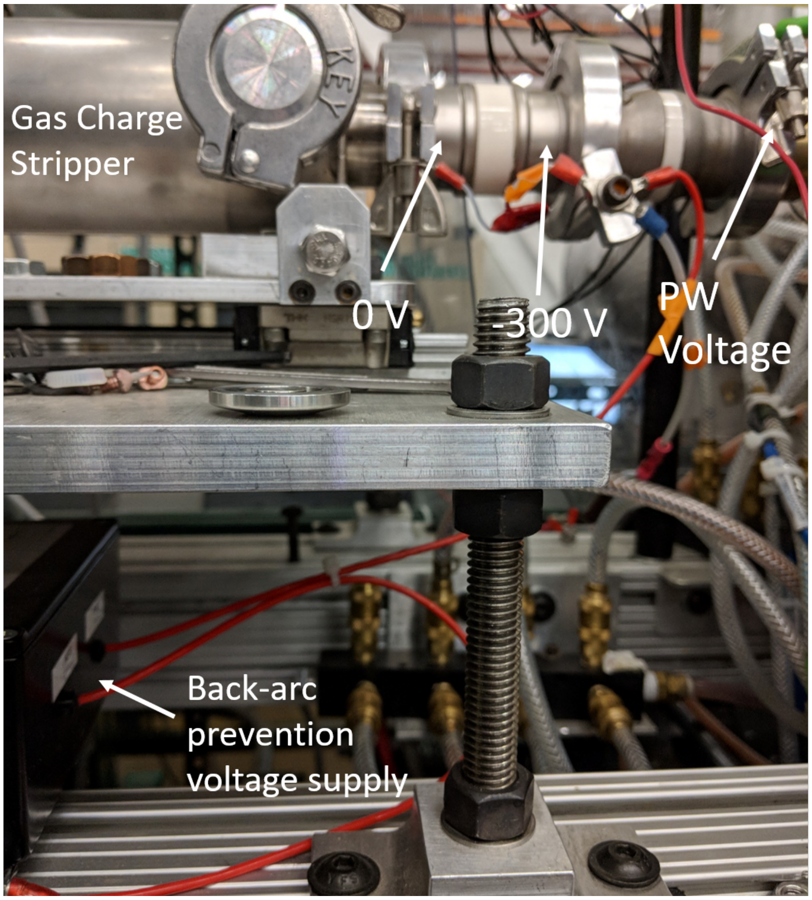

Figure 2.4: A photo of the region between GCS (shown on left side) and PW (out of view on right side). A voltage supply maintains a -300 V relative to the GCS in order to repel electrons that would generate an arc upstream towards the GCS rather than downstream through the PW.

this time for a 8x6mm configuration is shown in 2.5, this time showing some of the primary diagnostics used throughout this work.

The plasma window consists primarily of a cathode side and a set of individually insulated metal plates of floating potential which gradually step down the plasmas potential to the final grounded anode plate. These metal plates are what give this arc structure its name: cascaded arc. These wall voltages are established as follows: within the plasma, diffusion of the charged particles results in a portion of them colliding with walls of the channel. However, due to their vastly different masses and speeds, electrons and ions will collide with

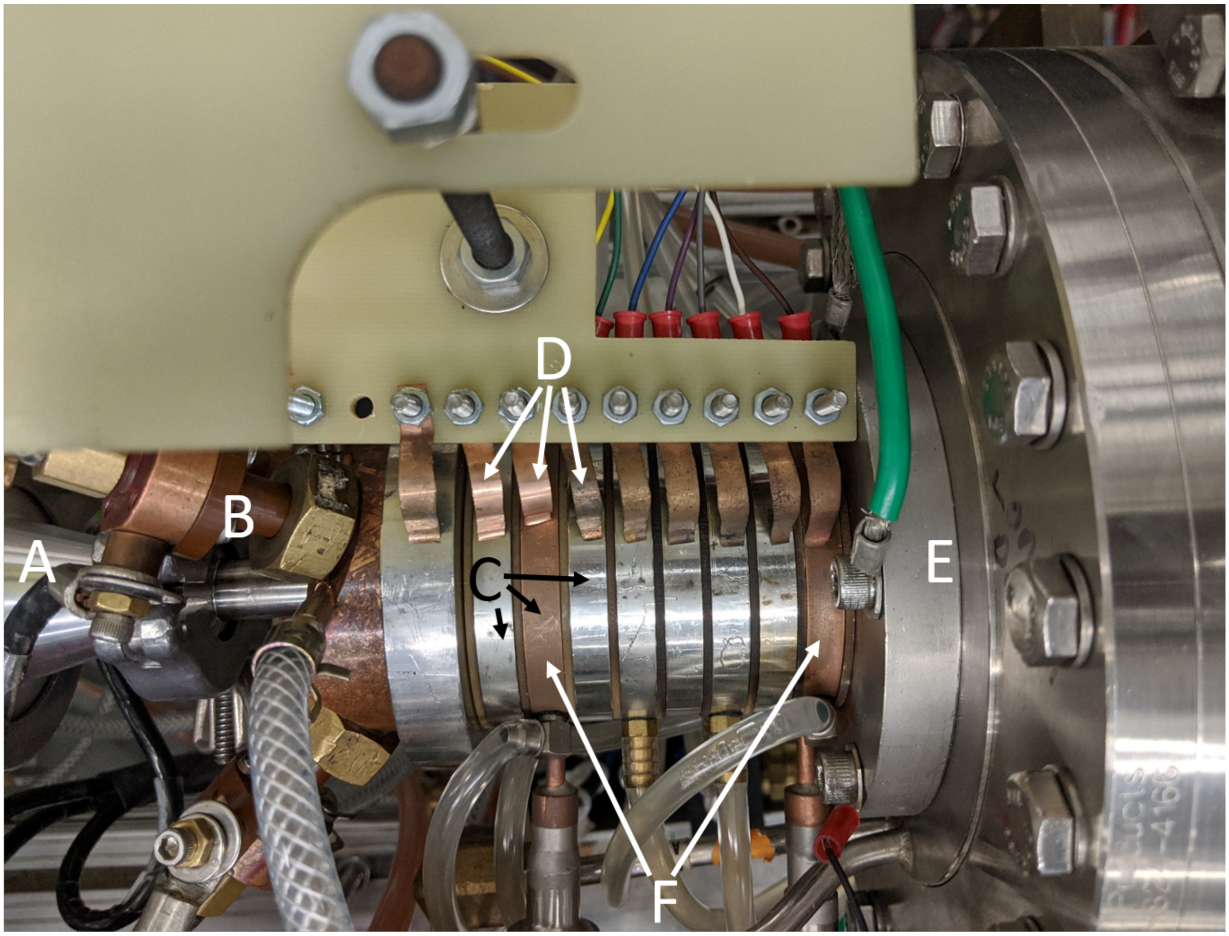

Figure 2.5: A photo showing another plasma window configuration, this time being a 8x6mm configuration and including several diagnostics used in characterizing the plasma. A. is the gas inlet connected to GCS, B. is one of the three cathodes inserted into the channel, C. are the PW cascaded plates, D. are copper fingers connected to voltage measurement setup described in Section 2.1.3.3, E. is the anode plate, and F. are diagnostic plates.

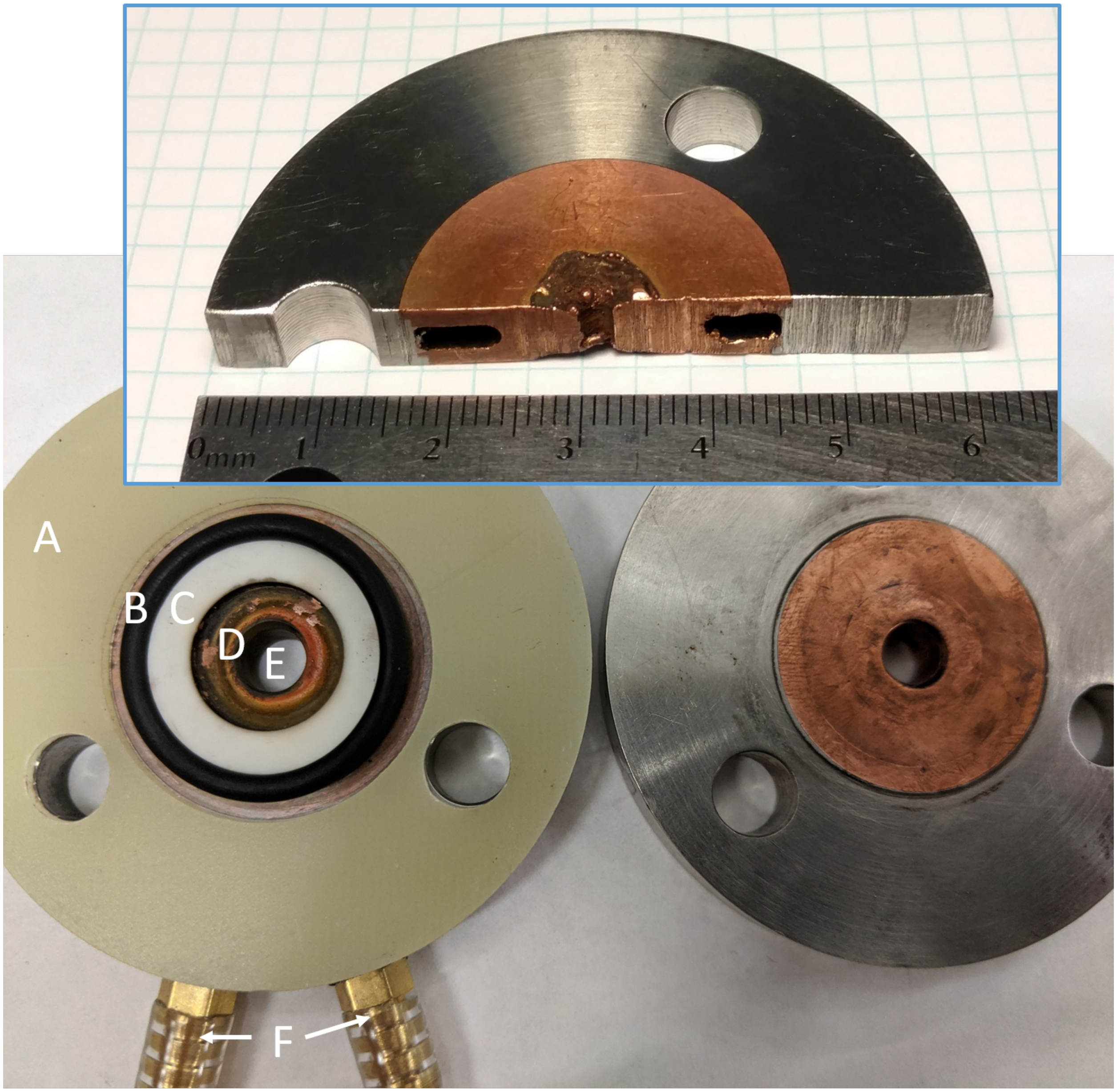

Figure 2.6: A photo of the components between PW plates and a bare plate. The labels are as follows: A. is the FR4 insulator, B. is the FFKM o-ring, C. is the alumina inner insulator, D. is the inner copper surface, E. is the plasma channel, and F. are the water coolant entry and exit ports. The top photo is of a cross sectional view of the plate, showing the coolant channel position and size.

the walls at different rates. For an electrode that is floating with respect to the plasma, this will result in a potential that is negative with respect to the bulk plasma potential.

Figure 2.6 illustrates the design of the plates and the components between the plates.

The plates are separated by a trio of concentric ring pieces: innermost is a ceramic insulator that protects the FFKM o-ring which is the middle component, and outermost is an FR4 insulating piece. These three ringed pieces provide insulation between plates so that their floating voltage and heat load can respectively be measured at multiple locations down the DC arcs channel in addition to allowing good vacuum sealing throughout the structure. Throughout this project, several different ceramic insulator materials have been used: boron-nitride (BN_3), aluminum-nitride (AlN), and alumina (Al_2O_3). Each plate has a channel for water coolant to pass surrounding the inner bore where the plasma is contained. Water of known flow rate and known supply and return temperatures is used as coolant, enabling one to easily calculate the amount of power removed for each plate via calorimetric analysis. The unique diagnostic plates that will be discussed in detail in Section 2.1.2 are made entirely of copper, whereas the other ordinary plates are comprised of a copper inner piece that is electron beam welded to a stainless steel outer piece.

The cathode segment consists of a holder which has three holes at azimuthally separated by 120 degrees, and at 30 degrees out from the longitudinal axis (arc-axis). The structure of the cathode holder is shown in Fig. 2.7. The cathode holder is a copper tube with an inner pathway to allow for water coolant similar to with the plates. Outside of this is a 2-piece insulating collar. The base part of this is a Vespel insulator (labeled C in Fig. 2.7) and functions as a spacer between the conducting metal of the electrode, and the housing structure (H). The other part is a hollow cylindrical jacket (B) that sits atop the Vespel base and extends along the remainder of the copper electrode piece (F). Additionally, an FFKM o-ring (D) is fitted on the outside of this insulator to provide vacuum sealing against the lip of the housing hole into which the cathode is inserted. Screwed into the top of this copper is a wide copper attachment called a shield in which is held the thoriated tungsten,

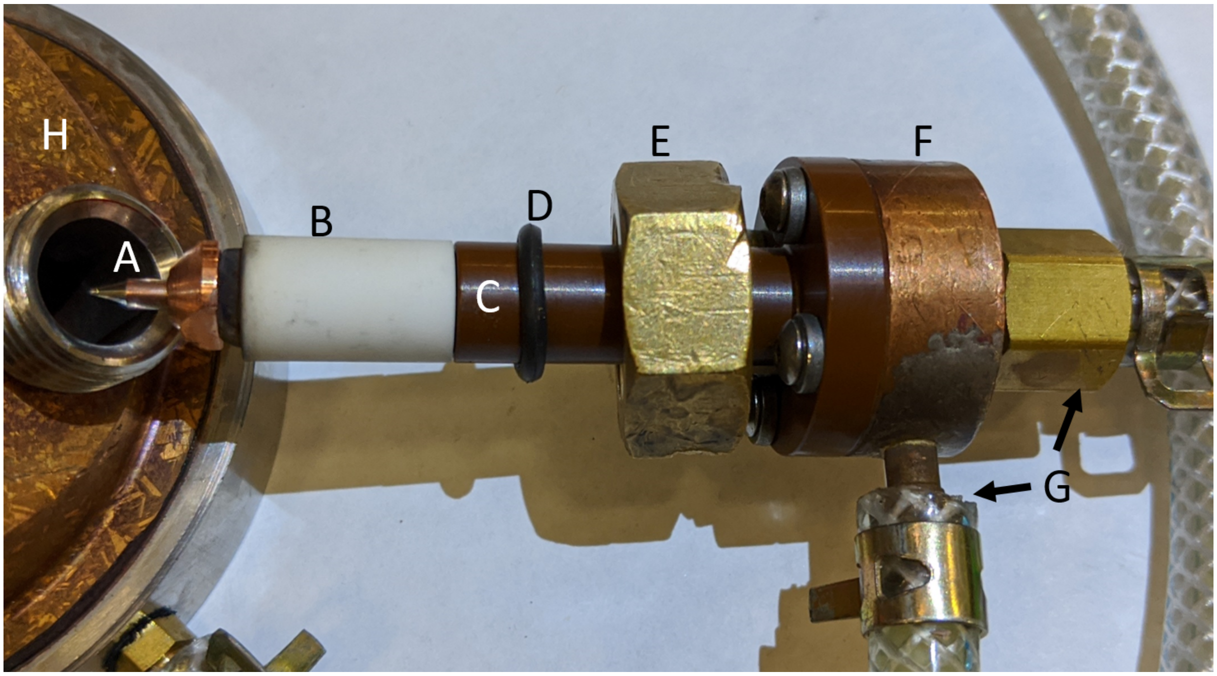

Figure 2.7: A photo showing the components of the plasma window's cathode structures. A is the W-ThO$_2$ cathode tip, B an alumina jacket, C a Vespel insulator, D a FFKM o-ring, E a nut to affix the structure to the housing, F the water-cooled copper holder, G the water inlet and outlet, and H the cathode housing.

W-ThO$_2$ cathode tip (A). The thoria is about 2% by mass. The thoriated tungsten cathode itself is a cone-tipped rod, 2.4 mm in diameter ending in a sharp tip whose conical full-angle is 30 degrees. The exposed cathode tip emerges 6.0 mm out of the copper shield. The W-ThO$_2$ tips are manufactured to be long enough to extend out the back of the shield by the threading, so that after some period of usage it may be pushed through and re-machined to get back to a clean surface of the dimensions shown in Fig. 2.8.

2.1.2 Procedure

The arc is always initiated in the fresh gas flow mode schematically represented in Fig. 2.2. This is done by opening the valves to maintain a constant, low flow in argon gas. If our ultimately desired gas to study is helium, we still initialize in argon as we have had very

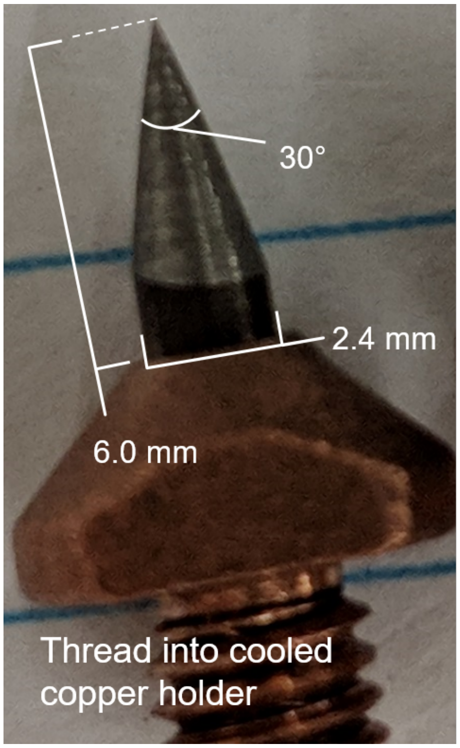

Figure 2.8: A photo indicating the dimensions of the exposed 2% by mass W-ThO_2 cathode tip inside the copper shield. This is a zoomed view of component A in Fig. 2.7.

little success in initializing the arc directly from helium and attempts usually resulted a spark generates in the opposite direction, from cathode backwards to the GCS, which can cause damage to other hardware. While keeping the gas flow relatively low (around 5 SLM), the arc is initiated using an Electro-Technic Products BD-10A Tesla coil (20 kV). This provides a large electric field, enabling an initial expulsion of electrons from the cathode in a field-emission regime. These electrons then ionize gas which are accelerated back to the cathode and heat it up, until a thermionic emission regime is reached. The arc then heats the gas, which effectively acts to partially plug the flow and causing the cathode-side pressure to increase, such that the emission regime transitions to thermal emission. This process occurs in a short enough duration that the Tesla coil need only be active for a fraction of a second. This is controlled via a foot-operated switch.

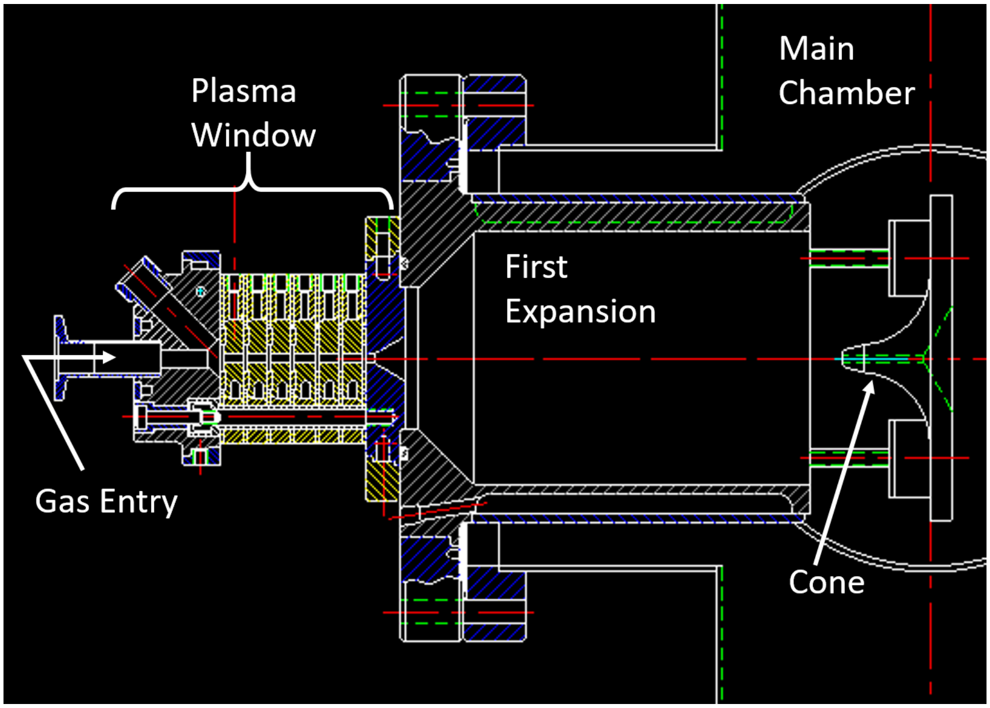

Figure 2.9: A drawing of the PW and part of the Main Chamber. The cone is also shown which acts as a heat sink for the hot plasma in the main chamber.

The anode plate is sealed against a large expansion chamber (referred to as the main chamber) with a Viton o-ring. This chamber has water cooling channels on several of its faces, and is grounded. Within the main chamber is a grounded structure referred to as the cone which is shown in Figs. 2.9 and 2.10, which much of the hot gas exiting the plasma window channel impinges upon, so this cone acts as a heat sink and so also is water cooled.

Attached to the main chamber is a sapphire glass viewport, a Granville-Phillips series 275 Mini-Convectron, and a large conductance (about 25 cm diameter) bellows which connects to a Edwards EH4200 Booster Pump and Edwards GV400 mechanical pump in series, which then exhausts in standard operation to atmosphere through a Varian Scroll pump. However, as mentioned earlier, this system can also be operated in a recirculation mode which is laid out in Fig. 2.3. This is transitioned to from the standard exhaust mode by closing off the scroll pump pathway whilst simultaneously opening a recirculation pathway. In recirculation

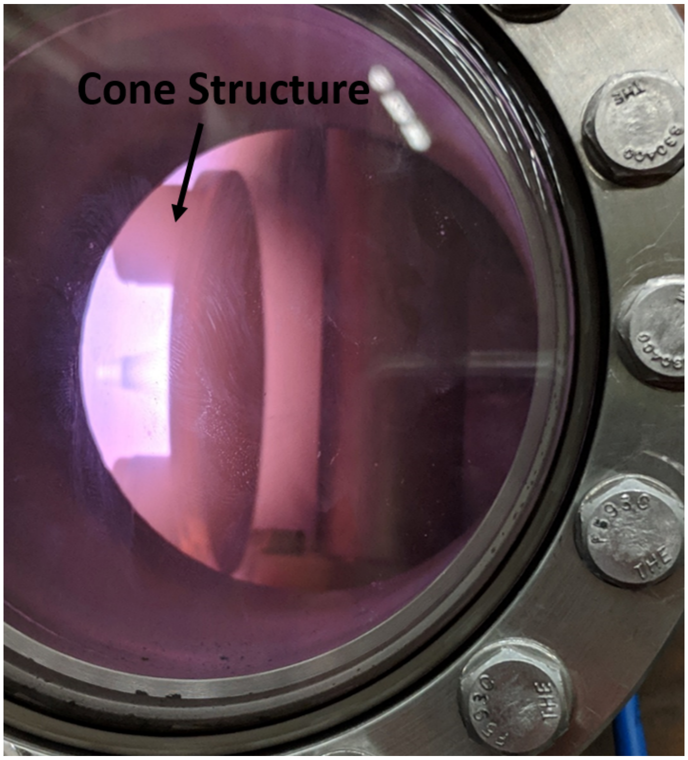

Figure 2.10: A photo looking through the viewport of the main chamber. The cone is visible, being bathed in the argon plasma exiting the PW.

mode, the gas feed is a large buffer chamber, shown in Fig. 2.12, rather than a gas cylinder. The gas flow rate is controlled by the parallel pairing of remote control and manual valve, then the gas passes through the GCS where static pressure is measured via an MKS Baratron 622B before flowing downstream back through the plasma window. This recirculation mode is of crucial importance for the plasma windows use with a gas charge stripper because the high degree of gas flow would otherwise rapidly deplete the reserve of gas feeding the device, becoming very expensive and wasteful.

The plasma window is sustained via the three cathodes, each of which are connected to two Sorensen SGA power supplies (400 V and 38 A limits each), for a total of 6 power supplies and a current limit of about 225 A. The full plasma window circuit as shown in Fig. 2.11 includes also an inductor-resistor series (1 mH at 100 A DC and 1 Ω respectively),

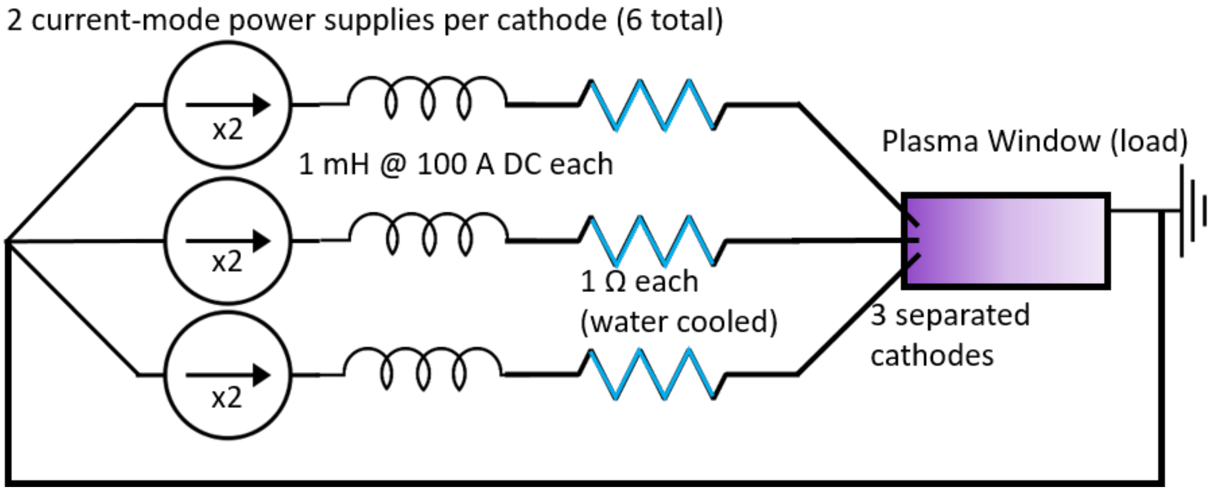

Figure 2.11: A diagram showing the plasma window circuit. Pairs of PW power supplies are in series with inductors and water cooled resistors to provide stability to voltage fluctuations. Three of these sets are in parallel, leading to the PW load.

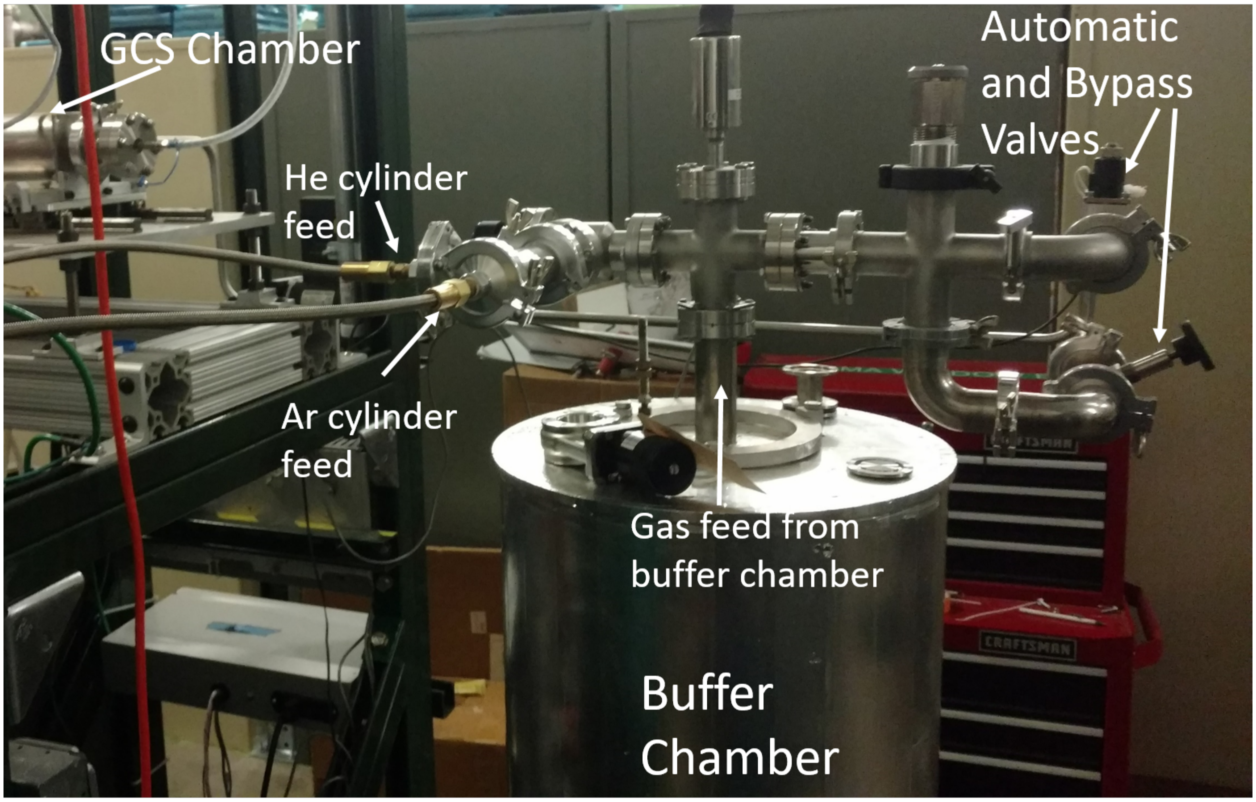

Figure 2.12: A photo of the gas-feed components of the PW. The GCS chamber can be partly seen in the top left corner of the photo, and the PW is even farther left (out of view here).

one per cathode, which provide stability to the arc since any transient behavior of voltage fluctuations is spread out in time as a result of the large time constant L/R of the series. Because the power dissipated through these resistors at currents of up to 70 A (per resistor), is quite large, they must be water-cooled. These power supplies are operated in current mode, the cathodes themselves being at floating voltage with the plasma, generally between 100 and 200 V. So, one of the primary controls of operating conditions will be the plasma window arc current.

The structure of the plasma window and the plates that comprise it has already been discussed, but a select few plates were manufactured with an additional feature. These, referred to as diagnostic plates, have a hole between the supply and return of the water coolant path, drilled down to the central bore, giving diagnostic access to the plasma at that plates location along the plasma window channel. This is then outfitted with an MKS Baratron 727A pressure gauge to determine the gas static pressure at that plates location, and a fiber optic feedthrough with a collimating lens for greater light acceptance, all of which can be seen in Fig. 2.13. In addition to fiber optic feedthroughs to receive the plasma emissions at the diagnostic plate locations, there is a fiber optic feedthrough positioned along the central axis (arc axis) at both the end of the CGS and the end of the Main Chamber. This provides a vantage point along the entire length of the arc from both the cathode-side (Front) and the anode-side (Back).

There are several notations regarding the arrangement of these plates in the PW that will be used extensively throughout this dissertation. One of the goals of this study is to examine the differences between arc performance in various different arrangements of plates, hereafter referred to as PW configurations. These are identified based on the number of them at specified aperture sizes as in the following examples: 8x6mm is a configuration consisting

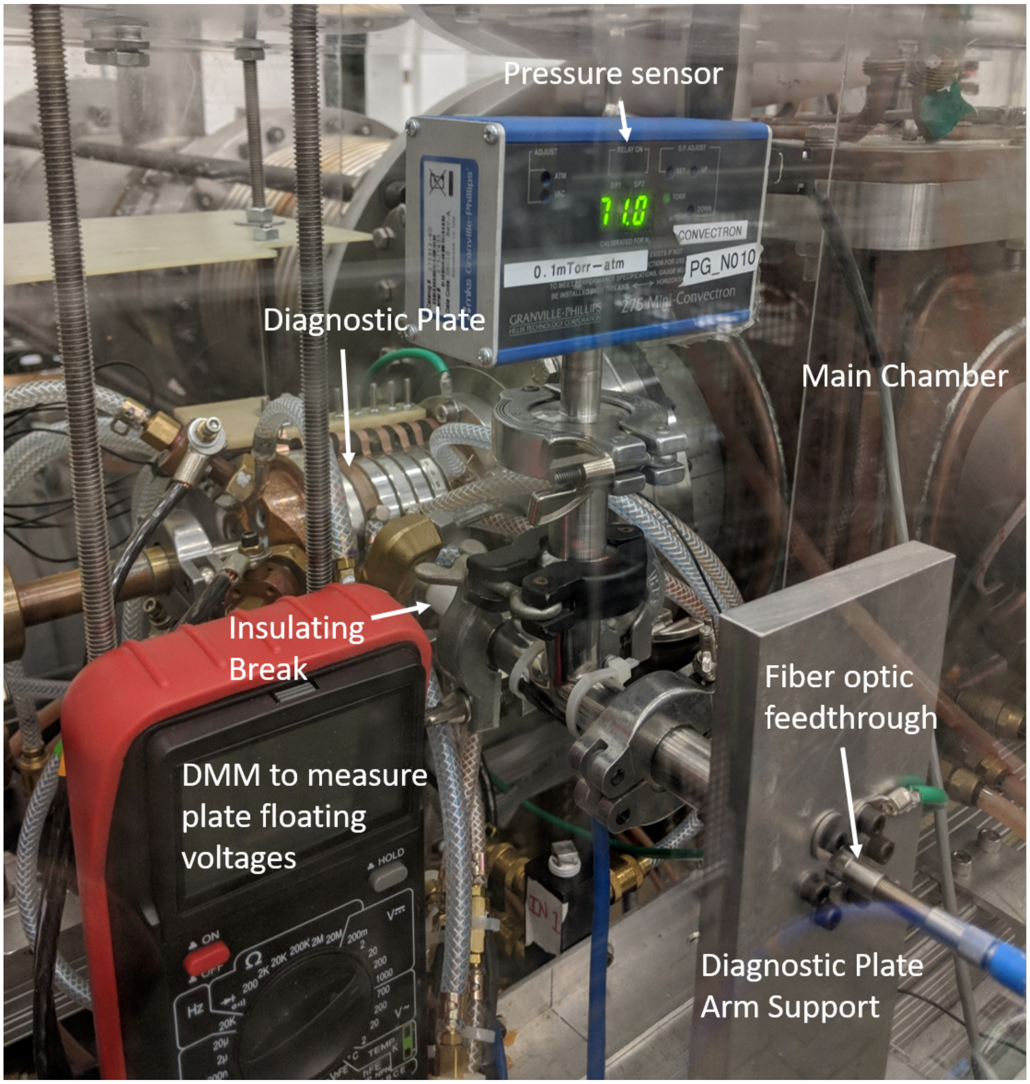

Figure 2.13: A photo indicating the setup of the diagnostic plate. The copper diagnostic plate itself can be seen positioned at P2/6 here. The diagnostic plate's fiber optic feedthrough and pressure sensor are also visible on the outward side of the diagnostic arm which is grounded. An insulating break separates this grounded side from the floating voltage of the plate.

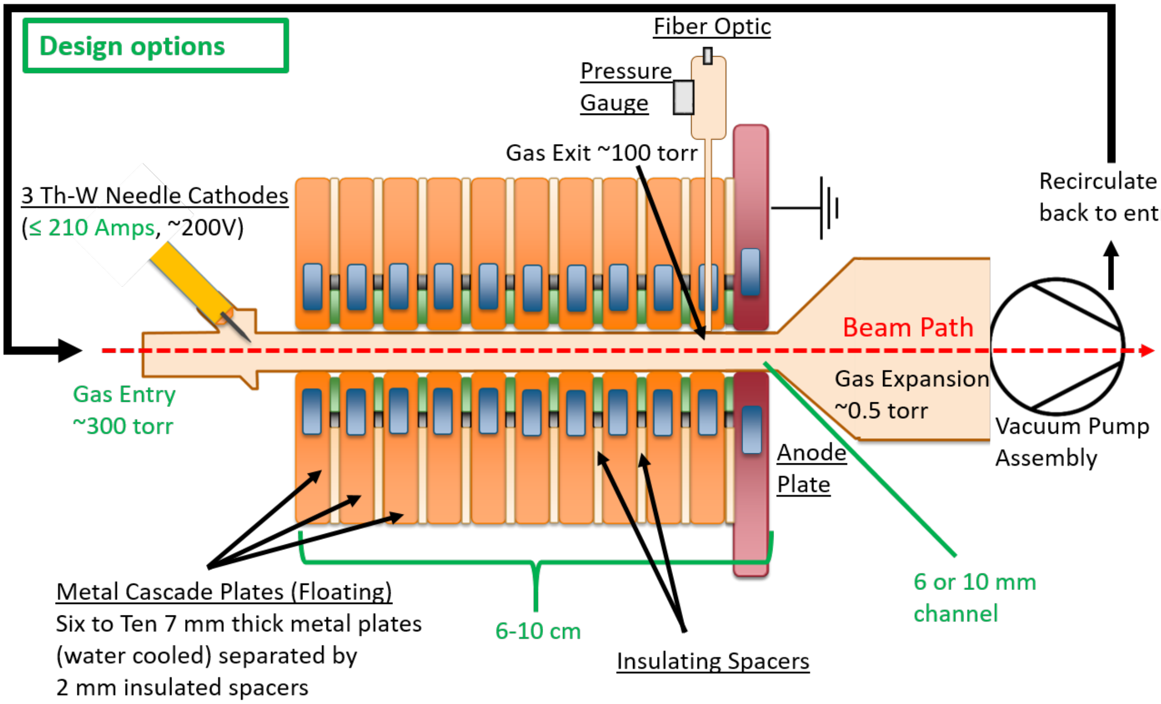

Figure 2.14: Cross sectional diagram of the plasma window and the primary components which comprise it . The insulating components and o-rings between the plates are shown in Fig. 2.6, and the cathode components are shown in Figs. 2.7 and 2.8.

of eight 6 mm aperture plates, while 1x6mm_7x10mm is a configuration consisting of one 6 mm aperture plate followed by seven 10 mm aperture plates. Reading the notation left to right translates to the plate arrangement from cathode to anode. The notation to refer to the diagnostic plate locations will be as in the following examples: P2/8 refers to plate 2 out of a total of 8 in that particular configuration.

2.1.3 Diagnostics

2.1.3.1 Spectrometer Characteristics

Calculations from the spectral measurements at these locations comprise a significant portion of the analysis conducted in characterizing the plasma within the plasma window as a function of operational conditions (pressure and arc current). This light is acquired by connecting fiber optic cables from the optical feedthroughs at the aforementioned locations, directly to an Ocean Optics HR4000. The spectra are displayed as spectral irradiance, with the abscissa being wavelength λ. This instrument has a 5 m wide entrance slit, a grating of 1800 lines/mm, calibrated for relative irradiance acquisitions. This calibration is performed using a bare-fiber viewing a StellarNet SL-1 2800K blackbody lamp, shielded from ambient light. This is the reference spectrum and will correct for the spectrometer's instrumental response function over the wavelength range.

A dark spectrum is also required. To minimize contribution of noise, both of these steps in the calibration process are performed by averaging a large number of consecutive scans. During long-duration operation, the spectrometer may require subsequent dark calibrations due to changes in ambient temperature causing small perturbations to light collection, causing the dark and reference calibrations potentially to drift. The used to obtain the relative irradiance calibration is:

$$I_{\lambda,T} = B_{\lambda,T} \frac{S_\lambda - D_\lambda}{R_\lambda - D_\lambda}\,, \tag{2.2}$$

where $I_{\lambda,T}$ is the calibrated relative irradiance at wavelength λ, and S_λ, D_λ, and R_λ are the sample spectrum (from the plasma in this case), the dark spectrum, and the blackbody lamp reference spectrum respectively at the corresponding wavelength and each given as counts. $B_{\lambda,T}$ is the function representing a blackbody's irradiance spectrum at a temperature corresponding to that of the blackbody lamp used for the reference spectrum. This is computed from Planck's law:

$$B_{\lambda,T} = \frac{2hc^2}{\exp(hc/\lambda kT) - 1}\,. \tag{2.3}$$

The intensity of emissions from the plasma window varies dramatically with operating conditions and observing location, so this calibration procedure must be performed with a range of different collection integration times from 15 ms to 10 s. A more reliable, though more complicated calibration could be performed using an intensity-calibrated standard, allowing us not only to not need to rely on the assumption that the blackbody lamp does indeed accurately replicate a blackbody of 2800 K, but also enables calculations of excited state densities and more reliable electron density measurements [46, 47, 52]. This was not employed for the present plasma window work.

2.1.3.2 Coolant Calorimetry

Water coolant temperatures are measured at locations both upstream and downstream of the hot component which it cools. The arrangement of coolant primary manifolds is one for each of the following sections of the test stand: the mechanical and booster vacuum pumps, the main chamber and the three 1 Ω resistors, and the cone structure. Additionally there are two primary manifolds dedicated to the plasma window structure itself. The Fluid Chillers WAT30000 chiller which pumps and cools the water flowing through the entire PW test stand is rated for 30 kW, and its cooling functionality is generally active for a period of several minutes followed by a cooling-inactive period of several minutes (though the water coolant is pumped at all times). Pure water is used because of its relatively large resistivity which limits the electrical current leaked through the water to ground.

The water flow rate in each of these primary manifolds is measured using liquid flow monitors by Universal Flow Monitors, rated for 0 to 5 GPM. All of the components (cathodes and plates) in the plasma window have a single coolant path, the only exception being the cathode holder which has two coolant paths. The coolant flow rate through each of these paths is determined simply as $1/N$ with N being the total number of coolant paths connected to that manifold. The power which is removed by the coolant is determined calorimetrically using:

$$H_w = c_p \dot{m}_c \Delta T\,, \tag{2.4}$$

where H_w is the power into the wall, c_p is the specific heat of water (4.184 kJ/kg*K), $\dot{m}_c$ is the coolant mass flow for that component, and ΔT is the difference in measured temperature from upstream and downstream of the plasma window component. Because the plasma is in a steady state, the power that is cooled equals the power with which the plasma heats the given component of the plasma window.

To properly make use of Eq. (2.4), one must also subtract out the null values that one reads for temperature difference of the temperatures down and upstream of the PW without any arc presence. This is done in two steps in this work: a chiller cycle null value is taken as the difference between the down and upstream temperature sensors (for a given PW component) over a time in which the chiller is active but the arc is not. Similarly, an ambient null value for the temperature difference is taken as the difference between down and upstream temperature sensors over a time in which both the chiller and the arc are inactive. This ideally is taken very close in time to the actual experiment. Sample acquisitions for both of these are illustrated in Fig. 2.15.

The corresponding temperature corrections from each of these null values are given simply by:

$$\Delta T_{null,j} = T_{in} - T_j|_{nulltype}\,. \tag{2.5}$$

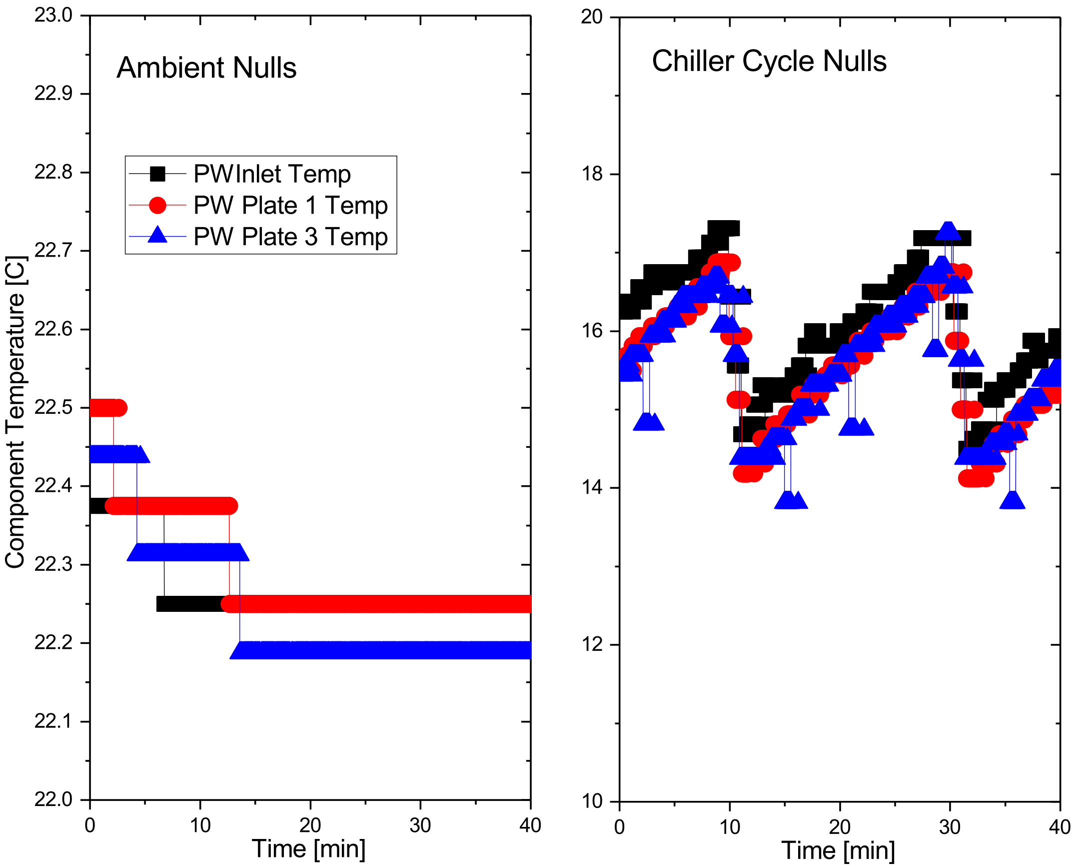

Figure 2.15: Sample acquisitions of both ambient null (left) and chiller cycle null temperature values.

Using this, one would replace the ΔT in Eq. (2.4) with $\Delta T - \Delta T_{null,j}$ for each PW component j, and taking the sum of the ambient and chiller cycle null values.

2.1.3.3 Plate Floating Voltages

A critical property of an arc plasma that dictates the dynamics within is the electric field that is sustained between the cathode side and the anode side. In a DC cascaded arc, the axial component of the electric field is taken to be approximately constant across a given cross-sectional area of the channel. This electric field can be determined at discrete locations along the channel axis of the plasma window by measuring the floating voltage of each plates enclosing the plasma and taking the gradient along the direction of the channel axis. This electric field is taken to be located at the midpoint between the adjacent plates whose voltages determined the local gradient. It should be stressed that it is assumed that the electric field in the bulk of the plasma is about the same in magnitude as that determined by this method from wall voltages.

The system used to measure the PW floating plate voltages consists of a G10 insulator platform positioned near the PW plates, and attached to it are copper fingers - one per plate and another for the cathode housing - connected to a voltmeter through a rotary switch. The switch is controlled with a G10 insulator rod so that each plate voltage can be measured. Components of this plate voltage measurement system can be seen in Figs. 2.5 and 2.13.

2.2 Optical Emission Spectroscopy

2.2.1 Introduction

Plasmas generally emit radiation across much of the electromagnetic spectrum and through a variety of mechanisms. Most important for the present work is intra-excited-state deexcitation processes which emit characteristic radiation. Wavelengths depend on the emitting species and the population of excited levels, while line shapes and relative emission irradiances depend on plasma properties such as electron temperature T_e and density n_e.

The primary tool used in this study to characterize the plasma via these line emissions is a spectrometer which is described in detail in Section 2.1.3.1. Light from the plasma is directed to this instrument via fiber optic cables and is interpreted as an irradiance-wavelength spectrum. This is worth explicitly pointing out because quantitative units of light flux are historically suffered from much ambiguity and name changes, generating confusion which is hopefully minimized here. Ref. [7] has an effective description which helps to dispel

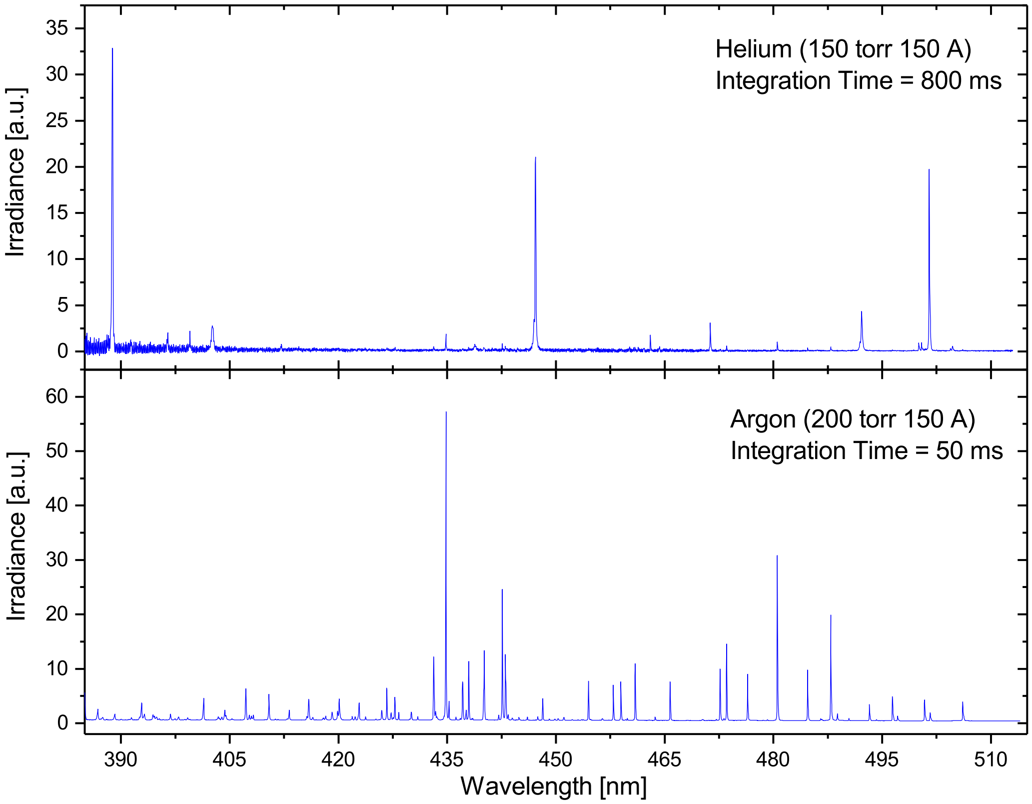

Figure 2.16: Sample spectra obtained from a 6x6mm PW, the vantage point being across a diagnostic plate positioned at P6/6. The spectra were collected with integration times of 800 ms and 50 ms for helium and argon respectively.

this confusion, but here it will be sufficient to just mention that irradiance, which is the property measured in this work, is a radiant power W (in Watts) impinging on a collection area A (in m^2). What is collected via the spectrometer is actually a spectral irradiance I_s, so is instead in units of $W/m^2/nm$, so to determine the overall irradiance I of an emission peak, the spectral irradiance must be integrated over the peak's wavelength extent. Sample spectra that represent typical collections are shown in Fig. 2.16 for a 6x6mm PW, for both argon and helium. These were collected via a diagnostic plate at P6/6 It should be noted that the emission irradiances between the two gases are quite different, with helium generally emitting weaker light in the range of the spectrometer (about 385 to 515 nm), and so different integration times of light collection are required.

In the energy regime relevant for the PW, the primary mechanism for excitation is by collisions with electrons rather than other heavy particles. This is because not only do the electrons generally have significantly higher energy than the heavy particles, but also electron-heavy collisions are much more frequent than heavy-heavy collisions. In plasmas of densities similar to those in the PW, it is likely that a significant portion of the population of the higher excited states arises from intra-excitation, or excitation to a higher energy level from a metastable or other already excited state. Particularly important are excitations from metastable states which are relatively low-lying excited states that do not readily decay back to the ground state due to selection rules preventing the transition. Ordinary excited states of a neutral or lowly-ionized ion may have lifetimes of just a few nanoseconds but that of metastables can be greater than milliseconds, up to seconds [53]. The relatively long lifetime of these states and their closer proximity in terms of energy to the higher excited states than the ground state mean that they can play a significant role in establishing the degree of ionization of the plasma.

To assess the relative importance of electron-impact excitations and ionizations from these metastable states compared to from the ground state, rate coefficients have been calculated for conditions similar to those measured in the PW for argon and helium, i.e. that $T_e = 1.5$ in argon and $T_e = 2.1$ in helium. These coefficients were calculated assuming a Maxwellian EEDF, an assumption further investigated in Section 3.1. Differential rate constant (DRC) values are calculated for ionization and excitation from both ground and metastable states using Eq. (1.13). This is therefore given by:

$$DRC(E, T_e) = f(E, T_e)\sqrt{2E/m_e}\,\sigma(E)\,, \tag{2.6}$$

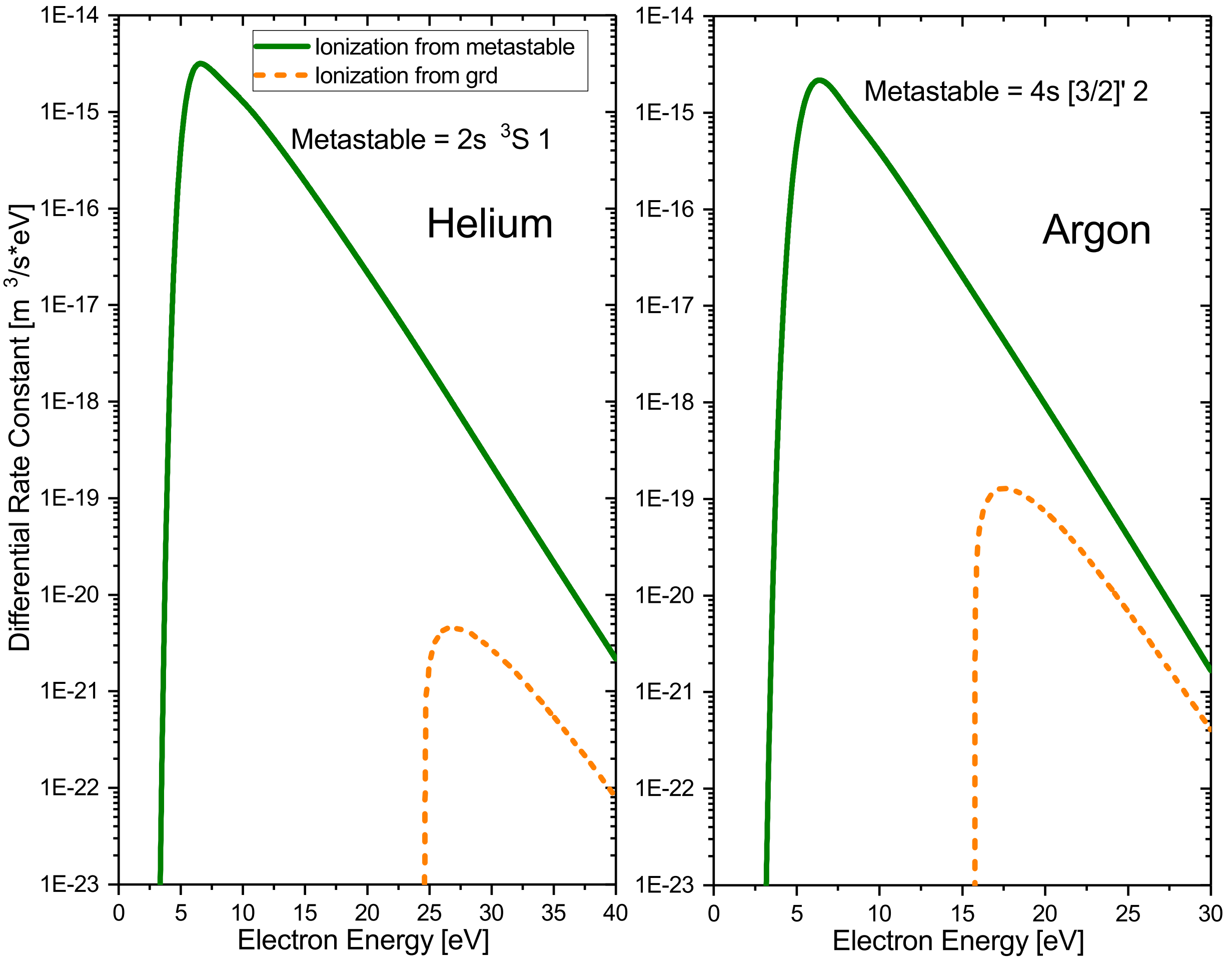

Figure 2.17: Differential rate constant for electron-impact ionization from the lowest-lying metastable level as well as directly from ground level, for both argon and helium. The argon test case has $T_e = 1.5$ eV and the helium has $T_e = 2.1$ eV.

in which E is the electron energy, T_e the electron temperature, $f(E, T_e)$ the Maxwellian EEDF value, and $\sigma(E)$ is the relevant electron-impact ionization or excitation cross section.

For ionization, a test case of this $DRC(E, T_e)$ as a function of the impacting electron's energy is shown in Fig. 2.17, using cross sections from Ref. [54] for argon and helium ionization from ground as well as argon ionization from the metastable, while the cross section for helium ionization from the metastable is obtained from Ref. [55]. Analogous plots for excitation are shown in 2.18. For both gases, the metastable is the lowest-lying excited state, which is identified in the figure. Results are summarized in Table 2.1. The

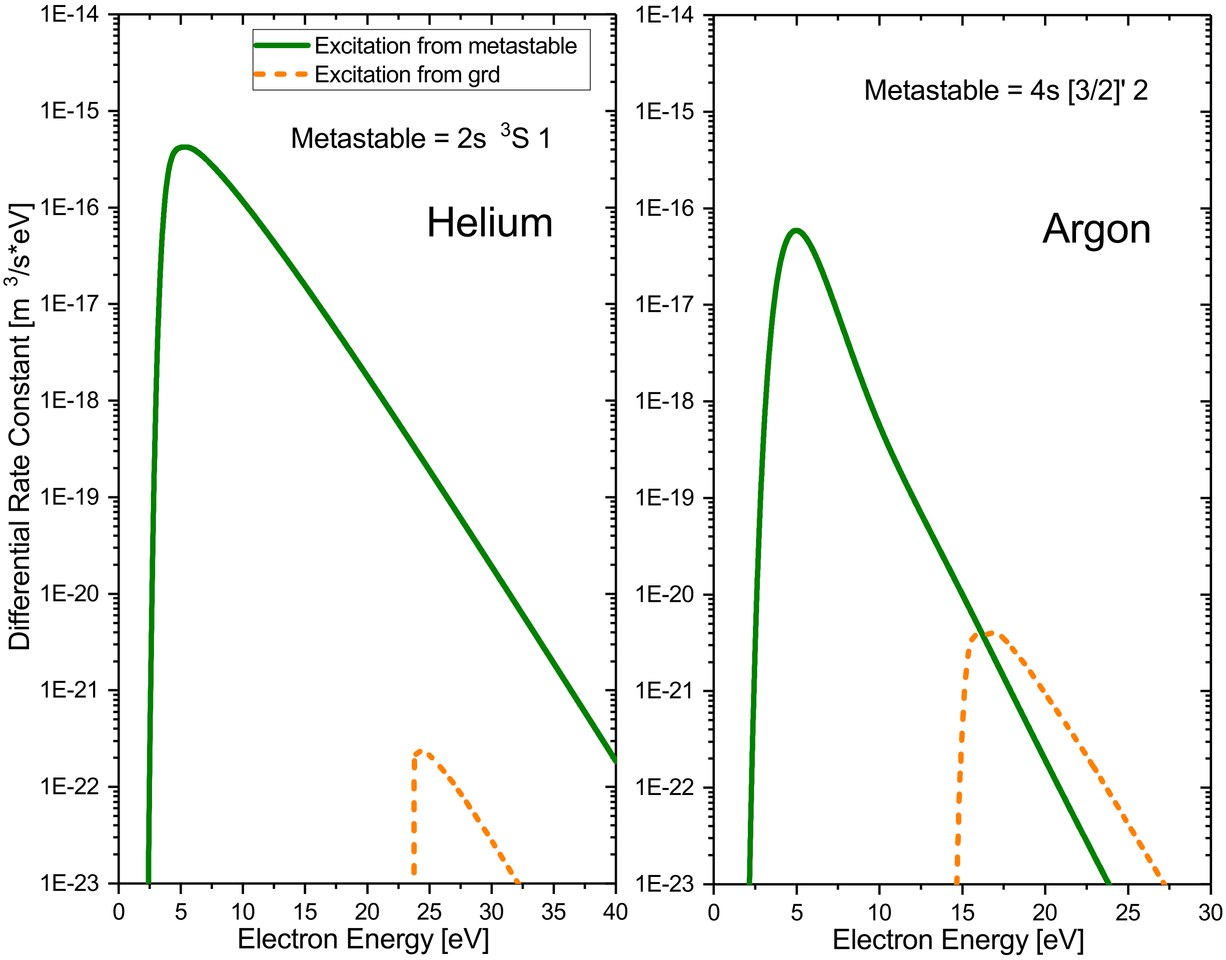

Figure 2.18: Similar to Fig. 2.17 but for excitation, this is the differential rate constant for electron-impacts to the lowest-lying metastable level as well as directly from ground level, for both argon and helium. The argon test case has $T_e = 1.5$ eV and the helium has $T_e = 2.1$ eV. The upper level is 5p [3/2]1 for argon and 4d 3D for helium.

cells highlighted in grey characterize the relative importance of excitations from metastable states. These, the ratio of rate constants (metastable / ground) represent the required ratio of densities (again metastable / ground) for the excitation or ionization rates from ground and from metastable to be equivalent. Relative metastable densities that exceed that ratio would imply ionization from the metastables is in fact the dominant ionization mechanism.

Table 2.1: Comparison of electron-impact ionization rates from ground and metastable levels in Ar and He. All rate coefficients are in [m^3/s].

Process	Helium	Argon
Excitation to an emitting state	To excited state 4d ^{3}D	To excited state 5p[3/2] 1
Excitation from ground	8.2×10^{-22} [m^3/s]	1.5×10^{-20} [m^3/s]
Excitation from metastable	2.1×10^{-15} [m^3/s]	1.4×10^{-16} [m^3/s]
Excitation Rate Constant Ratio	3.9×10^{-7}	1.1×10^{-4}
Ionization from ground	2.8×10^{-20} [m^3/s]	5.9×10^{-19} [m^3/s]
Ionization from metastable	1.4×10^{-14} [m^3/s]	7.0×10^{-15} [m^3/s]
Ionization Rate Constant Ratio	1.9×10^{-6}	8.4×10^{-5}

2.2.2 Electron Density - Stark Broadening

A plasma's electron density (also often simply called plasma density) is one of the key properties of a plasma which dictates its behavior and so is a good basis of comparison between different plasmas, or between a plasma and a corresponding model describing that system. The electron density dictates the rate at which the heavy particles are heated, which in turn impacts the mass flow through the arc as will be discussed in Section 3.3. Calculating this electron density can be performed via several different techniques and instruments such as Langmuir probes [56], laser interferrometry [57], Thomson laser scattering [58, 59] or optical emission spectroscopy (OES) [7, 38, 60].

Langmuir probes have the benefit of being able to determine a wider variety of other plasma properties that cannot be obtained by the other methods, however they can perturb the plasma locally, and in high pressure arcs their implementation suffers the added challenge of surviving in the dense and hot environment [61, 62]. Laser interferrometry and Thomson scattering can provide a higher accuracy measure of electron density as well as excellent spatial and temporal resolution [63], but requires a more complicated apparatus of laser and optics providing line of sight into the plasma, the plasma system itself, and a spectrometer which also must have line of sight into the plasma, to capture the effect of the laser for analysis. This also can perturb the plasma at the location where the laser is interacting with it. It is also likely that there is a low-density plasma along the length of the diagnostic channel that cuts through the diagnostic plate which could also emit radiation, though it is expected to be vastly dimmer than the plasma in the center of the arc, so we summarily exclude any effect from this.

On the other hand, optical emission spectroscopy has the benefit of being a non-invasive technique which makes use of the emission from atomic de-excitations. In the PW system, the diagnostic plate's optical line of sight is the central chord of the plasma channel at the specified plate location. The entry of this to the PW channel can cause a local perturbation to the plasma though it is expected to be minimal.

Broadly there are three physical processes that give rise to broadening of a spectral line, not including the effect of the instrument itself: natural broadening related to the emitting state's lifetime, Doppler broadening originating from the speed of moving emitters, and broadening resulting from interactions with other particles in the emitter's vicinity [7]. These mechanisms will be explored in minor detail here with references providing more elaboration, with the exception of Stark broadening which will receive a more detailed explanation here. This broadening originates from the interaction of the emitter with local electrons and ions.

Before attempting to make use of this phenomena to calculate electron density, it is necessary to briefly present the other mechanisms by which an emission line can be broadened. Rather than being an infinitesimally narrow line, every emission has a natural linewidth, owing to the finite decay time of the excited state and a corresponding energy uncertainty as necessitated by the Heisenberg uncertainty principle [52,64]. This linewidth is almost always several orders of magnitude finer than the others discussed here [47]. Brief explanations and relative broadening values will be calculated for conditions typical of those in the PW for the following broadening types in addition to Stark broadening:

1. Natural line broadening
2. Doppler broadening
3. Van der Waals broadening
4. Instrumental broadening

Doppler broadening occurs due to the random thermal motion of emitters, which then contributes red-shifting or blue-shifting of the emission; when including the effects of the random motion of a collection of emitters, the result is a Gaussian broadening of the emission line. Because the degree of Doppler broadening is related to the amount of thermal motion in the emitters, it is frequently used as a means of calculating a temperature of the emitters (gas temperature if the emissions are from excited neutrals). Doppler broadening takes the form [7]:

$$\frac{\delta\lambda_D}{\lambda} = \frac{2}{c}\sqrt{\frac{2kT\ln 2}{M}}\,, \tag{2.7}$$

in which T is the temperature of the emitting species, c the speed of light, and M is the mass of the emitting species.

The Doppler full-width-at-half-maximum (FWHM) to emission wavelength ratio $\frac{\delta\lambda_D}{\lambda}$, or relative broadening degree, is inversely proportional to the square root of the mass, so the effect will be more pronounced for helium than it is for argon. For a helium gas temperature of 3 eV (this is much higher than what is actually the case in the plasma window, so gives a far upper bound of expected broadening), this corresponds to a relative broadening degree of 2.1x10^{-5}. If this is significant relative to the other forms of broadening in the system, then

Table 2.2: Approximate relative line broadening degrees ($\Delta\lambda/\lambda$) for various mechanisms, for emissions in visible wavelengths. In argon, $T_e \approx 1.5$ eV, $T_g \approx 1.5$ eV, and $n_e \approx 2 \times 10^{16}$ cm^{-3}. In helium, $T_e \approx 2.5$ eV, $T_g \approx 1.5$ eV, and $n_e \approx 2 \times 10^{15}$ cm^{-3}.

Mechanism	Relative Broadening (Ar I)	Relative Broadening (He I)
Stark	1×10^{-4}	2×10^{-4}
Doppler	1.5×10^{-5}	6.6×10^{-5}
Natural	2×10^{-7}	2×10^{-6}
Van der Waals	3.7×10^{-7}	3.5×10^{-7}
Instrumental	1×10^{-4}	1×10^{-4}

it must be considered, but if it's smaller than other contributions, it may be ignored. This will be explored after defining the other broadening mechanisms.

Another broadening type is Van der Waals broadening, a form of pressure broadening resulting from the dipole interaction of an excited atom with the induced dipole of a neutral atom [64]. The analysis of this form of broadening requires knowledge of the interatomic potentials, and a complete treatment can be found in Ref. [7], Ref. [65], or Ref. [64]. Following those works, the Van der Waals relative broadening from of a neutral emitter from same-species neutral perturbers, or the FWHM to emission wavelength ratio, can be expressed as:

$$\frac{\delta\lambda_V}{\lambda} = 8.18 \times 10^{-19} \lambda (\alpha_p \bar{R}^2)^{2/5} \left(\frac{T_h}{\mu} \right)^{3/10} n_g \, . \tag{2.8}$$

In this expression, wavelength λ is in nm, and atomic polarizability α_p and neutral density n_g are both in cm^{-3}. Also in this expression, μ is the reduced mass of the emitter-perturber system in atomic mass units. Lastly, $\bar{R}^2$ is the difference of the square radius of the emitting atom's upper and lower levels, given in units of Bohr radii.

Finally, the instrument with which the emission spectrum is collected also contributes a degree of broadening to the emission, though this type has nothing to do with the plasma's properties. In the case of the spectrometer used in this work, an Ocean Optics HR4000 as described in Section 2.1.3.1, this turns out to be the dominant non-Stark contribution to the observed line shape and will be discussed in detail below.

Stark broadening analysis is a very commonly employed diagnostic used to ascertain the electron density of the emitting plasma. We begin with a conceptual description of Stark broadening. The degree of Stark broadening depends on two general factors: the local plasma environment and the atomic structure of the emitter, be it atom or ion [64]. Emitting atoms experience collisions with electrons in the plasma, whose local electric field [8, 66] perturbs the excited energy levels. This field is often referred to as the microfield, and is the field distribution inside the screening distance described in section 1.2, the Debye length of Eq. (1.2). At distances from a charged particle inside of the Debye, quasineutrality doesn't apply, hence strong fields may be present [67] at these small distances. In the theory discussed here, the microfield distribution are presented in terms of what is known as the Holtsmark field strength [66, 68] which is approximately the electric field strength generated at a the mean ion-ion separation distance and given in Eq. (2.10). Elaboration and equations pertaining to this are introduced in subsequent pages.

The perturbation from a projectile impinging on an emitter (an atom or an ion) is illustrated in Fig. 2.19. In a collision in which an emitter and a charged perturber particle (e.g. an electron) are separated by a distance R, their separation would start at a large distance then approach a minimum value (the impact parameter) before increasing to a large distance again as the perturber recedes. When many emitters encounter such collisions over a distribution of projectile energies and impact parameters, this perturbation ultimately manifests as a broadening and shifting of the emission peak profile. Additionally there is a contribution from collisions between the emitter and ions, which produce an asymmetry in

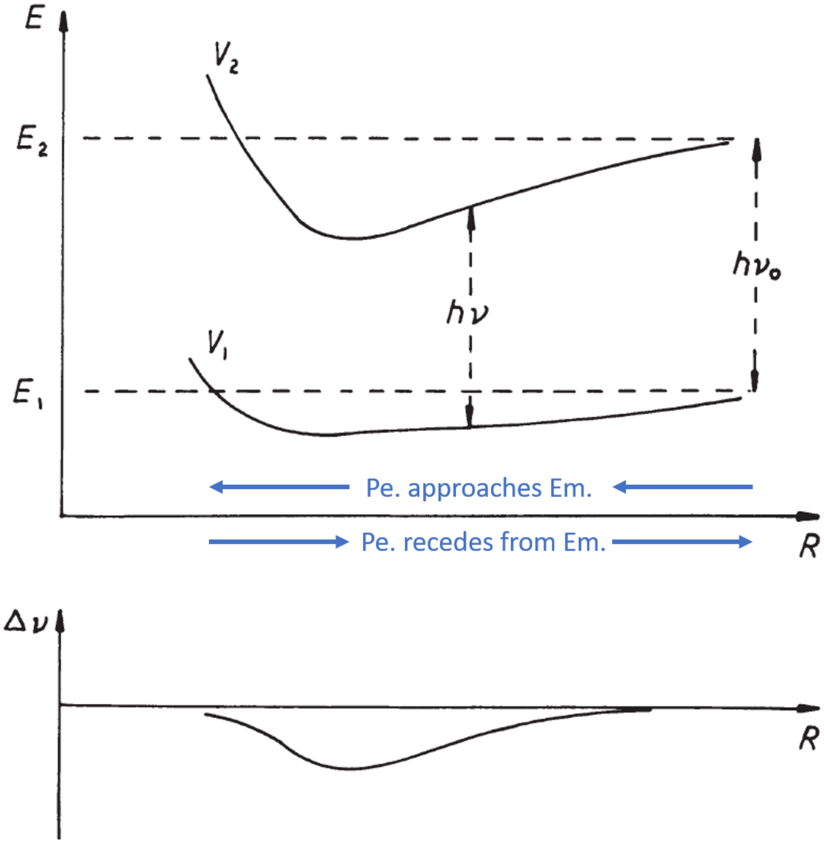

Figure 2.19: Reproduction of figure published in Ref. [7]. This qualitatively illustrates the perturbations of two energy states originally of energy E_1 and E_2 as a function of charged perturber distance R from the emitter. The perturbed energies V_1 and V_2 set the emitted photon energy $h\nu$. Perturber particle is denoted as Pe and emitter particle as Em.

the emission profile.

In working towards a mathematical expression for the Stark-broadened profile, there are a number of theoretical approaches determining the effect of emitter-charged-neighbor interactions on a line profile and how to utilize it in assessing electron density. Ref. [69] provides a nice review of these theories, while Ref. [66] provides a far more in-depth dive into one of these theoretical approaches, the same that will be utilized in this thesis. A decent starting point in establishing a theoretical framework for Stark broadening is the spectral power of one of these spontaneous electric dipole emissions from a single quantum-mechanical system. This is the point where Griem [66] begins a deep dive into Stark broadening. The lengthy process in going from this starting point to a final expression of Stark broadening profiles of the emission lines will not be presented in full here, and the reader is encouraged to look at the incredibly thorough presentation in the aforementioned Griem textbook for the mathematical details.

As mentioned above, the microfield distribution employed in this approach is given in terms of the normal Holtsmark field strength F_0, which is essentially the Coulomb field strength produced by a perturber located one mean ion-ion separation length r_p away from the emitter [66]. This distance is defined as:

$$r_p \equiv \left(\frac{3}{4\pi} \frac{1}{n_p} \right)^{1/3} , \tag{2.9}$$

and so the normal Holtsmark field strength is:

$$F_0 = 2\pi \left(\frac{4}{15} \right)^{2/3} \frac{Z_p e}{4\pi\epsilon_0} n_p^{2/3} , \tag{2.10}$$

and the microfield distribution is given by the normalized Holtsmark distribution $H_R(\beta)$ with β being the electric microfield strength F normalized to the normal Holtsmark field strength F_0, so:

$$\beta = \frac{F}{F_0} . \tag{2.11}$$

In these equations, Z_p and n_p are the perturber charge and density respectively, and e the elementary unit of charge. This Holtsmark distribution is obtained by assuming all particles to be statistically independent. Further details and derivations pertaining to this distribution

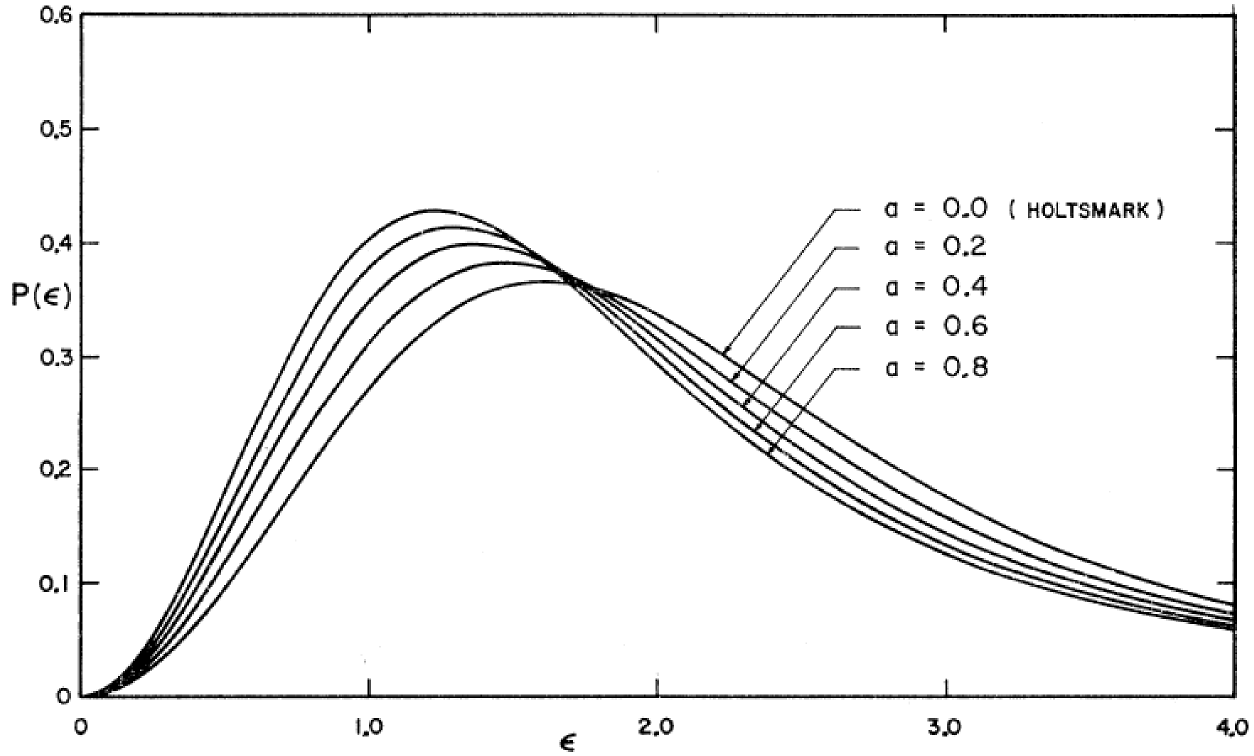

Figure 2.20: Reproduction of figure published in Ref. [8], illustrating changes to the microfield distribution with deviations from the Holtsmark distribution ($R = 0$), ϵ is in units of ϵ_0. Symbols are different than those used in the thesis: the Debye shielding parameter symbol is a, the field strength is ϵ, the normal Holtsmark field strength is ϵ_0, and the normalized distribution function is $P(\epsilon)$.

are found in Ref. [66], but the result for the normalized Holtsmark distribution is:

$$H_{R=0}(\beta) = H_0\beta \int_0^{\infty} x sin(\beta x) \exp(-x^{3/2}) dx\,, \quad H_0 = 2/\pi\,. \tag{2.12}$$

The last detail to mention regarding the background on the Stark profile is that the above description is applicable for situations where the parameter R is close to 0. This, called the Debye shielding parameter, is the ratio of the mean ion-ion separation to the Debye radius, expressed as:

$$R = \left(\frac{9e^6 n_e}{16\pi^2 (\epsilon_0 k T_e)^3} \right)^{1/6}\,. \tag{2.13}$$

To get an idea of its value in a plasma typical of the PW, take $n_e = 10^{16}$ cm^{-3} and $T_e = 1.5$ eV, which results in $R \approx 0.3$. In the work for this thesis, the simplification of $R = 0$ was taken, however, one could employ more accurate corrections, for example those described and calculated in Refs. [8] and [70]. In Fig. 2.20, a reproduction of a figure published in Ref. [8], it can be seen how the microfield distribution is adjusted from being the formerly described Holtsmark distribution for $R = 0$ to different forms as R increases. In this figure, the Debye shielding parameter symbol is a, the field strength is ϵ, the normal Holtsmark field strength is ϵ_0, and the normalized distribution function is $P(\epsilon)$.

With the details of the electric microfield established, we can now move to the general Stark profile shape. The profile is influenced by both electron-emitter interactions as well as ion-emitter interactions. The electron-emitter interactions require what is called the impact approximation, a view which is characterized by the collisions that occur rapidly compared to the duration the atom radiates. These collisions are governed by linear Stark effect perturbations to upper and lower wavefunctions of the emissions which gives rise to a symmetric and shifted Lorentzian-shaped profile. In contrast, ion-emitter interactions require what is called the quasi-static approximation, which assumes that the perturbation imposed by the colliding particle is nearly constant over the entire duration that the atom is radiating. These collisions have a component of quadratic Stark effect perturbation, which results in asymmetry as well as additional broadening introduced to the profile [7,64,66]. The reason the quadratic Stark effect perturbations result in asymmetric broadening while linear Star effect perturbations result in symmetric broadening is that the Stark shift resulting from any given collision is given by:

$$\delta\lambda_{if}(F) = C_{if}F^{n}\,, \tag{2.14}$$

where if denotes the initial and final states, F the perturbing field strength (recall the Holtsmark distribution of this field), C_{if} being a constant associated with the transition, and $n = 1$ and $n = 2$ being the case for linear and quadratic Stark effects respectively. Broadening then is a result of many of these occurring over the aforementioned distribution of the perturbing fields [66].

Ultimately, the Stark broadening profile is parameterized with the electron-broadening parameter w_j, profile shift d, and asymmetric ion contribution α. The Stark broadening profile $j(\lambda)$ for an emission of unshifted wavelength λ_0 is given by:

$$j(\lambda) = j_A \int_0^{\infty} \frac{H_R(\beta)}{1 + [\frac{2(\lambda - \lambda_0 - d)}{w_j} - \alpha\beta^2]^2} d\beta \,, \tag{2.15}$$

What is measured by the spectrometer is a convolution of the instrumental profile (IP) and the Stark profile in Eq. (2.15), so:

$$(I * j)(\lambda) = \int_{-\infty}^{\infty} I(t) j(\lambda - t) dt \,. \tag{2.16}$$

Here, the IP is given by $I(\lambda)$, which is simply recast in the equation in terms of a dummy variable t. The nature of the IP of the spectrometer used in this work is discussed below. Once the IP has been ascertained, a least-squares minimization fitting routine is performed to obtain the following parameters from Eq. (2.15) as a part of Eq. (2.16): electron broadening width w_J, asymmetry parameter α, profile center $(\lambda_0 + d)$ (note, the Stark shift d itself is not determined here), and profile amplitude j_A. In reality, this can be simplified by imposing a constraint on the width w_J and asymmetry parameter α such that they both provide the same electron density n_e, because both of these parameters scale with n_e. These scalings are given by:

$$w_J \propto n_e \,, \tag{2.17}$$

and

$$\alpha \propto \frac{F_0^2}{w_J} \propto n_e^{1/3} \,. \tag{2.18}$$

As a result, one can use calculations of w_J and α at specified plasma conditions, as listed in Appendix IV of Ref. [66], to couple the two parameters together, reducing the total number of parameters that must be fitted by one.

Finally, the instrumental profile used in this work will be described in more detail. As mentioned above, the fitting routine used to extract the Stark width (and therefore electron density n_e) critically relies upon knowing the instrument's own line profile since the overall observed profile is a convolution of the instrumental profile and the Stark profile, as in Eq. (2.16). This profile arises as a result of the intrinsic characteristics of the internal optics and collection components of the spectrometer such as entry and exit slits, gratings, or detector properties [71]. Zonal aberrations in the optics can contribute to this, as could optical misalignments, or some source of nonuniform angular intensity distribution of light entering the spectrometer [72]. This is due to the fact that the light enters the spectrometer with some angular spread, and so the aberrations, misalignments, and other physical imperfections can produce a net effect of slightly different optical pathways for a particular wavelength. The result of this is a perceived spread of the light of that wavelength, which we call the instrumental profile [71–73]. A nice description of all the spectrometer components and how they impact the ultimately observed spectrum can be found in Ref. [7].

Frequently, IPs are reasonably assumed to be Gaussian [64, 71]. However, this is not always appropriate [71–73], and it is indeed inadequate in describing the shape of the Ocean Optics HR4000 instrumental profile which is wavelength-dependent and appears to defy any convenient analytical form. One possibility that could be further explored though is that the spectrometer's IP through at least some part of its wavelength range obeys a skew-normal distribution, which Ref. [71] mentions is sometimes appropriate. This was not done in this work. Instead, to ascertain what this shape truly is, low pressure gas discharge lamps of He and Ar gas were used, which produce linewidths much narrower than the instrumental profile width observed, indicating the results are broadened purely as a result of the instrumental effects. The result of this is shown in Fig. 2.21, which shows the collected emission profile at three wavelengths across the spectrometer's wavelength range. For each line whose Stark width is to be experimentally determined, an instrumental peak must be measured at that wavelength (this makes the low pressure gas lamps a greatly convenient choice), and the profile determined by applying a cubic spline to the measured peak points. Ref. [74] suggests that the spectral width of detector pixels should ideally be about 10-20% of the FWHM of the instrumental profile, but in the case of the Ocean Optics HR4000 instrument available for the PW studies, this can be seen in 2.21 to be a far less ideal 30-40% of the FWHM. This means that the points defining a peak are quite sparse, and the application of the cubic spline to determine the IP doesn't fully capture its shape. Utilizing a spectrometer that had a longer focal length and/or the option of the user switching diffraction gratings (greater groove density means narrower wavelength range but superior resolution) would likely have afforded greater calculation reliability to this study. In Ref. [64], it is suggested that ideally the instrumental broadening is at most 1/10 of the full width of the observed profile, a condition which is not the case for the present work, especially in argon where the

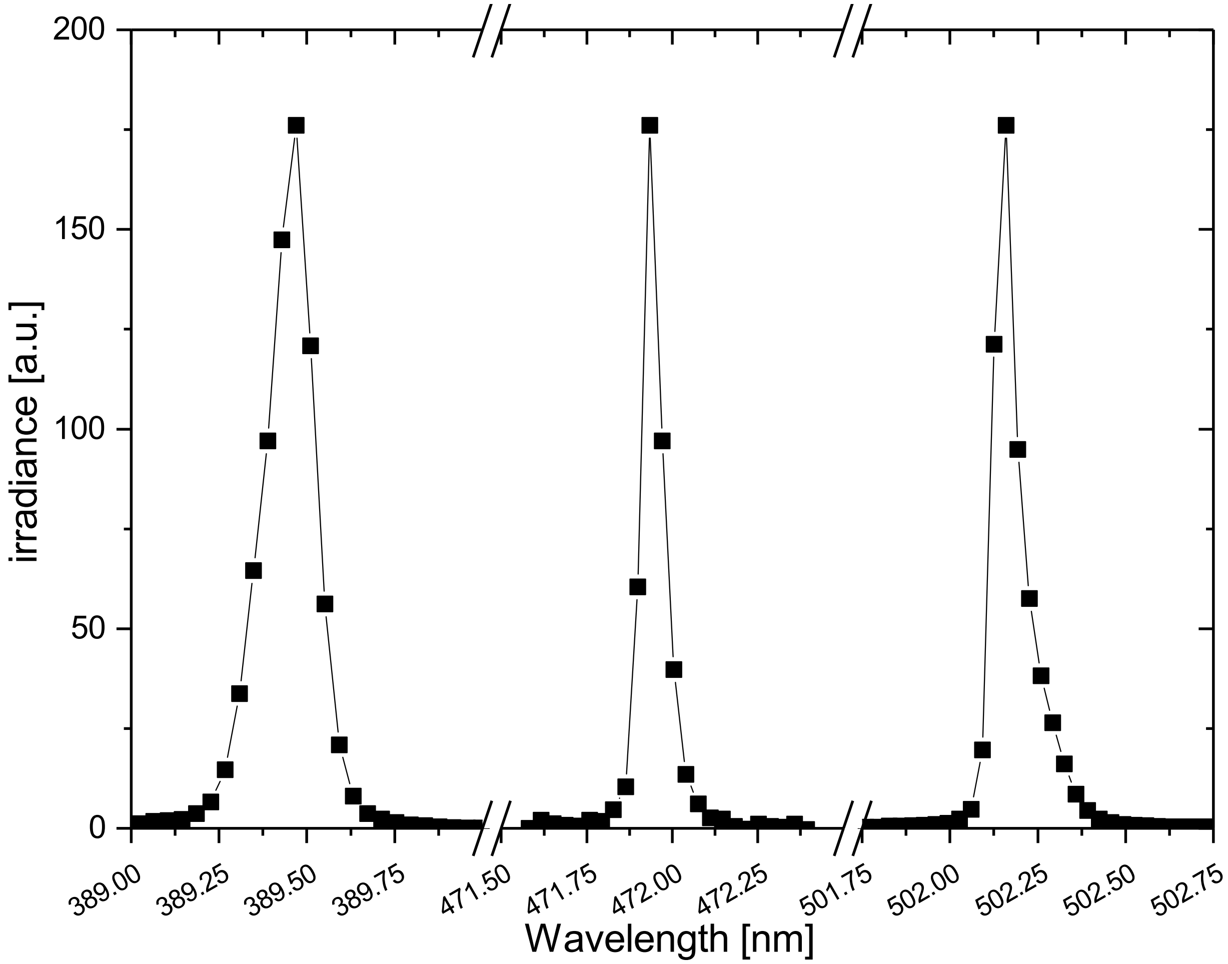

Figure 2.21: Instrumental profiles for the Ocean Optics HR4000 spectrometer used in this project. These profiles were acquired using a low pressure He gas discharge lamp.

instrumental broadening can be up to about half the total measured width.

It should be noted that in the helium arc, some emissions are observed to have nearby forbidden components which arise at higher electron densities [75, 76]. These are emissions close in energy to allowed transitions, and can manifest where perturbing electric microfields from high electron densities results in mixing of wave functions that ordinarily are disallowed through usual dipole selection rules [66, 75]. This ordinarily forbidden transition is induced at the expense of the allowed transition, and at the electron densities in the PW, is generally about 20% the irradiance of the latter, but for much higher electron densities, can be of roughly equal and even greater amplitude than the allowed transition at densities between 10^{17} - 10^{18} [77, 78]. The presence of such forbidden components is observed in the PW spectra collected for a couple lines: the 447.15 nm line ($1s2p\,^3P^0 - 1s4d\,^3D$) has a forbidden component lying at 447.0 nm ($1s2p\,^3P^0 - 1s4f\,^3F^0$), and the 492.19 nm line ($1s2p\,^1P^0 - 1s4d\,^1D$) has a forbidden component lying at 491.9 nm ($1s2p\,^1P^0 - 1s4f\,^1F$). For both of these localities, the upper states are coupled through the perturbing electric field via the Stark effect [77] which is produced by charged neighbors in the vicinity of the emitting particle. As a result, the compared characteristics of the allowed and forbidden components of the emission provide another probe of the electron density. The behavior of these emission components with plasma conditions have previously been thoroughly examined e.g. in the works of Refs. [75–80].

The authors of Ref. [77] provide an empirical formula for the relationship between the He 447.15 nm allowed-forbidden separation s and the plasma's electron density n_e and temperature T_e. However they suggest this empirical relation is applicable for electron densities between 5x10^{16} to 7x10^{17} cm^{-3}, which is well above typical PW electron density. This expression is given as:

$$log_{10}(n_e) = 21.5 + log_{10}\left[\left(\frac{s}{s_0}\right)^{b(T_e)} - 1\right] \tag{2.19}$$

,

with

$$b(T_e) = 1.46 + \frac{8380}{T_e^{1.2}} \tag{2.20}$$

,

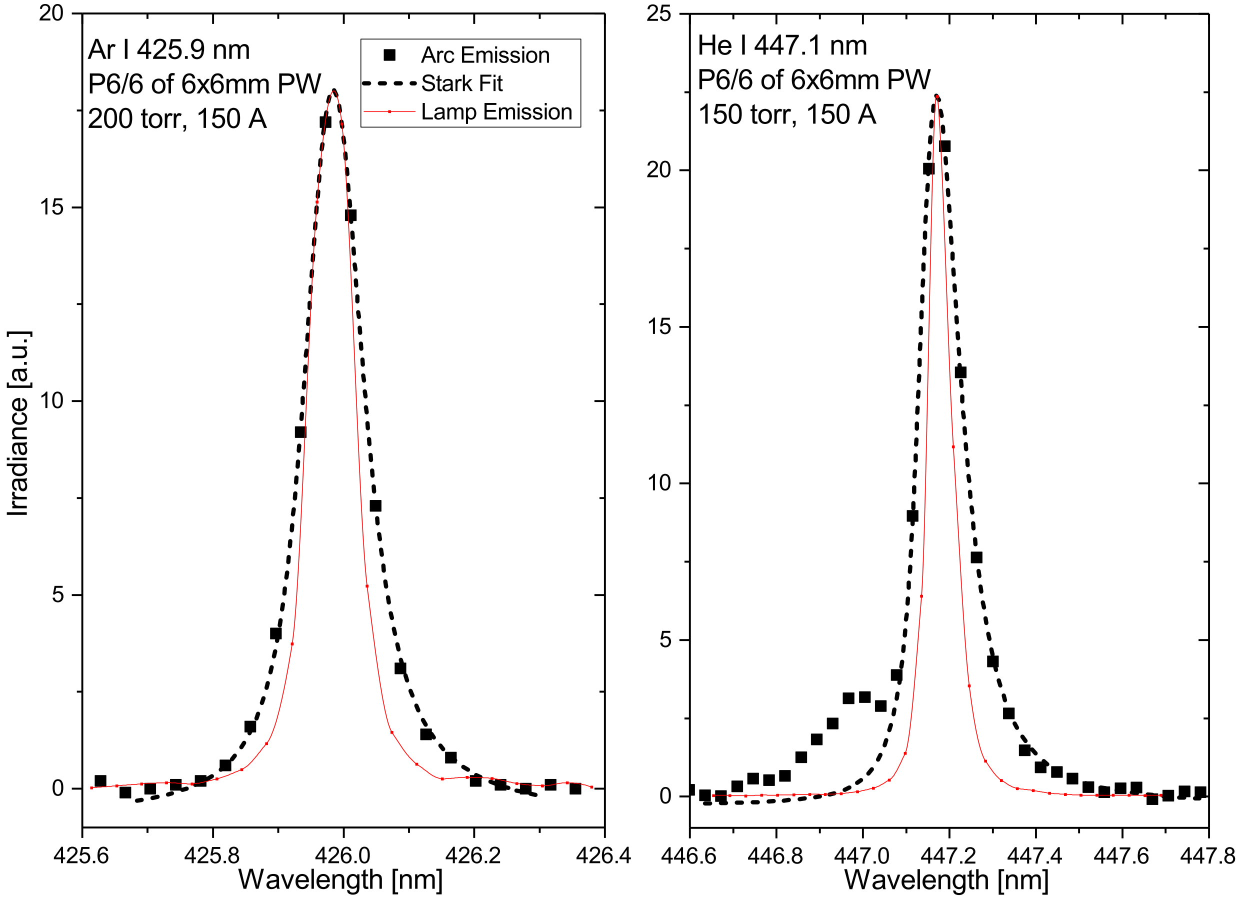

Figure 2.22: Sample Stark fits for the Ar I 425.9 nm and He I 447.1 nm emissions respectively, for a representative operating condition of 200 torr (150 torr for He) and 150 A in a 6x6mm PW, collected at P6/6. Instrumental profiles obtained by low pressure lamp discharge are also shown. A forbidden component on the blue wing of the primary He peak is also seen (this is not fitted).

in which electron temperature T_e is in K, s and s_0 are in nm, and n_e is in m^{-3}. The value of s_0 is given as 0.1479 nm.

One potential improvement in the Stark profile fitting routine, particularly for those He lines with forbidden components, would be to fit the entire profile to a calculated one, rather than fitting the approximate parameterized profile in Eq. (2.15). Ref. [75], and more recently Ref. [76] for example have calculated profiles for the He 447.15 nm line at a variety of plasma conditions, and in fact also include the 447.0 nm forbidden component characteristics, which is not fitted in the routine described and utilized in this thesis. In Fig. 2.22, the Stark broadening and forbidden component features described in the previous several paragraphs are illustrated, along with Stark fits performed using the routine described above.

It is therefore important to get an idea of how close the electron density obtained from Stark profile fits are to the average electron density over the cross sectional area at some given axial location. Diagnostic plates available in this project provide a line of sight only across the central chord of the channel's cross section, and as a result an Abel transformation to obtain radial distribution of the electron density is not possible. Having optical access to off-center chords as well would enable one to more reliably determine the radial behavior of emission irradiances and electron densities. Not having those measurements made here, we will look to previous measurements and the PLASIMO model for a prediction of the shape of the electron density profile. Results published by Timmermans et al in [81] in an argon cascaded arc illustrate determined electron density radial profiles as seen from an end-on view.

2.2.3 Electron Temperature

Another key property of a plasma that can be used characterizes its behavior is the electron temperature, given by T_e which plays a prominent role in the rates of interactions within a plasma. As mentioned in Chapter 1, the EEDF is often assumed to be Maxwellian and given by Eq. (1.14), a claim which will be quantitatively examined in Section 3.1. As a result, as first mentioned in Section 1.2, for a given binary electron-impact reaction the rate constant can then be obtained by:

$$K(T) = \left(\frac{1}{\pi\mu}\right)^{1/2} \left(\frac{2}{kT_e}\right)^{3/2} \int_0^\infty E\,\sigma(E)\exp^{-E/kT_e} dE\,, \tag{2.21}$$

in which $\sigma(E)$ is the process cross section as a function of energy, T_e is the electron temperature, and μ is the reduced mass (for electron-heavy collisions, this is essentially the electron mass m_e).

The observed intensity of a given emission line is given by:

$$I = \frac{S_a}{4\pi r^2} n_u A_{ul} \Delta E\,, \quad \Delta E = E_u - E_l = hc/\lambda\,, \tag{2.22}$$

where subscripts u and l refer to the upper (or emitting) state and lower state respectively [47,82]. Note that all fine-structure states are grouped together into one, for the purposes of this work. Additionally, S_a is light acceptance area at a location r away from the emitters (and assuming an isotropic emission), n_u is the emitter density, and ΔE is the emitted photon energy and the energy difference between upper and lower levels. Lastly, A is the spontaneous emission rate, which is obtained through a quantum electrodynamics treatment of the emission [45], namely for a transition from sublevel m_u of the upper level u to all possible m_l sublevels of the lower level l:

$$A_{ul} = \frac{8\pi e^2 \Delta E}{3\epsilon_0 h^2 c^3} \sum_{m_l} \left| \langle 1 m_l | \vec{r} | 2 m_u \rangle \right|^2 . \tag{2.23}$$

Note that in Eq. (2.22), every factor is either a property of the emission or the light collection system, with the only exception being n_u which is a property of the plasma within. Therefore, establishing a connection between the plasma's properties and the resulting excited state population distribution for the collection of possible excited states means that one can use the corresponding collection of emission irradiances to probe those same plasma properties [7, 46, 47]. When electron-impact collision rates dominate over radiative rates, then the relative populations of excited states assumes a Boltzmann distribution such that for states 1 and 2:

$$\frac{n_2}{n_1} = \frac{g_2}{g_1} \exp\left(-\frac{E_2 - E_1}{k T_e} \right) , \tag{2.24}$$

where g is the state degeneracy, E the state energy, and T_e is the electron temperature, reflecting the fact that the levels assume their densities via electron-impacts [7]. If it is the case that radiative processes are insignificant compared to collisional processes for all excited states, the system can be said to be in local thermodynamic equilibrium (LTE), and this condition generally requires a rather high electron density, greater than the value obtained in the PW in this work. However, even at electron densities lower than the LTE limit, the highly excited states may still meet the requirement of collisional processes dominating over radiative processes and therefore Eq. (2.24) can still hold for these highly excited levels, a conditions which is called partial local thermodynamic equilibrium (PLTE). This is not always the case, and the conditions under which two given states obey Eq. (2.24) is discussed in more detail in Section 2.2.3.1. If the plasma conditions do not meet the requirements for at lease PLTE for the emissions being observed, it is still possible for the emission states to obey a Boltzmann distribution and therefore Eq. (2.24) would hold as long as T_e is replaced by a generic excitation temperature T_{exc} [44].

The spectral irradiances of the emissions are captured by the spectrometer discussed in Section 2.1.3.1, but the emission's overall irradiance is smeared over some wavelength range due to the broadening mechanisms mentioned in Section 2.2.2. Spectral irradiances are irradiances per unit wavelength, whereas the overall emission irradiance (what can properly just be called irradiance) is integrated over the peak's wavelength or frequency extent. In Chapter 4 of Ref. [7], the author provides a rather comprehensive discussion of these and more often confusing terms pertaining to light fluxes and their detection. As a result, from here on out when emission irradiances are mentioned, it is the value obtained by integrating over the line profile. Furthermore, Eq. (2.22) would be correct for the case in which the emitted photons do not suffer from any reabsorptions elsewhere in the plasma prior to detection. If this condition is met for a given transition, it is said to be optically thin. The case of optically thick lines is treated in Section 2.2.4, but we will assume that the only lines which sustain any appreciable reabsorption will be resonance lines which decay to ground state. Combining Eq. (2.22) and the state density scaling in Eq. (2.24), and maintaining the general form in which T_e is replaced by T_{exc}, the emission properties can be rearranged as:

$$\ln\left(\frac{IA}{g_u}\right) = -\frac{E_u}{kT_{exc}}\,. \tag{2.25}$$

This expression can be applied to multiple emission lines and X-Y points where $X = E_u$ and $Y = \ln\left(\frac{IA}{g_u}\right)$. Note that the geometric factor $\frac{S_a}{4\pi r^2}$ would be just an additive constant

Table 2.3: Selected Ar II emission properties for lines studied in this work.

λ [nm]	Emitting state [Config., Term, J]	E_u [eV]	g_u	A [s^{-1}]	Accuracy
457.93	3p4.(3P).4p ^{2}S^o 1/2	19.973	2	8.00x10^7	<10%
458.99	3p4.(1D).4p ^{2}F^o 5/2	21.127	6	6.64x10^7	<3%
460.96	3p4.(1D).4p ^{2}F^o 7/2	21.143	8	7.89x10^7	<3%
473.59	3p4.(3P).4p ^{4}P^o 3/2	19.261	4	5.80x10^7	<3%
480.60	3p4.(3P).4p ^{4}P^o 5/2	19.223	6	7.80x10^7	<3%
487.99	3p4.(3P).4p ^{2}D^o 5/2	19.680	6	8.23x10^7	<3%
500.93	3p4.(3P).4p ^{4}P^o 5/2	19.223	6	1.51x10^7	<10%

Table 2.4: Selected He I emission properties for lines studied in this work.

λ [nm]	Emitting state [Config., Term, J]	E_u [eV]	g_u	A [s^{-1}]	Accuracy
438.79	1s5d ^{1}D 2	24.043	5	8.9889x10^6	<0.3%
492.19	1s4d ^{1}D 2	23.736	5	1.9863x10^7	<0.3%
501.57	1s3p ^{1}P^o 1	23.087	3	1.3372x10^7	<0.3%
471.32	1s4s ^{3}S 1	23.594	9	3.1736x10^6	<0.3%
402.62	1s5d ^{3}D 3,2,1	24.043	26	6.6926x10^6	<0.3%
447.15	1s4d ^{3}D 3,2,1	23.736	26	1.3882x10^7	<0.3%

to this expression, but has been dropped from this equation due to it simply being an offset value. From this, performing a simple linear fit allows one to use the slope to determine T_{exc}. This is the commonly employed Boltzmann line method [46, 47, 82].

The emission properties listed in Tables 2.3 and 2.4 are obtained through the NIST database [83], and further information on the notation used for the excited electronic states can be found in Ref. [84].

In the wavelength range of the Ocean Optics HR4000 spectrometer used (about 385 to 515 nm), the observed Ar I emissions do not span a wide range of upper state energies, making the Boltzmann line method unreliable for these emissions, however Ar II lines are plentiful, intense relative to background, and have a relatively large span of emitting state energies so these are used for determining T_{exc} in argon arcs in this work. Ultimately, Ar II lines appear to be adequate for determining electron temperature, but this is not true for observed emissions helium. This will be explained in Section 2.2.3.1. This would confirm the suspicion that the T_{exc} obtained via Boltzmann plot for helium emissions is not representative of the actual electron temperature T_e because it is far lower, around 0.3 to 0.6 ev, than would be expected necessary to maintain ionization to sustain the arc. It is therefore required to have another means of backing out what the electron temperature T_e is from relative He I emission irradiances. As a result, we will need to explore an additional tool to back out an electron temperature resulting in the observed relative He I emissions. This tool is called a collisional-radiative (CR) model, and will be explored in Section 3.2.

2.2.3.1 Applicability of Partial Local Thermodynamic Equilibrium

In partial local thermodynamic equilibrium (PLTE), high-lying excited states of an atom or ion are in thermal equilibrium with electrons, and follow Saha-Boltzmann distributions [44, 52, 85],. The significance of this is that the excitation temperature which defines the distribution of the excited states, T_{exc} is equivalent to the electron temperature T_e. Many different theoretical approaches to determining the conditions under which PLTE is applicable, which are briefly summarized in [85]. All are predicated on the condition that above a certain level threshold, electron-impact rates for a given transition should exceed the corresponding radiative rates by at least an order of magnitude [52, 85]. Level populations n_k of levels above the threshold are related to the next ion stage ground-state population n_i via the Saha-Boltzmann relation [52, 85]:

$$\frac{n_e n_i}{n_k} = \frac{2g_i}{g_k} \frac{(2\pi m_e k T_e)^{3/2}}{h^3} \exp\left(-\frac{(E_{ion} - E_k)}{kT_e} \right). \tag{2.26}$$

In this expression, g_i is the degeneracy of the ground state of the ion, g_k is the degeneracy of the excited state k, E_{ion} is the ionization energy (relative to the ground state), E_k is the energy of level k, and electron mass, density, and temperature are given by m_e, n_e, and T_e respectively.

When this equation is satisfied, the levels are said to be in Saha excitation equilibrium. The task then is to determine what the threshold level is, above which Eq. (2.26) is valid, and therefore a Boltzmann plot of emissions originating higher than the threshold provides an excitation temperature such that $T_{exc} = T_e$. The descriptions of various workers' criteria for this PLTE threshold are frequently somewhat ambiguous, particularly for non-hydrogenic systems atomic excitation and ionic excitation distributions, a category into which the PW studies in both helium and argon fall, although it is sometimes assumed, particularly for light elements, that highly excited states are close enough to hydrogenic that derived criteria can still apply to them [50, 86, 87]. We will start by examining the criterion established by Griem [50, 52]. This criterion, in terms of an equivalent excited principal quantum number n_{cr} (note this n represents a quantum number, not a number density such as n_e) is given by:

$$n_{cr} \approx \left[\frac{5}{\pi} \frac{z^7}{n_e} \left(\frac{\alpha_f}{a_0} \right)^3 \right]^{2/17} \left(\frac{kT_e}{z^2 E_H} \right)^{1/17}. \tag{2.27}$$

With this, for excitations originating from a state exceeds this critical principal quantum number n_{cr}. In this, a_0 is the Bohr radius (if in units of cm then the electron density will be in units of cm^{-3}), α_f is the fine structure constant, E_H is the ionization energy of hydrogen, and z represents the ionization stage ($z = 1$ for neutral excited states, $z = 2$ for singly-ionized excited states, etc.). This can be rearranged to obtain instead a critical electron density $n_{e,c1}$ for emission lines of known quantum number n:

$$n_{ec1} \geq \left[\frac{5}{\pi}\frac{z^7}{n^{17/2}}\left(\frac{\alpha_f}{a_0}\right)^3\right]\sqrt{\frac{kT_e}{z^2 E_H}}\,. \tag{2.28}$$

Griem mentions this criterion is properly applicable only to hydrogenic systems [50], however also mentions that it should also be relatively appropriate for higher excited levels of light atoms or ions. Despite it often being applied to Ar I and Ar II plasmas, it's not clear if the upper levels of Ar I and Ar II do obey a hydrogenic energy scheme and therefore it is unclear if this is appropriate in these plasmas [82, 88].

A second criterion is derived in Ref. [44] and is utilized in Ref. [88], which is approximately:

$$n_{ec2}\sqrt{T_e}\left(\frac{E_H}{\Delta E_i}\right)^{9/2} z \geq 8\times 10^{17}\,. \tag{2.29}$$

The critical electron density evaluated with this criterion, n_{ec2} is in units of cm^{-3}. The ΔE_i is the ionization energy of the state in question. In this, T_e is given in eV. Rearranging, Eq. (2.29) gives the criterion in terms of electron density:

$$n_{ec2} \geq 8\times 10^{17}\frac{1}{z\sqrt{T_e}}\left(\frac{\Delta E_i}{E_H}\right)^{9/2}\,. \tag{2.30}$$

The third criterion that will be mentioned here is that in Ref. [87]. This third criterion,

Table 2.5: PLTE criteria for He I and Ar II emissions. Argon T_e is 1.5 eV and the Ar II level under consideration is 4p ^{4}P^o 5/2. For Helium T_e is 2.0 eV and He I level is 3p ^{1}P^o.

Criterion	Ar II critical n_e [cm^{-3}]	He I critical n_e [cm^{-3}]
1	6.8×10^{14}	1.4×10^{14}
2	9.9×10^{15}	2.8×10^{13}
3	7.1×10^{15}	4.9×10^{16}

with the electron density again in units of cm^{-3}, is given by:

$$n_{ec3} \geq 1.15 \times 10^8 z \frac{g_j}{g_i} \sqrt{kT_e} \frac{(E_j - E_i)}{E_H^{3/2}} \frac{\sum_{h<j} A_{jh}}{f_{ij}} \; \Phi_{1,2}\left(\frac{E_j - E_i}{kT_e} \right). \tag{2.31}$$

In this, states j (upper) and i (lower) originate from adjacent levels whose energies and degeneracies are given by E and g respectively, and E_H is the ionization energy of hydrogen. Note that for this, energies and kT_e should be in the same units. Also included in this equation is the summed rates of all other transitions originating from the upper state j, $\sum_{h<j} A_{jh}$ and the oscillator strength between the adjacent levels f_{ij}. Finally there is also a factor $\Phi_{1,2}\left(\frac{E_j - E_i}{kT_e} \right)$ which is tabulated in Ref. [87], which are factors associated with electron-impact excitations.

Some estimates of these critical electron densities from all three references are presented in Table 2.5, for both helium and argon. The electron temperatures of 1.5 and 2.0 eV for argon and helium respectively and the Ar II and He I levels used as a test case has one of the lowest emitter state energies in the wavelength range observed for Ar II and He I respectively. These states are given in the caption of Table 2.5. A sizeable amount of spread exists between the critical electron densities given by the methods, in all three cases for Ar II, the measured electron densities which in the argon PW generally exceed 1×10^{16} [cm^{-3}] are sufficient to achieve PLTE for the emitting states in our observation range. For the case of helium, the conclusion is less obvious, as the measured electron density is typical around

2×10^{15} [cm^{-3}], which results of the first two criteria suggest allows PLTE, but the third criteria does not. Given this uncertainty for He I emissions, we will not assume the existence of PLTE for these emitting states and therefore that the He I $T_{exc} \neq T_e$. However, for the Ar II emissions, we will assume the existence of PLTE for the observed emitting states and therefore that Ar II $T_{exc} = T_e$.

2.2.4 Radiation Reabsorption

Radiation emitted through the process of de-excitation can be reabsorbed at a different location within the plasma via the inverse process. Taking a packet of photons whose initial intensity is $I(\lambda)$, impinging on a layer of absorbing particles (these would be those particles in the lower excited state corresponding to the emission whose reabsorption we are investigating), ds thick. The loss of intensity of that original packet of photons is:

$$dI(\lambda) = -I(\lambda)\sigma_{abs}(\lambda)n_l \, ds \, , \tag{2.32}$$

where σ_{abs} is the photon absorption cross section and n_l is the absorbing state density. Integrating this over an absorbing distance D:

$$I(\lambda) = \exp(-\sigma_{abs} n_l D) \, . \tag{2.33}$$

The quantity inside the exponent on the right hand side is often grouped into the unitless parameter $\tau(\lambda)$, called the spectral optical depth of the plasma at wavelength λ [45, 89, 90], so:

$$\tau(\lambda) = \sigma_{abs} n_l D \tag{2.34}$$

,

with the photon absorption cross section is given by:

$$\sigma_{abs} = \frac{\lambda_0^4}{4\pi c}\frac{g_u}{g_l}A\, f(\lambda) \tag{2.35}$$

.

In this, the emission's central wavelength is given by λ_0, c is the speed of light, g_u and g_l are the upper and lower state degeneracies respectively, A is the Einstein spontaneous emission rate, and $f(\lambda)$ is the absorption profile (we will assume this to be of the same shape as the emission profile). As noted previously, Stark broadening is the dominant source of non-instrumental broadening (the absorption occurs entirely within the plasma, so the instrumental profile plays no role here) for the Ar I and He I lines in this work. However, it should be pointed out that Ar II emission lines have significantly narrower Stark broadening, such that it is on the order of the Doppler broadening degree. For simplicity though, we will still assume that we can just look at the Stark profile in Eq. (2.15) and even further simplify matters by ignoring the ion-broadening contribution, giving us an emitting/absorbing profile that is purely Lorentzian. This vastly simplifies the analysis and lets us write a relatively compact expression for the absorption profile:

$$f(\lambda) = \frac{w_j}{w_j^2 + (\lambda - \lambda_0 - d)^2}\,. \tag{2.36}$$

As before, w_j is the Stark width and d is the Stark shift for the particular emission line in question, at the plasma electron density. With this one can determine the spectral optical depth across the emission profile, $\tau(\lambda)$. Resonant emissions which decay to the ground state will have have a much larger absorbing density n_l as well as a much greater absorption cross section σ_{abs} due to the lines being much narrower than emissions which correspond to decays to still-excited states, these are the lines which will suffer the must reabsorption by far [66].

If the plasma is both absorbing and emitting (this is the case for the PW), this optical depth can be used to calculate what is called an escape factor $g(\tau(\lambda))$, essentially the fraction of the total emitted light over the distance which ultimately escapes the plasma. An escape factor of 1 means there is negligible absorption and the line is said to be optically thin. The spectral escape factor is given by [90]:

$$g\Big(\tau(\lambda)\Big) = 1 - \left(\frac{\lambda_0}{\lambda}\right)^3 \left[1 - \exp\Big(-\tau(\lambda)\Big)\right], \tag{2.37}$$

though what is more often reported is the overall escape factor, obtained by averaging over the profile so that:

$$g(\tau) = 1 - \int \left(\frac{\lambda_0}{\lambda}\right)^3 \left[1 - \exp\Big(-\tau(\lambda)\Big)\right] f(\lambda) d\lambda\,. \tag{2.38}$$

Some implicit assumptions that are fairly reasonable in this are that stimulated emission has been ignored, and the absorbing and emitting profiles are identical in shape, which effectively means the plasma is uniform [90].

2.3 Cathode Longevity

As mentioned in Section 1.1, the application of the plasma window as a charge stripper for an ion accelerator facility naturally demands that the plasma window be capable of operation continuously for the duration of a typical experiment which utilizes the accelerator facility. For example, at the NSCL where experiments are conducted on nuclear properties of primarily rare isotopes, the duration is maximally about two weeks, as mentioned in Section 1.1. There are a great many cathode-specific variables which can impact their operating lifetime, especially in the case of using tungsten doped with impurities that lower the work function (WF). Due to attention in the PW project being concentrated on plasma phenomena and long-term arc stability challenges, empirical data on cathode lifetime is very limited for the PW study at this point. Here an effort is made instead to survey relevant literature and compile conclusions, so that suggestions for PW cathode improvements can be made. Some studies seem to suggest that, although the PW studied in this thesis was unable to operate continuously for nearly this length of time, cathode operation in arcs of up to 1000 hours is possible. In Ref. [91], using an argon cascaded arc very similar to our own, operating around 50 A and a half-atmosphere, it is claimed that their thoriated tungsten cathodes typically operated for about 500 hours before replacement was needed. In Ref. [12], the authors operated their thoriated tungsten cathodes in a 60 A arc at 600 torr beyond 1000 hours.

Although dimensions may vary from study to study, all references in this section which investigated cathode performance in various conditions used cone-tipped-rod cathodes, the same geometry type used for the plasma window. It is well known that for an electron to escape from the cathode and participate in electric current to the anode, it must either overcome the WF, or tunnel through the potential barrier. A great many materials are used in a great many applications, but a survey of literature in this work will primarily be focused on the performance of tungsten, WF = 4.6 eV, doped with thoria (ThO_2), reduces WF to 2.8 eV or lanthana (La_2O_3), reduces WF to 3.0 eV [92], also referred to as thoriated tungsten and lanthanated tungsten respectively. In the PW work, thoriated tungsten cathodes were primarily used.

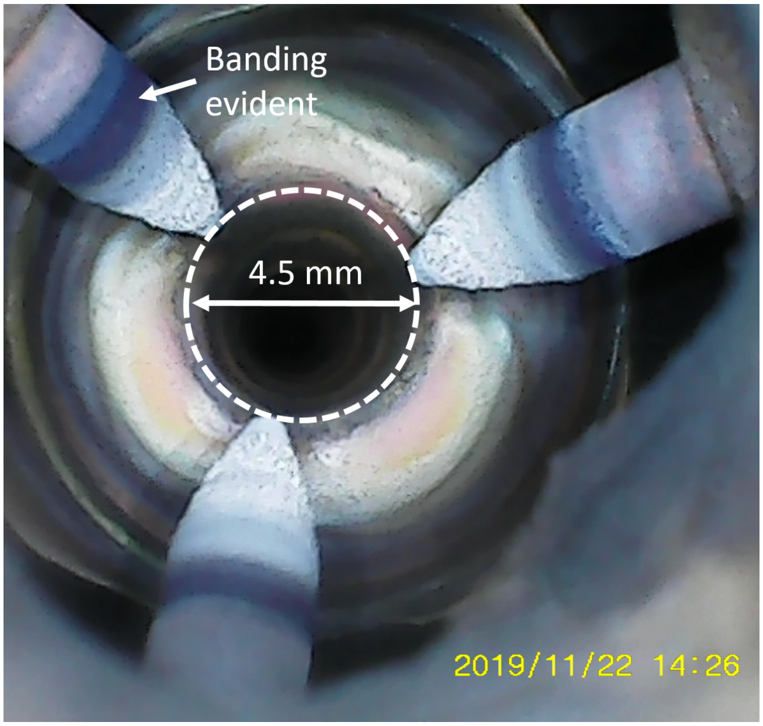

Figure 2.23: View of the NSCL PW cathode tips from inside the cathode housing, looking down the channel towards the anode. Banding structure is visible on the used ThO_2-W cathodes, signifying regions of varying thorium concentrations, as described in Refs. [9–11].

Some features of the cathodes that are necessary for plasma window operation are a sharp tip, so that the arc can be initialized via field emission (using a Tesla coil), even though it subsequently maintains electron supply and current via thermionic emission, as first mentioned in Section 2.1.2. In our system, the cathode housing has three channels into which the cathode needles are inserted such that their tips are on a 4.5 mm diameter circle. This can be seen in Fig. 2.23 which shows a view of used cathodes tips inside the housing, looking down the channel towards the anode. The channel diameter in the cathode housing is about 13 mm diameter, shown in Fig. 2.24. The channel diameter subsequently reduces down to the PW channel size of 6 mm or 10 mm, depending on the aperture of the first plate.

Broadly, the two phenomena impacting cathode lifetime are shape deformation and mor-

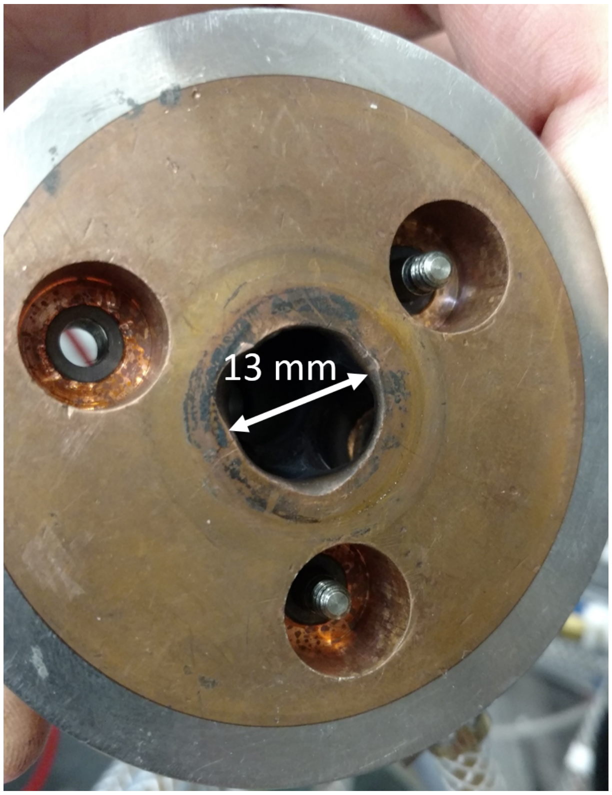

Figure 2.24: Cathode housing (without cathodes), view from the PW-side face. The housing channel is 13 mm diameter, which then constricts down to 6 or 10 mm diameter, depending on the aperture of the first PW plate.

phology changes [10, 12, 93]. Drawing conclusions regarding optimization of cathode characteristics is challenging due to the interplay between numerous properties and phenomena such as cathode geometry, cathode material, gas used, cooling, and current density [10, 94]. The emission-enhancing dopants mentioned earlier in this section provide a reduced WF on the surface of the cathode, yet being in a matrix of tungsten provides shape stability due to its high melting point. Without the presence of the WF-lowering dopant, the operating temperature of the cathode is much higher, and the material removal rate is far greater. This higher operating temperature manifests as a result of a greater cathode fall potential being necessary to drive ion collisions of sufficiently high energy to exceed the large WF to the electron emissions which sustain the arc. Evidence of this can be seen in Fig. 2.25. In this, pure tungsten cathodes and thoriated tungsten cathodes were each tested for about the same amount of operating time, about 30 minutes. The pure tungsten cathodes suffer substantially greater shape deformation, having the neck reduced as well as the formation of surface roughness. This illustrates the necessity of having a WF-lowering dopant in the cathodes.

During cathode operation, there are two competing processes which effect the presence of the WF lowering dopant (consider thorium) on the cathode surface: desorption or evaporation of thorium atoms from the hot surface, and the supply via diffusion from the cathode bulk [95]. In this cathode modeling study, it was concluded that there are primarily two regimes of cathode operation. The first one is characterized by a lower operating temperature, and in this regime there is nearly a monolayer of thorium coverage over the cathode's emitting surface. Over time this thorium coverage degree decreases until reaching some critical value, beyond which the surface temperature rapidly rises and the dopant coverage rapidly decreases to nearly zero, signaling the arrival of the second operation regime.

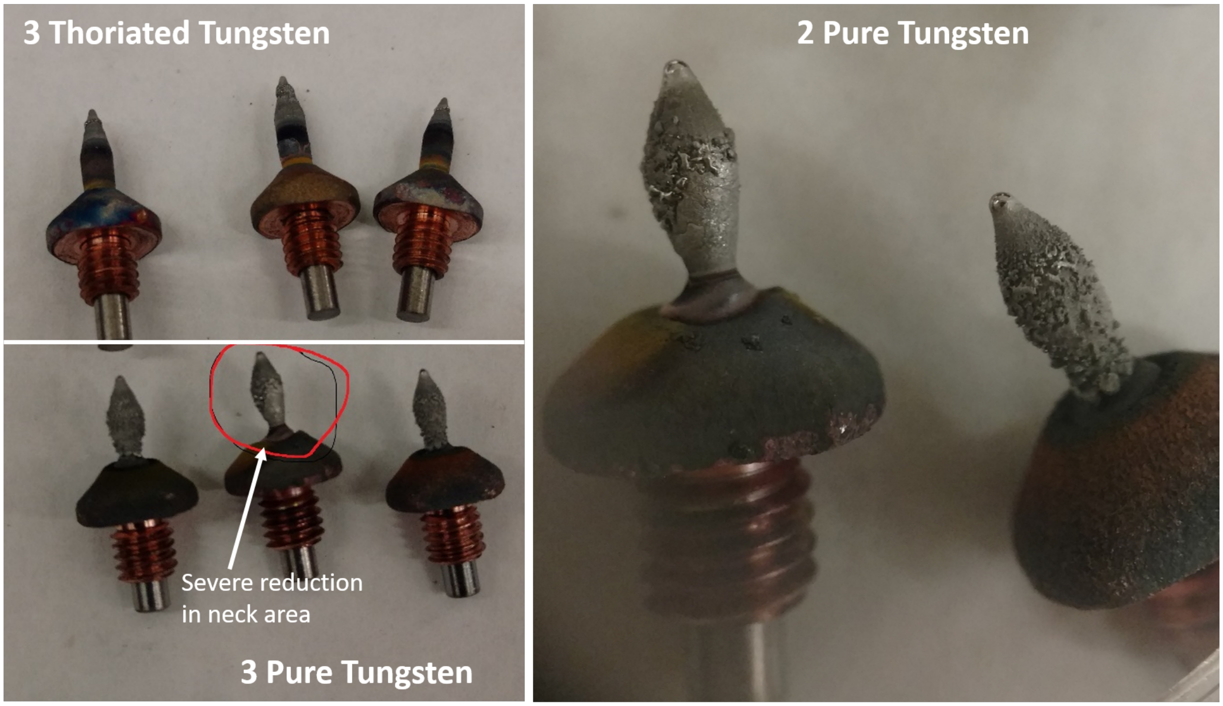

Figure 2.25: Top-Left: Thoriated tungsten cathodes after about 30 minutes of operation. Bottom-Left: Pure tungsten cathodes after about 30 minutes of operation. Right: Zoom of the pure tungsten cathodes, illustrating neck reduction and formation of surface roughness.

Now the operating temperature is much higher and cathode material will be more rapidly depleted. In Ref. [95], this is identified as effectively the end of cathode operating lifetime.

There are some key findings in Ref. [95] that are worth mentioning. Firstly, the authors determined that an often-overlooked contribution to the cathode's internal temperature distribution is Joule heating from the current. Higher temperatures in the vicinity of the emitting surface encourage thorium diffusion to it and therefore delay the aforementioned rapid removal of surface thorium and rapid surface temperature increase, thus extending the cathode lifetime. Therefore, while higher currents result in more rapid surface thorium removal, that removal is compensated to a greater degree by the higher Joule heating. In general, the authors present the conclusion that a shallower temperature gradient through the cathode enables greater cathode lifetime, supporting the same conclusion obtained in

Ref. [93]. A cathode model of the sort established in this publication could be helpful in guiding improved PW cathode designs.

In the modeling study of Ref. [93] it is emphasized that the potential lifetime of a rare earth oxide doped tungsten can be extended by a favorable temperature distribution within. The case investigated here was W-ThO_2, and although chemical processes were neglected in this study, the author found that the balance between adsorption of dopants from the cathode surface, and diffusion-replenishment of those dopants from the cathode bulk to the surface were key in establishing the cathode's service lifetime. Additionally, the author concluded that longer electrodes, owing to a less steep temperature gradient, allow for greater diffusion and therefore extend the cathode lifetime. Diffusion in shorter electrodes can only occur over a shorter length. The authors furthermore posit that a thinned diameter, or neck, along a cylindrical cathode can potentially increase the lifetime by acting to increase thermal and diffusive resistance, though it's suggested experimental investigation is needed to provide evidence one way or the other. Similar to what was described in Ref. [95], Nemchinsky posits that there are distinct stages in the lifetime of a refractory metal cathode doped with a rare earth oxide (thoria in this case). An initial stage in which intense diffusion results in a thick layer of thorium, though diffusion is overtaken by evaporation from the surface at some point, and eventually only a monolayer of the thorium remains on the surface. This process precedes the two stages focused on in Ref. [95]. In the second stage, parts of this monolayer are evaporated so that the overall coverage ratio is less than unity, causing the work function and surface temperature to increase. This then results in accelerated evaporation and diffusion.

In a separate modeling study, in Ref. [96], the same author studied the effects of gas swirl on the rate of erosion of cathodes, although this was studied for a hafnium cathode operated in an oxygen plasma gas. In this it was shown that erosion rate is significantly enhanced with greater gas swirl in the vicinity of the cathode. The posited rationale is that the inclusion of swirl enhances the flow at the cathode and effectively acts to sweep away ions from the cathode region. It is unclear what the implications are for arc stability from the degree of swirl in the cathode vicinity, though it may suffer as well. This has relevance to the PW setup because of the several channel size changes in the vicinity of the cathode: entrance of cathode housing is 10 mm diameter, then it opens to 13 mm where the cathodes are inserted to the channel (see Fig. 2.24), then constricts down to the 6 or 10 mm diameter of the first PW plate.

One negative attribute of thoriated tungsten cathodes was investigated in Ref. [11] in which it is suggested that while thoria-activated tungsten electrodes are useful regarding the ease with which the arc can be initiated using them, they are prone to instability. The study investigated investigated cathodes of a number of different rare earth oxide dopants in tungsten, found lanthana-activated electrodes to overall sustain longer lifetimes. The W-La_2O_3 electrodes were shown to have the lowest work function and therefore the lowest operating temperature. During operation, the local quantity of oxides tends to decrease, and large tungsten crystals form at the tip of the W-ThO_2, as opposed to the W-La_2O_3 which was somewhat more resilient to this effect, and so had more consistent operation with time. For this reason, the authors found that La_2O_3 can more easily migrate through the cathode bulk to the surface to replace the emitting material that is vaporized during operation. The arc discharges were around 200 A for up to 1 hour of continuous operation. Electrode geometry in this study was similar to that in the present PW work, a cylindrical base (1.6 to 3.2 mm diameter) with a conical tip.

Conversely, one feature that negatively impacts the appeal of W-La_2O_3 was investigated by Ref. [97], which is so-called flickering of the arc, caused by fluctuations of the cathode attachment point. The authors of this study find that W-La_2O_3 electrodes suffer a greater flickering effect than do W-ThO_2 electrodes. The flickering is attributed to the much lower adsorption energy of La (5.6 eV) than Th (7.4 eV) which may result in more rapid surface impurity depletion, in addition to the higher vapor pressure of La than Th resulting a lower thermal stability of the surface.

Flickering has also been observed in the plasma window, likely attributable to the same phenomena. In some cases, it is sufficient to cause the arc to collapse and a cessation of current flow, which in the plasma window has almost always occurred during helium operation rather than argon. We refer to this occurrence as the arc collapsing, and it is not surprisingly a highly undesirable occurrence and any measure that can be employed to reduce its likelihood should be explored.

In Ref. [98], some properties of W-ThO_2 and W-La_2O_3 cathodes were examined in both pure argon gas and in argon with oxygen impurity gas. They concluded that the the presence of oxygen enables rapid oxidation of the cathode surface, which then first evaporates, dissociates, and finally the tungsten is redeposited a ways from the hot tip, forming a rim at a distance away from the tip which depended on cone angle and arc current. The authors furthermore observed a constriction of the arc from the cathodes with the addition of 1% oxygen to argon gas, causing a greater temperature at the attachment point. All in all, it is concluded that the presence of oxygen impurity in the plasma reduces the usable lifetime of the cathode, which only adds to the importance for the PW to be used with pure gas targets in the context of gas charge stripping.

Authors of Ref. [12] discuss the impact of different dopant concentrations on cathode performance, and are notably one of the exceptionally few studies to have observed behavior after very long term operation, both after 400 and 1500 operation hours. In addition to the crystallographic orientation of the emitting surface, the work function can be dramatically influenced by the adsorption of atoms of higher electronegativity than the base material (tungsten in this case). The authors provide an example of an oxygen layer on tungsten increasing the work function by more than 1 eV, and an opposite effect for atoms of lower electronegativity adsorbed such as thorium or lanthanum on tungsten. Existence of long-duration emission requires low evaporation rate of the emission-enhancing oxide. These authors noted that the cathode burn-back (length of cathode removed during operation) over 400 hours of operation of W-La_2O_3 for their particular setup is around 0.4 mm, and didn't discern any clear trend with respect to the impurity concentration.

Also noted in this work is the fact that thorium's low vapor pressure compared to other explored elements including lanthanum, as shown in Fig. 2.26. This is a copy of a figure in Ref. [12] that indicates that to achieve the same vapor pressure of metallic thorium, a cathode with lanthanum needs to be 400 K less than the thorium one. However, although thorium has a lower vapor pressure than lanthanum, it has a higher work function and so higher temperature. The degree of this temperature difference is also mentioned in the work of Ref. [10] to have a range of between 200 and 500 K depending on the size of grain boundaries. This brings us to another key result of their work, that the larger the size of grain boundaries, the lower the work function for thoriated tungsten cathodes, since the farther from the boundaries the less thorium evaporates from the surface.

In Ref. [10], thoriated tungsten cathode surface features were examined after up to an hour of operation with several parameters under investigation, including the plasma gas composition (argon or helium), and the cathode geometry (pointed tip or flat tip). It was found that for both cathode geometries, when operated in helium the cathode temperature

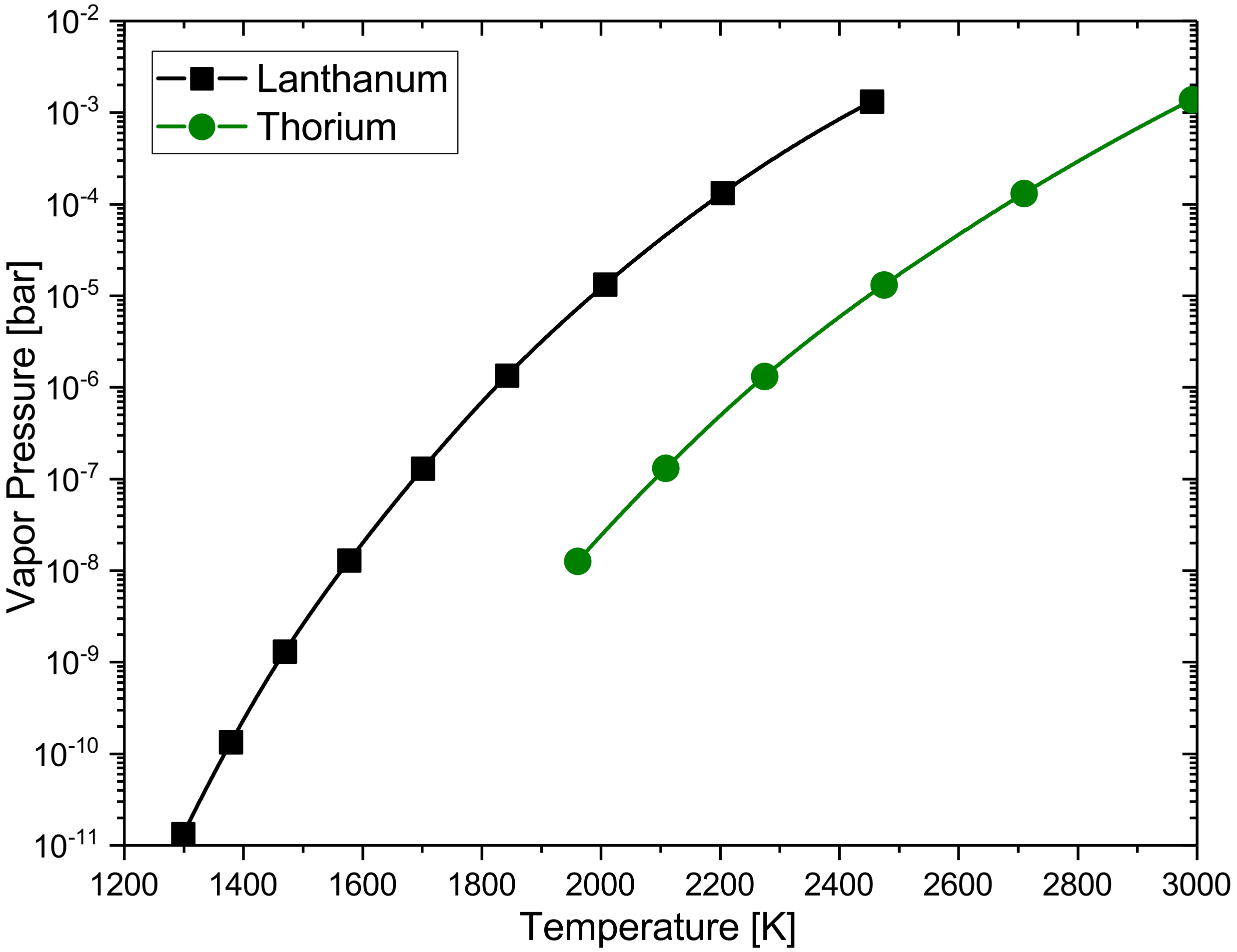

Figure 2.26: From data published in Ref. [12], this figure shows vapor pressures of metallic thorium and lanthanum as a function of temperature.

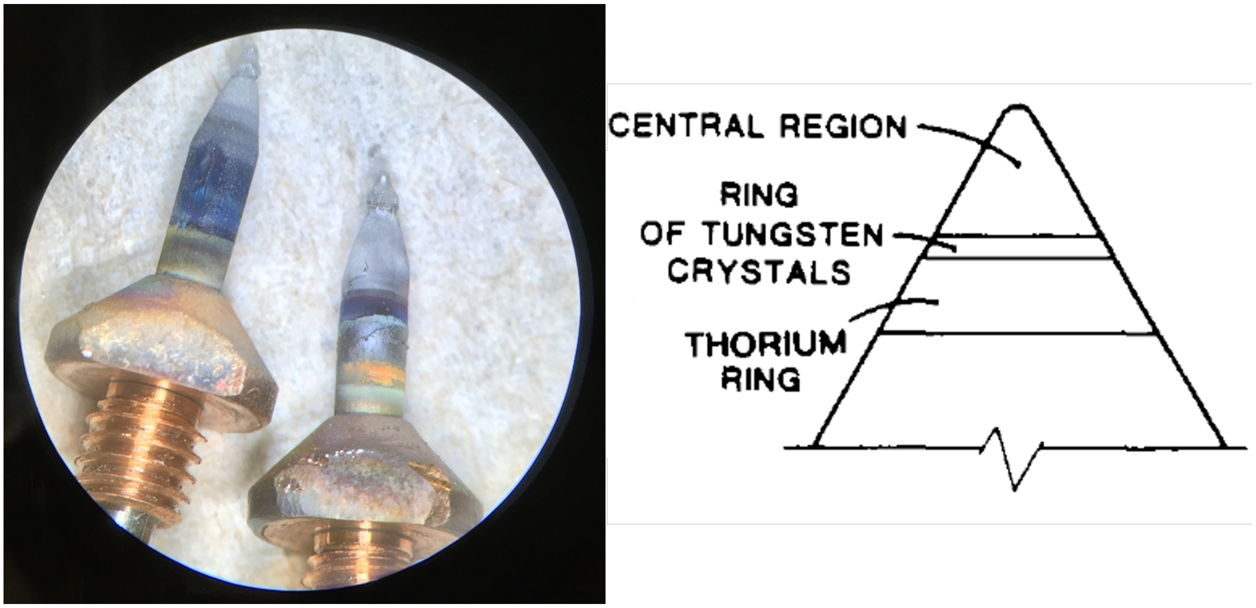

Figure 2.27: Left: A photo of PW cathodes after operation in He gas, showing a series of bands at different distances from the cathode tip. Right: a copy of a figure published in Ref. [10] which investigated similar behavior for thoriated tungsten cathodes operating in helium. Their surface morphology studies enabled identification of the bands as labeled.

was much greater than that in argon, resulting in rapid vaporization of cathode material which then was ionized and redeposited back to the cathode as ionic current. The energy released at the cathode surface by impinging ions determines the cathode temperature, and is a function of the ionic current (suggested to be 15 to 50 % of the total current density), the ionization energy, and the cathode fall potential drop. The overall effect is that when operated in helium, the cathode surface temperature is much higher than in argon, and approaches the boiling point of tungsten (5930 K). The redeposition occurs farther away from the tip of the cathode, resulting in bands of different materials.

The authors found that, in argon after about 5 minutes of operation, the thoria in the cathodes was mobilized and migrated towards the cathode surface, then moving laterally and forming high-concentration thoria regions. As a result of this migration and the accompanying change in surface work function, during this period the total arc voltage drops from

29 V to 26 V. Although the authors concluded there was a significantly greater amount of vaporization for the cathodes in helium, the net cathode mass loss was similar in both gases.

Given this complexity of material concentration banding of the cathodes evolving through use, and doing so differently in argon or helium, it is likely that cathodes operated, for example, in argon for some period of time prior to shifting to helium operation would have their properties and operable lifetime adjusted from those if it were operated only in helium from the start. Understanding of this potential phenomena could greatly benefit from additional research. This is relevant to operation of the PW because it was necessary in our work to initiate the arc in an argon flow first and then transition to a helium flow.

Chapter 3

Background and Models

The models presented in this section are included to lend support to measurements of certain plasma properties as well as to enable calculation of others that are not measured.

3.1 Electron Energy Distribution Function

As with all collections of particles, there exists for the electrons in the PW a distribution of their associated random kinetic energies, which is characterized by an electron temperature T_e. Fully equilibrated, the distribution function takes on a Maxwellian shape (this was also briefly mentioned in Section 1.2), given by:

$$f(E,T) = 2\sqrt{\frac{E}{\pi}}\left(\frac{1}{T}\right)^{3/2}\exp\left(-\frac{E}{T}\right), \tag{3.1}$$

This distribution is expressed such that the integral of the entire distribution, over all energies E, is equal to unity. The temperature T is identified as the electron temperature T_e if the EEDF is a Maxwellian shape, otherwise it is identified as an effective electron temperature T_{eff}. However, there are instances where this form is inadequate for describing the electron energy distribution function (EEDF), as mentioned in [99]. The reason this may occur in plasmas is because electron-impact inelastic processes - excitations or ionizations of the heavy particles - cause the impacting electron to lose kinetic energy by at least the corresponding threshold energy. If the electron temperature T_e, is such that these threshold energies lie within the less-populated tail of the distribution, then rapid inelastic occurrences may result in depletion of the high energy electrons in the distribution tail and hence elevated importance of elastic energy losses. The process of restoring the shape back towards Maxwellian shape (sometimes called Maxwellization) occurs primarily through electron-electron collisions. This section is devoted to examining rates of such inelastic processes and determining if Eq. (3.1) is appropriate for describing the electron energy distribution function (EEDF), or if the rapidity of inelastic collisions is sufficient to cause deformations in the EEDF tail.

In existing literature, thorough investigations of the appropriateness of a Maxwellian EEDF for a plasma regime typical of the PW are very few. Generally it is simply taken as an assumption that the EEDF in most achievable arc environments is Maxwellian, and indeed in Ref. [50], Griem claims that in plasmas of at least moderate density and low temperature ($n_e \geq 1 \times 10^{16}$ cm^{-3} and $T_e \leq 5$ eV), the EEDF is almost always Maxwellian. This is attributed to electron-electron collisions being so frequent that they can overcome any EEDF tail-depletion mechanisms, i.e. ionization and excitation, especially from the low-lying energy levels Ref. [87]. However, the actual collision frequency threshold criteria for electron-electron collisions is not mentioned. In Ref. [87] it is also mentioned that super-elastic electron collisions that force an excited state into a state of lower energy may also play a role, however we'll not examine these here. The conditions in the PW usually meet the above density and temperature requirements, but in the interest of thoroughness, it's worth making a short excursion to quantitatively investigate the likelihood that our typical arc plasma of the PW has a Maxwellian-shaped EEDF.

We do so by considering relative frequencies of two inelastic, tail-depleting processes: excitations from the ground state to the lowest-lying excited state, and ionizations from the ground state. These are then compared to the frequency of electron energy-transfer collisions which push the EEDF back towards a Maxwellian shape. If the former are many orders of magnitude less than the latter, we will assume that the EEDF does not stray far from a Maxwellian shape. We consider the reactions from ground state and not those from the metastable states for several reasons: firstly, we have a means of obtaining reactant density - i.e. the neutral density n_n - modeled via PLASIMO (discussed in detail in Section 3.5) which is likely a decent approximation of the ground density n_{grd} in the PW, so $n_{grd} \approx n_n$. We do not have a straightforward means of obtaining for example the metastable-state densities. Our second reason, however, is that the inelastic processes such as ionization originating from such metastable states have much lower threshold energies than the processes from the ground state. As a result, the threshold energy where electrons can first start participating in the reaction from a metastable state has substantially more electrons than at the threshold energy for the process from the ground state. This is illustrated in Fig. 3.1 by comparing the EEDF value at the ground-excited or ground-ion threshold energies given by the drop lines (black for Ar and red for He) to the approximate threshold value for ionization from metastable (the purple drop line, approximate for both gases). In this figure, the black solid curve is the EEDF for a temperature typical of the Ar discharges in the PW and the red dot-dashed line similarly for He discharges.

An energy-transfer collision frequency, as defined in Ref. [100], is the rate at which the pre-collision kinetic energy of a projectile-target pairing changes divided by the pre-collision kinetic energy. The velocity-dependent electron-electron collision frequency is given by [100]:

$$\nu(v) = 8\pi n_e \left(\frac{e^2}{4\pi\epsilon_0} \right)^2 \frac{ln\Lambda}{m_e^2 v^3} \tag{3.2}$$

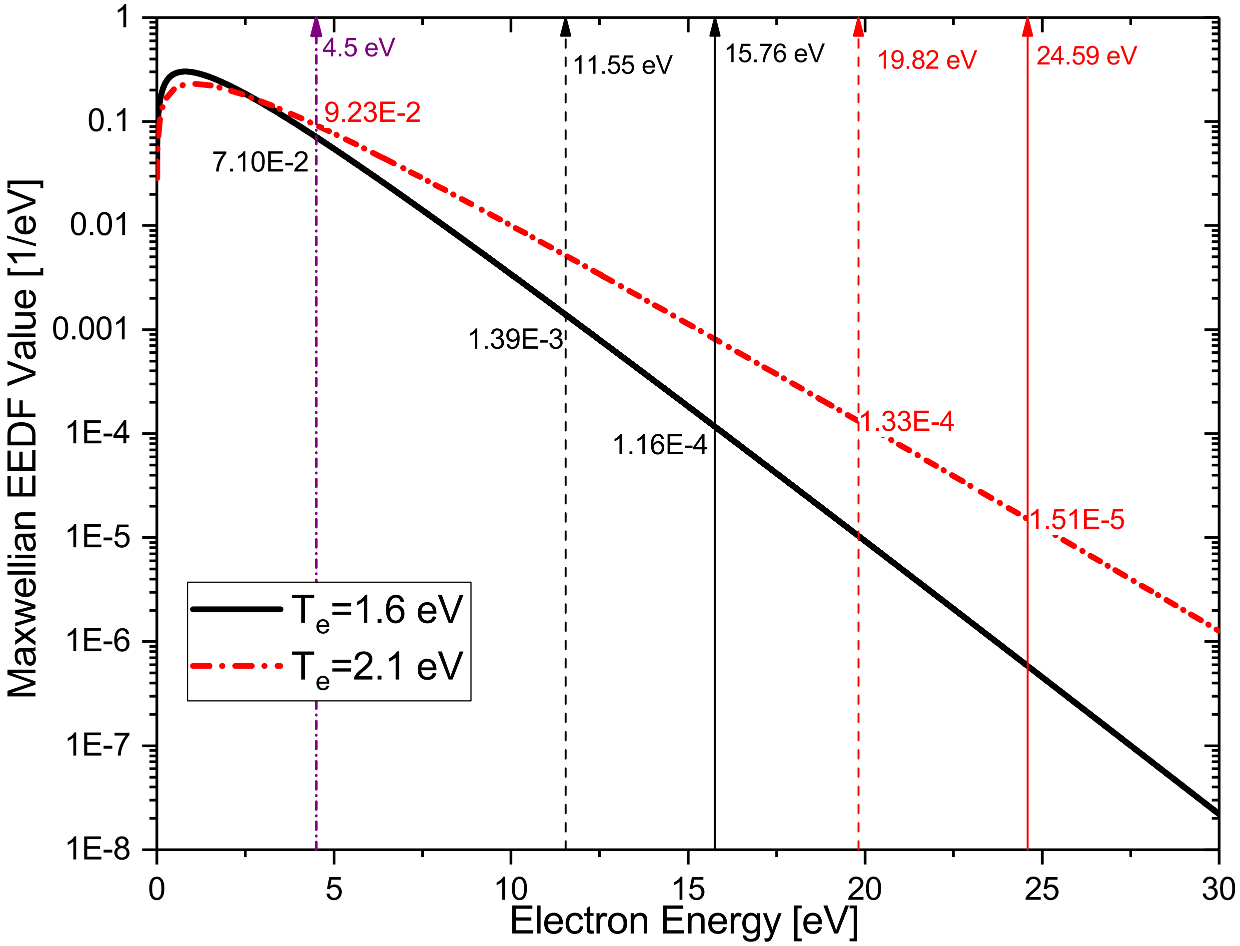

Figure 3.1: Maxwellian EEDFs for two electron temperatures, one typical of Ar PW discharges (black solid line) and one typical of He PW discharges (red dot-dashed line). For that element's corresponding line, drop lines are given for the lowest-lying excited state and ionization energies, as well as at 4.5 eV (close to the value for ionization from the lowest metastable level for both gases).

Averaged over a Maxwellian EEDF, the mean collision frequency is given by:

$$\nu_{ee} = \frac{n_e}{3\sqrt{2\pi}} \left(\frac{e^2}{4\pi\epsilon_0} \right)^2 \frac{4\pi}{\sqrt{m_e T_e^3}} \ln\Lambda \,. \tag{3.3}$$

In these, electron density, mass, velocity, and temperature are given by n_e, m_e, v, and T_e respectively, and $\ln\Lambda$ is the Coulomb logarithm, which is the logarithm of the maximum to minimum impact parameters for binary collisions of two charged particles. In a plasma, the Debye shielding provides the value of maximal impact parameter and the minimal impact parameter is the classical distance of closest approach [5]. This results in:

$$\langle \zeta \rangle = \frac{2(m_1 m_2)}{(m_1 + m_2)^2} \frac{\sigma_m}{\sigma_{sc}} \,. \tag{3.4}$$

In this, σ_m is the momentum-scattering cross section and σ_{sc} is the full scattering cross section. As a result, any such elastic collision between a heavy particle and an electron implies that there is very little energy exchange, whereas for electron-electron collisions, $\langle \zeta \rangle = 1/2$. This is the reason for the claim that electron-electron collisions are by far the most dominant mechanism in restoring the EEDF shape and thus the reason we focus on this rather than electron-heavy collisions as a means of Maxwellization [101]. Table 3.1 illustrates the relative frequencies of interactions discussed in the preceding paragraphs under conditions typical of the PW. In the first table, the identifiers OC1 and OC2 are shorthand for “operating conditions set 1” and “operating conditions set 2” and their corresponding GCS pressure and arc current values are indicated in the table. Note that all of these calculations are performed based on measurements obtained at P2/6 of a 6x6mm PW.

To examine the effect of the inelastic processes on the EEDF, we start by assuming that the initial EEDF is a Maxwellian shape, so that previously mentioned rate constant

Table 3.1: Plasma properties used to study Maxwellization of the EEDF.

Property [units]	Value for He OC1	” for He OC2	” for Ar OC1	” for Ar OC2
GCS Pressure [torr]	150	150	200	200
Arc Current [A]	105	150	60	180
Electron Density [cm^{-3}]	1.8×10^{15}	2.3×10^{15}	1.2×10^{16}	2.5×10^{16}
Electron Temperature [eV]	1.9	2.0	1.25	1.47
Neutral Density [cm^{-3}]	1.2×10^{17}	1.1×10^{17}	2.2×10^{17}	5.5×10^{16}
Electric Field [V/m]	1270	1300	820	1260
e-e energy transfer collision frequency [s^{-1}]	9.3×10^{9}	1.0×10^{10}	8.9×10^{10}	1.5×10^{11}

equations can be used, namely Eq. (2.21). Next, we use the measured electron density n_e for a given set of PW conditions to determine how many electrons (per unit volume) exist per energy, corresponding to this initially Maxwellian EEDF, so that for a bin at energy E and width ΔE:

$$n_{eb}(E) = n_e f(E) \Delta E \, . \tag{3.5}$$

The volumetric occurrence rate at which a given inelastic process results from collisions with electrons within this energy bin at energy E is given by:

$$R_u(E) = n_{eb}(E) n_{grd} \sqrt{\frac{2E}{m_e}} \sigma(E) \, . \tag{3.6}$$

The symbol R_u denotes that this is the upper bound of the rate because it assumes that the EEDF initially is a Maxwellian shape. The ground-state density n_{grd} as mentioned previously is approximately the neutral density n_n, $f(E)$ is the EEDF value, and $\sigma(E)$ is the cross section for the inelastic process. We assume that these energy bins are fine enough that the EEDF doesn't significantly change from one to an adjacent one, and they are indeed constructed that way for the analysis that follows. This we can compare with the volumetric

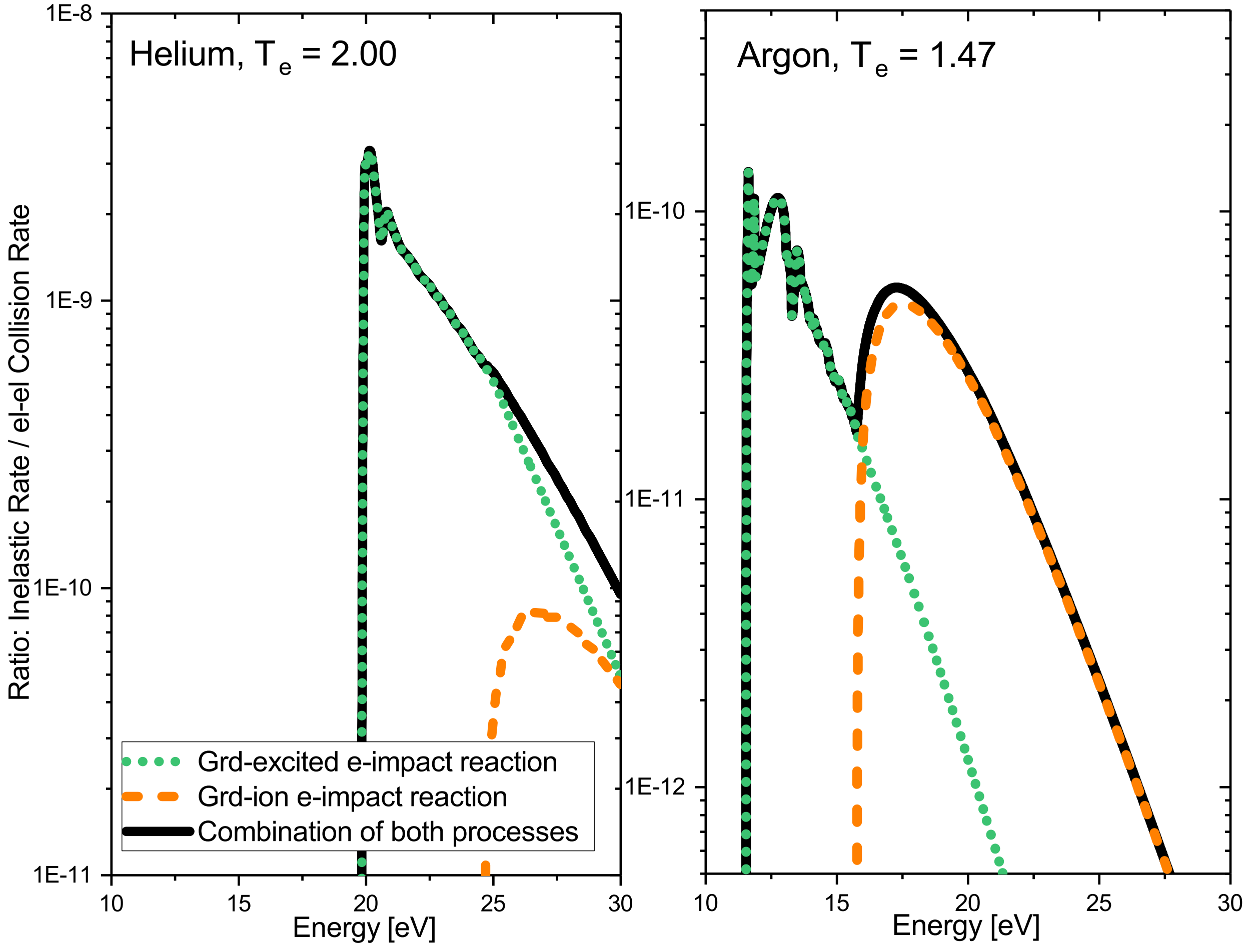

Figure 3.2: The ratio of inelastic process rates from ground state, to the electron-electron collision rate $n_e\nu_{ee}$. The inelastic process rate is determined as a function of energy, so that an occurrence is triggered only from electrons at energy E. On the other hand, the electron-electron collision rate is the rate over the entire EEDF.

(Maxwellian-averaged) electron-electron collision rate $n_e\nu_{ee}$ using Eq. (3.3), which is a mean value over the whole EEDF. It would be more proper to compare instead the rate of energy transfer via the inelastic process as well as electron-electron collisions which change the participating electrons' energies. This is necessary to consider because the high energy tail would actually be re-populated more slowly than the overall electron-electron collision rate would suggest because most collisions between a high energy electron and any other electron will result in the former losing energy rather than gaining. This method is incorporated in

Boltzmann solvers, as is mentioned below.

The ratio of these two volumetric process rates is shown in Fig. 3.2 for both a helium case and an argon case, corresponding to the set of operating conditions He OC2 and Ar OC2 identified in Tab. 3.1. From this it can be seen that within a unit volume the combined - considering excitation to the lowest-lying excited state as well as ionization, both from ground state - inelastic process rate is at least 8 orders of magnitude lower than the electron-electron collision rate taken over the entire EEDF in helium and at least 9 order of magnitude lower in argon, suggesting that we could expect only a minor deviation from Maxwellian shape.

Cross section data for the inelastic processes examined were obtained via Ref. [54] for helium and via Refs. [102, 103] for argon. The inelastic process rates are many orders of magnitude lower than the electron-electron collision rate, we expect that the plasma in the PW is well-described with a Maxwellian EEDF. It must be noted that the measured electron density and temperature which this Maxwellization test relies upon are likely the values close to the center of the plasma. Towards the edge, we expect a much reduced electron density, a somewhat reduced electron temperature and heavy temperature, and a therefore much increased ground state density [81]. However, since the central region is expected to be the region where emissions primarily originate from, potential departure from Maxwellian EEDF is less consequential in the outer edges of the arc.

Another point to note is that Boltzmann solver models such as BOLSIG+ can also be used to conduct in a more detailed fashion the type of analysis illustrated in this Section [104]. This model assumes a spatially uniform plasma (over the scale of the collisional mean free path) that is also steady-state. These assumptions should be adequate for studying the core of the PW arc. Using initialized cross sections for collisional processes of interest,the code

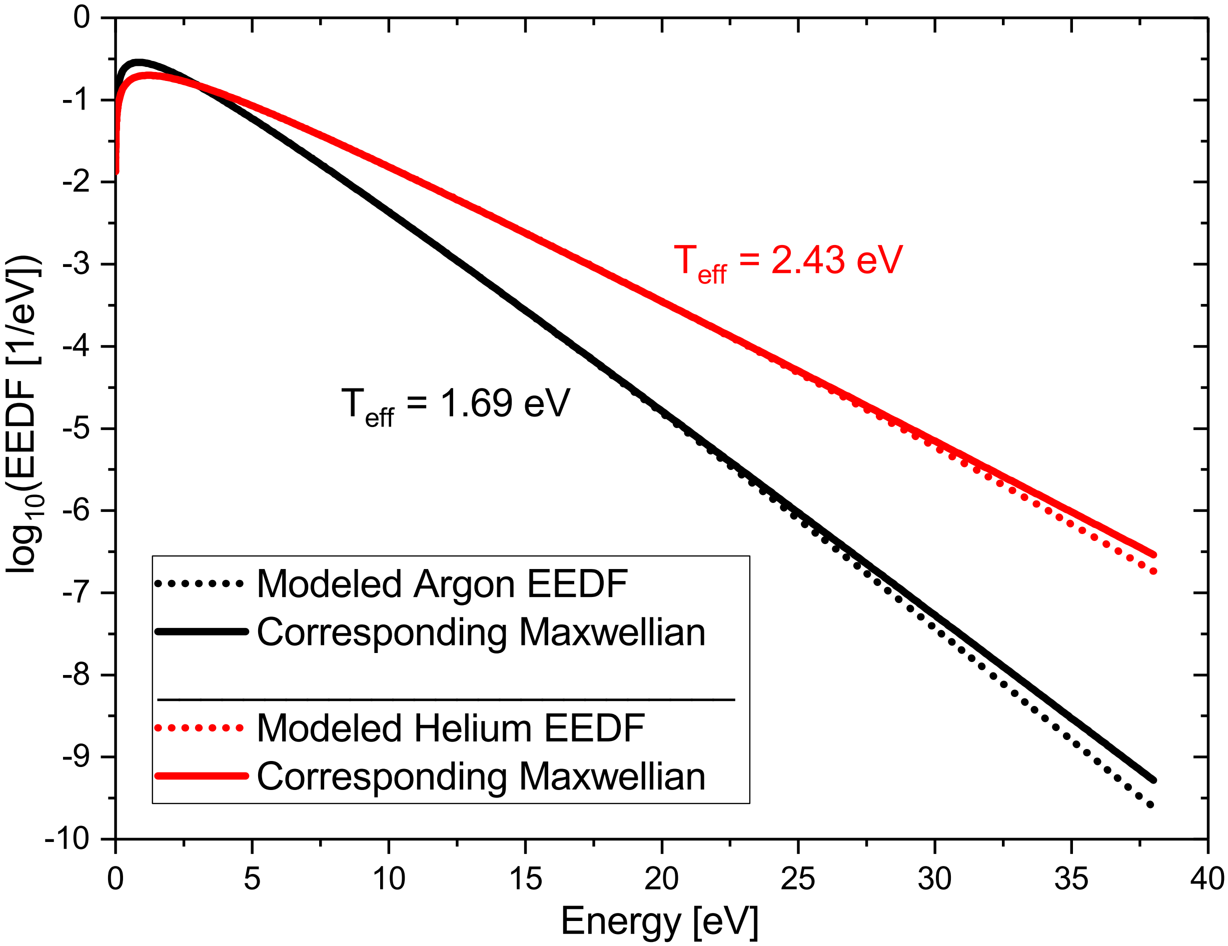

Figure 3.3: Results of BOLSIG+ calculations by applying the operating conditions for He OC2 and Ar OC2 in Tab. 3.1. Shown also are the effective electron temperatures. Dotted lines are the EEDFs solved for by BOLSIG+ and solid lines are the corresponding Maxwellian EEDFs whose electron temperature T_e matches the effective temperature T_{eff} of the dotted line EEDF.

solves the Boltzmann equation, given by:

$$\frac{\partial f}{\partial t} + \mathbf{v} \cdot \nabla f - \frac{e}{m_e}\mathbf{E} \cdot \nabla_{\mathrm{v}} f = C[f]\,, \tag{3.7}$$

in which f is the electron distribution in six-dimensional phase space, v the velocity coordinates, e and m_e are elementary charge and electron mass respectively, $\mathbf{E}$ is the electric field, ∇_{v} is the velocity-gradient operator, and finally $C[f]$ represents the rate of change in distribution f resulting from collisions (of all types) [104].

Applying the BOLSIG+ model to test cases for the PW, using the same parameters indicated in Tab. 3.1, we can examine the steady-state EEDF shape relative to a pure Maxwellian one. The results for the same operating conditions examined previously - He OC2 and Ar OC2 from Tab. 3.1 - are shown in Fig. 3.3. From this it is clear that there is some modest deviation from Maxwellian shape at the higher energy values. For the work in this thesis however, we shall proceed through analyses assuming that the EEDF is close enough that it may be considered Maxwellian.

3.2 Collisional-Radiative Model (HeCRM)

As mentioned in Section 2.2.3, electron temperature in the helium plasma window arc can not so easily be obtained via a Boltzmann plot as it can in the case of argon. A collisional-radiative model is necessary to compare modeled and measured relative emission intensities, to determine the electron temperature. This model involves calculating densities of the numerous excitation and ionization states found in the plasma [105].

The transient behavior of a given state's density n_k is given by:

$$\frac{dn_p}{dt} = \sum R_{pop} - \sum R_{depop}\,, \tag{3.8}$$

in which R_{pop} and R_{depop} broadly are the rates by which that state's population increase and decreases respectively. Including all possible population-changing mechanisms except spatial removal mechanisms (diffusion), this becomes:

$$\begin{aligned}\frac{dn_p}{dt} = -n(p)\left[\sum_{q<p} A(p,q) + n_e \sum_{q\neq p} C(p,q) + n_e S(p)\right] \\ + \left[\sum_{q>p} n(q)A(q,p) + \sum_{q\neq p} n(q)C(q,p) + \sum_{q<p} n(p)B'(q,p)\right] \\ + n_i n_e \left[n_e \alpha(p) + \beta(p) + \beta_d(p)\right]. \quad (3.9)\end{aligned}$$

With this notation, $q < p$ indicates level q is higher than p and (p, q) indicates the process goes from state p to state q. Changes in state can be from spontaneous photon emission with rate A, photon absorption with rate B', electron-impact excitation or de-excitation with rate C, ionization with rate S, three-body recombination with rate α, radiative recombination with rate β, and dielectronic recombination with rate β_d. This symbolism is taken from that of Refs. [14, 15], in which a CR model for singly-ionized helium plasma is applied. This is the same CR model which we will utilize here to analyze the helium plasma window. Only a limited description of this model will be given here and the reader is referred to the above referenced works and references therein for more extensive details of the inner workings of their CR model, called the HeCRM. In our application of this model, we will exclude the photon absorption terms whose rates are given by B', for reasons of dramatically simplifying the application of the model, since the radiation trapping effect is non-local and takes into account the spatial distribution of the states.

In what T. Fujimoto in Ref. [15] and M. Goto in Ref. [14] call Formulation II, all states are considered to be in a quasi-steady-state condition with the left-hand-side of Eq. (3.9) being 0, with the exception of the neutral ground state and ion state. In this formulation, after a great deal of algebraic manipulations, Eq. (3.9) for all of the excited states other than the neutral ground and ion states can be expressed as a sum of two terms, one proportional to the neutral ground state population and one proportional to the ion state population. Each state's population can then be given by:

$$n(p) = R_0(p) n_e n_i + R_1(p) n_e n_{grd} \,, \tag{3.10}$$

in which now all the state-coupling rates are now wrapped up into two reduced population coefficients $R_0(p)$ and $R_1(p)$. The term proportional to ion density n_i signifies transitions moving downwards in energy, and the term proportional to the ground state density n_{grd} signifies transitions moving upwards in energy [106]. To understand specifically how these population coefficients include all of the different rates presented in Eq. (3.9), the reader is again referred to Refs. [14, 15]. These population coefficients are functions of the state p as well as both electron density n_e and electron temperature T_e. Thus the system of equations for densities of every excited state can be obtained for a specified n_e and T_e and with this synthetic excited state population distribution also obtain a synthetic emission intensity spectrum. The relationship between the emitting state densities $n(p)$ and the corresponding emission intensities was given by Eq. (2.22). Dropping the geometric factor in that equation, the synthetic emission intensity for an emission from state p to state q is:

$$I_s(p, q) = n(p) A(p, q) \Delta E(p, q) \,, \tag{3.11}$$

where $\Delta E(p, q)$ is the energy of the photon emitted in the de-excitation process. Note that since this doesn't include any geometric factors, the intensity scale is arbitrary. In practice, what is done for the present work is to initialize the HeCRM with electron density n_e as measured via Stark broadening, and assume quasineutrality so $n_i = n_e$. Additionally, a value for the ground state density n_{grd} is required. It will be assumed at this point that the ground state constitutes the vast majority of the un-ionized species so that the ground state density is essentially the neutral density n_n which by using Dalton's law of partial pressures (which will be more thoroughly introduced in the next section) in Eq. (3.17), can be expressed as:

$$n_{grd} \approx n_n = \frac{1}{kT_h}\Big(P_p - n_e k T_e\Big) - n_e\,. \tag{3.12}$$

Since the heavy particle temperature T_h in Eq. (3.12) is not known via measurement, and is only calculated through the 1D analysis that will be described in Section 3.3, which itself depends on the electron temperature value T_e, we must rely on an alternative method to obtain n_{grd} for the HeCRM. This alternative method will be to use the PLASIMO arc modelling package that will be thoroughly described in Section 3.5 to determine the neutral density n_n and equate with n_{grd}.

Everything is now in place to initialize the HeCRM using modeled values of ground density n_{grd}, electron density n_e, and a set of test electron temperature values, which will be identified as T_t. So, for each T_t there will be a synthetic spectrum created to quantitatively compare with the measured one. To conduct such a comparison, the first step is to obtain (with a given T_t) for each emission the ratio of synthetic to measured intensity to obtain a set of ratios $\{R(T_t)\}$. For a synthetic spectrum that perfectly matched the measurement, each emission member of the $\{R(T_t)\}$ would be the same value, so we want to determine the degree of relative deviation from this ideal simulation case.

A straightforward technique to do so is by determining which test temperature T_t gives the minimum coefficient of variation (ratio of standard deviation to mean) for that temperature's

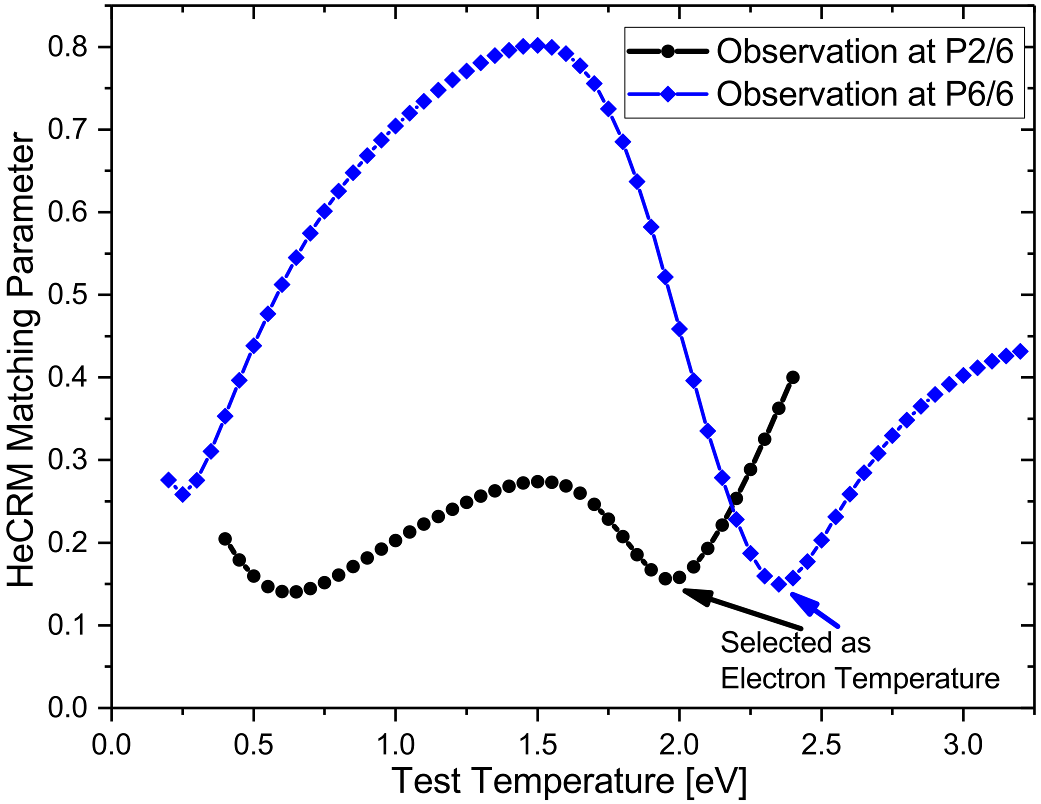

Figure 3.4: Matching Parameter for HeCRM synthetic spectra compared to measured spectra of a 200 torr GCS pressure, 120 A arc in 6x6mm PW geometry, at two measurement locations. The model was initialized for P2/6 with $n_e = 2.0 \times 10^{15}$ cm^{-3} and $n_g = 1.1 \times 10^{17}$ cm^{-3}, and for P6/6 with $n_e = 1.5 \times 10^{15}$cm^{-3} and $n_g = 6.6 \times 10^{17}$cm^{-3} (n_e from measurement and n_g from PLASIMO model).

corresponding set $\{R(T_t)\}$, which will be referred to from now on as the Matching Parameter (MP). This is the test electron temperature which generates a synthetic spectrum that best reflects the measured spectrum, and this temperature will be deemed the real electron temperature T_e. The HeCRM was used with a similar though slightly different analysis procedure in a test case discussed in Ref. [14], again to determine electron temperature (and density in that case) from a set of experimental emission intensities. A figure illustrating the process used in the present work is shown in Fig. 3.4. This result is for a He 6x6mm PW, with GCS pressure of 200 torr and arc current of 150 A, observed both at P2/6 and P6/6.

An interesting feature that results from this analysis technique is that there are in fact two local minima of MP values, and so two best-fitting T_t values, which we identify as T_{lo} and T_{hi}. The lower of these temperatures, like the measured excitation temperature T_{exc}, is seemingly too low to sufficiently result in ionization throughout the channel. A comparison of measured and synthesized emission intensities at both the T_{lo} and T_{hi} is given in Fig. 3.5. Therefore it is the higher matching temperature which is identified as the electron temperature in helium.

3.3 1D Model

The goal of this section is to assess what is most impactful in establishing the PW's mass flow and understanding the nature of its reduction from that of a corresponding non-arc gas flow. The procedure in analyzing the momentum-balance equation is similar to that used in Refs. [41, 107], although the various authors utilize the transport equations given in Section 1.2 by taking different transformations and assumptions, e.g. in Refs. [39, 108–110]. The

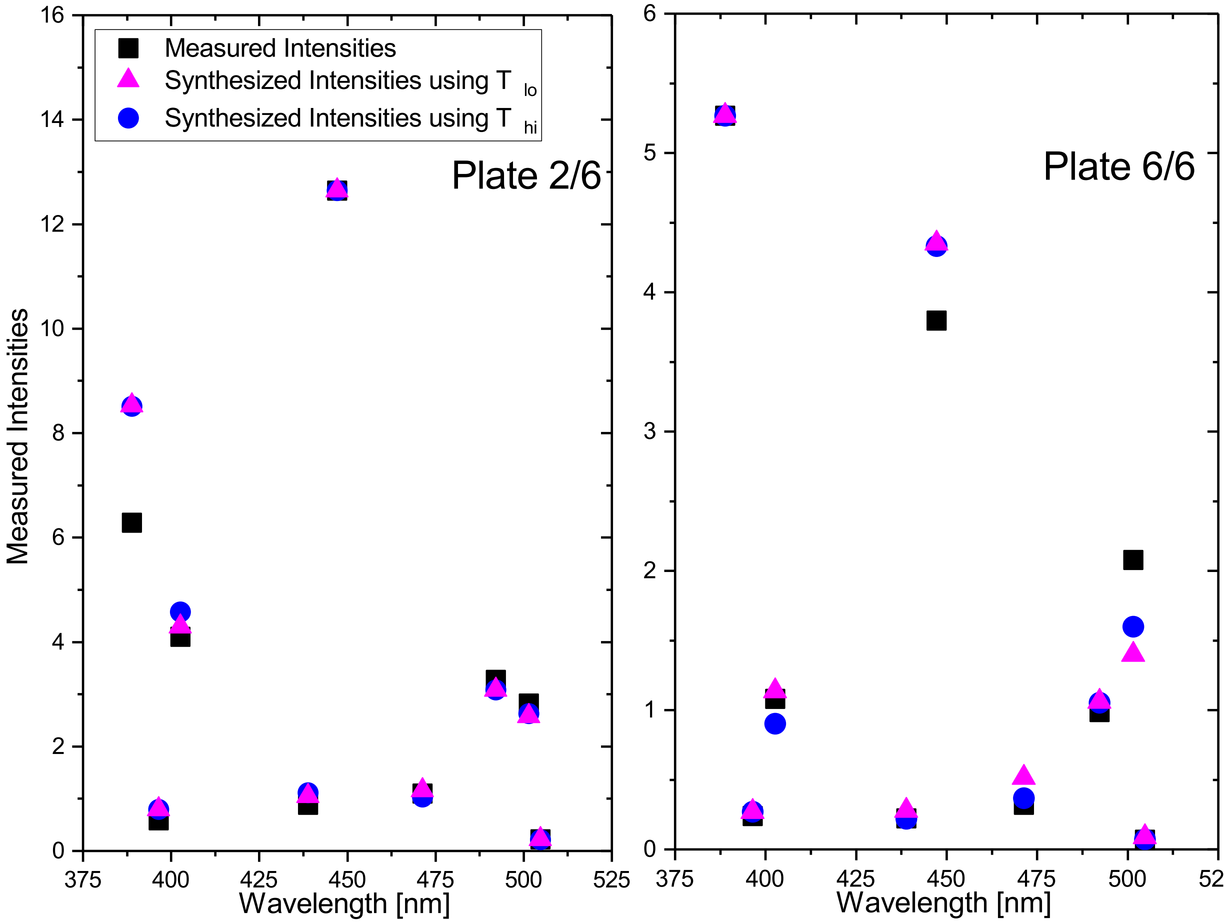

Figure 3.5: Measured and synthesized irradiances corresponding to the selected both the lower and upper matching temperature values in Fig. 3.4 (T_{lo} and T_{hi}). The temperature T_{hi} is selected as the electron temperature.

behavior of the mass flow $\dot{m}$ will be investigated using the momentum balance equation:

$$\frac{\partial}{\partial t}(mn_a\mathbf{u}_a) + n_a m(\mathbf{u}_a \cdot \nabla)\mathbf{u}_a + \nabla P_a + \nabla \cdot \overset{\leftrightarrow}{\pi} - qn_a(\mathbf{E} + (\mathbf{u}_a \times \mathbf{B})) = S_m \,. \tag{3.13}$$

3.3.1 Overall Momentum Balance

We will focus on the momentum balance equation which can be analyzed to obtain an expression for mass flow in terms of other properties. We will start by summing (3.13) over each species in the arc channel: neutrals, ions, and electrons. Due to their light mass, the electrons won't appreciably contribute to mass density or flow velocity due to their minute mass compared to the neutrals and ions. The result is:

$$mn(\mathbf{u} \cdot \nabla)\mathbf{u} + \nabla P_p + \nabla \cdot \overset{\leftrightarrow}{\pi} = 0 \,, \tag{3.14}$$

where the total plasma pressure is P_p, u is the hydrodynamic velocity, essentially the heavy particle flow velocity u_h given by:

$$\mathbf{u}_h = \frac{\dot{m}}{m_h A n_h}\hat{z} \,, \tag{3.15}$$

where n_h is heavy particle density, A is channel area, and m_h is heavy particle mass. There is no flow in the radial direction throughout the arc channel, so taking only the z-component of the flow velocity is justified, and this also means that plasma pressure P_p is constant with respect to radius at any axial position. It is furthermore assumed all the properties are axisymmetric, and no angular-dependence exists for any variables. A relation can be obtained between heavy particle density n_h and total plasma pressure P_p by invoking an equation of state as Dalton's law of partial pressures, which assumes each species of the plasma (electrons, ions, and neutrals) each obey an ideal gas law, such that:

$$P_p = \sum_a n_a k T_a \,, \tag{3.16}$$

As alluded to earlier in Section 1.2, it is assumed that both neutrals and ions possess approximately the same temperature, deemed simply as heavy particle temperature T_h. As it was mentioned in Section 1.2 and is conveyed in Ref. [41], this is a reasonable assumption because the energy-exchange in collisions of like-mass particles is much more efficient than collisions between a neutral or ion and an electron due to the mass disparity. In this case then, a quasineutral plasma with electrons, ions (charge state 1 only), and neutrals, Eq. (3.17) can be expressed as:

$$P_p = P_h + P_e = n_h k T_h + n_e k T_e = (n_n + n_e) k T_h + n_e k T_e \,. \tag{3.17}$$

From this, the heavy particle density n_h can be obtained as:

$$n_h = \frac{P_p - n_e k T_e}{k T_h} \,. \tag{3.18}$$

One can also obtain the ionization degree α, the ratio of ions to heavy particles (assuming, as always, quasineutrality so $n_i = n_e$) as:

$$\alpha = \frac{n_e k T_h}{P_p - n_e k T_e} \,. \tag{3.19}$$

The stress tensor $\overset{\leftrightarrow}{\pi}$ for the plasma has components given by:

$$\pi_{\alpha\beta} = -\eta\left(\frac{\partial u_\alpha}{\partial x_\beta} + \frac{\partial u_\beta}{\partial x_\alpha} - \frac{2}{3}\delta_{\alpha\beta}\nabla\cdot\mathbf{u}_h\right). \tag{3.20}$$

The last term of Eq. (3.14) is the viscous term and intrinsically relies on radial behaviors as well as axial, so to apply it in this 1D simplification, we will average its value over the channel radius. The components of the stress tensor $\overset{\leftrightarrow}{\pi}$ are given by Eq. (3.39), so the z-component of the tensor-divergence is:

$$\left(\nabla\cdot\overset{\leftrightarrow}{\pi}\right)_z = \frac{\partial\pi_{rz}}{\partial r} + \frac{1}{r}\frac{\partial\pi_{\phi z}}{\partial\phi} + \frac{\partial\pi_{zz}}{\partial z} + \frac{\pi_{rz}}{r}. \tag{3.21}$$

Ignoring the ϕ-dependent term, using the components of Eq. (3.39) in Eq. (3.21), the viscous term becomes:

$$\left(\nabla\cdot\overset{\leftrightarrow}{\pi}\right)_z = -\left[\frac{\partial\eta}{\partial r}\frac{\partial u_z}{\partial r} + \eta\frac{\partial^2 u_z}{\partial r^2}\right] - \frac{4}{3}\left[\frac{\partial\eta}{\partial z}\frac{\partial u_z}{\partial z} + \eta\frac{\partial^2 u_z}{\partial z^2}\right] - \left(\frac{\eta}{r}\frac{\partial u_z}{\partial r}\right). \tag{3.22}$$

Lastly, we will relabel the average of this viscous term for brevity, defining the term as G, where the angle brackets signify that it is an average over the channel radius:

$$G \equiv \langle\left(\nabla\cdot\overset{\leftrightarrow}{\pi}\right)_z\rangle. \tag{3.23}$$

The role of viscosity is different than that used in Refs. [41, 107], in which the viscosity term $\nabla\cdot\overset{\leftrightarrow}{\pi}$ is taken to be $\frac{1}{2}\rho u^2\frac{f}{D}$ where friction factor f represents friction with the wall and ρ is the plasma's mass density. This means that the only term retained from Eq (3.22) was the $\left(\frac{\eta}{r}\frac{\partial u_z}{\partial r}\right)$ term in their work. However, empirically it appears that for the plasma in the PW, each term within Eq (3.22) is significant relative to the others, so dropping any of them cannot be justified.

The aim now is to establish an expression for the mass flow in the plasma using these previous equations. After some algebra, Eq. (3.14) can be rearranged to give:

$$mnuu' + P_p' + G = 0\,. \tag{3.24}$$

From here, the next step is to re-express the velocity u_h and its derivative in terms of the mass flow. Here, primes represent axial derivatives, so in the z-direction. Using Eq. (3.15) and taking its axial derivative as:

$$u_h' = -\frac{\dot{m}}{m_h A}\frac{n_h'}{n_h^2}\,. \tag{3.25}$$

Now, plugging Eq. (3.15), (3.25), and (3.22) into Eq. (3.24), we end up with an equation for the mass flow $\dot{m}$:

$$\dot{m} = \sqrt{mA^2\left(\frac{n_h^2}{n_h'}\right)\left(P_p' + G\right)}\,. \tag{3.26}$$

It is worth pointing out that both n_h' and P_p' will be negative in sign. The latter is obvious; the pressure must decrease along the direction of flow because this pressure change is what establishes the flow in the first place. The former is not as immediately obvious, so to elucidate we differentiate n_h in Eq (3.18) to give:

$$n_h' = \frac{-T_h'}{kT_h^2}\left(P_p - n_e kT_e\right) + \frac{1}{kT_h}\left(P_p' - (n_e kT_e)'\right). \tag{3.27}$$

Here, we note that since we expect T_h to generally rise as the gas moves down the channel,

T_h' will be positive and since we mentioned above P_p' is negative in sign, the only term in Eq. (3.27) which can be positive is the $-(n_e k T_e)' \equiv P_e'$, where we note that by Dalton's law of partial pressures we can just define this electron pressure axial derivative. Empirically, it seems that this the electron pressure doesn't change substantially because while T_e generally increases as we move down the channel's length, n_e generally decreases.

We can now more clearly understand what is contributing to reduced mass flows observed in the PW. We see that the heavy density and its axial derivative, n_h and n_h', play a large role. The rate of pressure drop P_p' and the viscous term G also play a part, but we see that it's possible only one really contributes if the other is small relative to it. We therefore will seek to compare the values of these terms, with results presented in Section 4.2.6.

There is one more consideration regarding the effect of viscosity on the flow, which is the contribution of viscous heating of the heavy particles, compared to other heating mechanisms. This is necessary to understand because the heating influences the behavior of the heavy particle density n_h and its derivative which are factors in Eq. (3.26). These factors appear in energy balance equation first mentioned in Section 1.2, and restated here as:

$$\frac{\partial}{\partial t}\left(\frac{3}{2} n_a k T_a\right) + \nabla \cdot \left(\frac{3}{2} n_a k T_a \mathbf{u}_a\right) + n_a k T_a \nabla \cdot \mathbf{u}_a + \left(\overset{\leftrightarrow}{\pi} \cdot \nabla\right)\mathbf{u} + \nabla \cdot \mathbf{Q} = S_E \,. \tag{3.28}$$

From this, an expression for the energy balance of heavy particles in particular is given as:

$$\nabla \cdot \left(\frac{3}{2} n_h k T_h \mathbf{u}_h\right) + n_h k T_h \nabla \cdot \mathbf{u}_h = S_e + Q_v - \nabla \cdot \mathbf{q}_h - Q_{rad} \,. \tag{3.29}$$

Terms on the left side of this equation represent the kinetic energy terms (thermal and flow) of the flowing plasma, and the terms on the right side represent the source terms. Of these, S_e is the external energy source term which here is the energy obtained through collisions with more energetic electrons, Q_v is the energy generated from viscous dissipative heating, $\nabla \cdot \mathbf{q}_h$ is the heat flux term through conduction, and Q_{rad} is the term for energy lost due to radiation. In this work, only this last term will be assumed insignificant compared to the others and dropped. An additional note that will not be considered here is mentioned in Ref. [111] is that an additional energy source term could be added related to the energy of chemical reactions or inelastic collisions between the heavy particles. In this thesis, the primary reason for bringing up Eq. (3.29) and its terms is to provide context for the viscous heating term Q_v and the term to which it will be directly compared, the electron heating term S_e.

For the source term S_e, also referred to as the energy exchange term since it is the electron-to-heavy energy exchange rate per unit volume, we must note that the energy exchange is essentially uni-directional, causing the heavy particle temperature T_h to ever approach the electron temperature T_e [28]. This term is given by:

$$S_e = \frac{3}{2}\frac{2m_e}{m_h} n_e \nu_{eh} k (T_e - T_h)\,, \tag{3.30}$$

where m_e and m_h are the electron and heavy particle mass respectively, n_e is the electron density, T_e and T_h are the electron and heavy particle temperatures, and ν_{eh} is the momentum-transfer collision frequency between electrons and heavy particles, which is the sum of electron-neutral and electron-ion momentum-transfer collision frequencies:

$$\nu_{eh} = \nu_{en} + \nu_{ei}\,. \tag{3.31}$$

The collision frequency between a projectile species and a target species n_{tar} particles is defined as:

$$\nu = n_{tar} \langle v_r \sigma_{cs} \rangle \, , \tag{3.32}$$

where σ_{cs} is the interaction cross section between pair of particles under consideration and v_r is the relative velocity of the two particles, and the angular brackets denote that this is taken as an average over collision speeds. Momentum transfer collision frequency is defined as the frequency with which a given species has its momentum deflected by 90 degrees, either via a single collision or by successive smaller-angle collisions. Energy exchange between electrons and heavy particles slower by a factor of $\frac{2m_e}{m_h}$. This is why a disparity between electron and heavy temperature often exists [28, 29].

To make use of Eq. (3.30) for this calculation requires a connection between the electron-heavy elastic collision frequency ν_{eh} and measured quantities. This connection can be established through the plasma's electrical conductivity σ, a property which can be ascertained via measurement of the cascaded plate floating voltages of the plasma's enclosure as described in Section 2.1. To do so, take the electrical conductivity to be defined based on:

$$\mathbf{j} = \sigma \mathbf{E} \, , \tag{3.33}$$

where $\mathbf{j}$ is the current density and $\mathbf{E}$ is the electric field. We then can equate Eq. (3.33) with an alternative expression for the current density being related to electron drift velocity $v_{d,e}$ and electron density n_e, namely:

$$j = v_{d,e} e n_e \, . \tag{3.34}$$

Next we need to express the electron drift velocity $v_{d,e}$ in terms of the collision frequency ν_{eh}. This drift velocity is obtained by integrating the force on the electron in the field **E** over a time equal to the inverse of the collision frequency. In the axial direction, this axial velocity is then given by [28]:

$$v_{d,e} = \frac{eE_z}{\nu_{eh} m_e} \,. \tag{3.35}$$

Inserting Eq. (3.35) into Eq. (3.34) and equating with Eq. (3.33), we obtain:

$$\nu_{eh} = \frac{e^2 n_e}{\sigma m_e} \,. \tag{3.36}$$

Finally then, we obtain a useful expression for the electron heating term:

$$S_e = \frac{3m_e}{m_h} n_e k \Big(T_e - T_h \Big) \frac{e^2 n_e}{\sigma \, m_e} \,. \tag{3.37}$$

For the next term in to work out in Eq. (3.29), the viscous heating term Q_v, recall the expression from the full 3D energy balance equation Eq. (1.8), in which the viscous heating term Q_v is the part of the equation given by:

$$Q_v = \Big(\overset{\leftrightarrow}{\pi} \cdot \nabla \Big) u_h = \sum_\beta \pi_{z\beta} \frac{\partial u_z}{\partial \beta} \,, \tag{3.38}$$

where $\overset{\leftrightarrow}{\pi}$ is the stress tensor, whose components are given by:

$$\pi_{\alpha\beta} = -\eta \left(\frac{\partial u_\alpha}{\partial x_\beta} + \frac{\partial u_\beta}{\partial x_\alpha} - \frac{2}{3} \delta_{\alpha\beta} \nabla \cdot \mathbf{u}_h \right) \,, \tag{3.39}$$

in which η is the viscosity, and x is just a spatial coordinate. The procedure used to determine the value of the viscosity η itself will be outlined in Section 3.4, but it's sufficient here to say that it is a function of both heavy temperature T_h and ionization degree α. Applying this to Eq. (3.38) gives the form of the viscous heating term which can be inserted into Eq. (3.29):

$$Q_v = \left(\overset{\leftrightarrow}{\pi} \cdot \nabla\right) u_h = \eta \left[\frac{1}{2} \left(\frac{\partial u_z}{\partial r} \right)^2 + \frac{4}{3} \left(\frac{\partial u_z}{\partial z} \right)^2 \right]. \tag{3.40}$$

Now, expressions for both the electron heating term S_e and the viscous heating term Q_v have been obtained. As with the relative terms in the mass flow equation Eq. (3.26), these two heating contributions will be compared in Section 4.2.6, with the viscous heating term taken as an average over the channel radius as it was for the mass flow equation.

3.4 Viscosity

In the previous sections, the viscosity played an important role in the evolution of the heavy particle temperature T_h, and by extension the heavy particle density n_h, ionization degree α, and mass flow $\dot{m}$. Viscosity is a fluid friction property that effects the rate of flow through a channel, with greater viscosity results in a lower mean flow velocity. Hirschfelder, Curtiss, and Bird developed the kinetic theory by which the transport coefficients - viscosity, diffusion, and conductivity - can be determined in any pure gas or multi-component mixture, including those with charged particles interacting under Coulomb potentials [112]. As a result, this kinetic theory will be used to calculate viscosity in the plasma window as a function of calculated values. Particularly, the heavy particle temperature T_h and ionization degree α are critical values that impact the viscosity; greater temperature increases viscosity, while greater ionization degree decreases it. We will need the previously obtained a useful form of the ionization degree α:

$$\alpha = \frac{n_e k T_h}{P_p - n_e k T_e}\,, \tag{3.41}$$

where n_e is the electron density, k the Boltzmann constant, T_h the heavy particle temperature, T_e the electron temperature, and P_p the total plasma pressure.

It is through collision integrals that the dynamics of collisions enter into the determination of these transport coefficients [112]. These collision integrals, whose type is identified by l and s, are defined as:

$$\Omega_{ij}^{(l,s)} = \sqrt{\frac{kT}{2\pi\mu_{ij}}}\int_0^\infty e^{-\gamma^2}\gamma^{2s+3}Q^{(l)}(g)d\gamma\,, \tag{3.42}$$

with the cross section for a collision of type l given by:

$$Q^{(l)}(g) = 2\pi\int_0^\infty (1 - cos^l(\chi) b db\,, \tag{3.43}$$

and

$$\chi(g,b) = \pi - 2b\int_{r_{min}}^\infty \frac{dr/r^2}{\sqrt{1 - \frac{b^2}{r^2} - \frac{\phi(r)}{\frac{1}{2}\mu_{ij}g^2}}}\,. \tag{3.44}$$

Eq. (3.44) is the angle of deflection in a collision governed by potential $\phi(r)$ and impact parameter b. The unitless parameter γ is defined as:

$$\gamma^2 \equiv \frac{\mu_{ij}g^2}{2kT} = \frac{E}{kT}\,, \tag{3.45}$$

in which μ_{ij} is the reduced mass of species i and j, g the relative velocity between them, and so E is just their kinetic energy.

In this work, relevant cross sections ($Q^{(l)}$) have been obtained from the literature, as a function of collision energy. For argon, cross section information was obtained from Ref. [113] and for helium it was obtained from Ref. [114]. As a result of these being in terms of collision energy, it is desirable to re-express (3.42) as a function of energy E instead of γ. Doing so yields:

$$\Omega_{ij}^{(l,s)} = \sqrt{\frac{1}{8\pi\mu_{ij}kT}} \int_0^\infty e^{-E/kT} \left(\frac{E}{kT}\right)^{s+1} Q^{(l)}(E)dE\,. \tag{3.46}$$

With the framework of the collision integrals established, they can now be put to use in determining viscosity. The first step to doing that is to calculate the viscosity corresponding to a pure substance, considering each member of the mixture in isolation. The first approximation to the viscosity for a pure substance, is [112]:

$$[\eta_{ii}]_1 = \frac{5}{8}\frac{kT}{\Omega_{ii}^{(2,2)}}\,. \tag{3.47}$$

Now, beginning with ions and applying the above set of equations to particles interacting under a Coulomb potential, we obtain:

$$Q_C^{(2)}(E) = 4\pi b_0^2 \left[\ln\left(1 + \left(\frac{\lambda_D}{b_0}\right)^2\right) - \frac{(\lambda_D/b_0)^2}{1+(\lambda_D/b_0)^2}\right], \tag{3.48}$$

in which, for nonisothermal and quasineutral plasma with only singly ionized particles present, the Debye length from Section 1.2 is:

$$\lambda_D = \sqrt{\frac{\epsilon_0 kT_e}{e^2 n_e}}\,, \tag{3.49}$$

and the parameter b_0 is known as the classical distance of closest approach, given by [5]:

$$b_0 = \frac{e^2}{4\pi\epsilon_0 \mu g^2} = \frac{e^2}{8\pi\epsilon_0 E}\,. \tag{3.50}$$

This expression for the cross section is then substituted into Eq. (3.47) to obtain the viscosity associated with the particles interacting via the Coulomb potential. Note that in Eq. (3.46), the presence of $\sqrt{\mu_{ij}}$ in the denominator implies that collisions between electrons will contribute much less to the viscosity than will collisions between ions. As a result, in this work, electron contributions to viscosity will be neglected, and calculations for the overall viscosity of the plasma fluid will be obtained by considering it as a mixture of neutrals and ions.

The next piece necessary is a quantity denoted by $[\eta_{12}]_1$. The 1 outside the brackets identifies that this is for the first approximation (higher order approximations are not employed in the present work), and as per the description in Ref. [112], this quantity can be regarded as the coefficient of a hypothetical pure substance that interacts in the manner species 1 and 2 do. For simplicity, it is assumed that the neutral-ion collisions also interact with the neutral-neutral collision cross section, which as mentioned previously are obtained from Refs. [113] and [114] for argon and helium respectively. As a result of the above assumption that the neutral-ion collisions are essentially the same as the neutral-neutral ones, we will treat $[\eta_{12}]_1 \approx [\eta_{11}]_1$ in this work.

For a binary mixture, the overall fluid viscosity depends upon the relative molar fractions and molecular weights of the two species as well as the viscosities of the corresponding pure substances. Adopting the notation used by the authors, species 1 denotes neutral, and species 2 denotes ion. The 1 outside of the brackets denotes the first approximation [112].

Thus:

$$[\eta_{mix}]_1 = \frac{1 + Z_\eta}{X_\eta + Y_\eta} \tag{3.51}$$

,

$$X_\eta = \frac{x_1^2}{[\eta_{11}]_1} + \frac{2x_1x_2}{[\eta_{12}]_1} + \frac{x_2^2}{[\eta_{22}]_1}\,, \tag{3.52}$$

$$Y_\eta = \frac{3}{5}A^*_{12}\left\{\frac{x_1^2}{[\eta_{11}]_1}\left(\frac{M_1}{M_2}\right) + \frac{2x_1x_2}{[\eta_{12}]_1}\left(\frac{(M_1+M_2)^2}{4M_1M_2}\right)\left(\frac{[\eta_{12}]_1^2}{[\eta_{11}]_1[\eta_{22}]_1}\right) + \frac{x_2^2}{[\eta_{22}]_1}\left(\frac{M_2}{M_1}\right)\right\}, \tag{3.53}$$

$$Z_\eta = \frac{3}{5}A^*_{12}\left\{x_1^2\left(\frac{M_1}{M_2}\right) + 2x_1x_2\left[\left(\frac{(M_1+M_2)^2}{4M_1M_2}\right)\left(\frac{[\eta_{12}]_1}{[\eta_{11}]_1} + \frac{[\eta_{12}]_1}{[\eta_{22}]_1}\right) - 1\right] + \left(x_2^2\frac{M_2}{M_1}\right)\right\}, \tag{3.54}$$

$$A^*_{12} = \frac{2}{3}\frac{\Omega^{(2,2)}}{\Omega^{(1,1)}}\,. \tag{3.55}$$

As mentioned at the beginning in this section, the viscosity depends primarily on heavy particle temperature T_h and ionization degree α. The relationship with the heavy particle temperature is a result of transmitting momentum of the flow towards the walls of the channel, and the relationship with the ionization degree is a result of the molar fraction of the mixture constituents in Eq. (3.51) and the fact that the pure-substance-viscosity terms are governed by different potentials depending on if they're neutrals or ions. Electrons contribute relatively little to viscosity due to their low mass and relative inability to affect the momentum of the heavy particles which transmit almost the entirety of the mass flow. This, again,

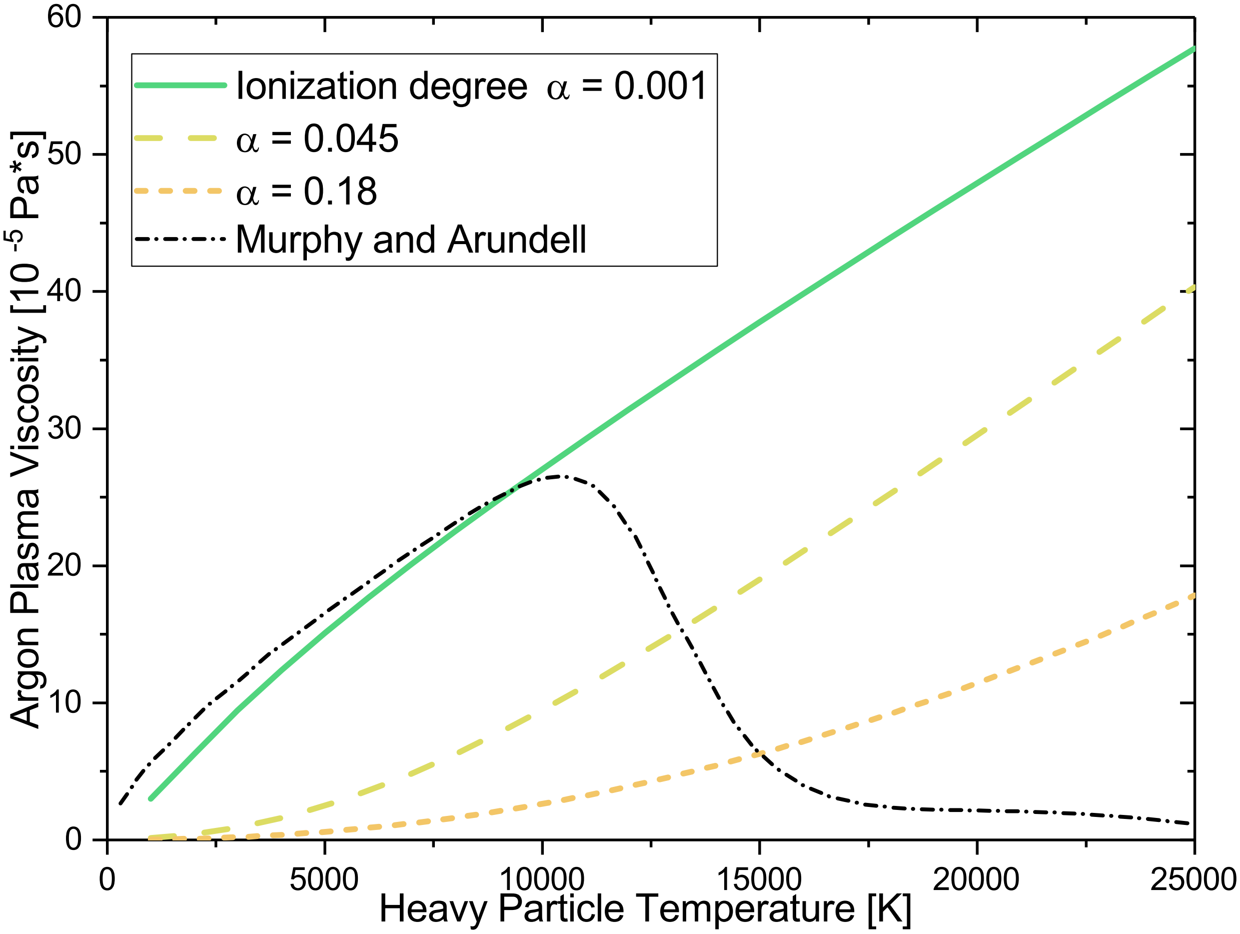

Figure 3.6: Argon plasma viscosity calculated using Chapman-Enskog kinetic theory described above. Viscosity values are calculated at three different ionization degrees to illustrate their impact. The black curve is that obtained by Murphy and Arundell [13] in which the assumption of Saha ionization equilibrium is taken.

is the reason electron effects are neglected in determining viscosity in the present work. Often when plasma viscosity is reported, it is under the assumption of Saha ionization equilibrium and $T_e = T_h$, so that ionization degree α and T_h are both functions of electron temperature T_e,to establish a convenient relationship between the temperature and the electron density (and ion density, following assumption of quasineutrality) [13, 115]. Saha excitation equilibrium was discussed briefly in Section 2.2.3.1, and Saha ionization equilibrium is similar except rather than applying to excited levels, it applies to two adjacent ionization stages.

However, Saha ionization equilibrium generally requires much higher electron densities than those attained in the PW, and is not a justifiable assumption to make in this case. Figure 3.6 illustrates viscosity in argon as a function of heavy particle temperature T_h at several ionization degrees α. Also in this figure is a previously reported calculation of argon plasma viscosity calculated by Murphy and Arundell [13], in which Saha ionization equilibrium is implicit. As a result, their calculation is a function only of temperature.

3.5 Plasma Simulation Model - PLASIMO

PLASIMO (plasma simulation model) is a plasma modeling package developed by the group for Equilibrium and Transport in Plasmas at Eindhoven University of Technology [111,116]. There are many different model packages that PLASIMO supports depending upon the type of plasma under consideration [116,117], but the package under consideration in the present work is designed for axisymmetric arc plasmas [111]. It is used to compare modeled properties with corresponding measured ones, and is investigated as a possible tool to assess plasma window arrangements and conditions otherwise not investigated or accessible through the course of this thesis work.

To gauge the reliability of this model in approximating the plasma window under specified operating conditions, several modeled plasma and flow properties can be compared to their measured counterparts determined experimentally on the NSCL plasma window test stand. These include gas pressure, electric field, electron temperature, electron density, and wall heating, results of all of which are presented and discussed in 4.2. If all relevant physics has been included in the model, the boundary conditions selected appropriately, and the properties mentioned above are relatively comparable to the experimental values, it is conjectured that the other properties such as viscosity η and heavy particle temperature T_h which are not easily determined experimentally can be estimated using the model's values. This then could be used in determining importance of these properties in limiting the gas flow, following the framework for obtaining an expression for mass flow $\dot{m}$ in Section 3.3.

Because the plasma window study is focused on a cascaded arc arrangement, PLASIMO's arc package is the one that will be discussed from this point forward. This foundation of this model relies upon the distinction between fast and slow plasma interactions. Fast interactions (order of 10^{-8} s) are kinematic (collisional) and radiative processes, and the slower ones (order of 10^{-3} s) are fluid interactions, such as convection, conduction, and diffusion. As a result, plasma is considered a fluid, within which at every location plasma parameters can be defined. In addition to this, the model makes several assumptions about the plasma flow [111]:

1. the flow is considered laminar
2. the flow is stationary (no time variation)
3. the plasma is axisymmetric
4. the principle of quasineutrality is upheld
5. there are two temperatures - T_e characterizing electrons and T_h characterizing the heavy particles, and these two temperatures need note be equal
6. kinetic energy distributions are all considered to be Maxwellian
7. sheath-associated mechanisms are disregarded

Radiative energy transport via absorption and re-emission is not considered, nor are the occupations of the excited states of neutrals or ions. The plasma is considered to consist of just ground state neutrals, ground state ions, and electrons. However, the excited neutral states are accounted for in an indirect manner by inclusion of step-wise ionization rates, in the form:

$$e + A \longleftrightarrow e + A^{*}\,, \tag{3.56}$$

$$e + A^{*} \longleftrightarrow 2e + A^{+}\,. \tag{3.57}$$

This step-wise ionization process would occur in addition to direct ionization of the unexcited neutrals to the ionized state (only the first ionization stage is considered in the PLASIMO models of both argon and helium). In these reactions, A^{*} is an effective excited species. A collisional-radiative model must be utilized to determine what the effective ionization rate from the collection of real excited states as a function of temperature. The argon PLASIMO model employs a step-wise ionization rate using results of Ref. [118], namely:

$$K_{si} = (7.314 \times 10^{-15})\sqrt{T_e}\exp(-12.06/T_e)\ [m^3/s]\,, \tag{3.58}$$

where T_e is given in eV.

The step-wise ionization process in helium was determined using a combination of HeCRM (described in Section 3.2) and ionization rates from metastable excited helium states, obtained in Ref. [119]. Since the PLASIMO model was not set up with explicit excited species present, it was necessary to use the HeCRM to ascertain the expected behavior of the metastable density as a function of electron temperature T_e. As a result, two step-wise ionization channels were included for the helium PLASIMO model, through the metastable states $1s2^3S$ and $1s2^1S$. These are given in Eqs. (3.59) and (3.60) as:

$$K_{si,1} = (1.21 \times 10^{-20}) T_e^{5.66} \mathrm{exp}(0.273/T_e)\ [m^3/s]\,, \tag{3.59}$$

$$K_{si,2} = (9.18 \times 10^{-22}) T_e^{5.99} \mathrm{exp}(-1.132/T_e)\ [m^3/s]\,. \tag{3.60}$$

In these two equations, T_e is in units of eV. These rates should only be applied for electron temperatures T_e close to the values under investigation here for the PW, around 2-3 eV.

Maxwellian velocity distributions are assumed for each particle species, and PLASIMO employs the continuity equations from velocity moments of the Boltzmann equation, as described in Section 1.2, with Eq. (1.6), (1.7), and (1.8). As described in Ref. [111], in PLASIMO's arc model the characteristic temperatures are allowed to differ between heavies (ions and neutral particles) and electrons, so $T_h \neq T_e$. As a result, energy balance of the plasma exists in two equations, one for electrons and one for heavies. These are, respectively:

$$\nabla \cdot (\rho_e \epsilon_e \mathbf{u}) + P_e \nabla \cdot \mathbf{u} + \nabla \cdot \mathbf{q_e} = Q_{Ohm} + Q_e \tag{3.61}$$

,

and

$$\nabla \cdot (\rho_h \epsilon_h \mathbf{u}) + P_h \nabla \cdot \mathbf{u} + \nabla \cdot \mathbf{q_h} = \overset{\leftrightarrow}{\pi} : \nabla \mathbf{u} + Q_h\,. \tag{3.62}$$

In these equations, u is the plasma bulk velocity:

$$u = \sum_\alpha (n_\alpha m_\alpha u_\alpha) / \sum_\alpha (n_\alpha m_\alpha)\,. \tag{3.63}$$

Due to their much smaller mass, electrons do not appreciably contribute to this velocity. Also in these equations, ρ is mass density, ϵ is the thermal energy per unit mass, P is the species pressure, $\overset{\leftrightarrow}{\pi}$ is the viscous stress tensor, Q_e and Q_h denote energy gain or loss for electrons or heavies respectively due to inelastic collisions or chemical processes, and Q_{Ohm} is the Ohmic heating term. For mass continuity and momentum balance, the equations are summed over all particles, resulting in whole-plasma forms given by, respectively:

$$\nabla \cdot (\rho \mathbf{u}) = 0\,, \tag{3.64}$$

and

$$(\nabla \cdot (\rho \mathbf{u}\mathbf{u}))_i = -(\nabla P)_i + (\nabla \cdot \overset{\leftrightarrow}{\pi})_i + (\mathbf{j} \times \mathbf{B})_i\,. \tag{3.65}$$

Additionally, the plasma equation of state is specified using Dalton's law of partial pressures in Eq. (3.17), with each species (electrons and heavies) obeying an ideal gas law in the form $P = nkT$.

PLASIMO's arc model will be generated in an axisymmetric configuration, so will be 2D, and excludes any rotational effects. A number of boundary conditions pertaining to plasma properties will need specification. The general setup of these that will be applied to the PLASIMO model of the plasma window are described in Table 3.5. These are specified according to cardinal directions, and the corresponding real boundary of each direction is given in 3.5, along with some other abbreviations relevant to the boundary conditions. These boundary conditions apply to the PLASIMO model used for a single-radius PW, e.g. 6x6m. Other model geometries consisting of two-radii PW configurations such as 1x6mm_7x10mm have also been explored though require additional boundary conditions, and tend to have more difficulty in achieving a converged solution, so the majority of the results from PLASIMO will be focused on this basic single-radius system. In these, the model simplifies the geometry of the plasma window, and is a simple cylinder rather than the ribbed structure of the true plasma window (since the metal plates and the insulators between have different inner radii), and it lacks the discrete wall/insulator components, with the model calculated voltage being a continuous drop from cathode to anode. So it could be thought of as analogous to a plasma window comprised of infinitely many and thin metal plates and insulators. Additionally, PLASIMO can not reliably model the unique plasma characteristics of the cathode and anode fall regions [116, 120] (more information on these regions can be found in e.g. Ref. [28]). The modeled region will be just the cascaded arc region, from about the location of upstream edge of the first PW plate down to the upstream edge of the anode, similar to the example studied in Ref. [111]. It was mentioned in Section 2.1 that metal plates are 7 mm thick and insulating pieces between are 2 mm thick. So the modeled region for a PW consisting of 6, 8, or 10 plates will be 54 mm, 72 mm, and 90 mm respectively. The meshing for the simple cylindrical PLASIMO model of a 6x6mm PW is shown in Fig. 3.7. Any given model is run until an overall convergence of greater than 10^{-8} is achieved.

One thing to note is that since this modeled region is from the upstream edge of PW plate 1 to the upstream edge of the anode plate, the modeled region inlet and outlet pressures will be obtained by extrapolating a linear pressure drop from two measured locations. The two measurement locations for the 6x6mm PW configuration are plates 2 and 6, and for the 8x6mm PW configuration is plates 2 and 8. The model's exit pressure BC is a constant Neumann value equal to the measured linear drop rate from the aforementioned two measured locations. Some plate pressures for a 6x6mm PW are shown in Fig. 3.8 for both helium

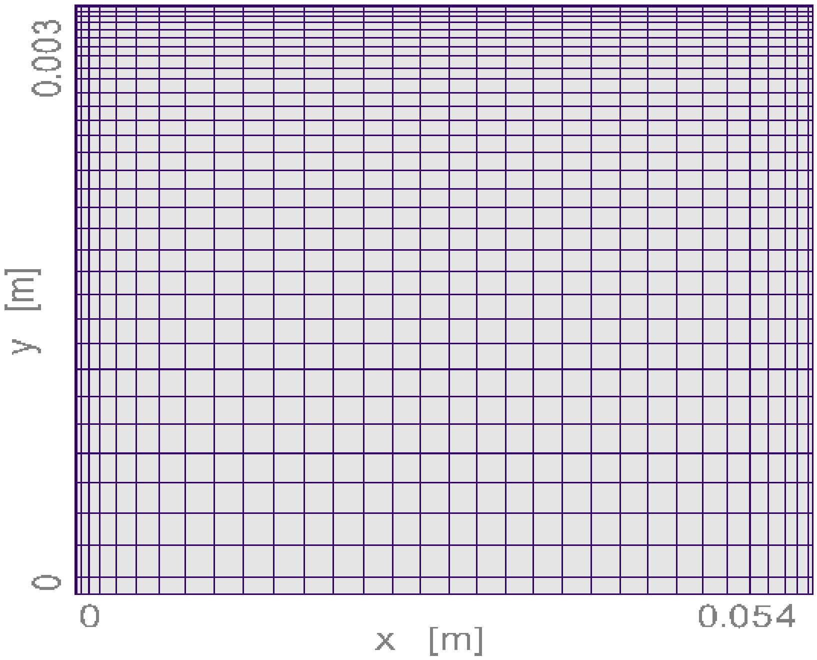

Figure 3.7: Mesh used for the PLASIMO 6x6mm PW model, in which the “x [m]” axis corresponds to the axial, or z-direction and the “y [m]” axis corresponds to the radial, or r-direction. The cathode and gas entry side is the west edge and the anode and gas exit side is the east edge, the north edge is the plasma-facing side of the enclosing metal plates, and he south edge is the axis of symmetry. In the vicinity of the west, east, and north edges, the mesh spacing is condensed for greater numerical stability.

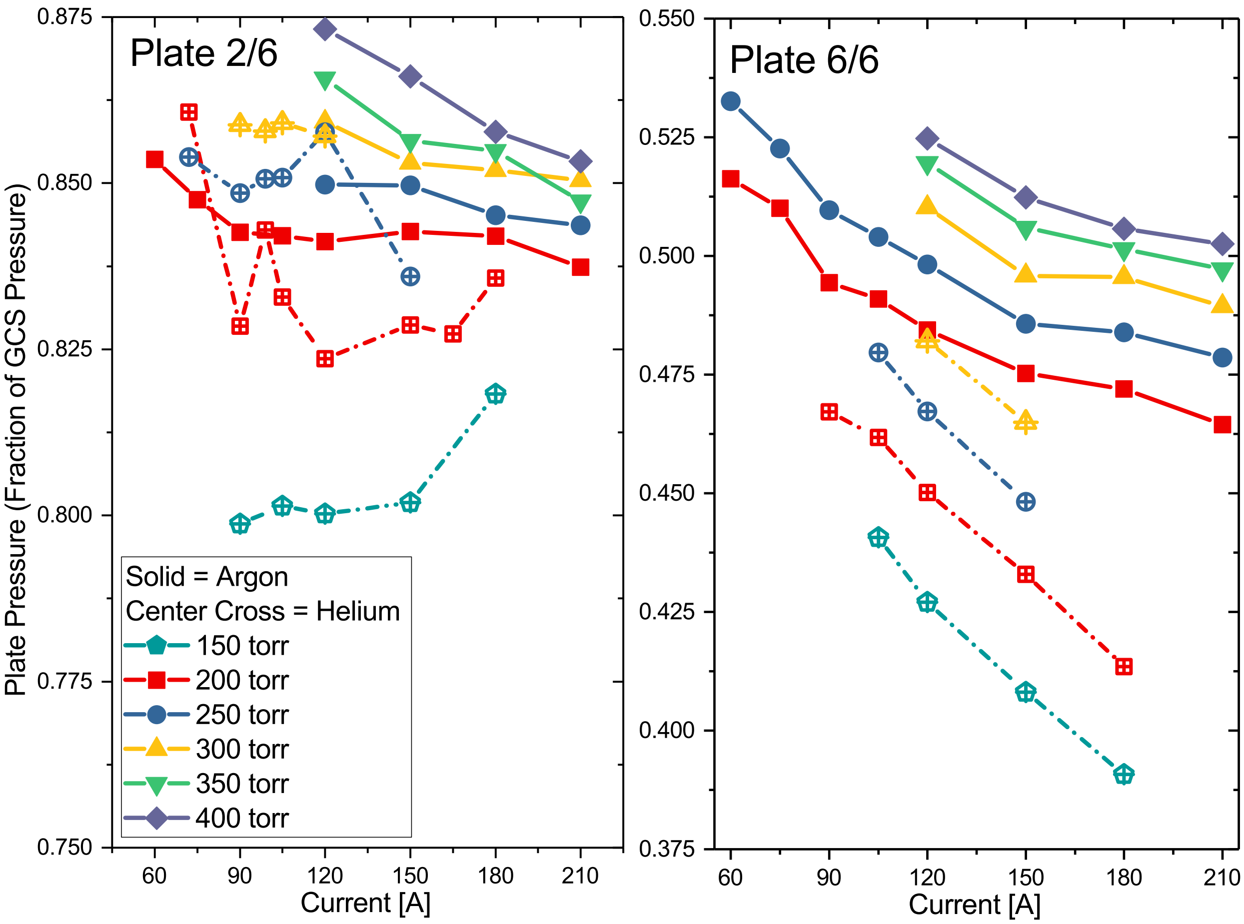

Figure 3.8: Measured plate pressures in argon and helium arcs of a 6x6mm PW, expressed as fraction of the GCS pressure. Plate pressures are given at the measured plate locations of P2/6 (left) and P6/6 (right, note the change in ordinate scales). Linear extrapolation of these pressures to the PLASIMO model region inlet and outlet provides the BCs used at those locations.

and argon arc. The pressures shown in this figure correspond to P2/6 and P6/6, so a linear extrapolation using these values is performed to the upstream edge of P1/6 and the anode position to obtain the pressure BCs for the corresponding PLASIMO model.

By doing this, the model's pressure boundary conditions end as just about 3% less than the GCS pressure for the model's inlet, and about 10% less than the measured plate 6 pressure for the model's outlet. It's possible that the linear extrapolation doesn't truly represent the pressure drop in the plate 1 to plate 2 or the plate 6 to anode regions, but it's

Table 3.2: PLASIMO boundary conditions abbreviations.

Abbreviation	Meaning
North	Plasma window enclosure (inner surface of cascade plates))
East	Cathode-side, gas inlet
South	Axis of symmetry or center axis
West	Anode-side, gas outlet to expansion
Temp	Temperature
H.	Homogeneous
Cst.	Constant
Dir.	Dirichlet
Neum.	Neumann
US	User-specified
TIF	Thermal Ion Flux
Rec. prob.	Recombination probability

Table 3.3: PLASIMO boundary conditions employed for PW models.

Property	North	West	South	East
Pressure	H. Neum.	Cst. Dir. (US)	H. Neum.	Cst. Neum. (US)
Velocity (z)	H. Dir.	Cst. Neum.	H. Neum.	H. Neum.
Velocity (r)	H. Dir.	H. Dir.	H. Dir.	H. Neum.
Heavy Temp	Cst. Dir. (US)	Profile Dir. (US)	H. Neum.	H. Neum.
Electron Temp	H. Neum.	H. Neum.	H. Neum.	H. Neum.
Ionization Degree	TIF, 90% Rec. prob.	H. Neum.	H. Neum.	H. Neum.

likely that the deviation from this would not substantially effect model results.

For the 1x6mm_5x10mm and 1x6mm_9x10mm, it is not explicitly known what the outlet pressure is. for purposes of obtaining something close to reality, these PLASIMO models have utilized the anode pressures determined for the corresponding GCS pressure and arc current of the 1x6mm_7x10mm setup. This introduces a degree of uncertainty, particularly for the helium case, is it is clear from examining other configurations such as 6x6mm that the outlet pressure depends more on the total PW length than it does in argon gas. However, we shall see that other factors render the two-radius PLASIMO models less usable than the single-radius models.

In addition to the boundary conditions in Table 3.5, it is necessary to specify an initializing composition of the plasma bulk region (non-boundary) region of the model.

Another input the user specifies is the current delivered to the system, which is subsequently used in determining the axial electric field strength E_z. PLASIMO takes the assumption of quasineutrality and as such does not solve Poisson's equation to determine electric field (as the net space charge will be zero under this assumption). Instead the axial-direction electric field is determined using the arc current I and the plasma conductivity $\sigma(r, z)$, integrated over the channel area, as:

$$E_z = \frac{I}{2\pi \int_0^R \sigma(r, z) r dr} . \tag{3.66}$$

This is the only component of the electric field that is considered in the bulk of the plasma of the model. This is a good approximation for the part of the arc which has a roughly homogeneous electric field, which for the plasma window is from about the second plate (from cathode-side) to the plate just upstream of the anode. In this homogeneous field region, as a DC arc, the time derivative of the magnetic field magnitude is 0 so $\nabla \times \mathbf{E} = 0$, and therefore there is no radial component E_r of the field [28]. However, from the cathodes to around the second plate, the measured component voltages indicate the axial field E_z has not yet reached homogeneity, a fact which appears to be independent of the current and pressure settings within the scope studied in this work. These facts can be observed in the next chapter in Figs 4.15 and 4.16.

The plasma conductivity $\sigma(r, z)$ used in Eq. (3.66) is one of several transport coefficients solved for in PLASIMO using Frost mixture rules [121] and Chapman-Enskog-Burnett [112] kinetic theory for transport coefficients, in which the transport coefficients are calculated in terms of Sonine-polynomial expansion coefficients. The other transport coefficients calculated are electron and heavy particle thermal conductivities, and plasma viscosity. In Section 3.4, the portion of this theory relevant for calculating viscosity was discussed.

For PLASIMO's viscosity, the first order approximation is used with the electron contribution neglected (as is the case in Section 3.4). For heavy particle thermal conductivity the third order approximation is used, and the electron-heavy interactions are again neglected. The electrical conductivity σ is calculated using Devoto's second order approximation, and assumes only electrons contribute the conductivity. The calculation of this approximation is thoroughly detailed in Ref. [122], but in short it relies on contributions from ion and neutral collisions with electrons, through an ordinary diffusion coefficient calculated using similar framework described in Section 3.4. Further details on the calculation of the diffusion coefficients is provided in Ref. [112]. For these transport coefficients, it is necessary to incorporate collision cross section information for neutral-neutral and neutral-ion collisions. Methodology for obtaining this is given in Ref. [123]. Now this electrical conductivity can be used in Eq. (3.66) to determine the local axial electric field. This electric field is then used in determining Ohmic power input Q_{Ohm} in Eq. (3.61) using:

$$Q_{Ohm} = \int \mathbf{j} \cdot \mathbf{E} \, dA \,. \tag{3.67}$$

Furthermore, the current density $\mathbf{j}$ is determined via Ohm's Law using:

$$\mathbf{j}(r,z) = \sigma(r,z)\mathbf{E}(z) \,, \tag{3.68}$$

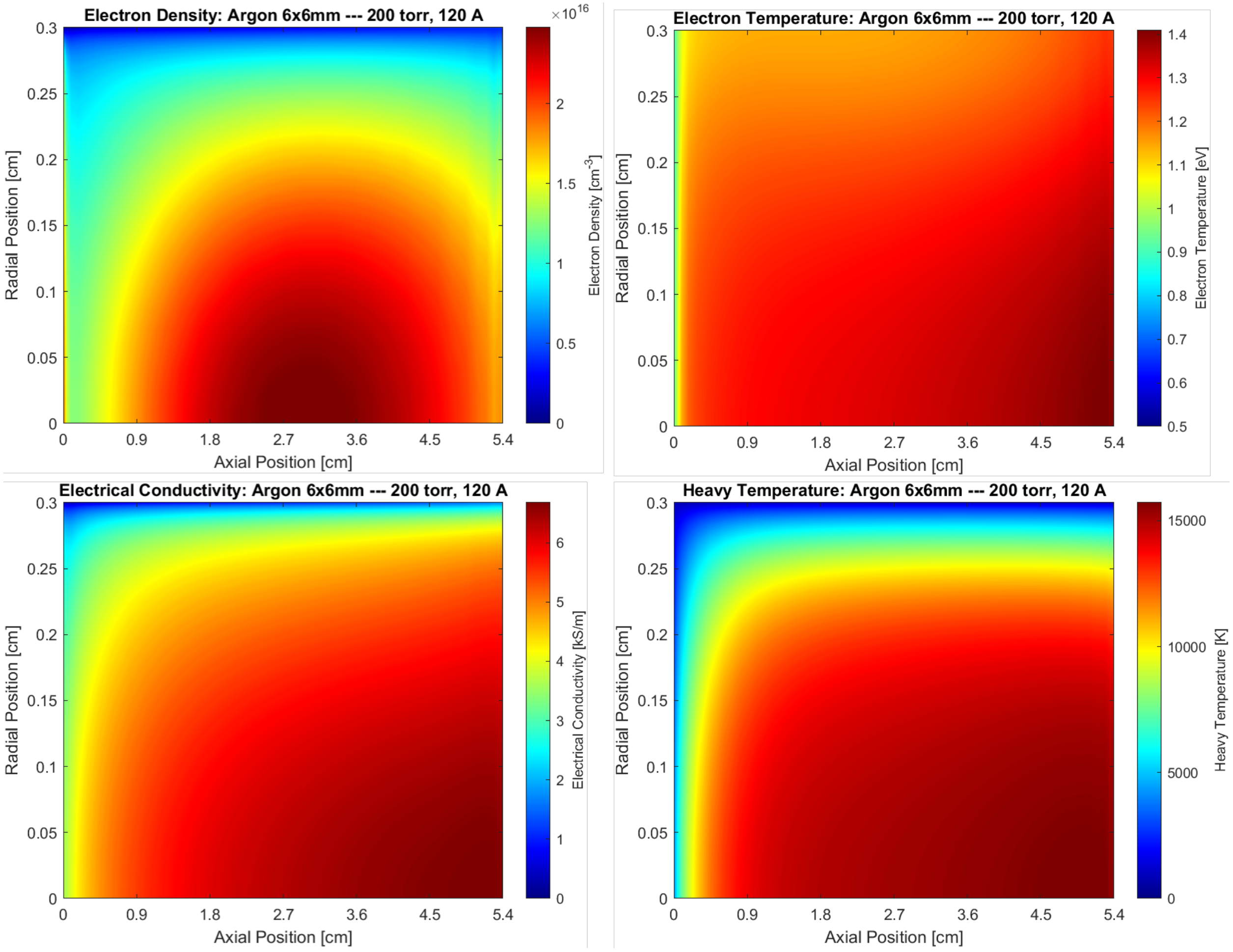

Figure 3.9: Several plasma properties from a PLASIMO model of a 6x6mm PW of argon at GCS pressure 200 torr and arc current 120 A.

so, coupling with Eq. (3.66):

$$\mathbf{j}(r,z) = \frac{I\sigma(r)}{2\pi\int_0^R \sigma(r,z) r dr}\,. \tag{3.69}$$

With that, the model is established and can be used to determine plasma properties and how they compare to measurement. Figure 3.9 shows some results from a converged argon PLASIMO model in a 6x6mm geometry with a GCS pressure of 200 torr and arc current of 120 A. As will be discussed in Section 4.2, the electron density n_e will be compared to the corresponding measurement by effectively reconstructing a Stark profile for an emitting

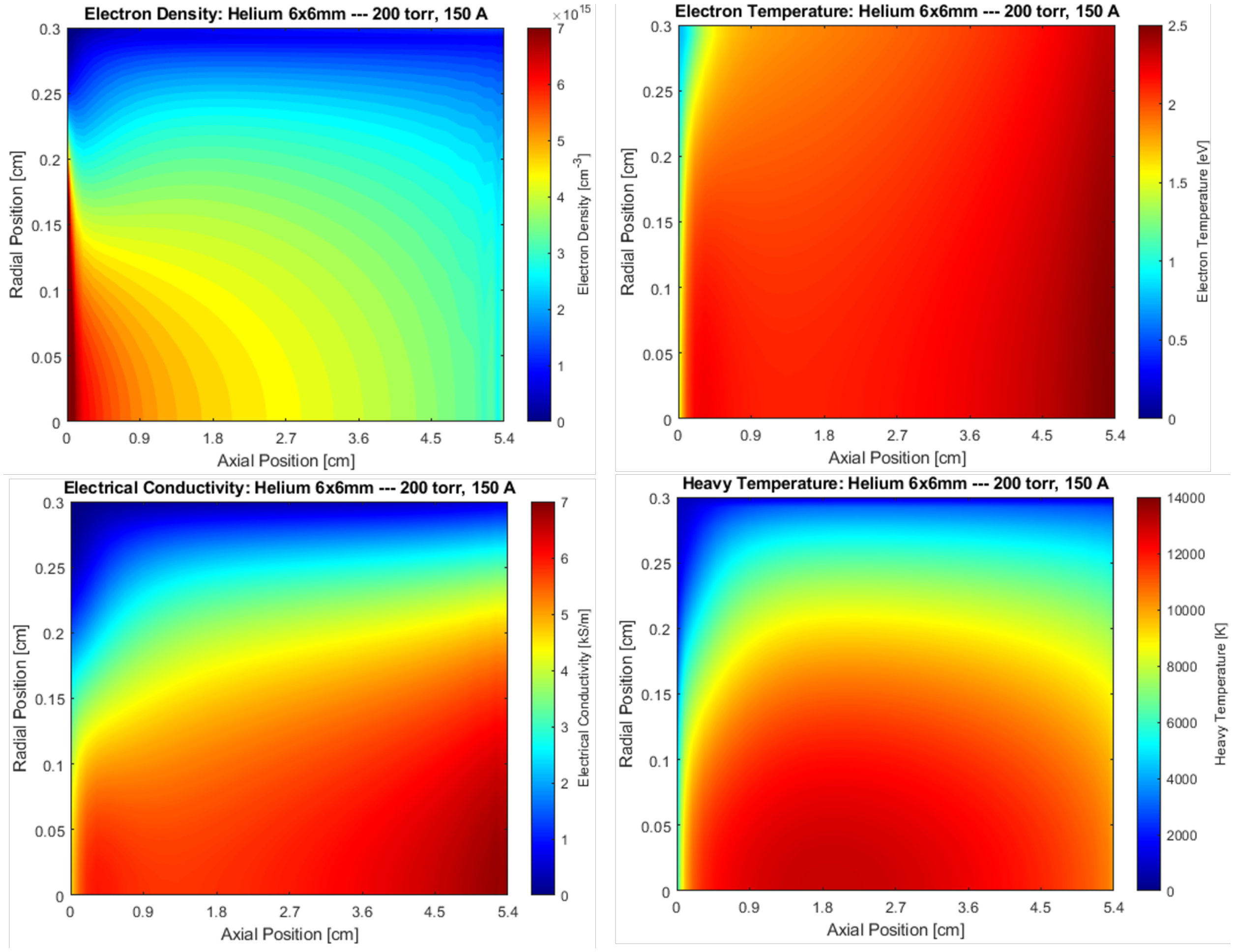

Figure 3.10: Similar to Fig. 3.9 but for helium. Several plasma properties from a PLASIMO model of a 6x6mm PW of helium at GCS pressure 200 torr and arc current 150 A.

plasma with the PLASIMO model's n_e radial profile at the axial position of the diagnostic plate where measurement occurs. Effectively this means that the model n_e value used for comparison will be close to the on-axis value. The same is true for electron temperature T_e. For plasma conductivity σ to compare with measurement, a radial average is taken over the model space at the axial location corresponding to the plate in question. A model value of heavy temperature T_h is also determined in this manner and will be compared with the axial T_h profile calculated via the methodology described in Section 3.3.

Generally, features in the argon PLASIMO model roughly match with the measured

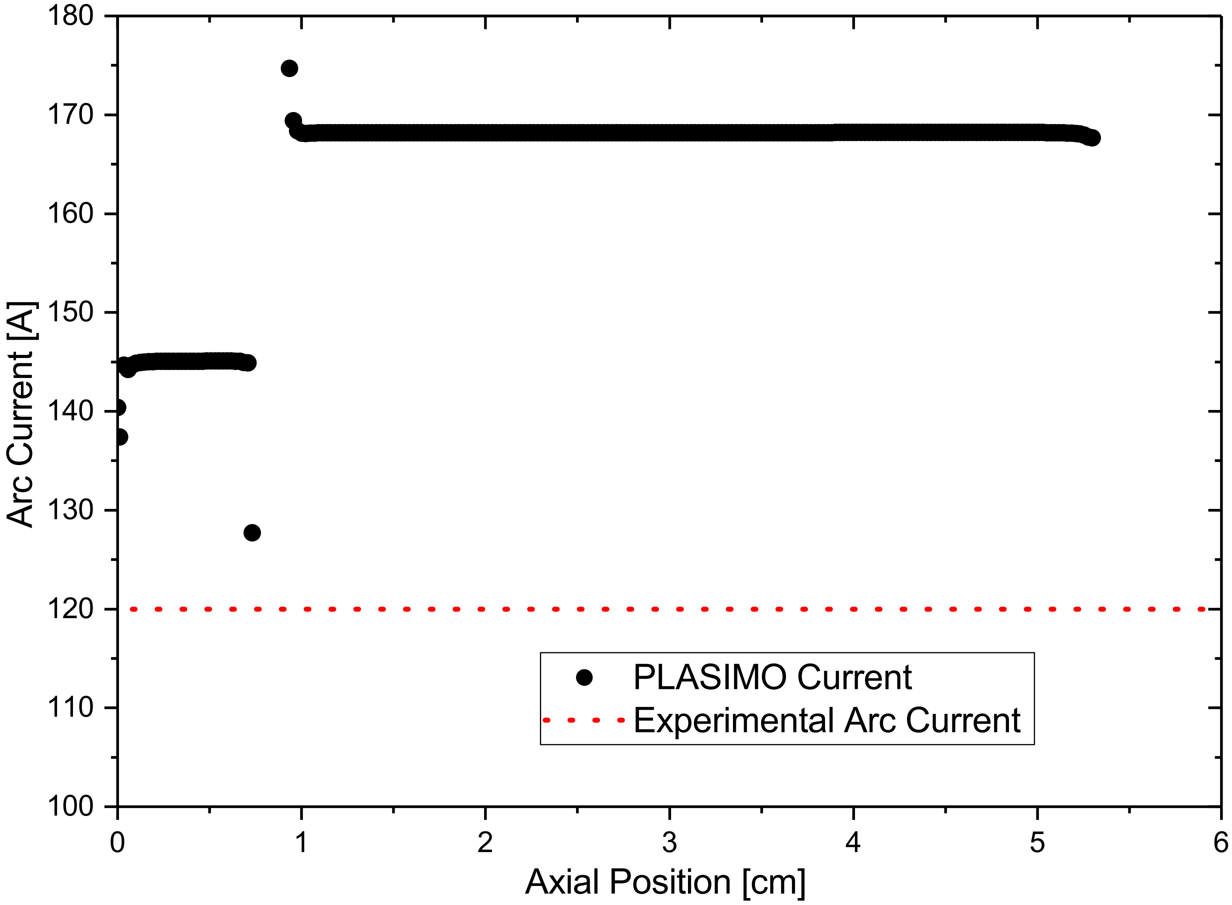

Figure 3.11: PLASIMO arc current for a 1x6mm_5x10mm model corresponding to a PW with 200 torr GCS pressure and 120 A arc current. There is a mismatch not only between the arc current in the two sections but also between both and the experimental arc current.

values, and the same is true for the helium PLASIMO model. Chapter 4 will go into depth with the comparisons of the various measured properties between the two gases and with the PLASIMO model.

PLASIMO models of the two-aperture configurations are more complicated than the single-aperture ones, and exhibited much more difficulty in obtaining a converging solution, particularly for helium models. The model calculates current density j via Ohm's law $\mathbf{j} = \sigma\mathbf{E}$. This amounts to using Eq. (3.69) for the single-radius models such as a 6x6mm PW. For the two-radius system however (e.g. a 1x6mm_5x10mm configuration), the total arc current is not necessarily preserved in going from the smaller radius section of the channel to the larger radius section, nor are either necessarily equivalent to the corresponding experimental arc current. This can be seen in Fig. 3.11 for a PLASIMO model of a 1x6mm_5x10mm PW in argon at 200 torr GCS pressure and 120 A arc current. Essentially, the two-radius model is intrinsically non-1D, and this particular PLASIMO model is designed for systems that have a single radius and so can be reasonably well approximated as 1D. This means that utilizing this type of model to assess the two-radius PW configurations is inappropriate. However, as will be discussed at length in Section 4.2, the single-radius PLASIMO models perform reasonably well and generate results that are comparable to measured values.

3.6 Effect of Plasma Window on Ion Beam

The NSCL plasma window test stand is actually just one half of the system that would be implemented on an accelerator beamline, for ease of experimentation. In an accelerator, there would be two plasma windows, one on either side of the high pressure GCS. It is necessary to quantify this system of the plasma windows and gas charge stripper impact on the beam passing through. The effect of this complete charge stripping apparatus on the beam comes about in primarily two forms: energy spread and emittance growth from scatterings with stripping gas particles, and beam-deflection from the magnetic field generated by the arc current. We will begin with the effect on the beam by the PW arc current I which generates an azimuthal magnetic field B_{PW}.

In both plasma windows, the electron current flows from the cathodes at the high pressure side to the anode on the low pressure side. The beam will first traverse one PW (electron current travelling in the opposite direction as ion beam) with its initial charge state, then

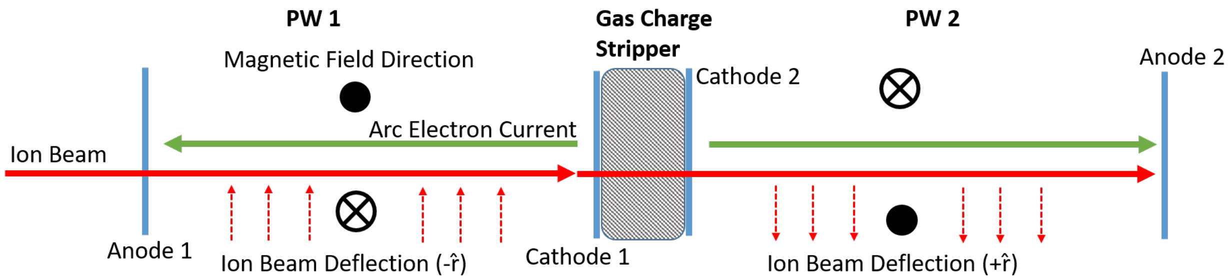

Figure 3.12: A diagram illustrating the orientation of an ion beam traversing the PW-GCS arrangement. Also shown are the magnetic field orientations from the PWs and the resulting deflection on a beam particle.

will be stripped in the GCS, and finally will traverse a second PW (electron current travelling in the same direction of the ion beam) which is oriented opposite of the first, with its post-stripped charge state. In the first PW with the electron current travelling antiparallel to the beam, the field will deflect beam particles continuously radially inwards, and in the second PW with the electron current travelling parallel to the beam, the field will deflect beam particles radially outwards. This is illustrated in the diagram of Fig. 3.12.

Consider a test case of an ion beam traversing a PW that is 8 cm long and carrying 180 A of arc current. A worst-case scenario would be if all the arc current is constricted and passes through a narrow radius column within the whole PW channel, and for beam particles just outside where this arc current travels. For this worst-case example, consider all the current to be within 1 mm diameter along the PW axis, and a test beam particle right at the edge of this current, which has initially zero transverse velocity. From Ampere's Law for particles outside then:

$$B_{PW} = \frac{\mu_0 I}{2\pi r}\,. \tag{3.70}$$

The Lorentz force dictates the degree of deflection experienced in both cases, so that:

$$\dot{\mathbf{v}}_{j,\perp} = \frac{Q_j}{m_b} c\beta B_{PW} \ \pm\hat{\mathbf{r}} \,, \tag{3.71}$$

where the subscript j denotes which PW the beam is within, m_b is the mass of a beam particle, Q is the charge state of the beam within PW j, β is the beam speed as a fraction of the speed of light, and $\dot{\mathbf{v}}_{j,\perp}$ is the deflection acceleration whose direction is given based on which PW the beam is in (see Fig. 3.12). With this one can obtain the deflection angle and distance at the end of each PW for the test particle, which are shown in Tab. 3.6. Angular deflections are moderately sized but changes in the radius of the beam test particle are small enough that the deflections will not be a concern for beam scraping on the inner surface of the PW plates. The values in this table can be compared to a test beam, which here will be the FRIB beam. The FRIB beam at the charge stripper can have a full beam size (radius) as small as 1.5 - 2.0 mm, with full beam normalized emittance around 1.5 π mm mrad. This corresponds to an angular extent of about 12.0 - 15.9 mrad. Therefore it can be seen when comparing to the angular deflection values listed in Tab. 3.6 to these nominal FRIB values, it is clear that under the assumptions discussed above that the angular deflections generated by the PW are not negligible. However, we must recall that this is under the assumption that ALL of the arc current is contained within a 1 mm diameter column along the PW axis. This is unlikely to be the case, so if we consider instead an arc where the current density $j(r)$ falls off as $1/r$ (such that $j(r)2\pi r = constant$), we would obtain instead for the PW magnetic field B_{PW}:

$$B_{PW} = \frac{\mu_0 I}{2\pi R} \,, \tag{3.72}$$

Table 3.4: Characteristics of beam particle deflections from the PW for several test beams each at 18 MeV/u. Beam particle is initially 1.5 mm from center-axis and has zero angle.

Property	^{238}U	^{40}Ar	^{16}O
Initial (PW1) Charge State	33+	8+	6+
Outgoing (PW2) Charge State	75+	12+	8+
Gamma	1.019	1.019	1.019
Beta	0.193	0.193	0.193
Single PW transit time [ns]	1.4	1.4	1.4
PW1 outgoing angle change [mrad]	-0.44	-0.64	-1.2
PW1 outgoing radius change [μm]	-18	-25	-47
PW2 outgoing angle change [mrad]	1.0	0.96	1.6
PW2 outgoing radius change [μm]	40	38	64

where now the field is constant in r and depends on the PW channel radius R. For a PW channel of 3 mm radius (6 mm diameter) which corresponds to the geometry discussed at length in Section 4.2, this results in a B_{PW} that is half of what is used for results in Tab. 3.6 and thus angular deflection values will also be reduced to half the values presented there. While this latter approach is likely a more realistic scenario, results presented in Tab. 3.6 represent the worst case scenario and therefore worth planning for.

These are the results only for particles matching the specified inlet parameters, but of course the full beam contains particles over a range of angles and positions. To understand the effect on the beam as a whole, F. Marti conducted a simulation of a beam packet consisting of 10^6 particles whose RMS (un-normalized) emittance is 0.802 pi mm mrad [1]. The effect of the PW is taken as a simple angular kick that would occur at the center of the PW length, assuming that the current distribution is entirely concentrated in within a radius of 1 mm. For this calculation, the cumulative current inside this stream increased quadratically with radius r up to $R = 1\,\text{mm}$, so the magnetic field inside this arc current

Table 3.5: Beam emittance values resulting from transit through the two PWs enclosing a GCS (GCS not considered here). RMS emittance results are for a ^{238}U beam with charge state 33+ for PW1 and 73+ for PW2, and each PW being 10 cm long and 150 A [1].

Location	RMS Emittance Value [pi-mm-mrad]
At PW1 center (before kick)	0.7992
At PW1 center (after kick)	0.8019
At PW2 center (before kick)	0.8019
At PW2 center (after kick)	0.8142

stream is:

$$B_{in} = \frac{\mu_0 I r}{2\pi R^2} \tag{3.73}$$

,

and outside it is given by Eq. (3.70). These two different forms result in nonlinear behavior for the particles of the entire beam bunch, which is why the beam emittance in this PW case will increase. The resulting effect on the beam emittance through both PWs is shown in Tab. 3.6. For this test case of a ^{238}U beam in a 180 A pair of PWs, it can be seen that emittance increases from 0.7992 to 0.8142 pi-mm-mrad, an increase of only 2%. It should also be noted that this would be the worst-case-scenario with all of the arc current being confined to a narrow stream in the channel, whereas it's expected that the arc current is actually spread over the entirety of the PW channel and therefore the effect on beam emittance would be further reduced.

The other effect on the beam comes from the gas charge stripper itself. The beam-gas scattering events within the stripper will result in a net divergence of the beam angle in all directions, but not appreciable change in beam position coordinates. The result for the beam's transverse emittance is qualitatively illustrated in Fig. 3.13 for two scenarios, the first in which the beam has a smaller extent but greater angle, and vice versa for the second

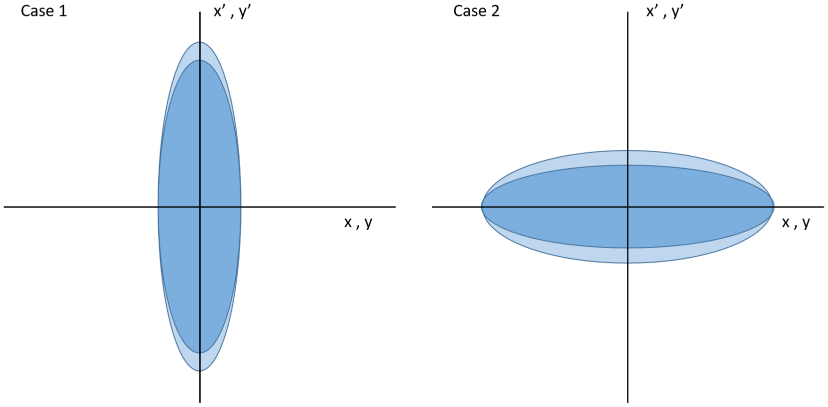

Figure 3.13: Two possible scenarios for beam Courant-Snyder ellipses at the entrance of the GCS. Beam-gas scatterings will cause angular deflections, growing the ellipse in the x', y' directions, and will have a greater overall area growth for Case 2.

scenario. It can be easily visualized then that for the second case, a much greater transverse emittance growth will occur, so the first case is the desired Courant-Snyder ellipse for the beam to have at the entrance of the GCS.

As mentioned in Section 1.1, some calculations of of energy spread for a U beam passing through a 225 torr and 375 torr He charge stripper were carried out in Ref. [3] (shown in Fig. 1.4). The obvious result of this is that energy spread rises rapidly as a function of the overall length of the charge stripping region, hence the desire for as short a charge stripper as possible. The mean charge state asymptotically approaches the equilibrium charge state, so there must be a user-decided optimization between higher charge states but greater energy spread (longer stripper) and vice versa (shorter stripper).

Chapter 4

Results and Discussion

4.1 Flow Rates in Plasma Window Configurations

It was shown in Fig. 1.6 that the plasma window can substantially reduce the flow rate of the gas leaking from the GCS. Understanding the degree of this reduction has been a core aim of this thesis, as is leveraging that understanding to optimize the PW geometry and meet all the needs of a gas charge stripper for an ion beam. Those necessities are an aperture wide enough to permit scrape-less beam passage (6 to 10 mm diameter) and as large a pressure as can be managed to achieve the desired degree of charge stripping in a short length (see e.g. Fig 1.3). In an effort to better understand how to optimize the PW geometry for those two factors, an important facet of this project has been the study of different geometries of the PW, referred to as configurations, and within those the corresponding flow rates for selected GCS pressure and arc current. The ion beam must pass through the PW without scraping on the enclosing walls, which is the reason PW aperture sizes of less than 6 mm are not considered for this application. This requirement encourages more consideration of a two-radius system such as 1x6mm_7x10mm, where the only 6 mm plate is nearest the charge stripper. Because the beam experiences angular deflections in the charge stripper, the beam will grow in extent over the length of the PW, so if the PW has a 6 mm plate in an otherwise 10 mm channel, it's best to have that plate on the cathode-side where beam size

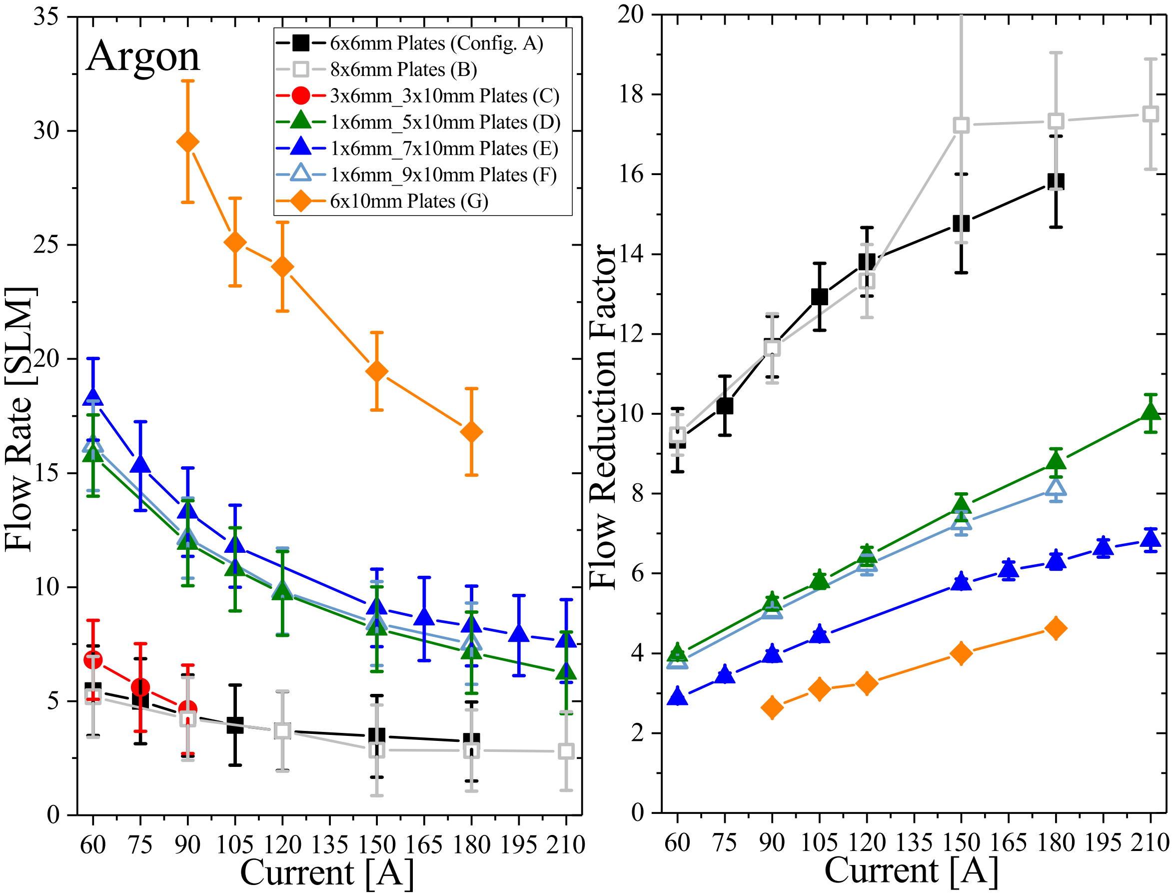

Figure 4.1: Argon flow (left) and flow reduction factor (right) data taken in multiple PW configurations, labeled A-G. All data is for a GCS pressure of 200 torr.

will be relatively small. Due to improvements to the PW system being applied after some data already had been collected for certain PW geometries, and the process of adjusting to a new configuration being a lengthy one, some PW configurations are lacking data at certain GCS pressures and/or arc currents.

Figures 4.1 and 4.2 illustrate several key points of the plasma window's flow rate restricting capabilities in different plate configurations. In an argon PW, the effect on flow rate of variations in total channel length for a 6 mm diameter channel is difficult to discern, as seen with Config. A and Config. B in the figure. In a helium PW though, it does appear that there is a benefit of reduced flow by extending the PW length. The drawback in extending

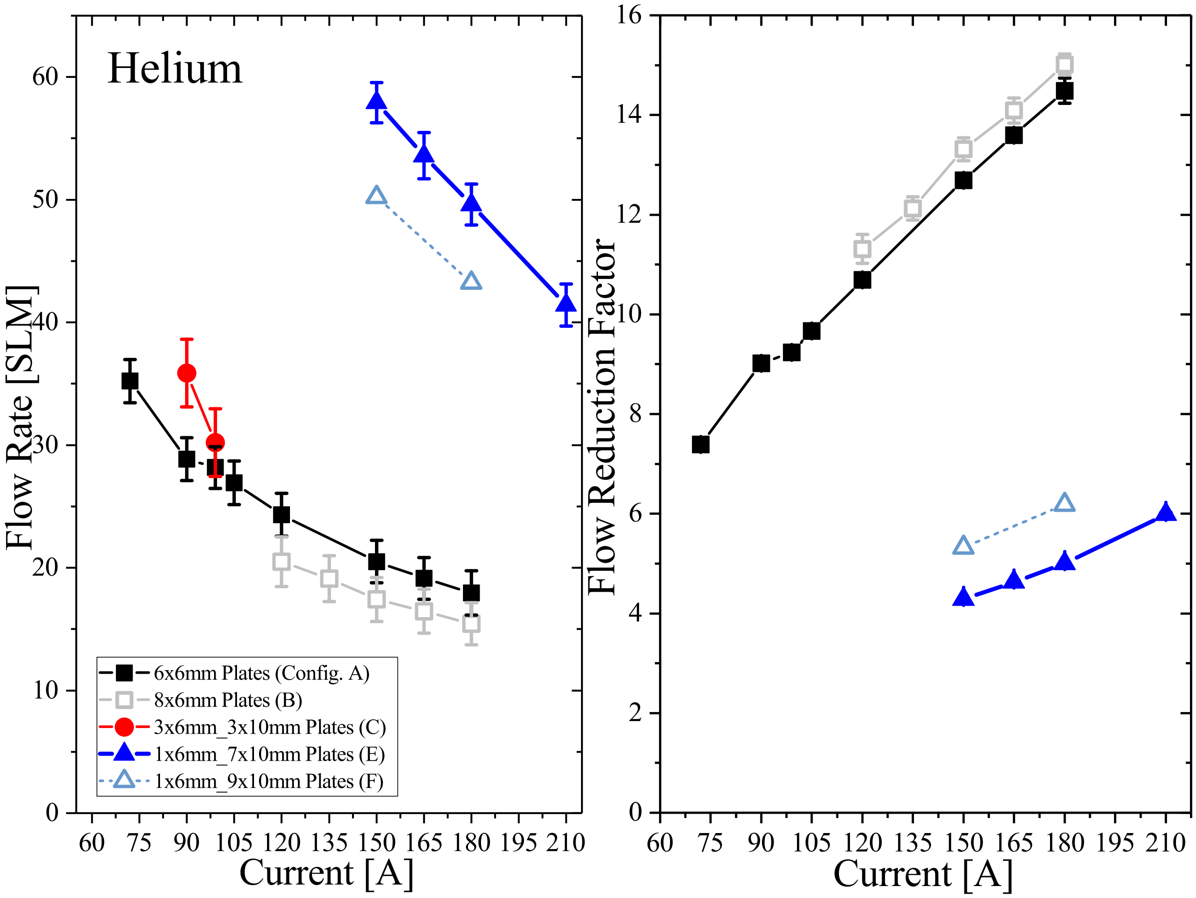

Figure 4.2: Similar to Fig. 4.1 but for helium. Helium flow and flow reduction factor data taken in multiple PW configurations, labeled A-G as in Fig. 4.1, however due to experimental limitations no data was acquired for configurations D or G, and data for F was extrapolated from data at other pressures in that configuration. All data is again for a GCS pressure of 200 torr.

the PW length however, as will be shown later in this chapter, is that overall arc voltage drop increases with the total distance, so there is a greater power being delivered to the arc that must ultimately be removed by the coolant. The longer distance additionally would result in more beam size growth. Given that the conductance of a channel is proportional to its area, it's no surprise that even with the arc, we see a substantial flow rate rise between a 6 mm diameter channel (Config. A) and one of 10 mm diameter (Config. G) in argon. We were unable to maintain a stable helium arc in a full 10 mm diameter channel so no Config. G data was collected for this gas. An additional feature of interest in Figs. 4.1 and 4.2 is noted by comparing the 3x6mm_3x10mm (Config. C) flow rates with those of 6x6mm (Config. A) in both gases. As a function of arc current, the slope of the former is much steeper and appears to approach that of the latter at currents above 90 A in argon. Unfortunately Config. C is one in which no data was obtained beyond 90 A (this was collected prior to an upgrade which increased the maximum arc current from 105 A to 210 A), but it is likely that at currents higher than about 100 A, the flow rate in this system will be essentially the same as in the case of Config. A. This suggests that, for currents in excess of this, there is very little benefit in a PW longer than 3 plates (recall the plates are 7 mm wide with 2 mm wide spacers). Such behaviors presumably also would be illustrated for e.g. a PW consisting of 2 plates, etc.

All of the measurements of plasma properties have been taken with the aim of determining how they depend upon the plasma window's controllable parameters - its pressure, current, and geometry. It is necessary to establish predictable behaviors of these properties because these in turn influence the mass flow through that same channel. The subsequent sections in this chapter are devoted to illustrating results of these measurements and their significance, beginning with single-radius PW configurations in Section 4.2, which primarily emphasises the 6x6mm PW configuration (Config. A) and then for double-radius PW configurations such as 1x6mm_7x10mm in Section 4.3, which will detail a smaller subset of results.

4.2 Single-Aperture Plasma Window Results

In this and the subsequent section, results from both gases will be introduced. Those in this section are from PW arrangements consisting of a single aperture size that extends the length of the channel.

As mentioned in Section 1.1, a gas charge stripper composed of helium produces the highest charge states in the transiting ion beam relative to other gas options (with the exception of hydrogen), but as a result of its low mass, also has a high leakage rate from the GCS. In addition, while the argon arc is quite stable and can be maintained through a very wide range of operating conditions, the helium arc is more difficult to manage. In order to even establish a stable arc in helium, we have found it necessary to initiate the arc in argon, and then slowly close the argon flow and simultaneously open that of helium. This is thought to be a result of helium's lower mass not being able to sufficiently heat the cathodes from a null current state to allow them to emit electrons enough to establish a stable arc. One thing that contributes to this difficulty of helium in the PW is that it has a rather high first ionization energy of 24.59 eV, as compared to argon's first ionization energy of 15.76 eV, as well as having lower ionization cross section values. As a result, helium requires a higher electron temperature to generate the same density of ions in the plasma.

4.2.1 PLASIMO Comparison Method

It should be noted that for electron density measurements, proper comparisons with PLASIMO require some assumptions. Firstly, at any axial location we naturally expect a radial distribution in electron and heavy particle densities and temperatures and so too would we expect a radial distribution of the intensities of emission lines. Some previous works indicate that the electron density tends to fall to about 1/10 of its central value near the edge of the arc channel of its central value [81]. We therefore expect a dramatic reduction in emission intensity distribution closer to the edge of the arc channel. We will denote this intensity distribution by $e(r)$. Additionally, since measurements take in light along the entire line of sight which cuts through the central chord of the arc channel, in order to properly compare PLASIMO model to measurement the modeled values should be a mean value over a region corresponding to the measurement and weighted by the emission intensity distribution mentioned above.

Firstly we will make a simple estimate of what the intensity distribution $e(r)$ would be. Measurements of this distribution in a cascaded arc setup similar to the PW has not been thoroughly examined or published, as of the time of this thesis, though it would be a very interesting arc characteristic to be explored. Lacking measurements, we can model an expected $e(r)$ using the HeCRM discussed in Section 3.2 using PLASIMO modeled n_g and n_e for a test case. The test case corresponds to data from P2/6 of a 6x6mm PW at GCS pressure 200 torr and arc current 150 A, and the results are illustrated in Fig. 4.3. An exponential decay is fitted, which will be taken as the intensity distribution $e(r)$ that will be used in the rest of the analysis in the subsequent paragraphs.

We must consider the volume of the arc channel whose emissions will transmit through

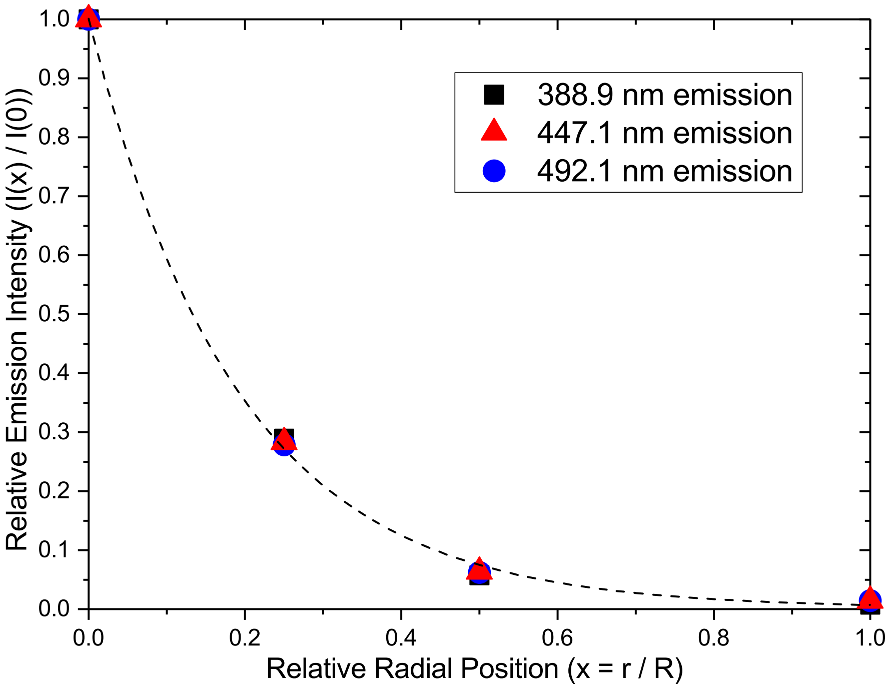

Figure 4.3: Simulated relative radial intensities for three selected emissions for a 6x6mm PW, using PLASIMO modeled data corresponding to P2/6, GCS pressure 200 torr, and arc current 150 A. The dashed line is an exponential decay fit, representing the radial intensity distribution $e(r)$ to be used.

the 1 mm diameter diagnostic port at the side of the channel. We assume all light that enters the port is collected by the receiver, and from this point forward all emissions mentioned are implied to be parallel to the diagnostic port. Consider such a port whose diameter is b, on the outside of the arc channel of radius R. Considering a succession of concentric, differential thickness cylinders that are coaxial with the arc channel, we must find the volumetric intersection of this cylindrical shell and the diagnostic port line of sight (LOS) cylindrical column. A far easier problem can be constructed if we consider that the diagnostic port LOS is instead a square column, each side being b wide. With this, it can be shown that for the cylindrical shells of $r < b/2$, the intersection volume (between that shell and the LOS column) is:

$$dV = 2\pi b r dr \,. \tag{4.1}$$

For cylindrical shells of $r \geq b/2$, only part of the shell intersects the LOS column, so:

$$dV = b\left[2\pi r\left(\frac{2}{\pi}\arcsin\left(\frac{2r}{b}\right)\right)\right]dr = 4br\sin^{-1}\!\left(\frac{2r}{b}\right)dr \,. \tag{4.2}$$

Given that each of these radii r corresponds to a different electron density $n_e(r)$, emissions from these shell-LOS intersections will each have a different profile whose shape is given by Eq. (2.15). For this analysis, it is necessary to use the width w_j, shift d, and asymmetry parameter α that parameterize the Stark profile corresponding to the radially-dependent electron density $n_e(r)$. To reconstruct a PLASIMO value for electron density which can be compared to measurement, a reconstructed Stark profile is sought, by considering the emission profile at each radius r. At each r, the emission profile must be normalized according to both the differential emission volume in Eqs. (4.1) and (4.2), and the emitter density given

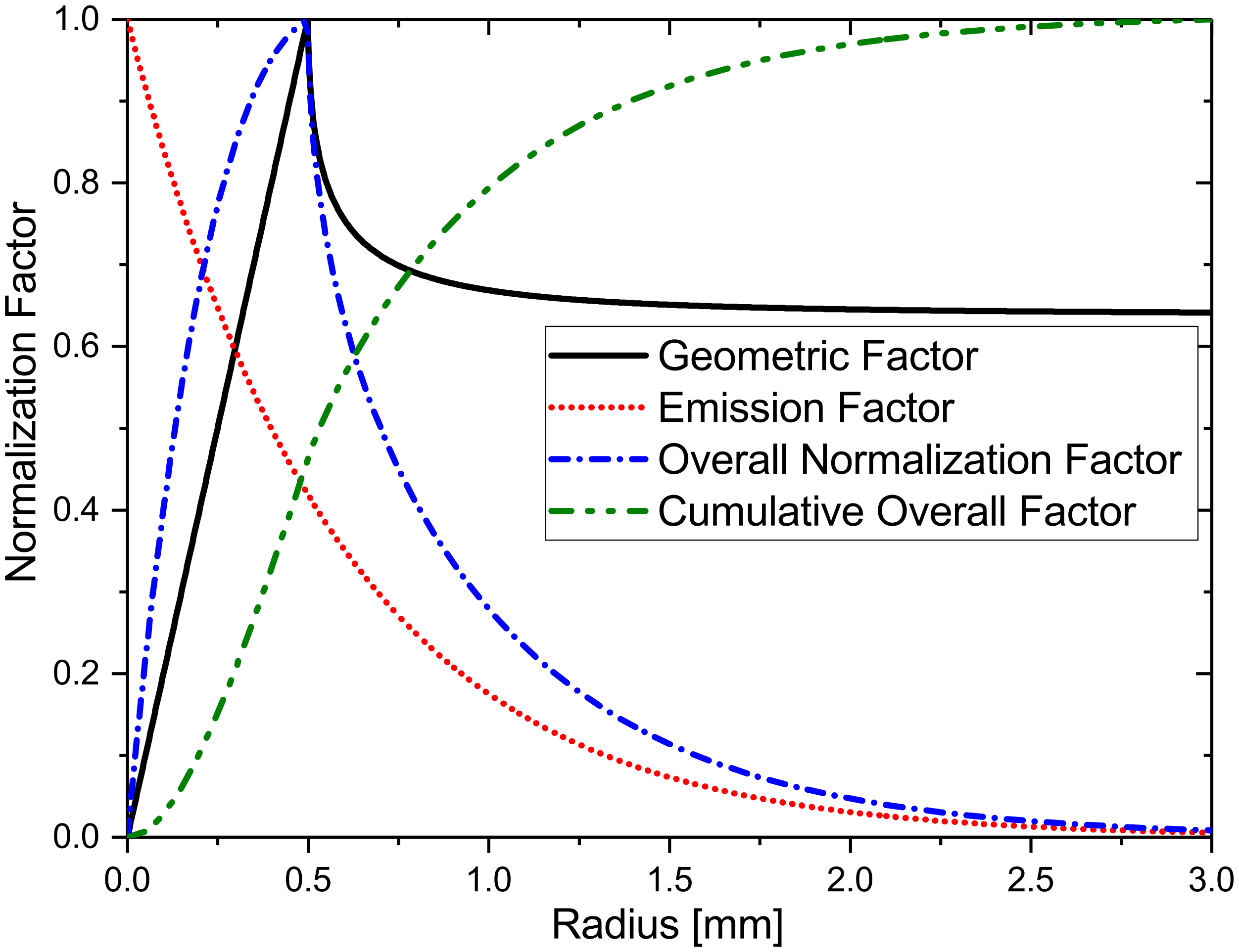

Figure 4.4: Normalization factors for reconstructing a would-be-observed Stark profile from PLASIMO measurements. The black solid line is the geometric normalization using Eqs (4.1) and (4.2), the red dotted line is the emission normalization factor from Fig. 4.3, and the blue dash-dotted line is the (renormalized) product of the other two curves. The green dash-dot-dot line is the cumulative integration of the blue overall factor.

by $e(r)$, explained in Fig. 4.3. These normalizations are obtained by setting the greatest value over the domain $0 \leq r \leq R$ equal to 1. These normalization values are shown in Fig. 4.4 for a 6 mm diameter PW channel. An overall normalization factor is obtained by multiplying the geometric and emission normalization factors (again the greatest value is reset to 1). The curve in green is the cumulative integration of the blue overall normalization factor, and this then represents the fraction of total collected emissions that originate within a given radius.

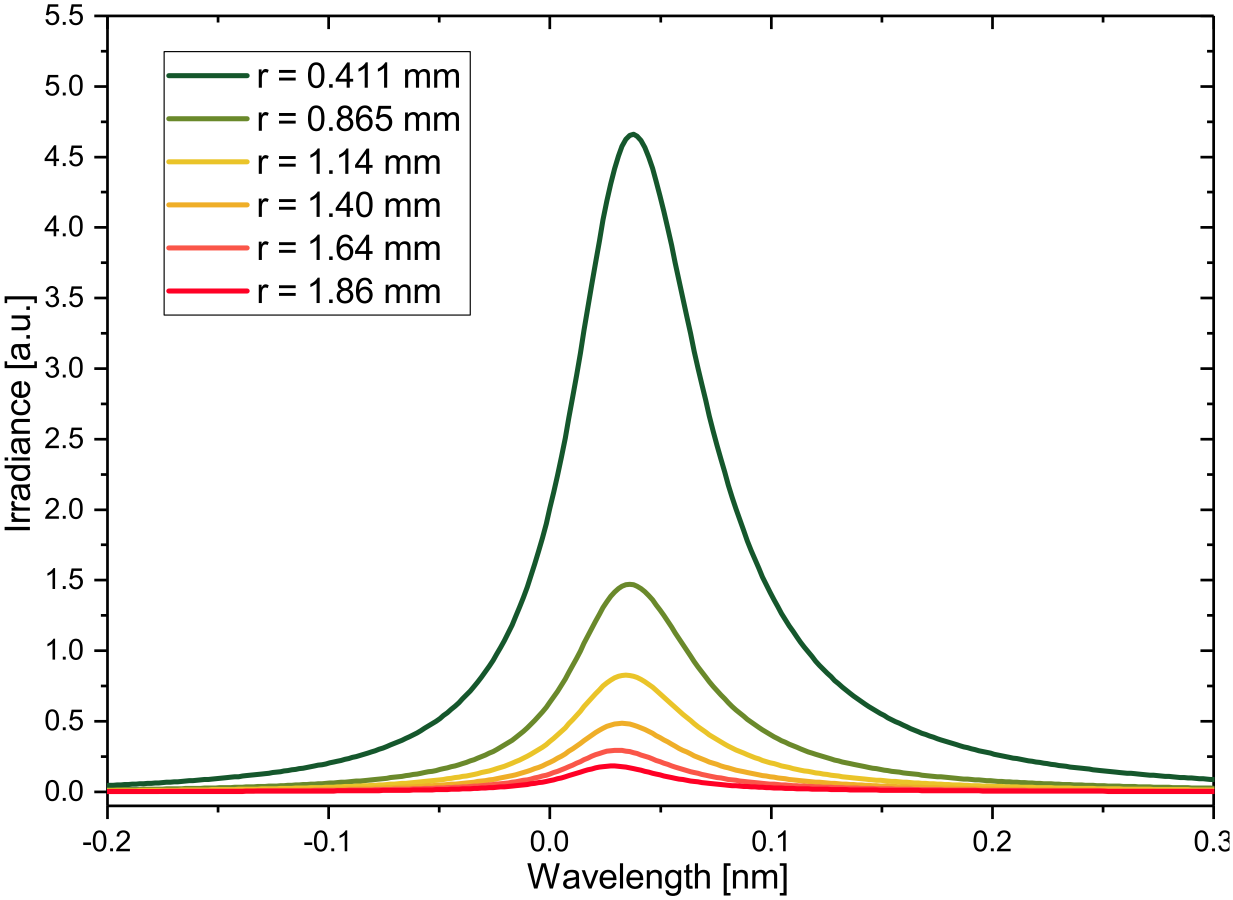

Figure 4.5: Stark profiles at selected radii, using overall normalization factors from Fig. 4.4. The profiles are constructed using Stark parameters corresponding to radial electron densities determined by PLASIMO for an argon 6x6mm PW, GCS at 200 torr and 120 A, at the axial location corresponding to P6/6.

To illustrate the behavior of the profiles as their parameters change with $n_e(r)$, a set of reconstructed Stark profiles at selected radii from a PLASIMO model of an argon 6x6mm PW, GCS at 200 torr and 120 A, (at the equivalent position of P6/6) is illustrated in Fig. 4.5. Each profile's irradiance integral is given by the corresponding total normalization factor from Fig. 4.4.

The final thing to consider before reconstructing a Stark profile and obtaining from it an effective electron density to compare with measurement, is to examine the effect of reabsorption of the emitted radiation over the extent of the profile. This reabsorption can occur anywhere between the emission point and the light collection point. This is included via Eqs. (2.32) - (2.36). Determining the effect of reabsorption relies on knowledge of the absorbing state density. This can be obtained via a CR model, such as that described in Section 3.2. For the arc conditions studied in the PW work for this thesis, the absorbing densities n_{abs} for emissions studied are typically lower than the ground state density by 6-7 orders of magnitude, based on the CR model results. Even taking the far more generous value of $n_{abs} \approx 10^{-4} n_{grd}$, the effect of reabsorption on distorting the overall reconstructed Stark profile appears negligible for the lines studied here (Ar I 425.9 nm and He I 447.1 nm). A sample of the effect on the overall reconstructed profile is shown for these emission lines in Fig. 4.6 for both $n_{abs} \approx 10^{-4} n_{grd}$ and $n_{abs} \approx 10^{-3} n_{grd}$. For the latter, it is clear that there starts to be some noticeable impact, though this is a far higher absorber density than expected. For the argon emission though, even the larger absorber density value doesn't result in any appreciable change in the profile shape.

The reconstructed profile $S(\lambda)$ itself can be expressed as:

$$S(\lambda) = \int_0^R j_{A=1}(r, \lambda) N_{G,e}(r) dr \, . \tag{4.3}$$

In this equation, Stark profiles at individual radii are given by $j_{A=1}(r, \lambda)$, with the subscript $A = 1$ simply to note that the area under the profile is normalized to 1. The overall normalization factor is given by $N_{G,e}(r)$, with the subscripts to declare that it includes both geometric and emission normalization factors. Explicitly then, this normalization factor is

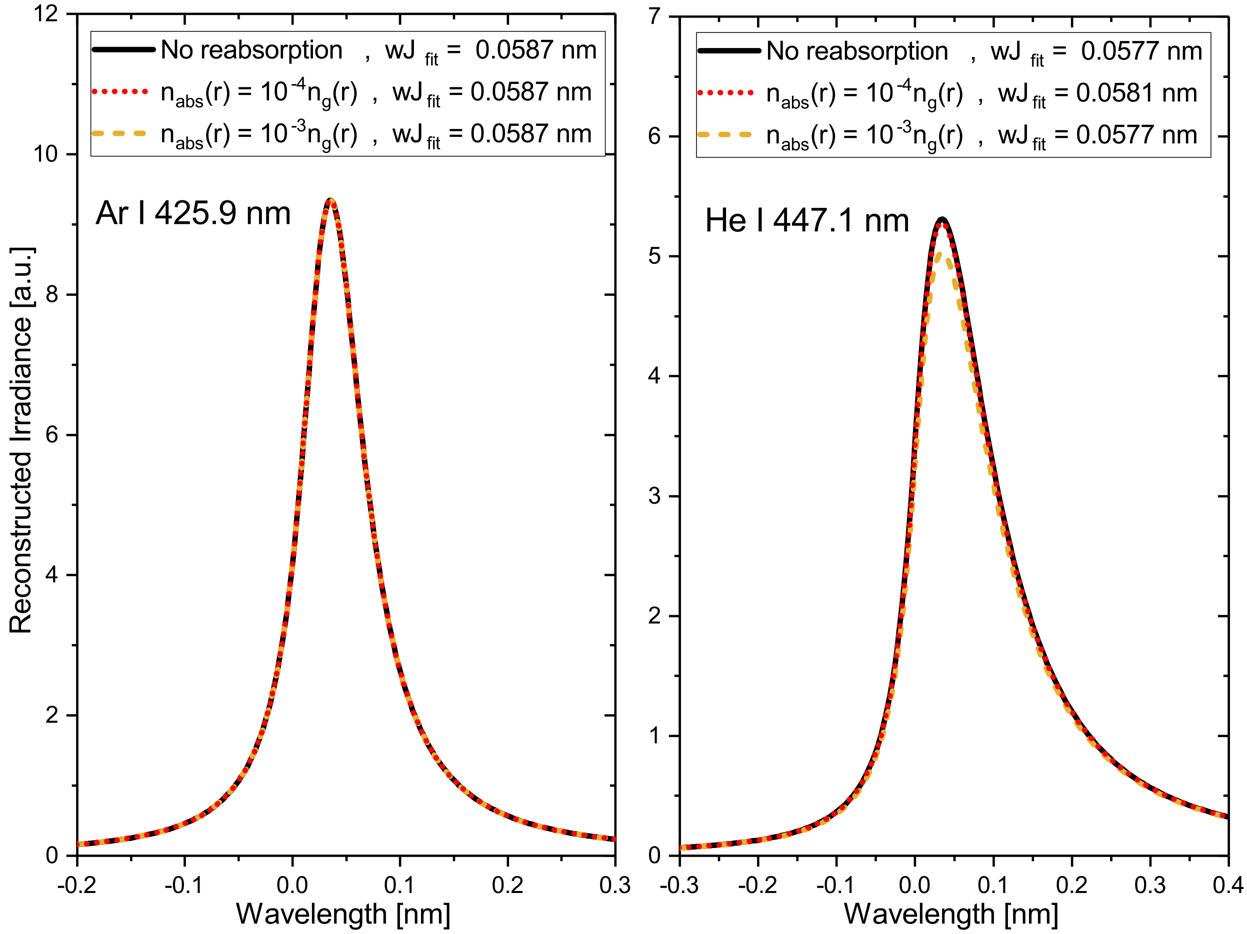

Figure 4.6: Reconstructed Stark profiles without any reabsorption as well as with, at two different absorber densities. This is for a 6x6mm PW, GCS at 200 torr and 120 A for both gases, at the axial location corresponding to P6/6.

given by:

$$N_{G,e}(r) = CdV(r)e(r)\,, \tag{4.4}$$

where C is chosen such that the greatest value of $N_{G,e}(r) = 1$. Now with the use of Eq. (4.3) we can obtain a reconstructed Stark profile from the entirety of PLASIMO's radial values of electron density, which we can then perform a Stark-profile fit to and obtain an effective electron density. At last, this electron density we obtain from the fit of a total reconstruction of an emission profile is the electron density that can be compared with measurement. For

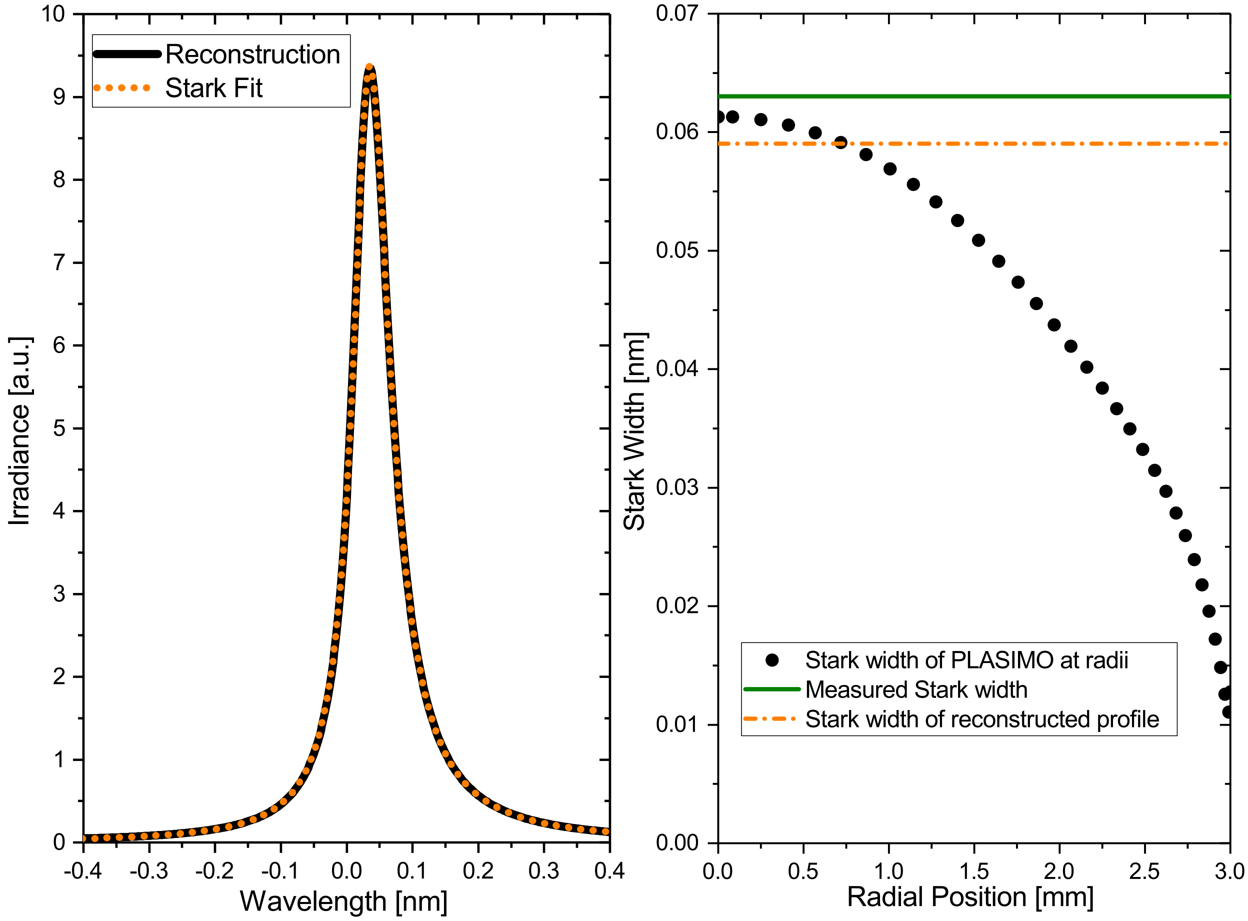

Figure 4.7: Left: The overall reconstructed profile and corresponding Stark fit using PLASIMO radial electron densities for an argon 6x6mm PW, GCS at 200 torr and 120 A, at the axial location corresponding to P6/6. Right: Comparison of various Stark widths. Black points are PLASIMO modeled values at radial values inside arc channel. The green solid line represents the Stark width measured during PW operation, and the orange dot-dashed line represents the Stark width of the fit to the PLASIMO overall reconstructed profile.

the same test case as above, an argon 6x6mm PW, GCS at 200 torr and 120 A, at the axial location corresponding to P6/6, the results are shown in Fig. 4.7.

This figure illustrates PLASIMO's modeled Stark width w_j as a function of radius r, as well as w_j determined from the fit to the overall reconstructed Stark profile, and the physically measured w_j value for the same operating condition of 200 torr and 120 A. These latter two are denoted in the figure as lines but it should be mentioned that the interpretation is simply that it's the value corresponding to the entire line of sight and does NOT mean these are values that are constant across the arc channel's radius. Analogous results for helium 6x6mm PW, GCS at 200 torr and 120 A, at the axial location corresponding to P6/6 are shown in Fig. 4.8.

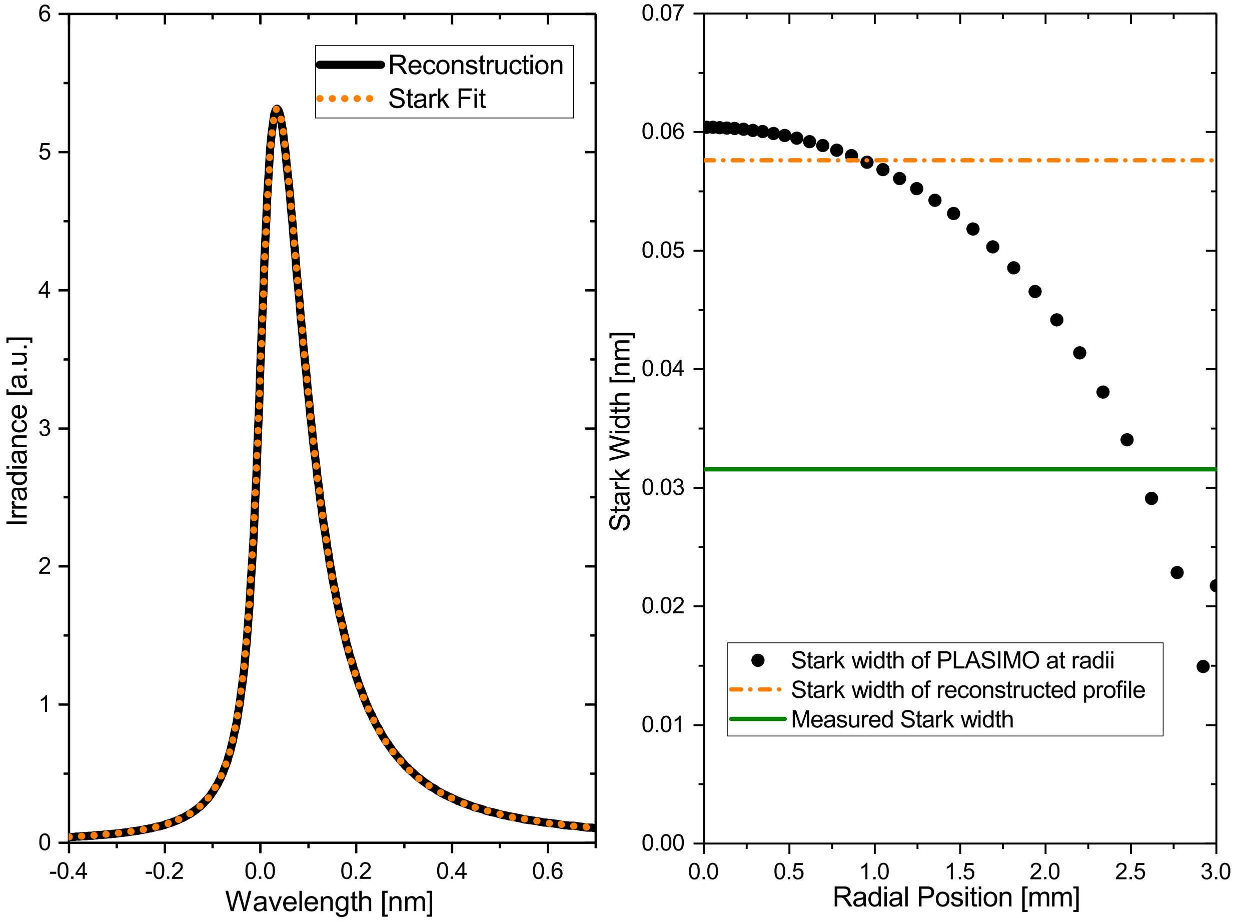

Figure 4.8: Left: The overall reconstructed profile and corresponding Stark fit using PLASIMO radial electron densities for a helium 6x6mm PW, GCS at 200 torr and 120 A, at the axial location corresponding to P6/6. Right: Comparison of various Stark widths. Black points are PLASIMO modeled values at radial values inside arc channel. The green solid line represents the Stark width measured during PW operation, and the orange dot-dashed line represents the Stark width of the fit to the PLASIMO overall reconstructed profile.

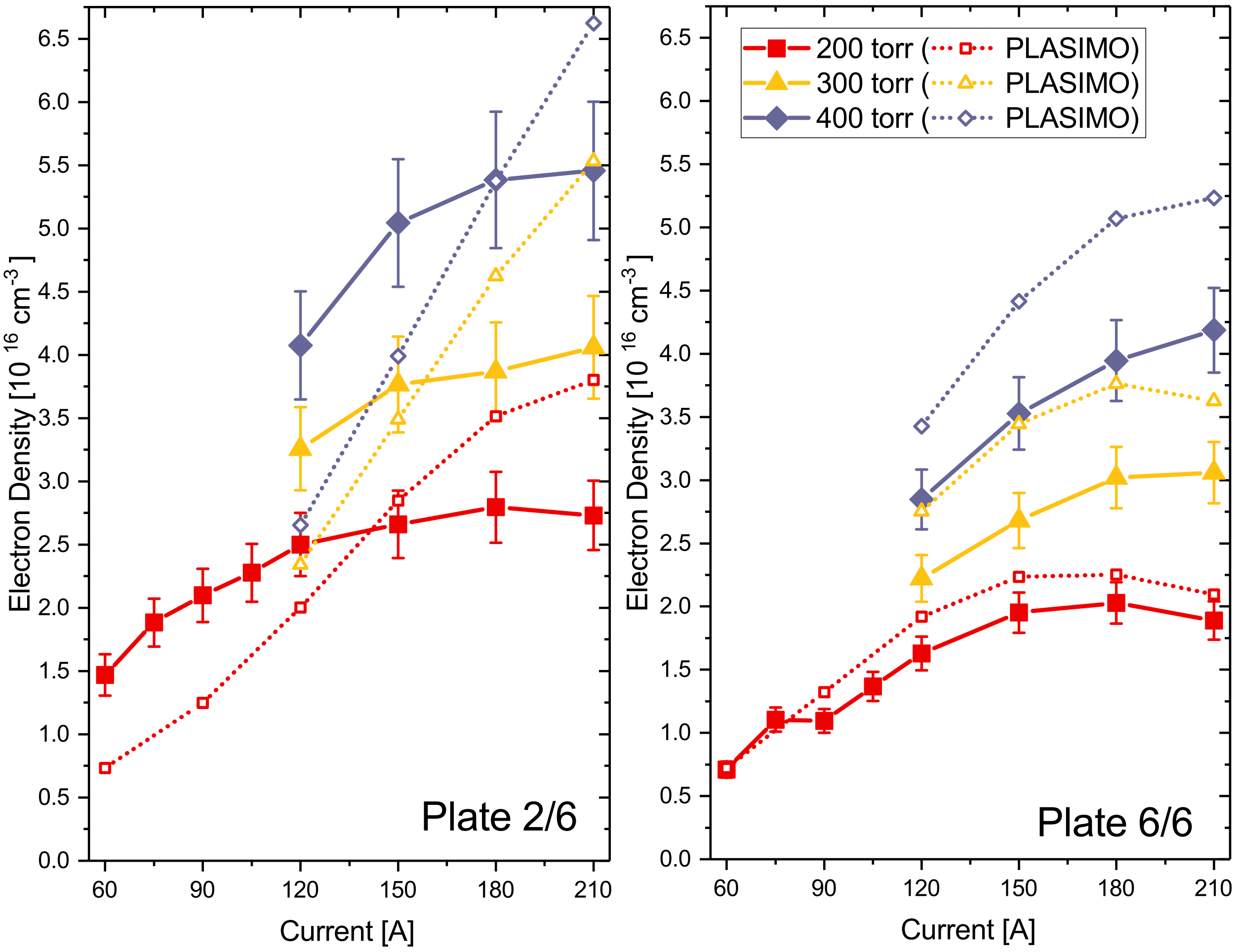

Figure 4.9: Electron densities in argon arc at two axial locations along the 6x6mm PW channel. The data set at left is taken at plate 2/6 and the data set at right is at plate 6/6. Comparisons with corresponding PLASIMO model electron densities at those axial locations are shown also obtained by a Stark fit to an overall reconstructed Stark profile.

4.2.2 Electron Density

Certain electron density trend behaviors are expected. We expect that increasing arc current will produce an increase in electron density due to a greater amount of electrons being expelled from the cathodes. As these electrons each contribute to ionization of the background gas particles, this increased electron density from the cathodes propagates down the entire length of the channel. Increasing GCS pressure would also contribute an increase in electron density, as the collision rate of the electrons and neutrals-to-be-ionized increases as a result

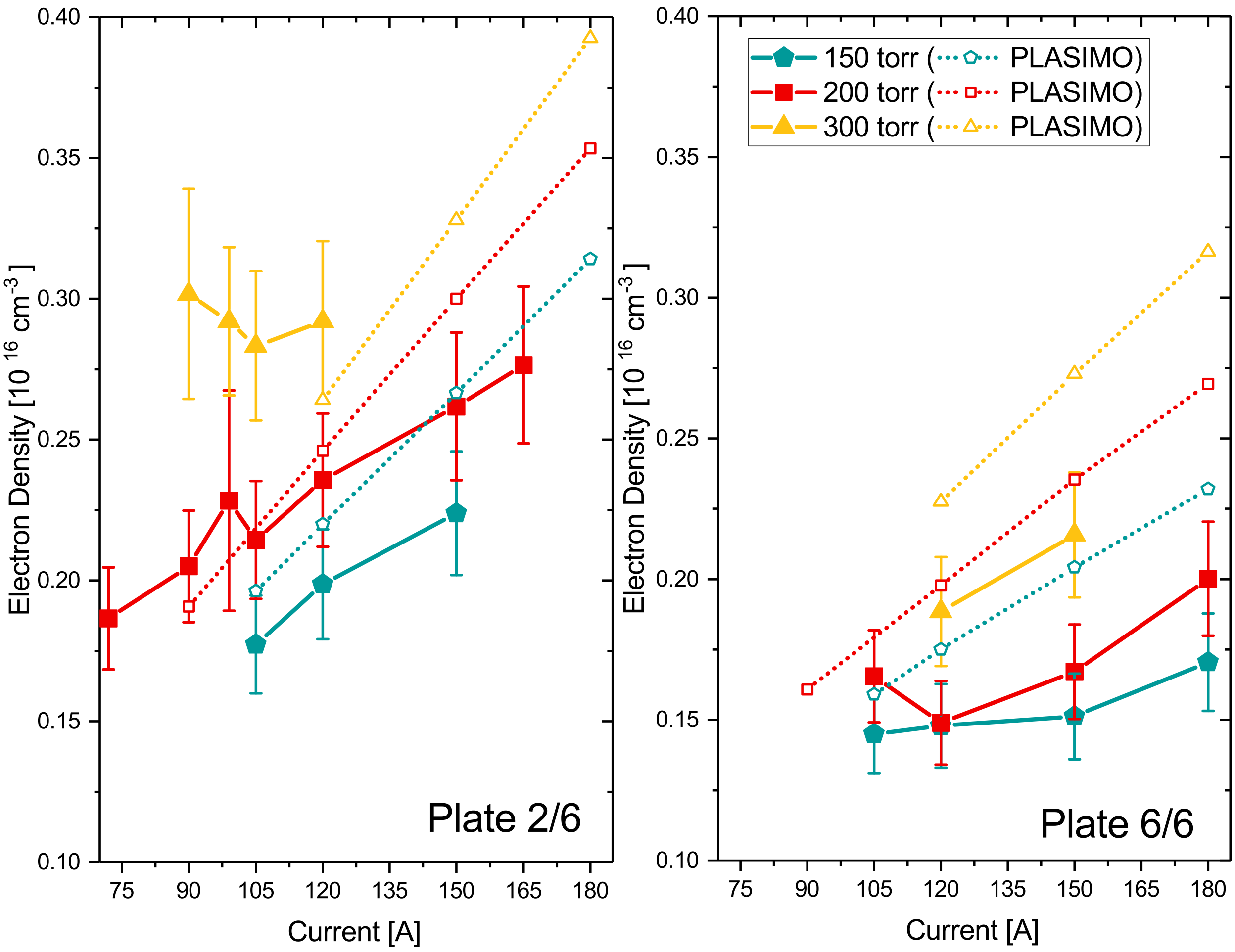

Figure 4.10: Similar to Fig. 4.9 but for helium. Electron densities in helium arc at two axial locations along the 6x6mm PW channel. The data set at left is taken at plate 2/6 and the data set at right is at plate 6/6. PLASIMO comparison data also shown.

of increased presence of neutrals, the ionization rate which is proportional to the neutral density is increased. Electron density as determined by Stark broadening (see Section 2.2.2) is calculated at diagnostic plate locations along the plasma window's length, as discussed in Section 2.1. Results of these calculations at two such locations - P2/6 and P6/6 - in a 6x6mm PW are shown in Fig. 4.9 for argon arc and Fig. 4.10 for helium arc. Since the electrons are the particles which are primarily responsible for heating the gas, the electron density dictates the rate of this heating. Additionally, the electron density is used in determining ionization degree as in Eq (3.19), as well as the mass flow relationship, described in Section

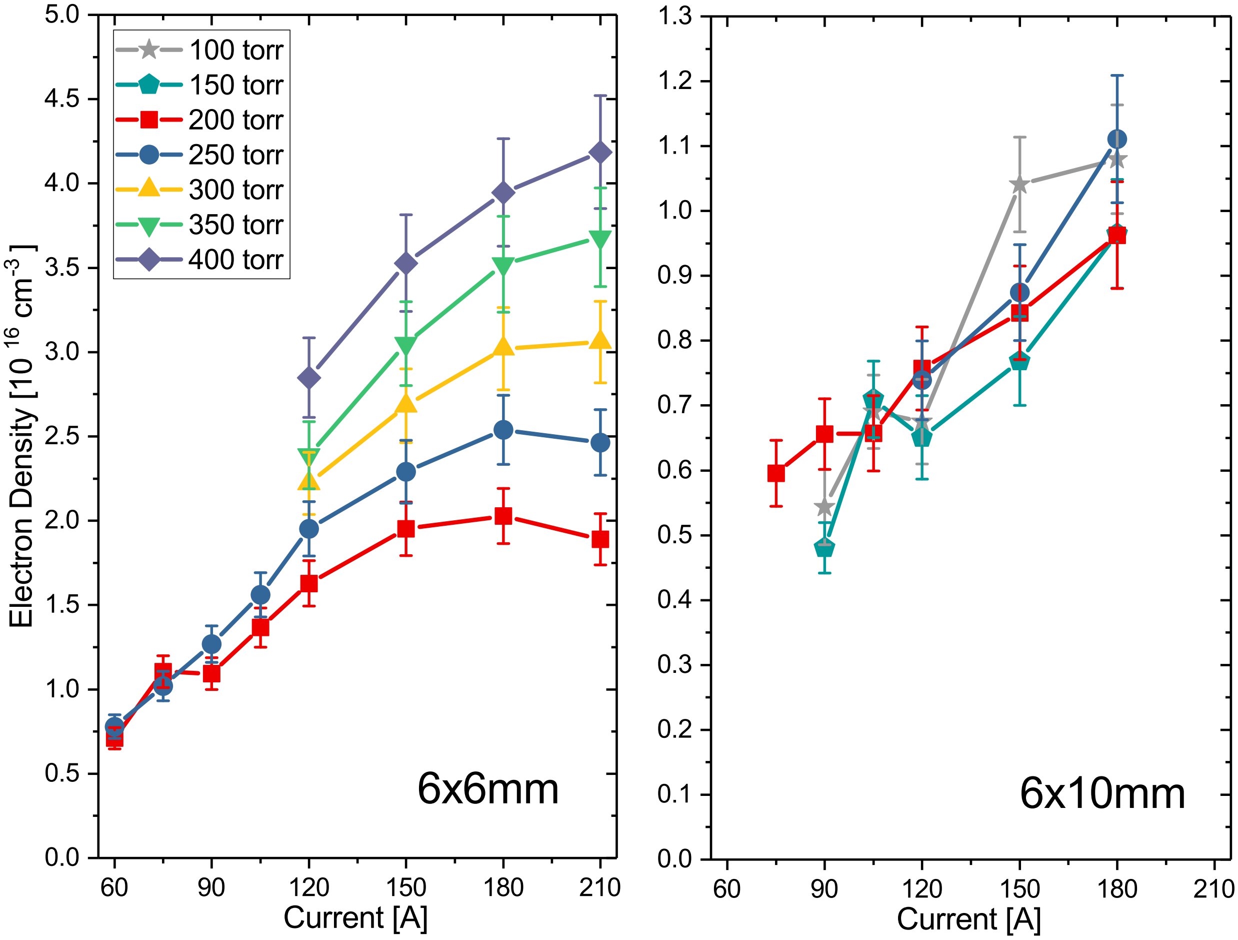

Figure 4.11: Electron density in argon PW for two different configurations, a 6x6mm (left) and 6x10mm (right). In both cases the electron densities are for P6/6.

3.3.

It is evident that the predicted behaviors mentioned in the preceding paragraph are borne out in the empirical results of Figs. 4.9 and 4.10, though n_e in the helium arc seems to have less dependence on the arc settings than in the case of argon. Furthermore, as a result of having both a higher ionization energy and lower ionization cross section (from ground state), helium's electron densities are generally about an order of magnitude less than those in argon. They additionally appear to have less variability with changing operating conditions. Additionally, in Fig. 4.11, a comparison is provided for n_e measurements in argon at P6/6 for a 6x6mm PW and a 6x10mm PW. Noting the difference in scales, the electron density n_e is vastly decreased in the larger-diameter channel. This is likely the reason why the helium arc was unable to be established with any semblance of stability for this 10 mm diameter channel geometry as mentioned in Section 4.1, assuming that it too would have a significantly lower electron density than the case of 6 mm diameter channel.

4.2.3 Electron Temperature

Electron temperature T_e is another essential plasma characteristic necessary to determine, and impacts calculations of numerous other plasma properties. As with any temperature, the electron temperature characterizes the kinetic energies associated a certain distribution of electrons, and strictly speaking the manner this electon temperature is employed in this work is valid only for Maxwellian EEDFs. It is for that reason necessary to know, or at least make realistic inferences about, the shape of the EEDF. In plasmas of sufficient density, the EEDF assumes a Maxwellian distribution because the electron-electron collision frequency which acts to redistribute energy is much greater than the frequency of inelastic collisions with the heavies which otherwise deplete the high energy electrons and cause a drop off of the tail of the EEDF. A more thorough discussion to determine the extent of this effect is presented in Section 3.1, the result being that it's very likely the EEDF is well-approximated by a Maxwellian shape.

The procedure used to determine electron temperature in argon is the creation of a Boltzmann line from spectroscopically collected relative emission intensities (see Section 2.2.3), whereas for helium, the relative emission intensities must be compared with results of a collisional-radiative model (see Section 3.2). As mentioned previously, the emissions observed at diagnostic plate locations are taken over a central chord of the channel's cross sectional area. Similar to the case of calculating n_e, it is assumed that the calculated T_e is the central, on-axis value due to most of the emitted photons originating from the innermost 1 mm of the arc as seen in Fig. 4.4.

Measured electron temperature for argon in a 6x6mm PW are presented in Fig 4.12, at locations P2/6 and P6/6. These results suggest that between these locations, the electron temperature through the discharge channel doesn't appear to change drastically, but generally does show a gradual increase from the cathode to anode side. Additionally, electron temperatures in lower pressure environments tend to be greater than those in higher pressures. This net result of a slight increase in electron temperature with distance down the channel is also seen in PLASIMO model results, as well as previous publications [41, 117].

The Boltzmann plot method is again applied for helium arc using emission lines indicated in Table 2.4. However, as explained in Section 2.2.3, this time the temperature obtained as the excitation temperature T_{exc} is unlikely to be equatable to the electron temperature T_e. The excitation temperatures are generally too small to really correspond to the electron temperature, being in the area of 0.5 eV. It is expected that the electron temperature is significantly higher than this, which motivates the need to utilize an additional tool, a collisional-radiative model. The model used in this work (HeCRM), originally crafted by T. Fujimoto [15] and later revisited and updated by M. Goto [14], as discussed in Section 3.2. Also in that section, the process for obtaining a synthetic spectra using the HeCRM is outlined, and relies on determining which set of measured emissions is close enough in their relative intensities to the set of synthethesized emissions, which are generated at a series of test electron temperatures T_t, selecting that temperature which best reproduces the measured relative intensities as the electron temperature T_e. Results of both excitation temperature T_{exc} from Boltzmann plot method and T_e determined using the HeCRM are

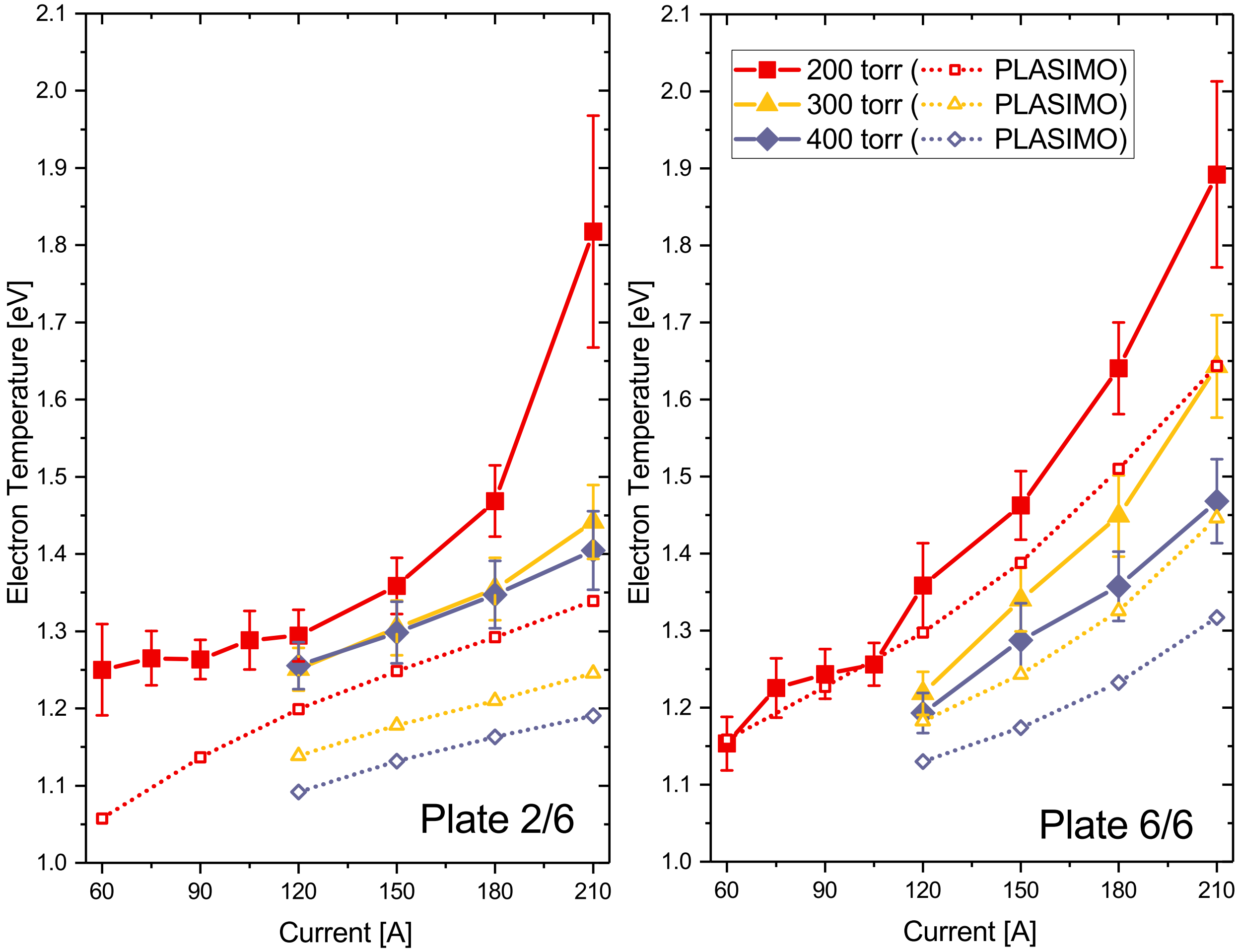

Figure 4.12: Electron temperature at plate 2/6 and plate 6/6 as determined by Boltzmann line method with Ar II lines in a 6x6mm argon PW. Dotted lines and open points show the result from PLASIMO model corresponding operating conditions. The model values have been integrated over the channel radius at the relevant axial location.

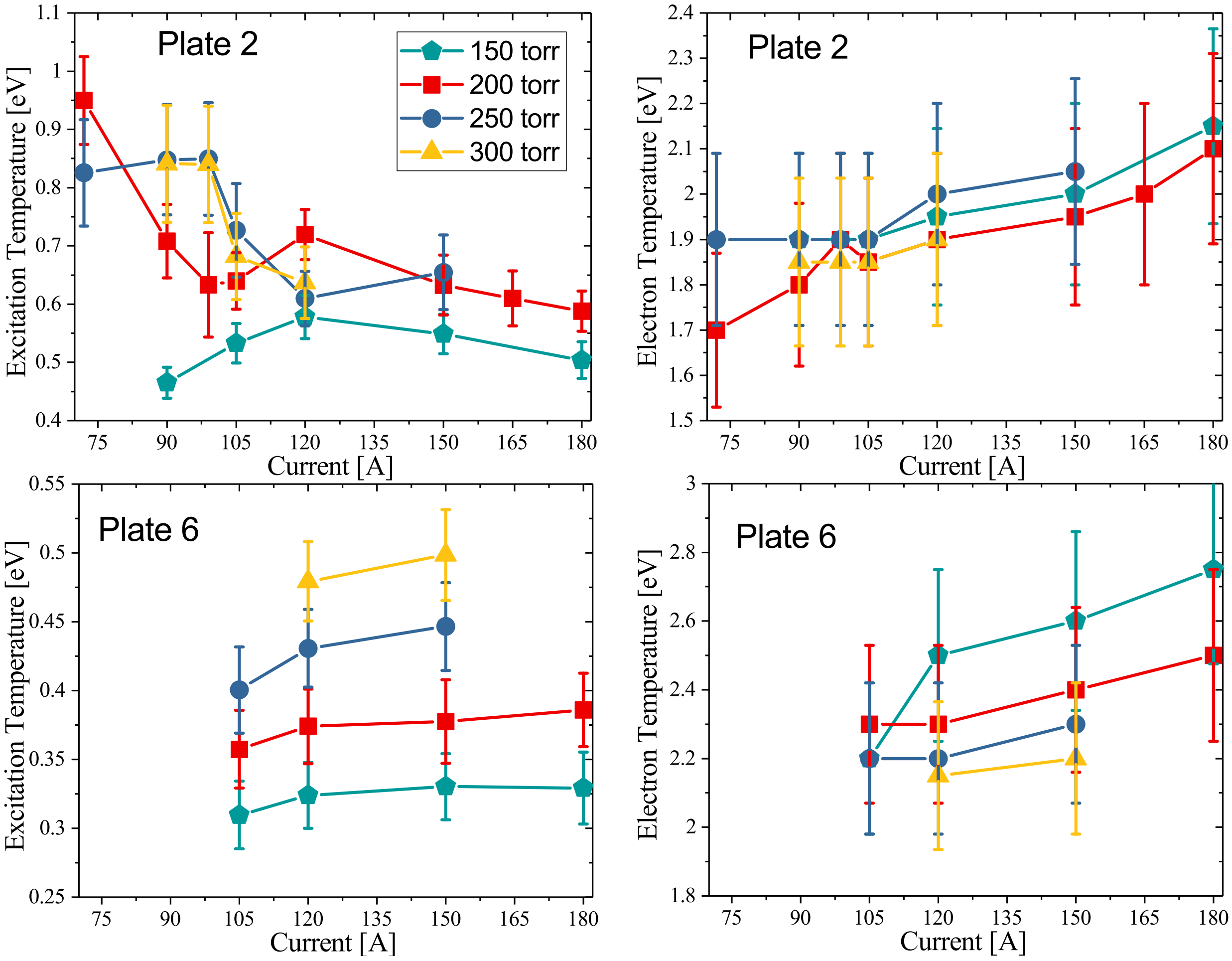

Figure 4.13: Measured excitation temperature T_{exc} from Boltzmann line method (left), and electron temperature T_e from comparison of measured relative intensities to those calculated using HeCRM. The top two plots pertain to plate 2/6 and the bottom two pertain to plate 6/6. Note the difference in scales of the y-axes.

shown in Fig. 4.13. As with Fig. 4.12 for argon, these helium results pertain to a 6x6mm PW at diagnostic plate locations of P2/6 and P6/6. An interesting feature here is that it appears that excitation temperature T_{exc} largely behaves oppositely than does the electron temperature T_e, with respect to GCS pressure and arc current.

These same electron temperature T_e results are also shown in Fig. 4.14 along with the corresponding PLASIMO modeled values. Here it is clear that the trends mentioned regarding T_e in argon from Fig. 4.12 are also evident here: T_e increases at higher arc currents and decreases at higher GCS pressures, and T_e increases somewhat between P2/6 and P6/6.

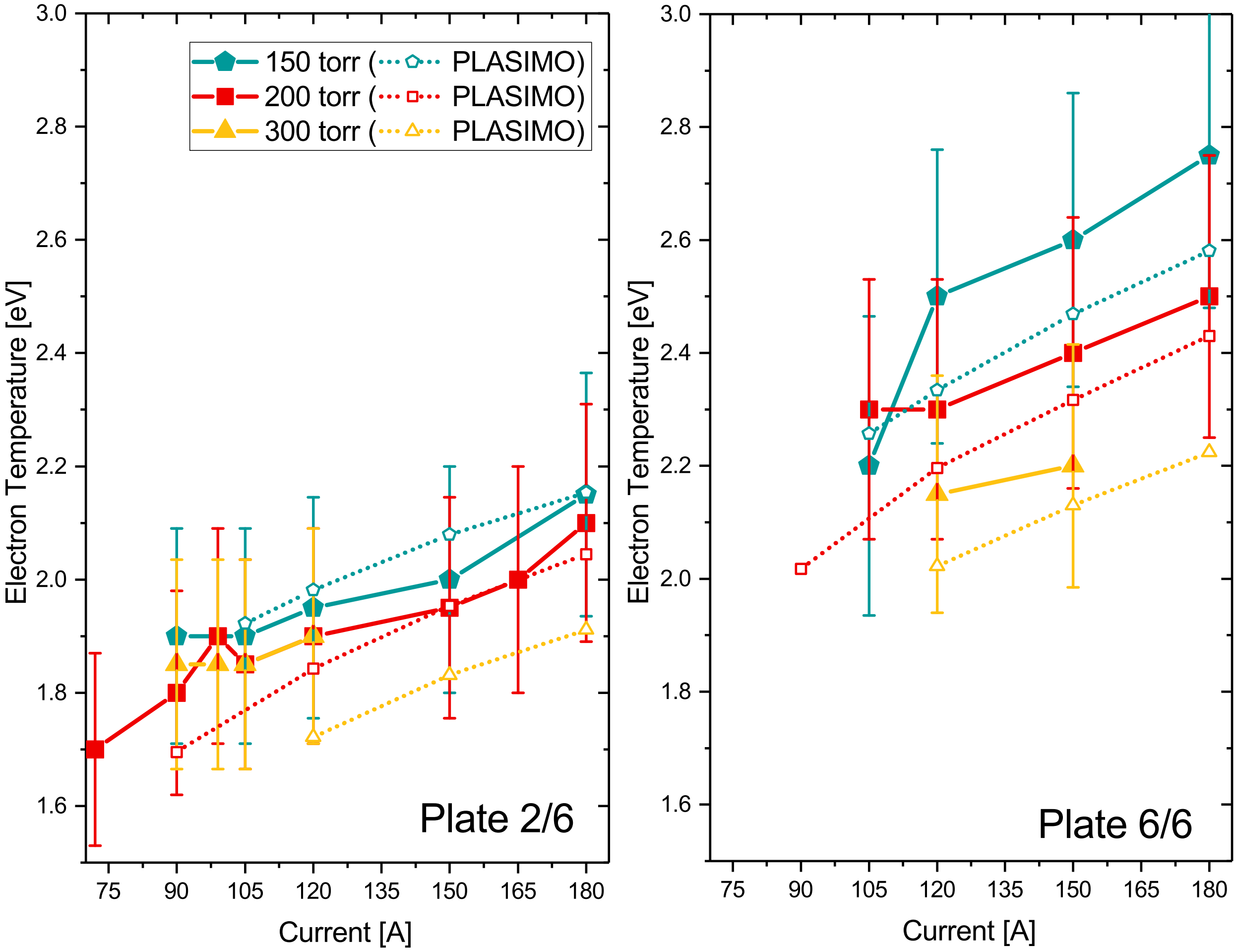

Figure 4.14: Electron temperature at plate 2/6 and plate 6/6 as determined by Boltzmann line method with He I lines in a 6x6mm helium PW. The collisional-radiative model [14, 15] in conjunction with measured electron densities from Fig. 4.10 to determine these electron temperatures. Dotted lines and open points show the result from PLASIMO model corresponding operating conditions. The model values have been integrated over the channel radius at the relevant axial location.

4.2.4 Electric Field and DC Conductivity

Another plasma property that plays an essential role in influencing the dynamics is the axial electric field, which is related to the electron energy gain and therefore the degree of heating

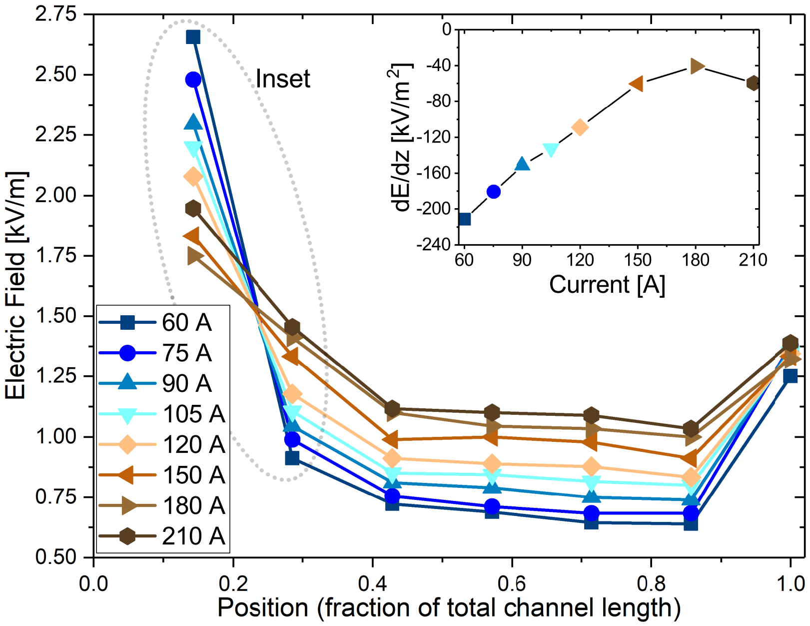

Figure 4.15: Electric field in argon 6x6mm PW with GCS pressure 200 torr, calculated from floating plate voltages. The inset is the derivative of this electric field with respect to axial position.

and ionization for the heavies. In Section 2.1.3.3, it was explained how the axial electric field E is obtained using the floating voltages of the metal plates enclosing the plasma. Note that the field is calculated from the difference of voltage between plates, so axial values for the field are set as the midpoint between the plates. This field provides a means of continually replenishing electron energy following inelastic collisions with the heavy particles, which deplete the electron kinetic energy. Figure 4.15 shows these electric field measurements in a 6x6mm configuration in argon of GCS pressure 200 torr as a function of the axial position, given here as a fraction of the total PW length, and Fig. 4.16 shows the electric field with the same conditions except in helium. In both gases the central region of the PW (corresponding to fractional position of about 0.4 to 0.85 in the figure), with starting point is defined as between plates 2 and 3, and ending point defined as between penultimate and ultimate pre-anode plates, conveys an electric field that is relatively constant over the region. This inner

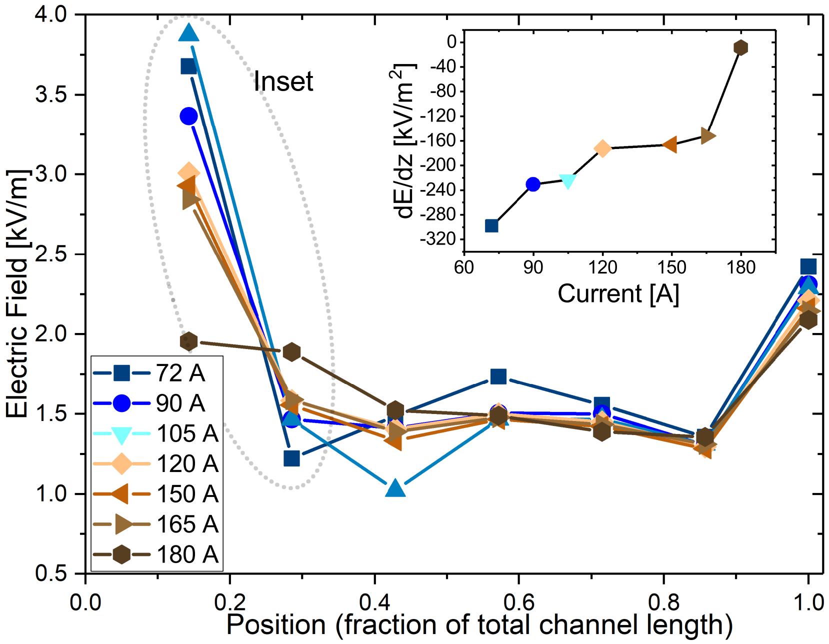

Figure 4.16: Similar to Fig. 4.15 but for helium. Electric field in helium 6x6mm PW with GCS pressure 200 torr, calculated from floating plate voltages. The inset is the derivative of this electric field with respect to axial position.

region, whose field is denoted as E_{in}, is shown in Fig. 4.17 for both gases as a function of both GCS pressure and arc current in a 6x6mm PW. As is clearly seen in this figure, helium's central electric field behavior as a function of current is different than that of argon. In the argon arc, increasing current results in an increasing E_{in}. In the helium arc however, this central region electric field is relatively unchanged with increases in current.

The axial behavior of the PW electric field is qualitatively very similar to that described in Chapter 10 of Ref. [28], including near the cathodes and anode. As seen in Figs. 4.15 and 4.16, a sharp increase in field strength is measured between the anode and the plate immediately adjacent to it. Ref. [28] outlines two possible contributions to this anode fall: one from the negative space charge in the near vicinity of the anode since ions are repelled towards the cathode, and another related to the contraction of the positive column's cross sectional area to the surface area exposed of the anode (this effect is notable if the latter is less than the former).

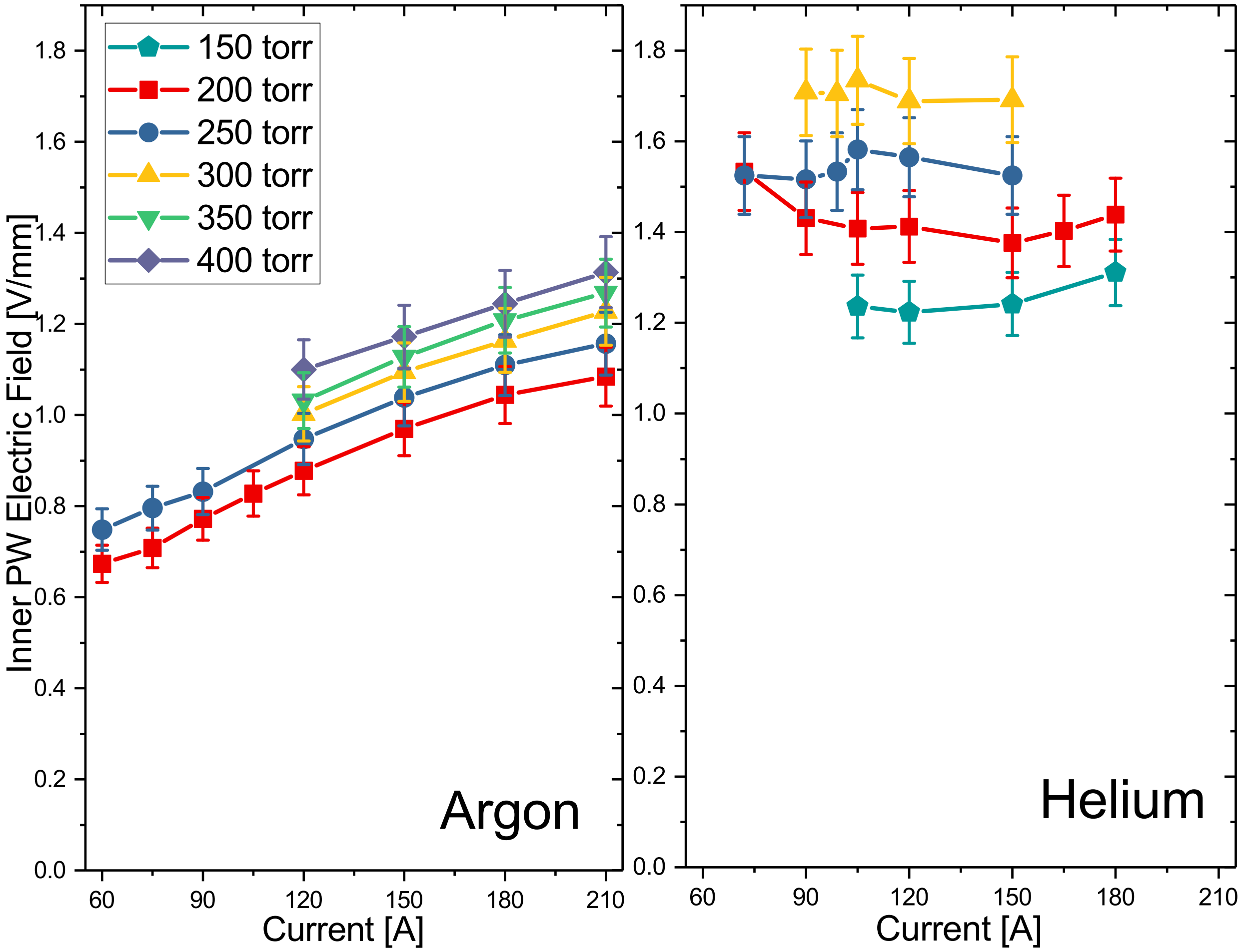

Figure 4.17: Inner electric field strengths E_{in} for arcs in 6x6mm PW at various GCS pressures and arc currents. The region's starting point is defined as between plates 2 and 3, and the ending point is defined as between penultimate and final pre-anode plate.

A sharp drop in electric field magnitude is also observed on the cathode side resulting from the cathode sheath layer formed in the cathode's nearest vicinity. This sheath is characterized by an enhanced density of positive ions which are attracted to the cathode surface's accumulation of negative charges that form the surface potential barrier [28, 124]. A striking feature of this side can be seen in the inset of these figures where the axial derivative of the electric field is plotted for the region circled in the primary figure. The field drops greatly from cathodes to the first plate (nomenclature is Cath-P1) for lower currents,

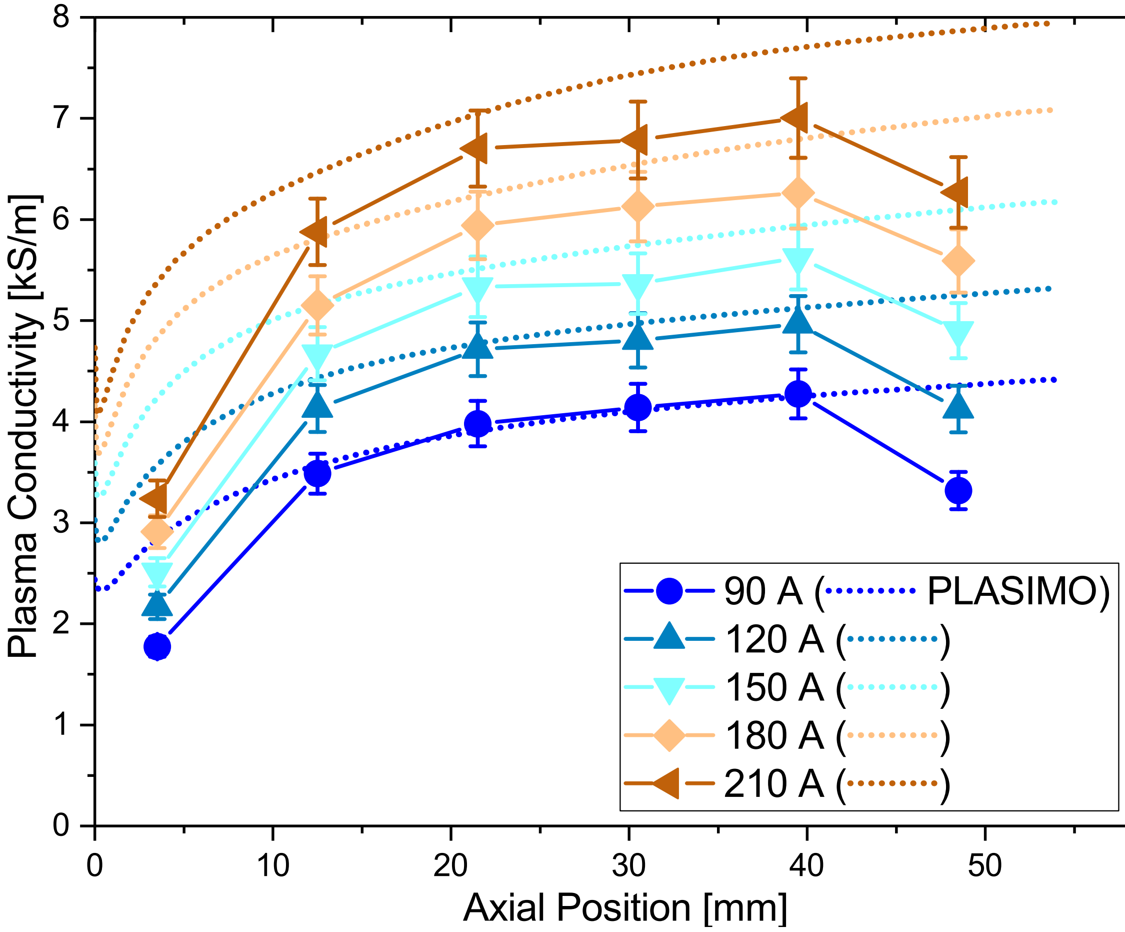

Figure 4.18: Electrical conductivity of the arc for several currents in a 6x6mm argon PW with GCS pressure at 200 torr. PLASIMO model results are shown as well. The model values have been integrated over the channel radius at the relevant axial location.

but exhibits shallower field drops at higher currents.

This electric field can be used to determine a mean plasma conductivity over the channel all the way down its length by assuming a uniform current distribution via Eq. (3.33). This is shown in Fig. 4.18 for a 6x6mm PW in argon, GCS pressure at 200 torr, and Fig. 4.19 for a 6x6mm PW in helium, also with GCS pressure at 200 torr. Also shown is PLASIMO modeled conductivity averaged over the channel area, which generally reproduces measured behavior and magnitude in the central region, though there are deviations at the cathode and anode regions, as a result of PLASIMO not being able to treat sheath effects [111, 120].

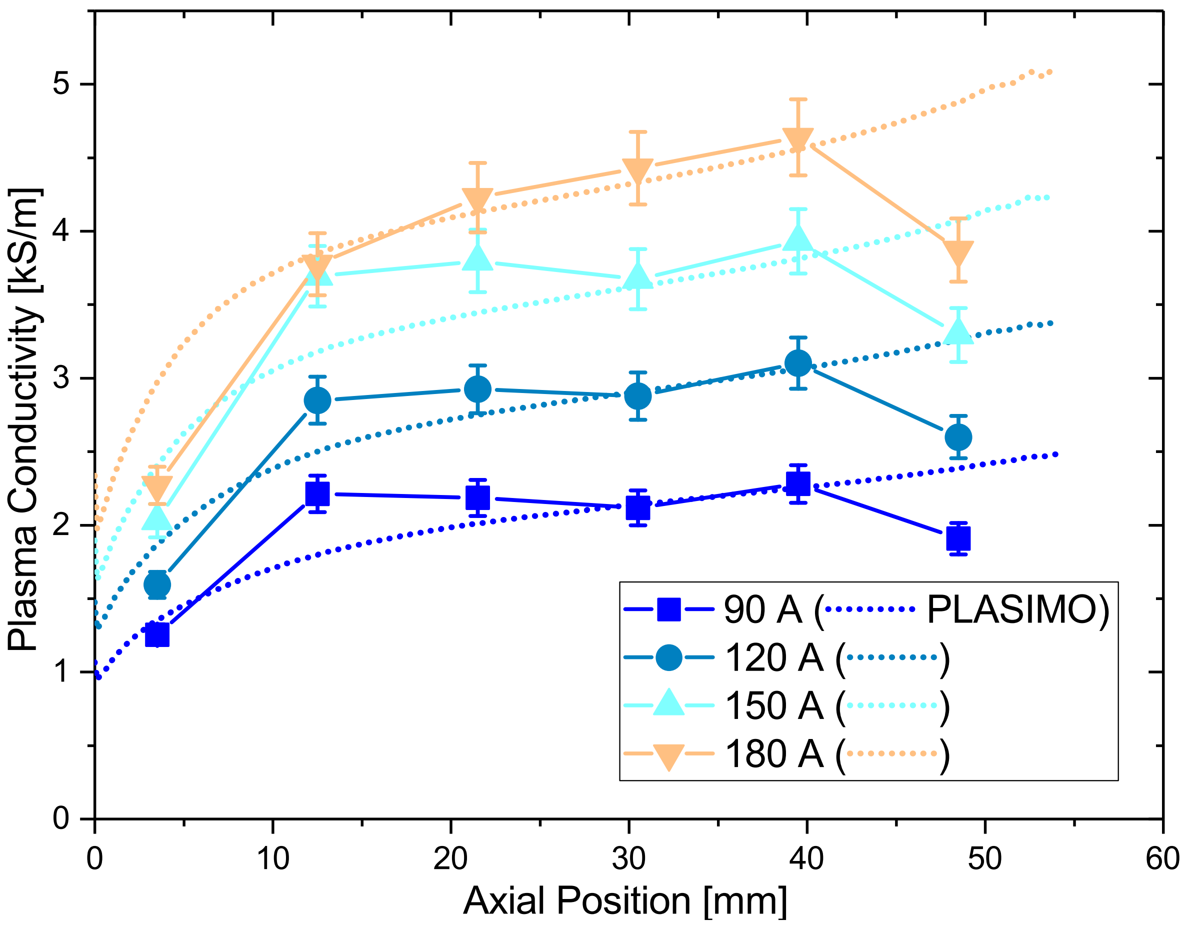

Figure 4.19: Similar to Fig. 4.18 but for helium. Electrical conductivity of the arc for several currents in a 6x6mm helium PW with GCS pressure at 200 torr. PLASIMO model results are shown as well. The model values have been integrated over the channel radius at the relevant axial location.

One distinction to note here is that the measured conductivity is obtained by assuming a uniform current distribution, whereas PLASIMO does not make this assumption and allows the current distribution to vary over the channel's cross sectional area.

It is worth pointing out that there is a degree of inherent uncertainty in the locations of calculated electric field and so plasma conductivity due to the width of the plates. From the plate structure described in Section 2.1, the metal plates are 7 mm wide and separated by 2 mm thick insulating spacers. As mentioned above, electric fields calculated from differences

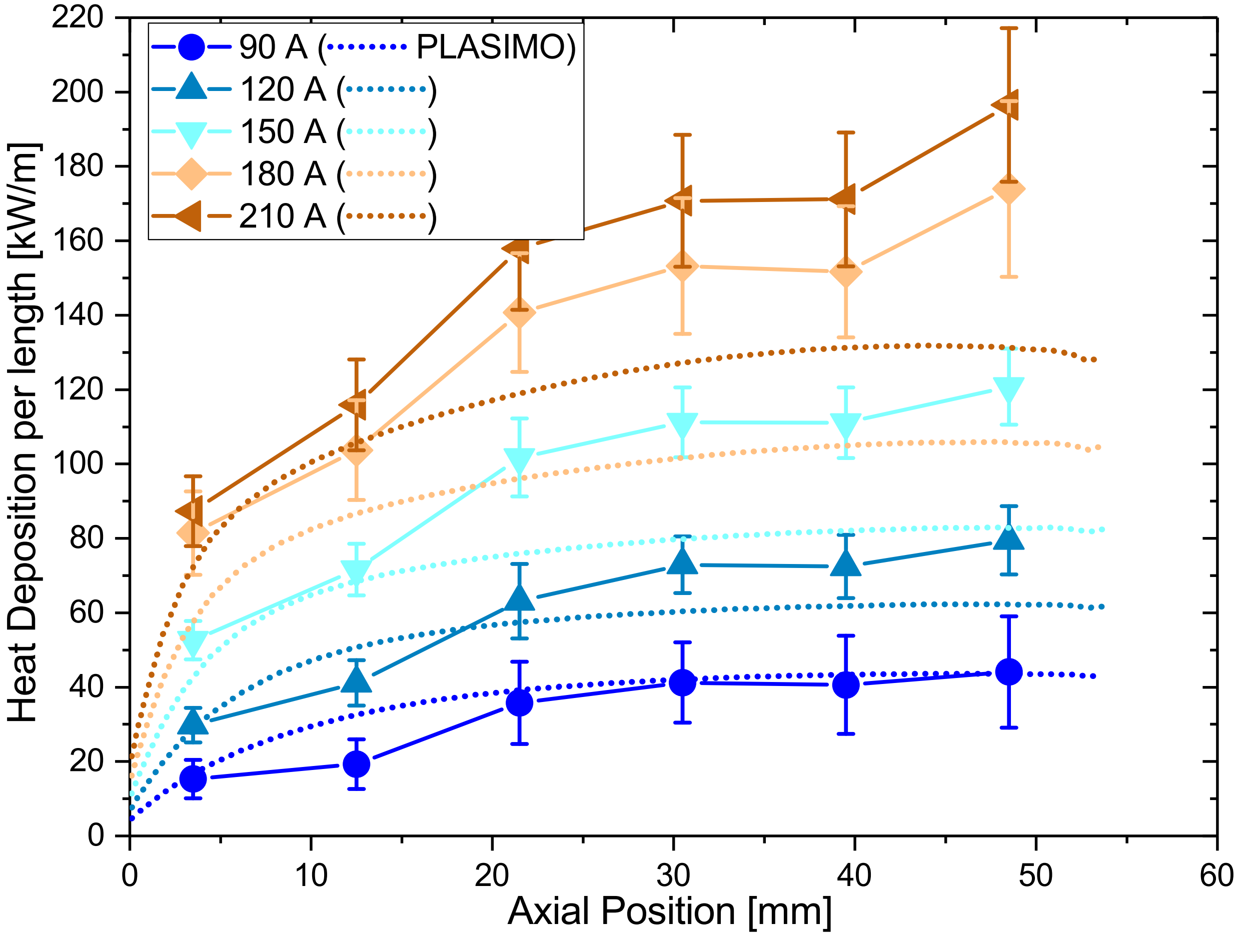

Figure 4.20: Power removed by water coolant for each PW plate in a 6x6mm configuration in argon arc. Each data set is taken at a GCS pressure of 200 torr.

in plate voltages are assumed to be the value at the midpoint between the plates (so 9 mm separations), and the electric field between cathodes and plate 1 is calculated using the distance from cathode tip to the midpoint of plate 1 (about 7.5 mm). Error bars shown in Figs. 4.18 and 4.19 are determined from a location measurement uncertainty of 0.5 mm and voltage measurement uncertainty of 0.05 V.

4.2.5 Component Heat Depositions

Another characteristic of the PW that is necessary to examine is the heat deposited by the arc into the cooled housing components. Not only will the results presented in this section hopefully assist future endeavors with cascaded arcs in adequately preparing for the heat load imposed by the arc, but they are also necessary to include phenomenologically in the 1D analysis model described in Section 3.3 for the term related to heat conduction. Since the PW is operated in a steady state condition, an equilibrium is established between the heat power from plasma to wall and the power from wall to water and is given as H_w. As described in Section 2.1.3.2, H_w is determined via calorimetric analysis of the water coolant. For each plate it is assumed that the power deposited per unit length is constant over the plate's plasma-facing wall.

The power deposited into the PW plates, H_w, is shown in Fig. 4.20 for an argon arc in a 6x6mm PW with GCS pressure at 200 torr. The corresponding plot for the helium arc of the same operating conditions is in Fig. 4.21. This makes evident an additional challenge of maintaining the helium arc as opposed to the argon one: the strain on the cooling system is considerably greater for helium of comparable operating conditions. It can be seen in both gases that there is a gradual increase in the power deposited to the plates from the cathode-side ones, moderately leveling off for the plates closer to the anode.

There is a feature of inconsistency in plate heating measurements of the diagnostic plates, which is illustrated in Fig. 4.22 An assumption for calculating the plate heat deposition is that each component connected to the same coolant manifold receives approximately the same flow rate. As explained in Section 2.1.3.2, the coolant flow rate for the entire manifold is measured. As a result, one potential reason for the behavior illustrated in Fig. 4.22 is

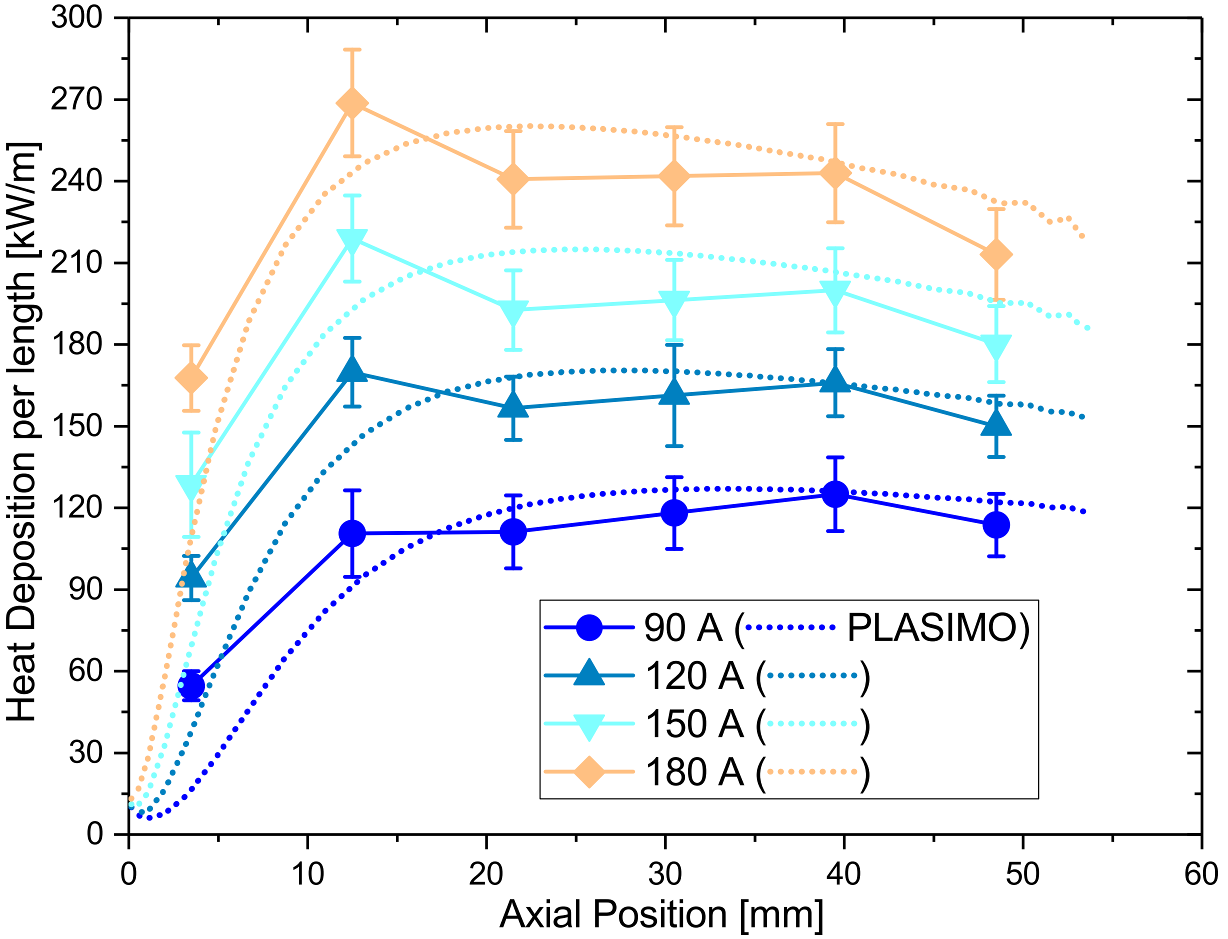

Figure 4.21: Similar to Fig. 4.20 but for helium. Power removed by water coolant for each PW plate in a 6x6mm configuration in helium arc. Each data set is taken at a GCS pressure of 200 torr.

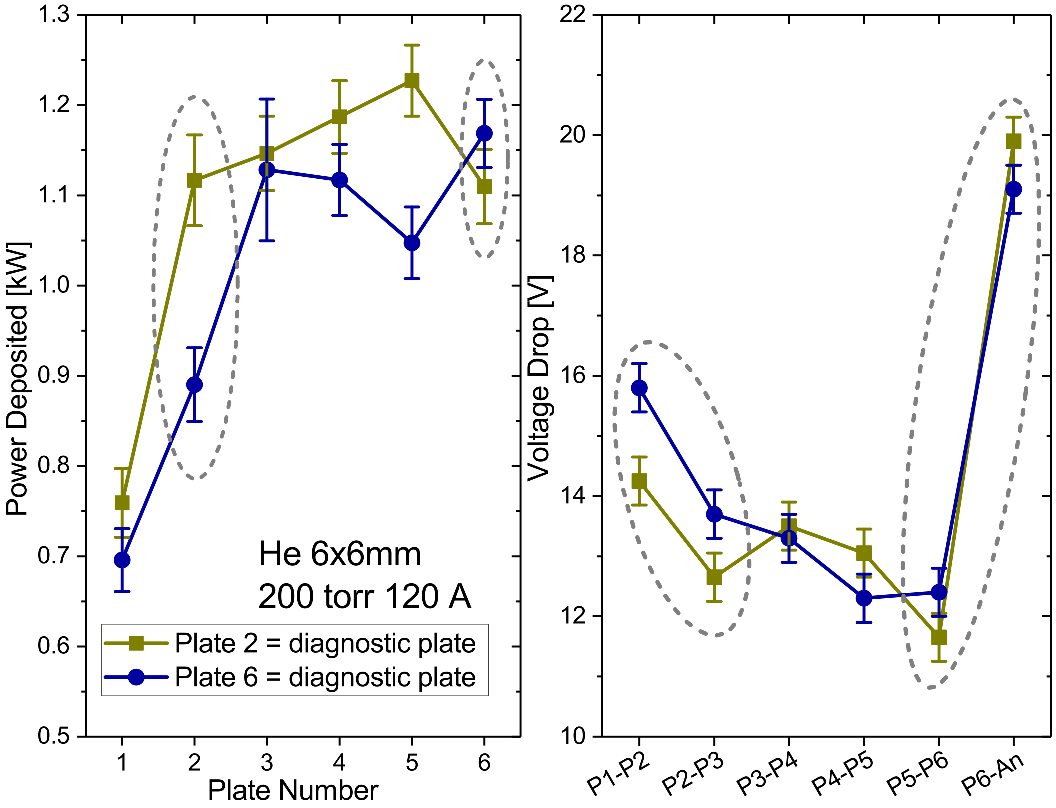

Figure 4.22: Shown are data from two separate collections from a 6x6mm PW in helium gas, one which had a single diagnostic plate at plate 2, and one which had a single diagnostic plate at plate 6. For both, GCS pressure was 200 torr and arc current was 120 A. At left is the power deposited to the plates determined by calorimetry and at right are voltage drops between adjacent plates. Circled regions highlight where behavioral differences between the two collections would be expected due to the diagnostic plate's presence or lack thereof.

that the non-diagnostic plates and the diagnostic plates may actually be receiving unequal coolant flows from the manifold.

For this particular PW system studied in this thesis, it became evident that for some operating conditions with the 8x6mm configuration, the power deposited into the anode-side plates was too great to be sufficiently cooled, and vacuum sealing failed each attempt. A system in which there is a greater number of cascaded plates could help alleviate this. There would not be a considerable change in power delivered to the arc and therefore to the wall as a whole, but with a greater quantity of plates, each one will sustain a lesser heat load.

4.2.6 Contributions to Flow Rate Reduction

As stated in the Abstract of this document, one of the principal goals of this work was to understand with greater clarity and quantitative support what specifically about the arc contributes to the flow rate reduction that it generates (see Figs. 4.1 and 4.2 for the flow reduction). As mentioned in Section 1.1, there have been suggested multiple mechanisms for the flow reduction, primarily the feature of the arc having a higher viscosity than that of the ordinary room-temperature-gas counterpart [35]. We will examine this claim by looking at the relative contribution of viscosity directly to the mass flow, where it appears in Eq. (3.26) as G, as well as indirectly by considering the effect of viscous heating of the plasma, given by the term Q_v (defined in Eq. (3.40)) described in Section 3.3. This effect of viscous heating impacts the evolution of the heavy temperature T_h which then influences the term $\sqrt{\frac{n_h^2}{n_h'}}$ in the mass flow equation Eq. (3.26).

As we see in Figs. 4.23 and 4.24, which show PLASIMO-modeled viscosity values averaged over 3/4 of the channel radius, the presence of the arc does indeed result in a greater viscosity than that of a room temperature gas. However, the expression obtained in Section

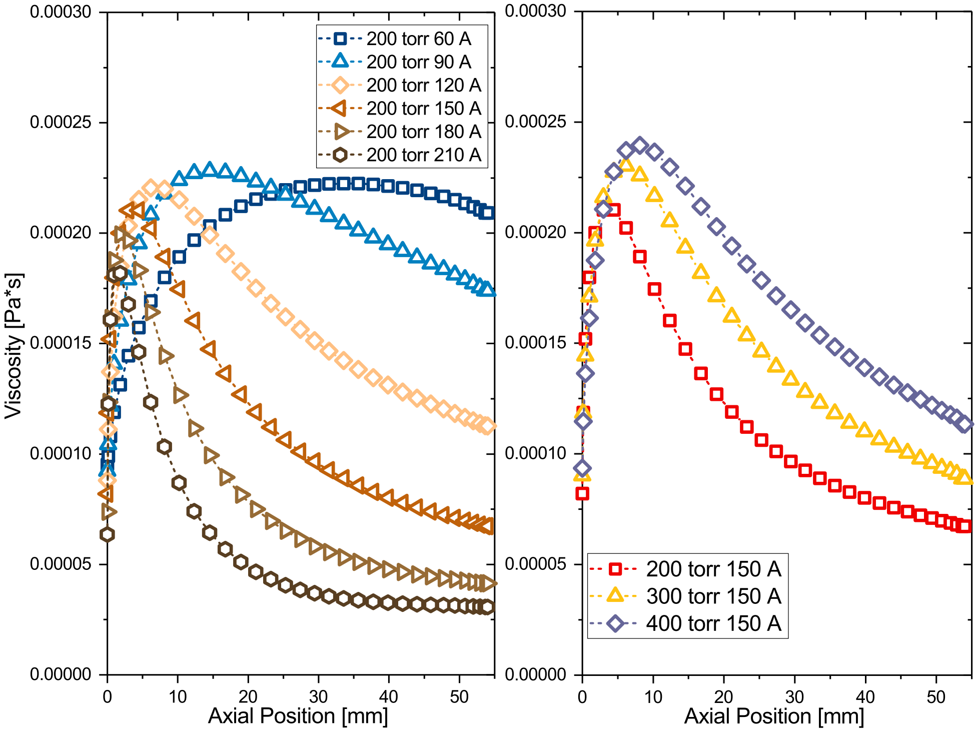

Figure 4.23: PLASIMO viscosity values for argon 6x6mm PW at axial points along arc channel. The viscosities were obtained by averaging over the inner 3/4 of the full channel radius. Left: GCS pressure at 200 torr and various currents. Right: GCS pressure at 150 A and various GCS pressures. The room temperature gas viscosity of argon is about 2.2×10^{-5} Pa*s.

3.3.1 for mass flow, Eq. (3.26), suggests that the significance of this viscosity for the mass flow depends upon the relative quantities of the viscous term G and the total plasma pressure drop term $-P_p'$ (the negative sign is included to make the term positive since P_p' itself is negative).

In Figs. 4.25 and 4.26, ratios $\frac{-P_p'}{G}$ of these two contributions to the mass flow are shown for a variety of PW conditions, using values obtained from PLASIMO models. From these, it is clear that for all conditions and at all axial points, the viscous term G is at most 20% of the pressure drop term.

It is thus clear that viscosity doesn't play a direct role in the mass flow. As a result,

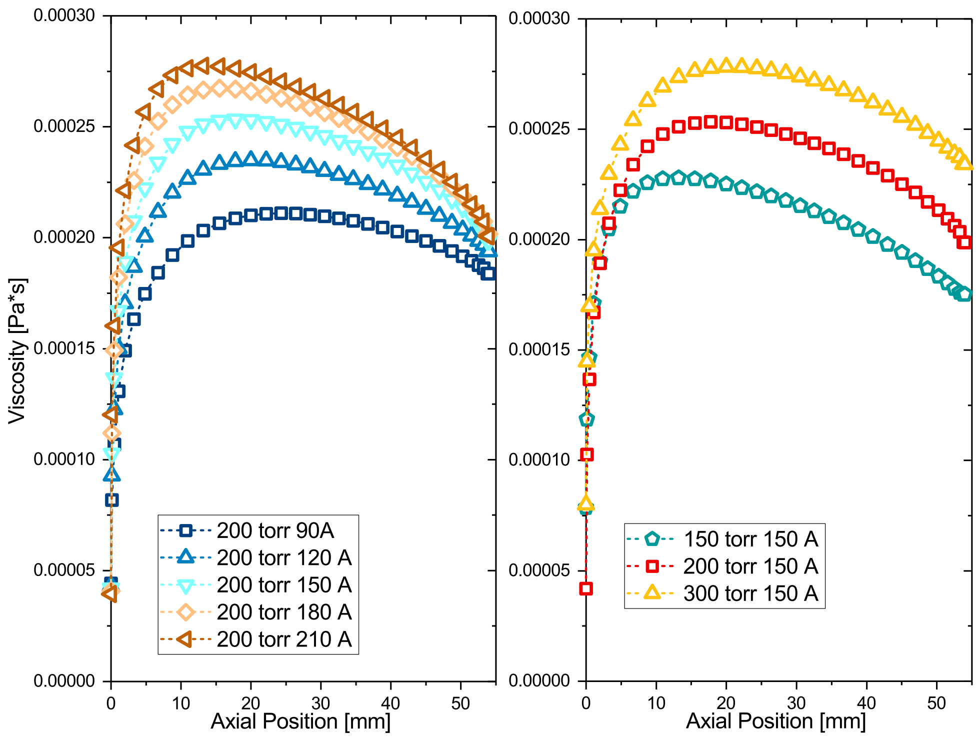

Figure 4.24: Similar to Fig. 4.23 but for helium. The room temperature gas viscosity of helium is about 2.0×10^{-5} Pa*s.

there are dominantly two factors which effect the flow rate: a density factor $\sqrt{-\frac{n_h^2}{n_h'}}$ and the pressure drop factor $\sqrt{-P_p'}$ where the negative sign is included to make the overall factors positive, since P_p' and n_h' themselves are negative. The behavior of the former, the density factor, is illustrated in Figs. 4.27 and 4.28 for argon and helium respectively. Greater values of this density factor result in greater mass flows. We can compare the behavior of this density factor with that of the aforementioned pressure drop factor $\sqrt{-P_p'}$, which is illustrated in Figs. 4.29 and 4.30. It is noted that, with a constant GCS pressure and varying arc currents, the pressure drop factor does not change significantly, contrary to the density factor which does change substantially. For a constant pressure, the heavy particle density n_h (see Eq. (3.18)) decreases as heavy temperature T_h, electron density n_e, and electron temperature T_e increase, and all three of these properties tend to increase with

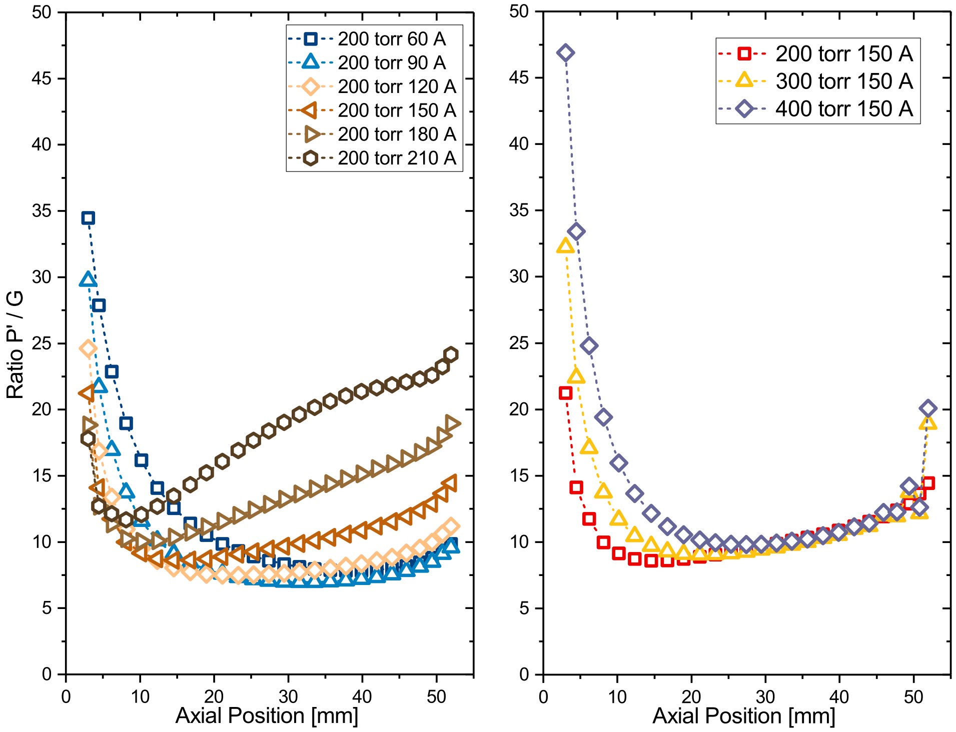

Figure 4.25: PLASIMO ionization degree values for argon 6x6mm PW at axial points along arc channel. These were obtained by averaging over the inner 3/4 of the full channel radius. Left: GCS pressure at 200 torr and various currents. Right: GCS pressure at 150 A and various GCS pressures.

arc current. Furthermore, the rate at which the heavy particle density changes down the channel, given by n_h', also increases with increasing arc current. Therefore it is concluded that it is primarily this density factor $\sqrt{-\frac{n_h^2}{n_h'}}$ which contributes to the mass flow reduction in the PW.

Though it was previously established that viscosity does not appreciably impact the mass flow in a direct manner, it can still indirectly influence the density factor $\sqrt{\frac{n_h^2}{n_h'}}$ explained above. As suggested earlier, to complete the conclusion that viscous effects are not playing a substantial role in the mass flow, we must look at the relative impact of viscous heating relative to other heating mechanisms. The mechanism which heats the heavy particles in the plasma are collisions with electrons, so we can compare this heating term defined by S_e

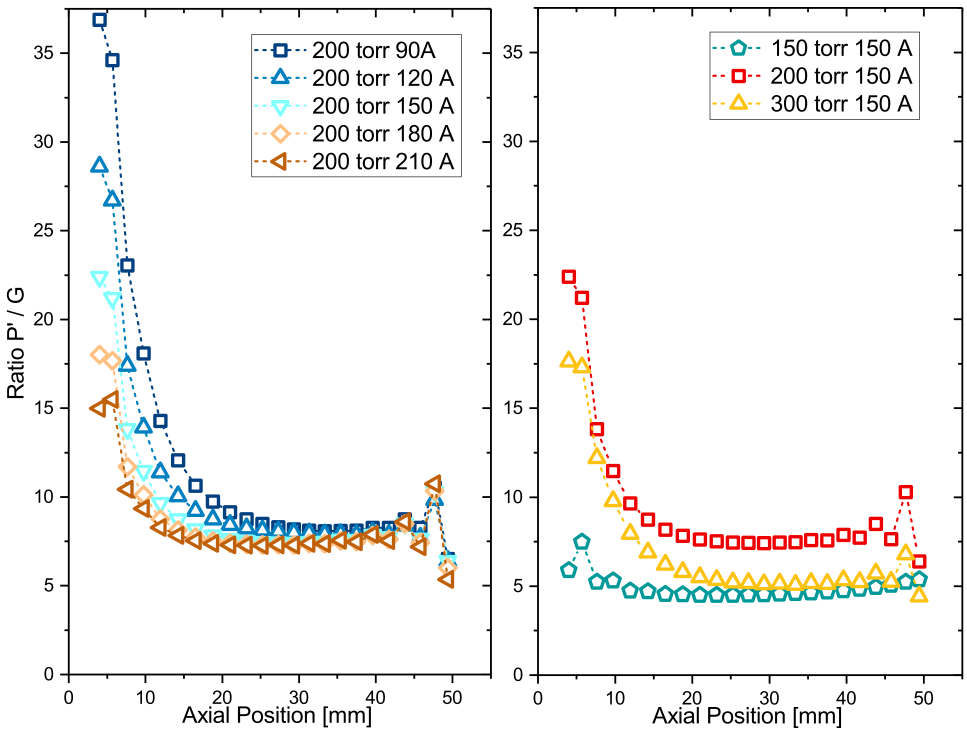

Figure 4.26: Similar to Fig. 4.25 but for helium.

in Eq. (3.30) to the viscous heating term defined by Q_v in Eq. (3.40). These two terms appear in the heavy particle energy balance equation Eq. (3.29). Ratios of these two terms $\left(\frac{S_e}{Q_v}\right)$ are shown in Figs. 4.31 and 4.32 for argon and helium respectively. These results are once again from PLASIMO model calculations corresponding to a 6x6mm PW at various operating conditions. These plots show that the electron heating term S_e is everywhere and for all conditions greater than the viscous heating term by at least an order of magnitude. Thus it has been shown that in these conditions, viscosity does not play a significant role in establishing the mass flow through the PW.

Concluding the comparisons in the single-radius systems between measurement and PLASIMO model will be the flow rate. For the 6x6mm PW this can be seen in Fig. 3.10, for both argon and helium at a variety of GCS pressures (different color/shape combinations in the plot) and arc currents. In argon it can be seen that the modeled flow rate is

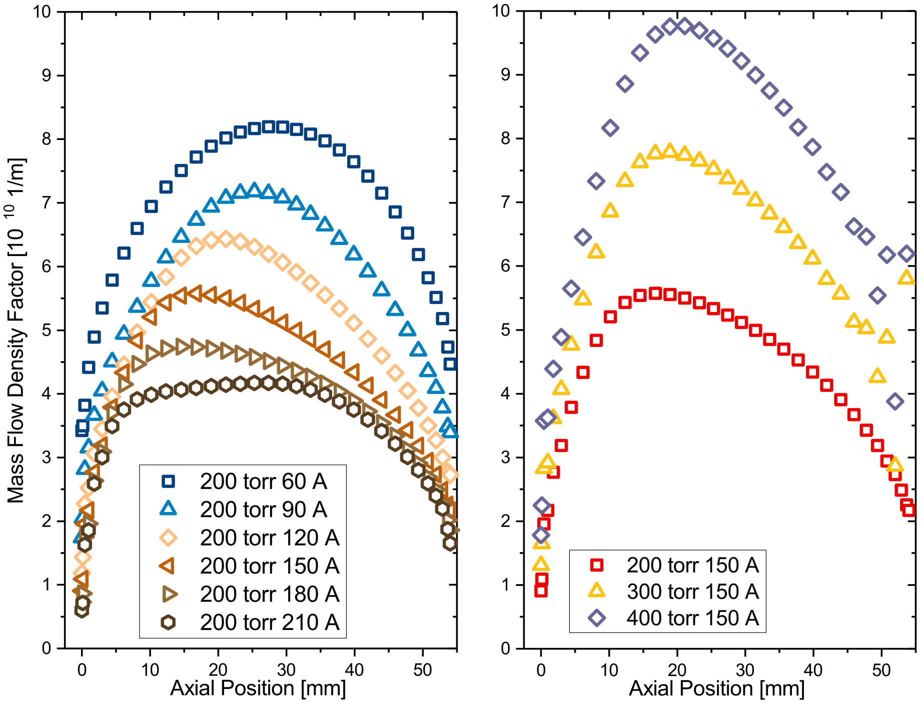

Figure 4.27: The density factor $\sqrt{\frac{n_h^2}{n_h'}}$ in argon plasma, determined via PLASIMO models of various operating conditions in a 6x6mm PW.

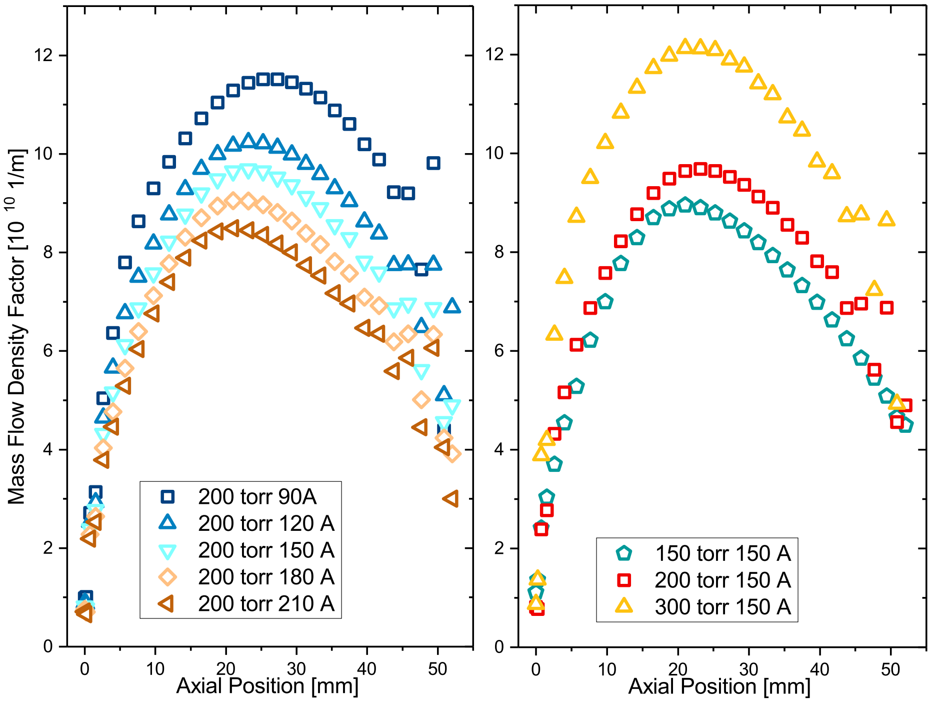

Figure 4.28: Similar to Fig. 4.27 but for helium.

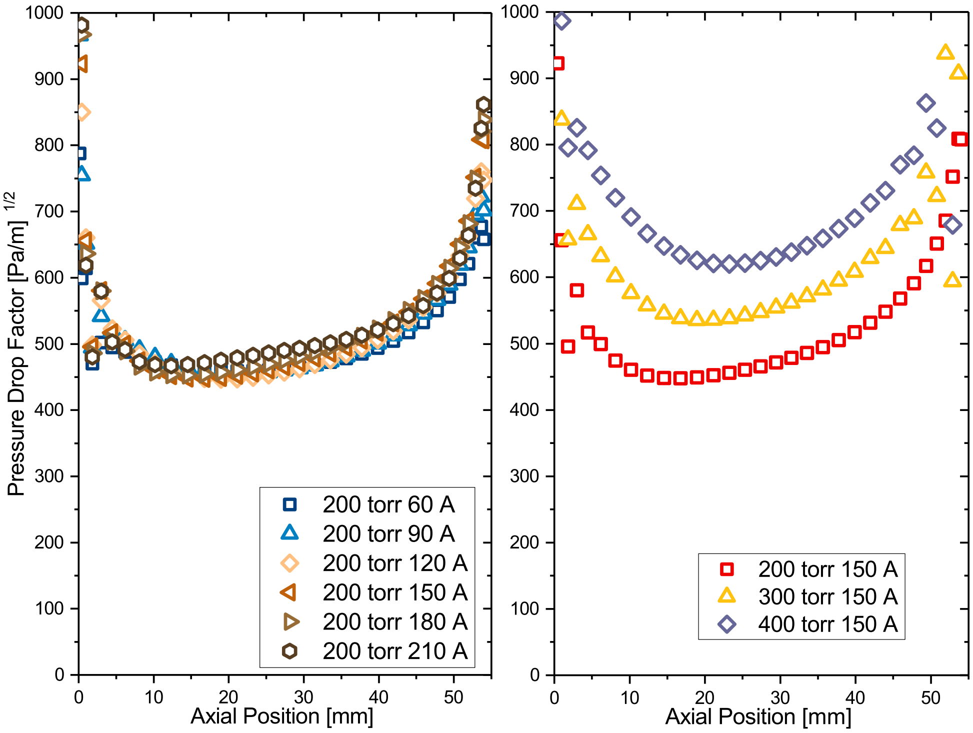

Figure 4.29: The pressure drop factor $\sqrt{-P_p'}$ in argon plasma, determined via PLASIMO model of various operating conditions in a 6x6mm PW.

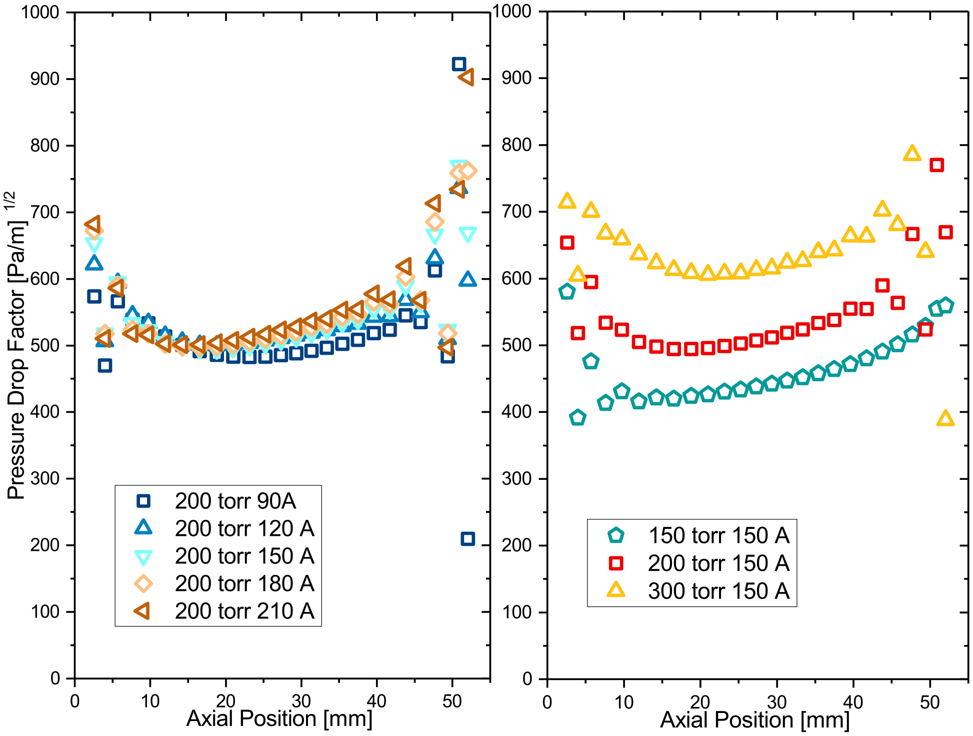

Figure 4.30: Similar to Fig. 4.29 but for helium.

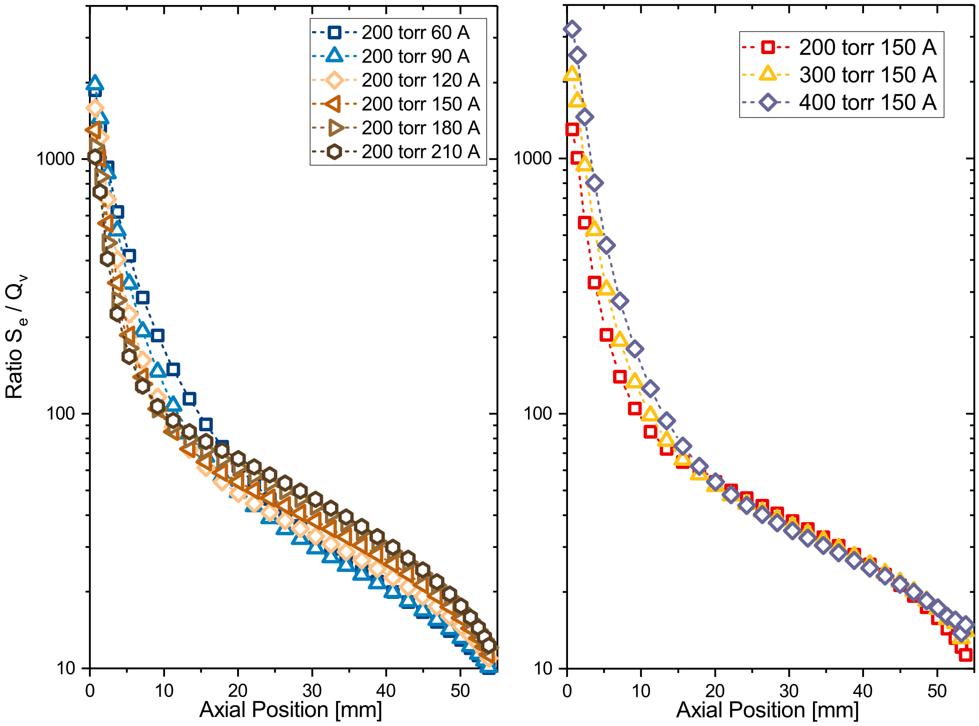

Figure 4.31: Ratio of electron collisional heating and viscous heating of the heavy particles for a variety of PLASIMO modeled conditions.

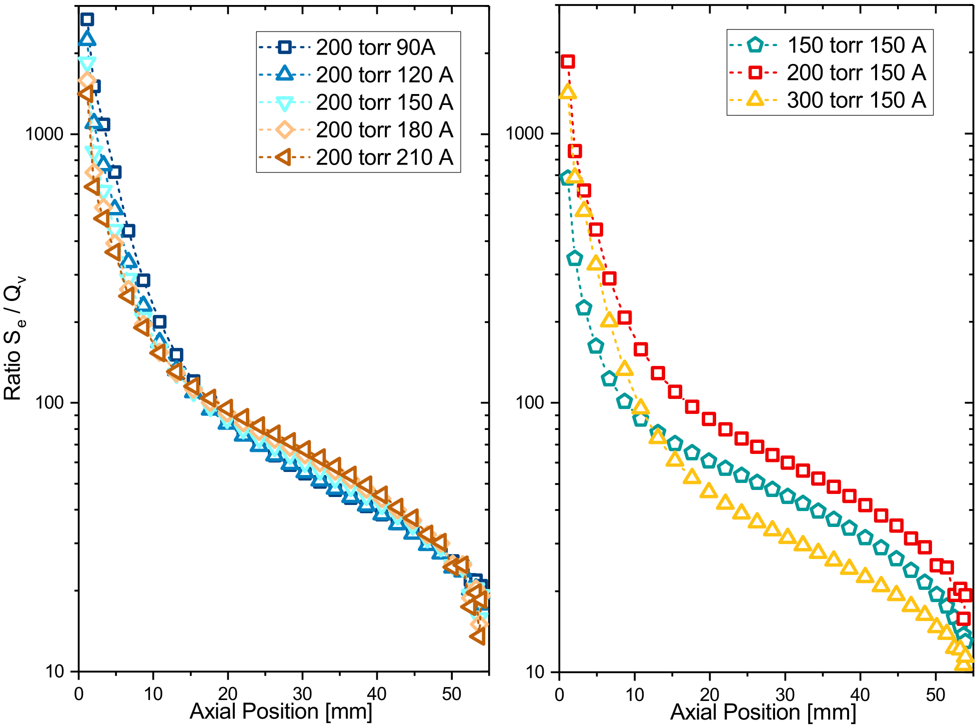

Figure 4.32: Similar to Fig. 4.32 but for helium.

slightly greater than the measured values, while the opposite is evident in helium. However it should be noted that the behavior with respect to GCS pressure and arc current is generally well-reproduced by the PLASIMO model.

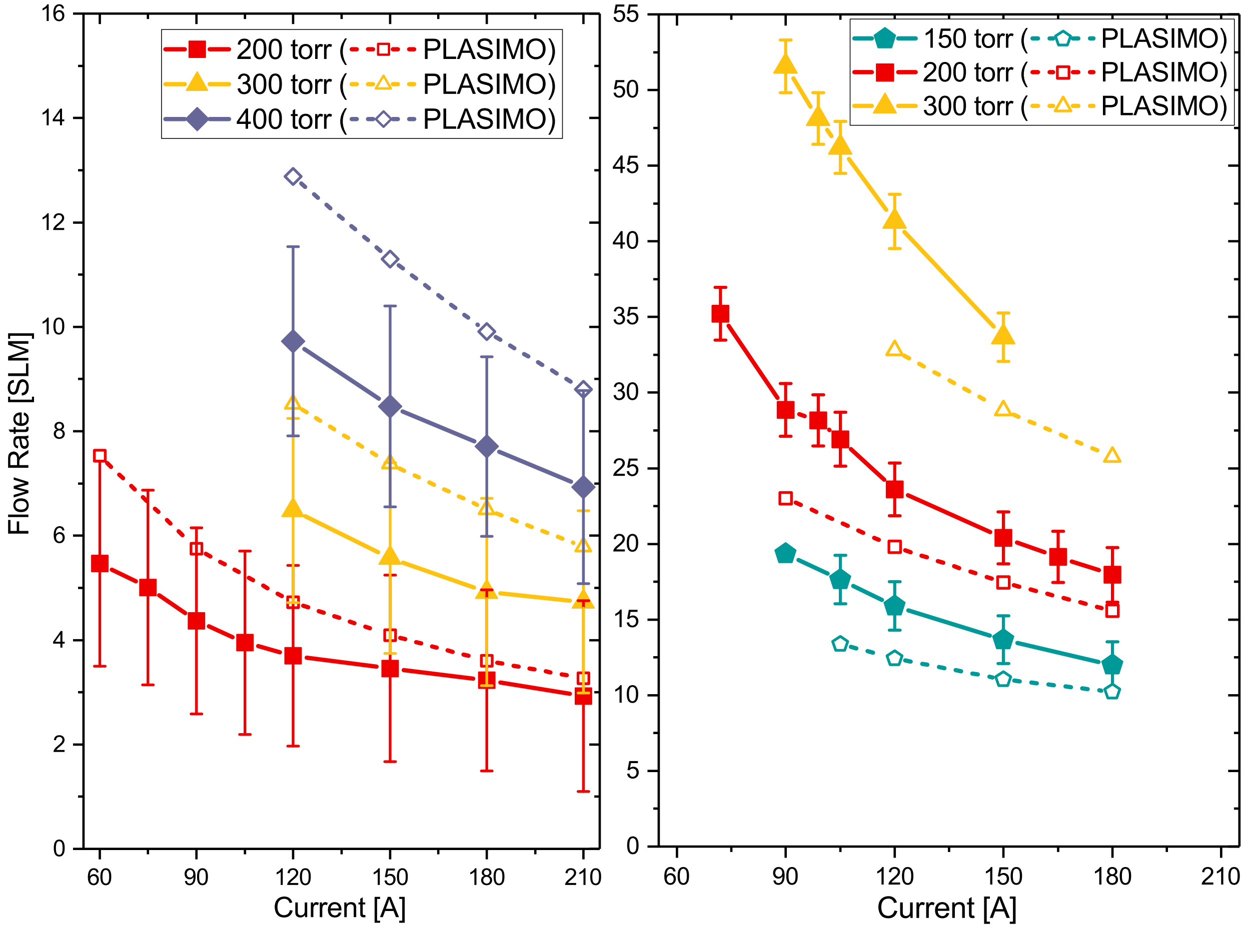

Figure 4.33: Flow rates in the 6x6mm PW configuration for both argon (left) and helium (right). Both measurements (solid points) and corresponding PLASIMO model values (open points) are shown. The different colors represent different GCS pressure settings.

Flow rates in both a 6x6mm PW and a 8x6mm PW are shown in Fig. 4.34, and the corresponding FRF values for these same configurations are shown in Fig. 4.35. Some of these behaviors were seen previously in Fig. 4.1 but are examined for multiple different GCS pressures here. In these figures, it can be seen that there is very little change in flow rate in argon increasing PW length from 6 plates to 8 plates, and in fact the FRF is slightly lower the 8x6mm configuration because the no-arc flow decreases when increasing the PW length from 6 plates to 8 plates. In helium, however, there appears to be a slight increase in FRF when the PW length is increased because, contrary to the behavior in argon, the flow rate through the PW arc does decrease modestly when PW length increases from 6 to 8 plates.

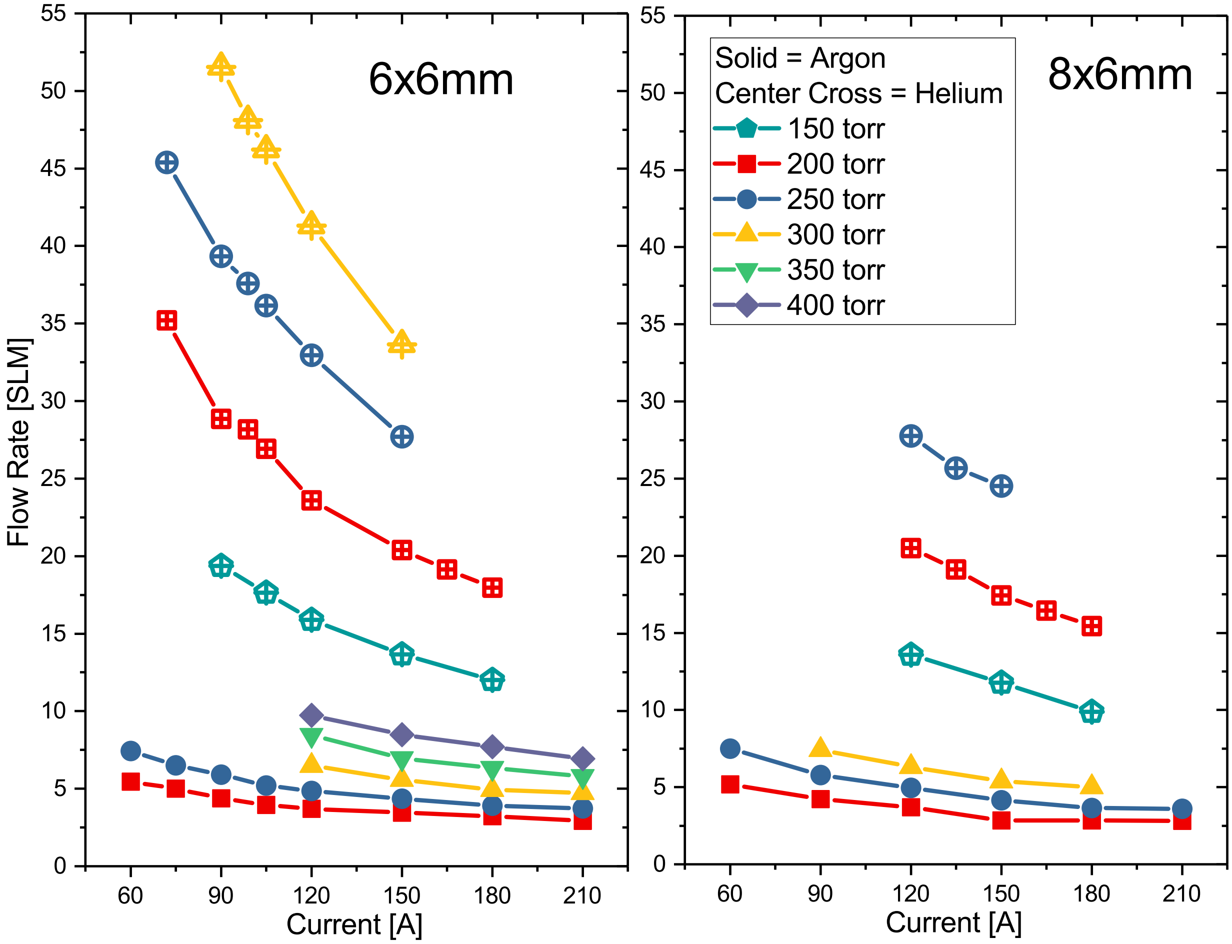

Figure 4.34: Flow rate in a 6x6mm PW and 8x6mm PW at various GCS pressures and arc currents in both argon and helium.

An alternative view of the FRF in Fig. 4.36 provides additional interesting information. In this figure, FRF is plotted against what is called the retained arc power, which is the difference of total arc power (calculated by taking the product of arc current and PW voltage drop) and the total power cooled in all PW plates (determine via calorimetric analysis). This

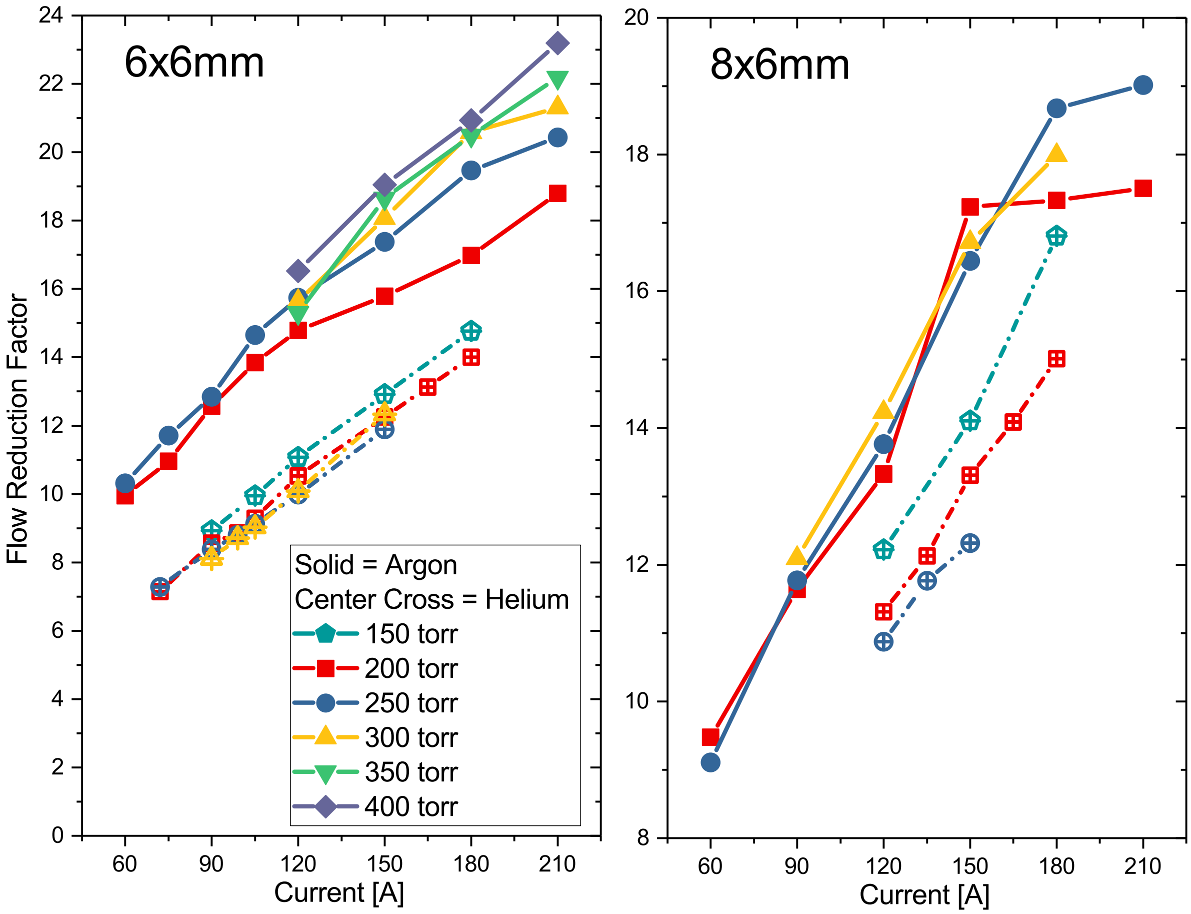

Figure 4.35: Flow rate reduction (FRF) in a 6x6mm PW and 8x6mm PW at various GCS pressures and arc currents in both argon and helium.

is the net amount of power available that could heat the plasma inside the PW channel. From this, it can be seen that the power going into the helium arc can be viewed as less efficient at higher GCS pressures than at lower ones, since as GCS pressure increases, it requires greater retained arc power to attain some given FRF value. It is also very interesting to note that in argon, the different GCS pressure curves have essentially converged to one line, whereas this is not the case in helium.

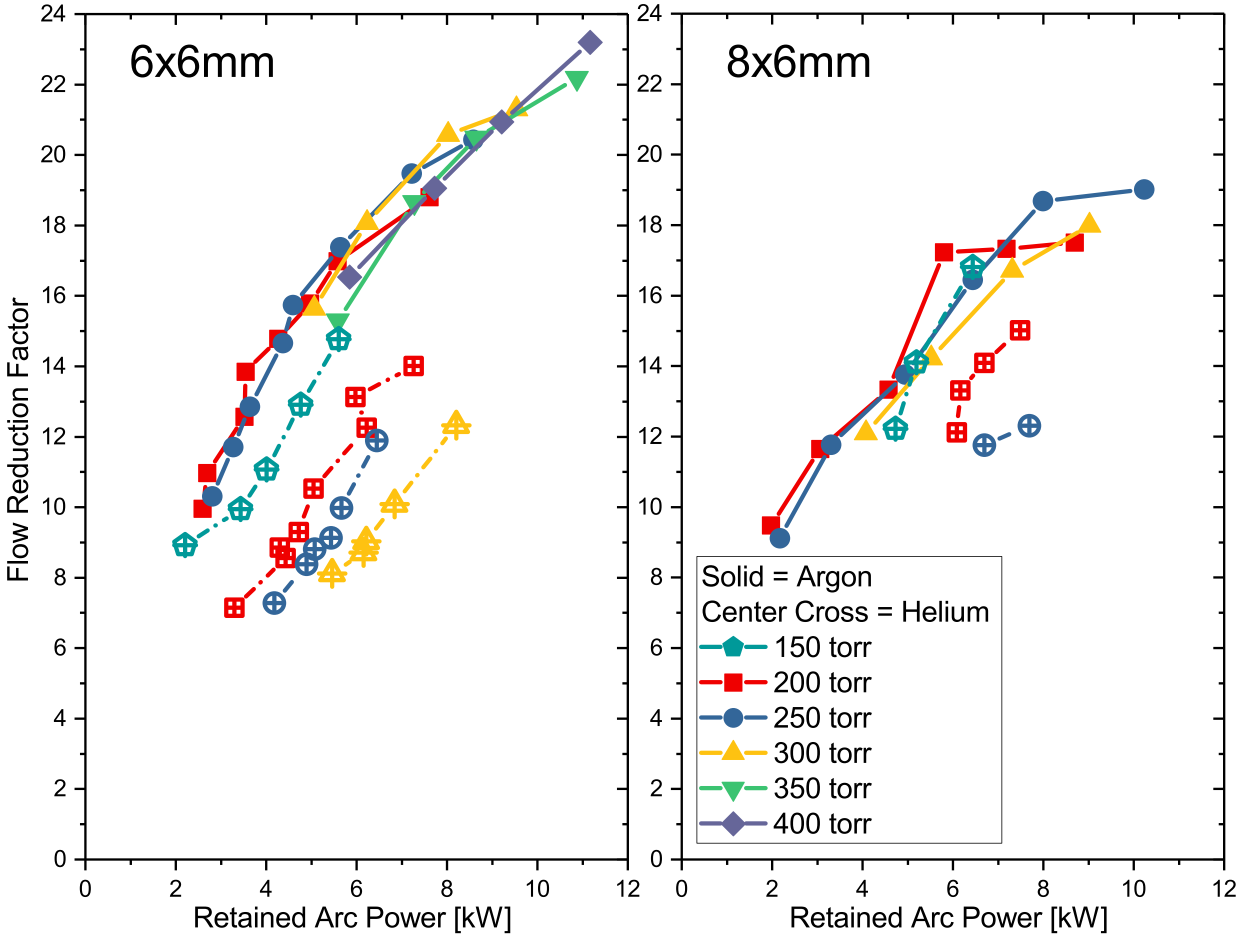

Figure 4.36: Flow rate reduction (FRF) in a 6x6mm PW and 8x6mm PW at various GCS pressures, plotted against retained arc power (rather than current as in Fig 4.35).

4.3 Two-Aperture Plasma Window Results

While the previous section focused on results for PW arrangements with a single aperture size down the length of the channel, this section will focus on a narrower subset of results from PW arrangements in which there are two different aperture sizes through the channel. For example a 1x6mm_5x10mm PW is arranged: cathodes → one plate of 6 mm aperture → five plates of 10 mm aperture → anode plate (the anode plate always has the same aperture size as the plate immediately upstream of it). The notation for these PW configurations is described in more detail in Section 2.1.2. These will hereafter be referred to as two-aperture or two-radii PW configurations.

Some results of spectral calculations and comparisons with corresponding PLASIMO values are shown in Fig. 4.37. This figure shows argon measurement and model comparisons of electron density n_e and temperature T_e in both 1x6mm_5x10mm and 1x6mm_9x10mm PW configurations with GCS pressure at 200 torr. The results are determined at the location of plate 1 for both configurations. As in the single-radius configurations shown in the previous section, there is decent agreement between measurement in model for much of the operating conditions studied, with an obvious exception being that the electron temperature of low current.

One possible reason for this lack of agreement at lower currents could be that at the assumption of PLTE discussed in Section 2.2.3.1 may no longer be justified for the emissions used, given that the electron density at these currents is below the threshold value for PLTE existence.This can be seen in greater detail with Figs. 4.38 and 4.39. The former illustrates electron density n_e again in 1x6mm_5x10mm (left side of the figure) and 1x6mm_9x10mm (right side of the figure) PW configurations in argon at plate 1, but this time for multiple GCS

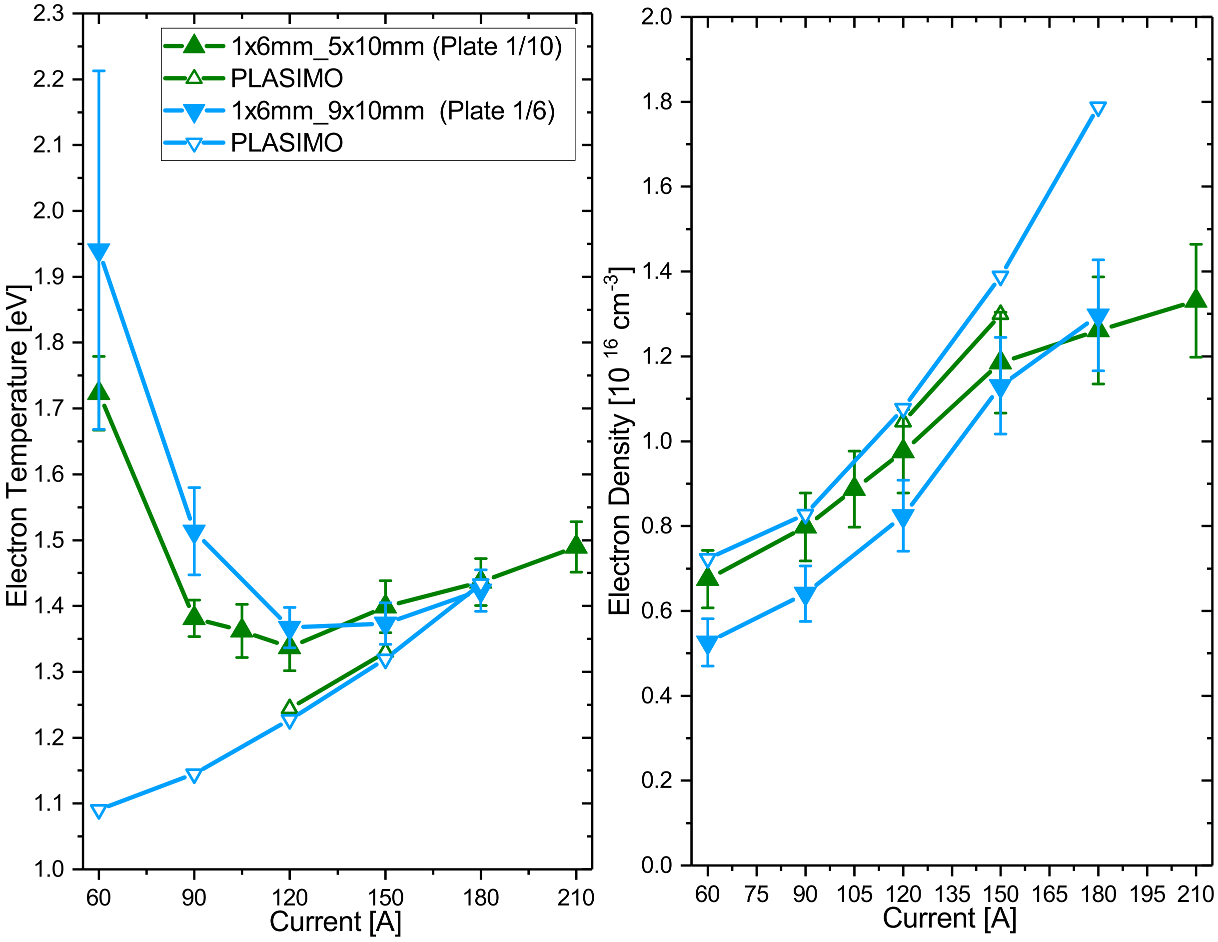

Figure 4.37: Measured electron temperature (right) and density (left) values in both a 1x6mm_5x10mm and 1x6mm_9x10mm PW in argon with GCS pressure of 200 torr. Also shown are corresponding PLASIMO model values. All properties are determined at the P1/6 or P1/10 position.

pressures (only measurements are shown, no PLASIMO results here). The latter is similar, except that it pertains to electron temperature T_e. We see from Fig. 4.38 that for the lower current settings, the electron densities are too low to satisfy two of the three examined PLTE criteria from Section 2.2.3.1, and for these the excitation temperature T_{exc} determined via the Boltzmann line method is likely diverged from the true electron temperature T_e. Note that the error bars in these figures do not reflect the applicability of PLTE or lack thereof.

Also of importance to examine in the two-radius system is the behavior of voltage drops

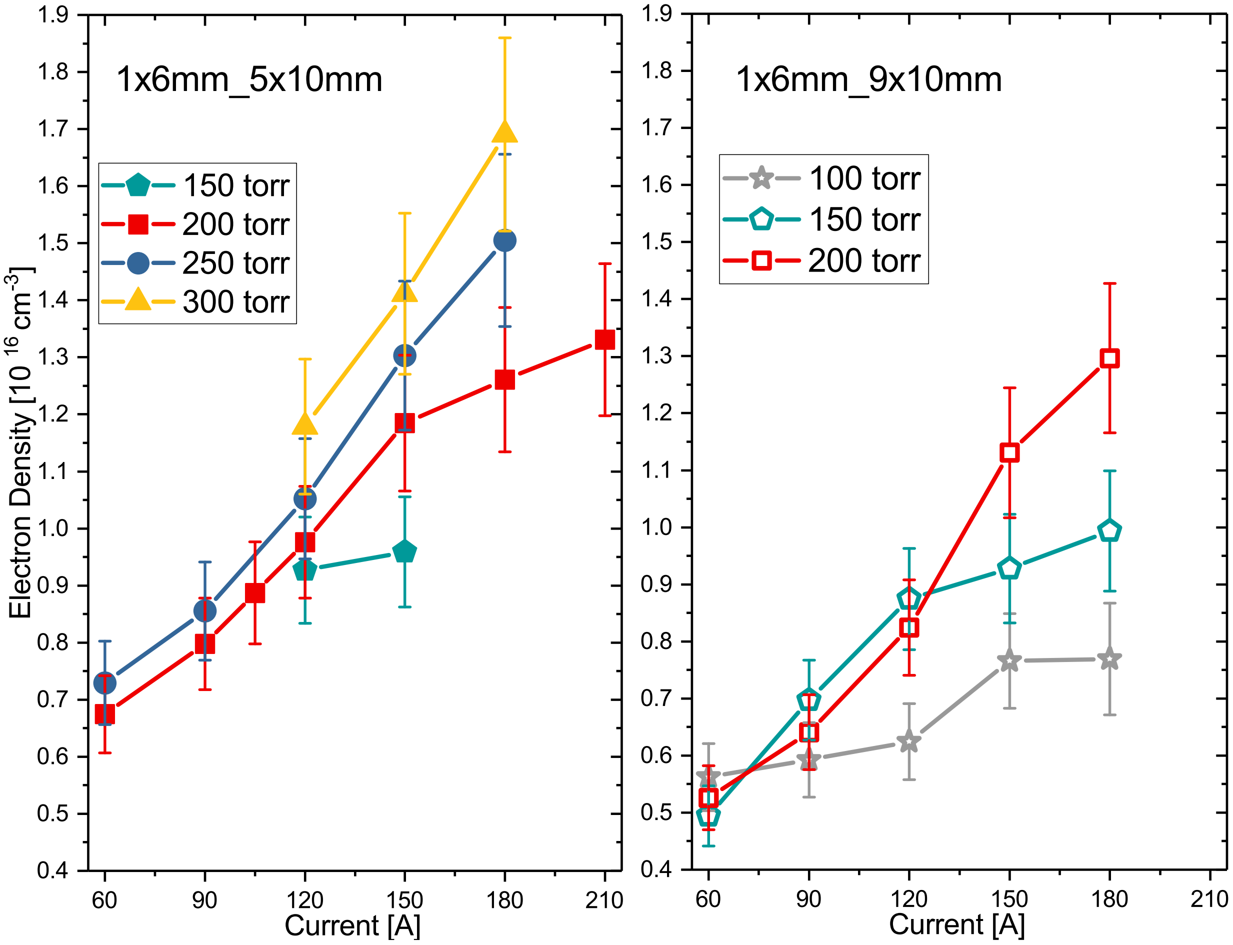

Figure 4.38: Measured electron density at plate 1 in 1x6mm_5x10mm (left) and 1x6mm_9x10mm PW (right) PW configurations in argon for a variety of GCS pressures and arc currents.

between components. We will see in Section 4.4.3 some dramatic consequences of the fact the voltage drop from P1 (the 6 mm aperture plate) to P2 (the first 10 mm aperture plate) in the two-radius systems examined is quite high. This can be seen in Fig. 4.40 for argon (left) and helium (right). In these plots, GCS pressure is 200 torr, and the PW configuration is 1x6mm_7x10mm. Note the change of ordinate scales between the argon and helium plots. From this it is clear that the helium arc experiences some dramatically large voltage drops, particularly across P1-P2. The region from cathodes-P1 encompasses the cathode fall region, which is always relatively large so that gas ionizations can be initiated in the cathode vicinity

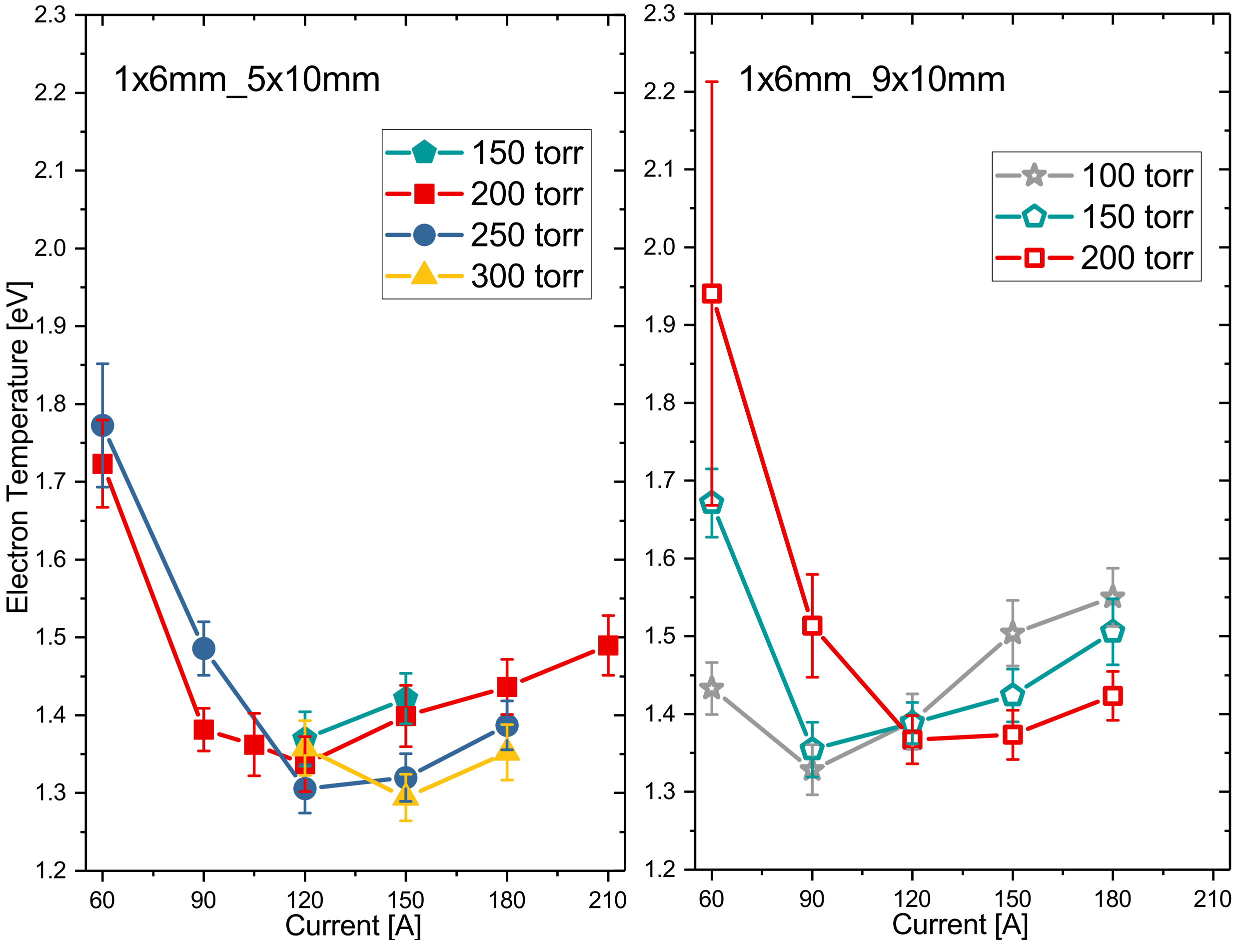

Figure 4.39: Measured electron temperature at plate 1 in 1x6mm_5x10mm (left) and 1x6mm_9x10mm PW (right) PW configurations in argon for a variety of GCS pressures and arc currents.

[28].

4.4 Lessons Learned and Potential Improvements

The lessons learned from the both the successes and shortcomings of the plasma window system described in this thesis are something this author hopes will be leveraged for the next generation of PW device. There is no shortage of challenges associated with implementing the PW with a gas charge stripper, but based on the present research and past studies

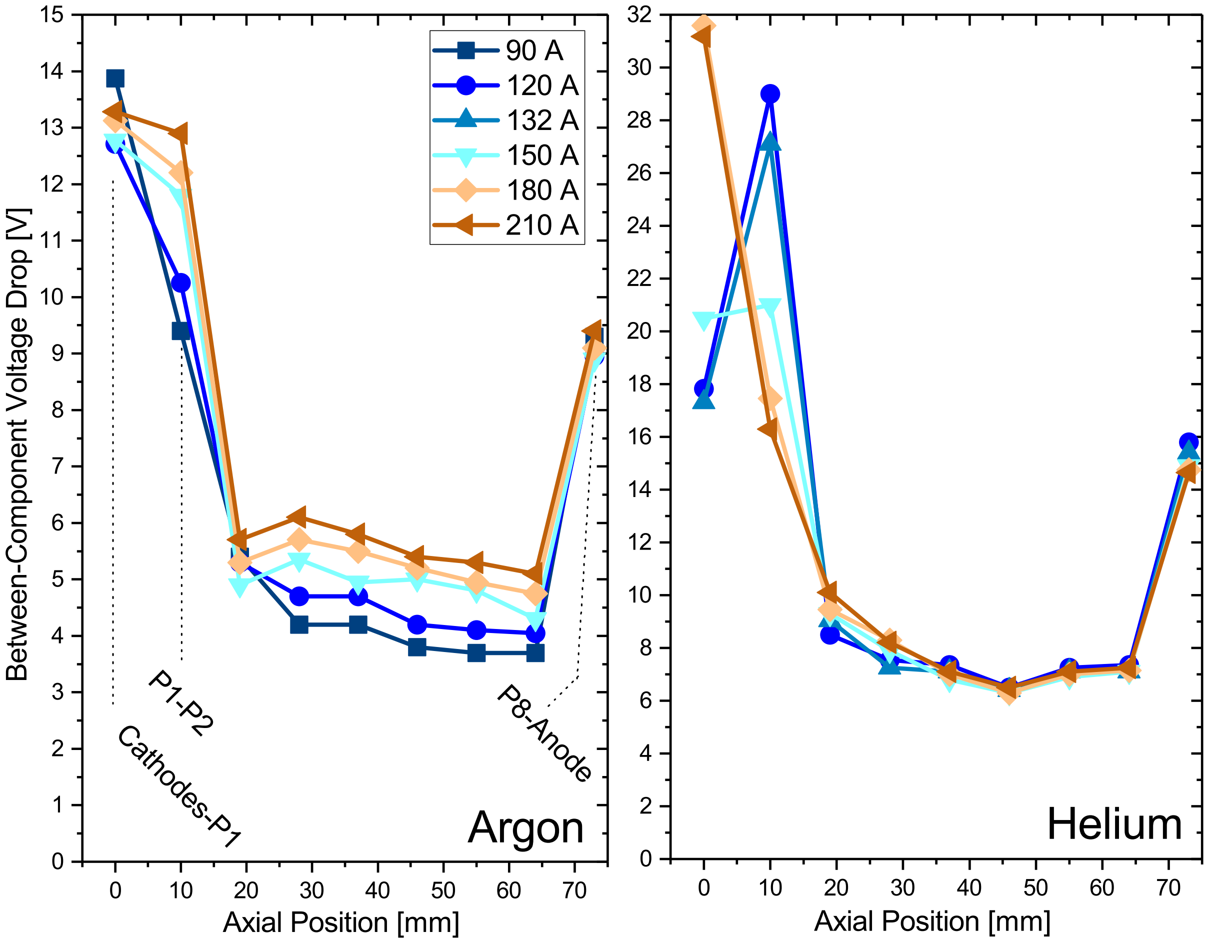

Figure 4.40: Voltage drops between PW components in a 1x6mm_7x10mm PW for both argon (left) and helium (right) arcs. For all cases, GCS pressure is 200 torr. Some of the PW components between which a data point is taken are labeled on the left plot. Those without labels are taken as between two adjacent plates, similar to the labeled P1-P2 point, and though not indicated, the left plot points follow identical labelings.

by other groups, this author is confident that the PW with a gas charge stripper, or as a means of isolating a gas target for any other application, is certainly possible. Though the suite of potential improvements laid out in this section would result in improved capabilities and performance, it is conceivable that not all can reasonably be implemented for a next generation PW. In this section, it will be useful for the reader to recall the characteristics of the PW and the test stand which were described in Section 2.1.

4.4.1 Cathode Structure

Discussion and conclusions about considerations for cathode usage in the PW were presented in Section 2.3, primarily by conducting a survey of existing literature on thermionic cathode usage with particular attention to thoriated and lanthanated tungsten studies in argon and helium arcs. A recap will be given here on some those conclusions and how they can be leveraged.

Recommendation Topic 1:

It is expected that the cathode lifetime scales with the current density emitted. It therefore would be beneficial in terms of supporting longer lifetimes to have a greater combined cathode emitting surface than presently in the PW. For example, the current setup with 3 thoriated tungsten cathodes could be changed to allow 6, or possibly more. Alternatively, a knife-edge ring cathode of thoriated tungsten is another option that could be explored since it offers a large emitting surface area. It is unclear how stable this arrangement would be, since emission tends to occur from a localized spot on the cathode. This arc attachment and the immediate vicinity have their morphologies changed with operating time, as discussed in Section 2.3, and may migrate to different zones if the WF-lowering-dopant composition near the initial cathode spot becomes less favorable for emission. In this sense it would possibly be beneficial having the relatively large surface area of the ring-like cathode.

Recommendation Topic 2:

In some instances it appears that the copper shields into which the thoriated tungsten cathode needles are inserted (see Fig. 2.8) can be deformed by the local plasma. An example of this is shown in Fig. 4.41. Sometimes it even appears that this copper shield, or the water-cooled copper cathode holder into which the shield threads, as is also illustrated in Fig. 4.41

with the label of possible emission site. It is therefore suggested that any copper holding component of the cathodes be positioned farther from the arc axis by using longer cathodes. As suggested in Ref. [93], a longer cathode would have the added benefit of promoting greater diffusion of thoria (if this is thoriated tungsten) in the cathode and extending its usable lifetime.

Recommendation Topic 3:

Due to there being several channel diameter changes in the vicinity of the cathodes with the present PW setup (entrance of cathode housing is 10 mm diameter, then it opens to 13 mm where the cathodes are inserted to the channel, then constricts down to the 6 or 10 mm diameter of the first PW plate), as well as the cathodes themselves positioned inside the gas flow, there may be a large degree of turbulence and swirl. As reported in Ref. [96], this swirl can contribute to substantially enhanced erosion time. One thing at the very least which could be done to help alleviate this would be to have a uniform channel diameter in the cathode vicinity.

4.4.2 Plasma Window Structure

Recommendation Topic 1:

Cracked or otherwise damaged o-rings are presently a frequent occurrence which results in air leaks. These leaks are highly problematic near cathodes in particular, since as discussed in Section 2.3 the presence of oxygen can decrease cathode lifetimes. This also would be a significant issue if in recirculation mode due to the gas impurity continuously building up. The recirculation mode would be absolutely necessary for operation with a gas charge stripper, so a redesign of the cathode plate and between-plate components shown in Fig. 2.6. One possibility for why the o-rings become damaged is that the plates at the part in

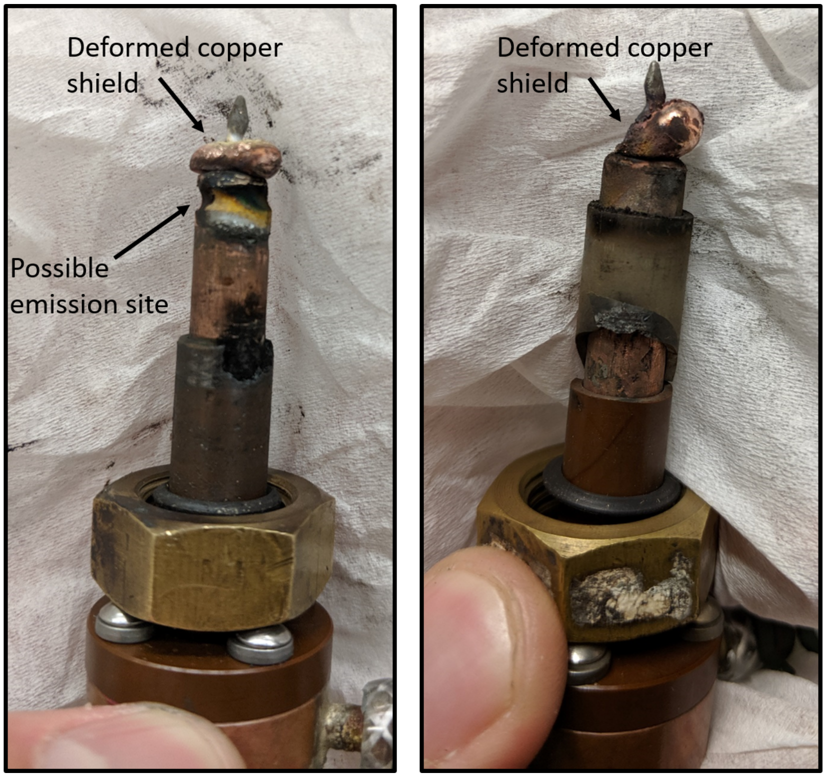

Figure 4.41: Photos of cathodes and their holders after attempting an arc in helium PW of 6x10mm configuration, which ultimately proved too unstable for data collection. The copper shield has been deformed and just below on the left photo there is an indentation in the copper holder, possibly due to this acting as an emission site.

contact with the o-rings become hot during the PW operation and so can cause thermal contact damage, as could the inner alumina insulator which is also in contact with the o-ring. Furthermore, when the plates are hot they thermally expand and therefore squeeze the o-rings even more. The frequent observation of o-ring damage could be attributed to this combination of factors. To address this, it is suggested that the plates be made radially larger to provide more space for these components. The o-ring could then be of a larger diameter, so that it is beyond radially beyond where the coolant loop (recall positioning of these plate features in Fig. 2.6) is inside the plate, so that it would be less likely to suffer any thermal contact damage from the plates. Additionally, one could leave a small space between this o-ring and the inner insulator to limit thermal contact damage from that as well (so there would be a gap between components B. and C. in the figure). Lastly, with a larger-radius plate, one could even place a redundant o-ring beyond the outer FR4 insulator (component A. in the figure) in case of failure of the inner.

Recommendation Topic 2:

It was noted that after long operation times, an accumulation of copper would often appear on the plasma-facing insulators between the plates, which because this primarily occurs on the cathode-side of the PW, presumably is a result of deposition of small amounts of copper removed from the copper cathode shields. this copper deposition often resulted in a conductive bridge between two plates on the cathode-side of the PW, effectively shorting the plates together. This is undesirable as it would result in a greater voltage drop between other plates, such that the total PW voltage drop remained relatively unchanged. As will be explained later, having excessive plate-to-plate voltage drops can be problematic. One potential solution to this issue of conductive bridging building up across the inter-plate insulators is to introduce a different plasma-facing shape for them, such as those illustrated

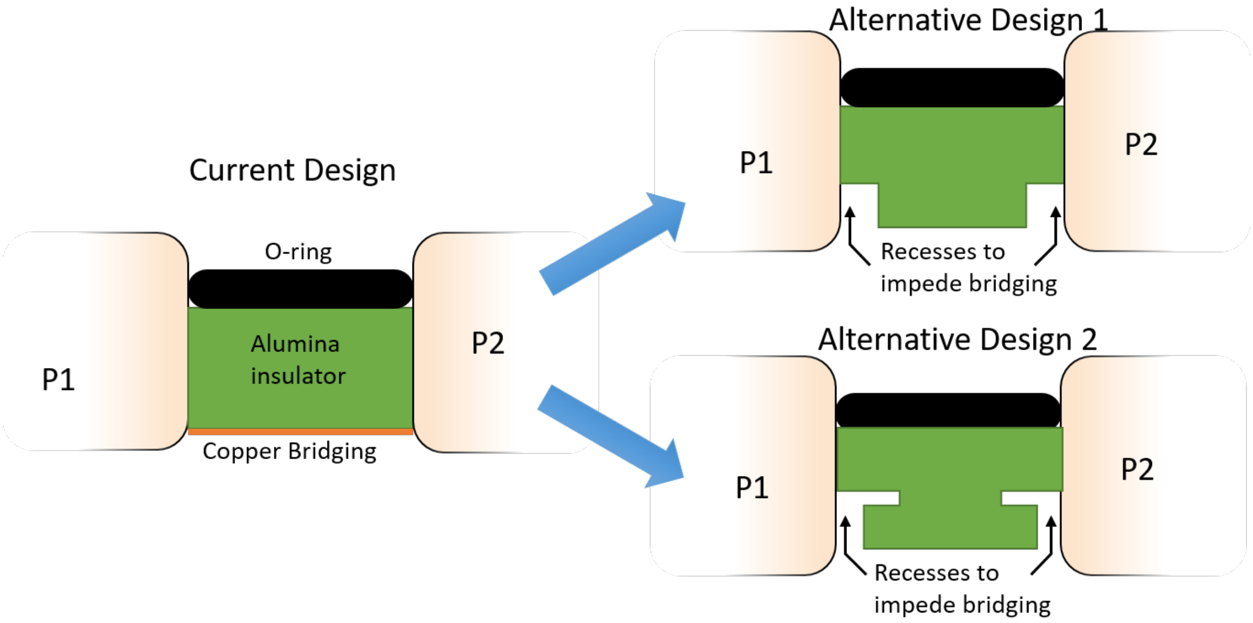

Figure 4.42: A pictorial representation of the undesired copper bridging effect that often occurs for cathode-side plates. Also shown are different possible insulator designs that may inhibit the copper bridging effect.

in Fig 4.42.

Recommendation Topic 3:

Though it shows promise for meeting the requirements of large-aperture while still having substantial flow-reduction capabilities (see Figs. 4.1 and 4.2), the PW configurations of 1x6mm_Nx10mm do have more issues than in a single-radius configuration which must be addressed for a next generation PW. The principal concern is related to the part of the channel which expands from 6 mm aperture plate to the first 10 mm aperture plate. Across these two plates there is always a relatively large voltage drop, greater that between any two adjacent plates elsewhere in the PW. As a result, ions within the expansion region feel a strong electric field backwards towards the exposed surface (on the anode-side) of the 6 mm aperture plate. For higher currents in particular, this can result in catastrophic removal of the exposed copper plate. This removed copper material was subsequently redeposited

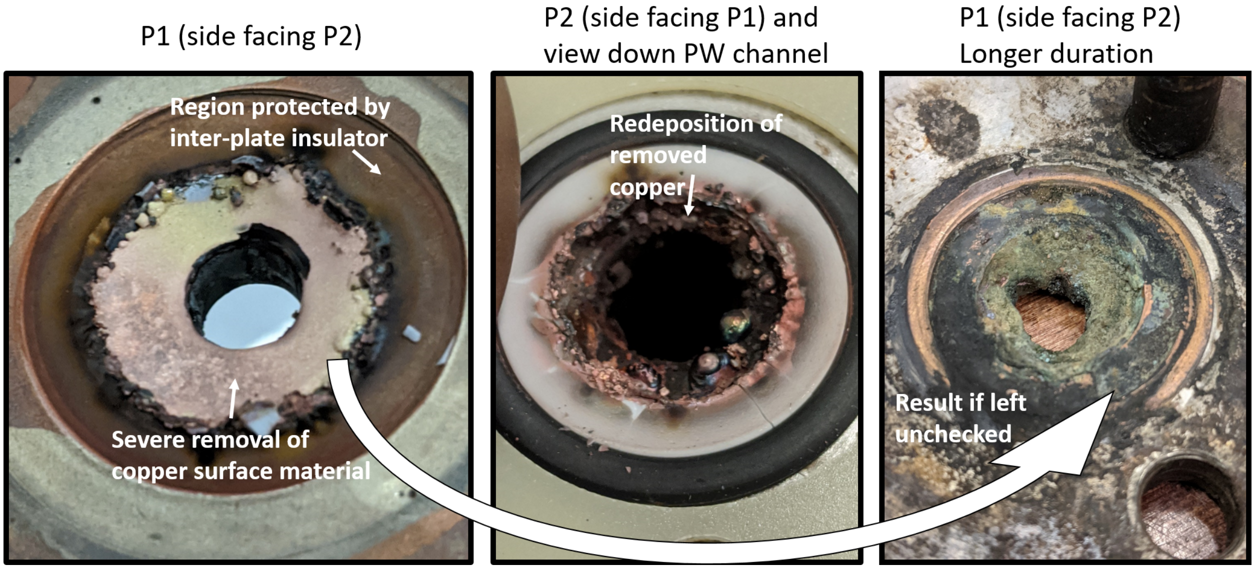

Figure 4.43: Left: A photo of dramatic and rapid copper removal from P1 in a 1x6mm_9x10mm PW operated in helium at 300 torr GCS pressure, 210 A arc current. Middle: The remove material was redeposited along the channel wall downstream of the removal site. Right: The result of continued copper surface removal, which has here cut through to the water coolant path, resulting in even more extensive damage.

along the PW channel walls, rapidly causing the bridging effect between plates discussed previously. This can be seen in Fig. 4.43. The left and center photos were taken after operating a 1x6mm_9x10mm PW in helium at 300 torr GCS pressure, 210 A arc current over a period of 100 minutes, and the right photo taken after operating a 1x6mm_7x10mm PW in helium at 300 torr GCS pressure, 180 A arc current over a period of about 18 hours (recall what the un-damaged plate surface looks like from Fig. 2.6). The voltage drop between P1 and P2 in the first case was about 30 V and in the second case was 24 V, which as was discussed in Section 4.3 and Fig. 4.40, is a characteristic of the expansion part of the two-radius PW configurations. Although this is a catastrophic problem, there are fortunately several possible steps that can be taken to reduce its likelihood.

Firstly, note from Fig. 4.43 that the copper material removal occurs on the part of the plate which is unprotected by the alumina insulator. As a result, one would expect that if this insulator had an inner diameter of 6 mm to match that of P1, the plate would not suffer such damage. Secondly, so long as the PW overall geometry is preserved, changes to plate count don't impact the the total PW voltage drop. As a result, the voltage drop between any two plates will be reduced if the total plate count is increased (again assuming PW overall geometry is unchanged), so having a larger number of plates would mean the drop between the 6 mm aperture plate and the first 10 mm aperture plate is decreased, so less energetic ion-plate collisions. Lastly, one could have a more gradual stepping from the 6 mm aperture to 10 mm aperture, e.g. having in between a plate of 8 mm aperture.

In addition to the above recommendations hopefully reducing the likelihood of the type of damage observed in Fig. 4.43, it's highly desirable to have an early detection of the problem, as well as appropriate interlocks to ensure that if it develops, the arc is automatically shut off to prevent further damage. The power supply voltage data can be continuously observed for any unexpected behaviors which may provide information that the arc is behaving unstably or destructively.

4.4.3 Recirculation

Recommendation Topic 1:

Recirculation of the gas that flows through the GCS and PW is an essential capability for long-term operation of the PW, particularly if the desired gas is helium, since simply expelling the gas to atmosphere is obviously expensive and wasteful. One success from this PW research was a 6-day continuously operated trial in recirculated helium, with the original GCS pressure set to 300 torr and arc current of 180 A, in a 1x6mm_7x10mm PW. It should be noted that this is the same type of PW configuration and similar operating conditions which generated the severe damage shown in Fig. 4.43, and while this long-duration trial

Figure 4.44: The three thoriated tungsten cathodes after a 6-day continuous operation run in helium at GCS pressure 300 torr and 180 A arc current. Also shown for comparison is an unused cathode.

did not result in such damage, an air leak did develop, causing a continuous accumulation of oxygen and nitrogen impurities which were observed in the continuous collection of spectra using the spectrometer described in Section 2.1.3.1. Air leaks such as this, as mentioned above, are particularly essential to prevent for recirculation as the impurities will build up continuously. As mentioned in Ref. [23], even small amounts of impurities can impede the charge stripping capabilities of helium.

After this run, the cathodes were examined to gauge their state after such long-duration operation. These are shown in Fig. 4.44 and it is clear they were substantially deformed over the course of operation. Ultimately the arc collapsed of its own accord, which is a still common occurrence in helium PW arc, and a highly uncommon one in the argon arc. In fact, this instability in the helium arc not only made data acquisition challenging, but but would certainly preclude the PW from reliably operating for long durations, and it is absolutely necessary that such instabilities be addressed if a future generation PW were to be used with a helium charge stripper in an ion beam. Unfortunately, the root cause(s) of this instability could not be conclusively ascertained in the work of this thesis, but it is likely attributed to sub-optimum cathode properties and the ensuing insufficient ionization of background gas to maintain the arc over its length. Towards this end, it is particularly crucial for a next generation PW to consider the possible improvements laid out above regarding cathodes and their usage. One thing that became clear however, is that the likelihood of this instability which can cause the helium PW arc to collapse increases at higher GCS pressures and at lower arc currents. To summarize, while this 6-day helium run was a successful step towards the PW being capable of isolating a GCS continuously over a long duration, shortcomings such as air leaks and cathode deformations must be addressed to ensure the desired stripping gas is maintained and the PW can operate continuously for a longer period.

Recommendation Topic 2:

When changing PW gas from argon to helium, Ar II emissions are observed to linger for some time after the argon feed has been closed and the flow has been transitioned to helium (the process is first described in Section 2.1.2). It is likely that some argon remains trapped near the cathode as a result of it having a much lower ionization energy than helium, so is more easily ionized in the vicinity of the cathodes, and then these ions fall through the cathode potential drop before recombining and being ionized again to repeat the cycle. The net result is a much slower depletion of the argon than would be expected. Figure 4.45 illustrates an example of this by looking at several emission peaks immediately following the transition from argon to helium flow for a 6x6mm PW with GCS pressure 200 torr and arc current 120 A. In this it can be seen that even after 3 minutes of operating in nominally pure helium, some Ar II peaks remain. It can also be seen that this is particularly problematic when attempting to determine plasma properties with the spectral acquisitions because the Ar II lines are substantially more intense than the helium ones. This is still in the fresh gas mode where the gas is expelled to atmosphere rather than recirculated.

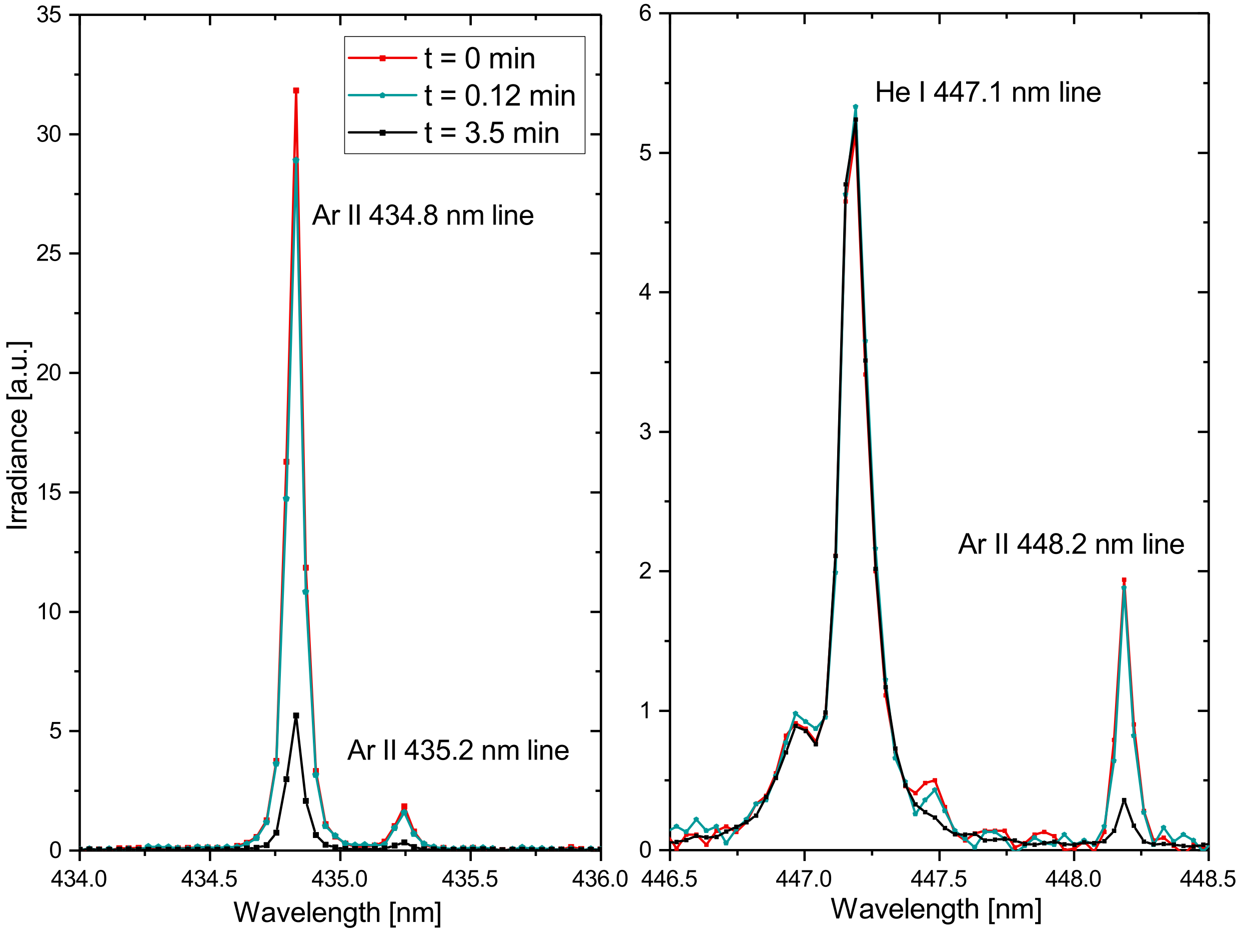

Figure 4.45: Spectral acquisitions at several different times, of two narrow wavelength windows. The Ar II emissions can clearly be seen to persist for several minutes after switching from argon to helium gas. This data was taken in fresh gas (expelled to atmosphere), not recirculation.

It is therefore recommended that the PW is operated in fresh gas for at least 20-30 minutes prior to recirculating, otherwise this argon gas will remain trapped with the helium. It's also possible that different operating conditions could help flush out the argon more so than others, though this possibility was not thoroughly explored in the presently-discussed research.

4.4.4 Plasma Window Performance Summary

As has been mentioned, to utilize the plasma window with a gas charge stripper, it is desirable to have as great a pressure as attainable with as low of a flow rate as possible, which is achieved by having a large arc current. Higher pressure and higher current both result in larger power deposition. A sizeable amount of this power is deposited into the cascaded plates enclosing the arc, and the remainder is deposited into the heat shielding cone structure within the expansion chamber and the expansion chamber walls themselves (these components are described in Section 2.1.2).

To provide an idea of what to expect for a power deposition from the arc for a next generation PW, Figs. 4.46 - 4.50 show the PW arc power in both argon and helium for the PW configurations studied in this work. Note that this is only the arc power, and other sources of power associated with operation of the PW include the power dissipated through the resistors described in Section 2.1.2 as well as the wall power of the vacuum pumps. The coolant system must be capable of managing at least the sum of all these powers. Using the same calorimetric technique described in Section 2.1.3.2, the system of vacuum pumps require about 5 kW of cooling power, while the power dissipated through the 1 Ohm resistors schematically shown in Fig. 2.11 is of course current-dependant, calculated as $P = I^2R$. All told, when the PW is operating with GCS at 300 torr or above (300 torr being a modest target

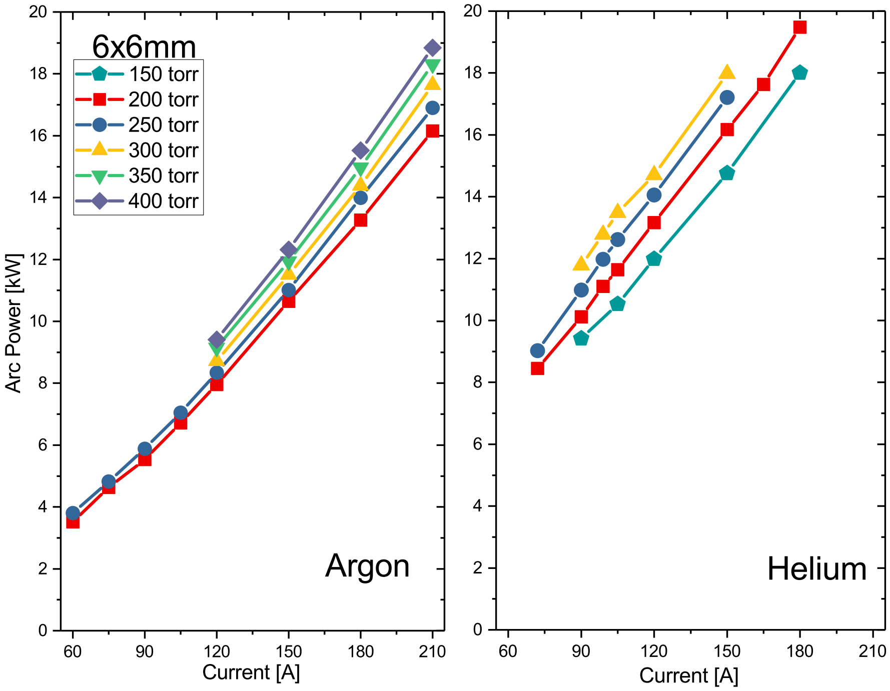

Figure 4.46: Arc power for various arc currents GCS pressures in the PW configuration of 6x6mm.

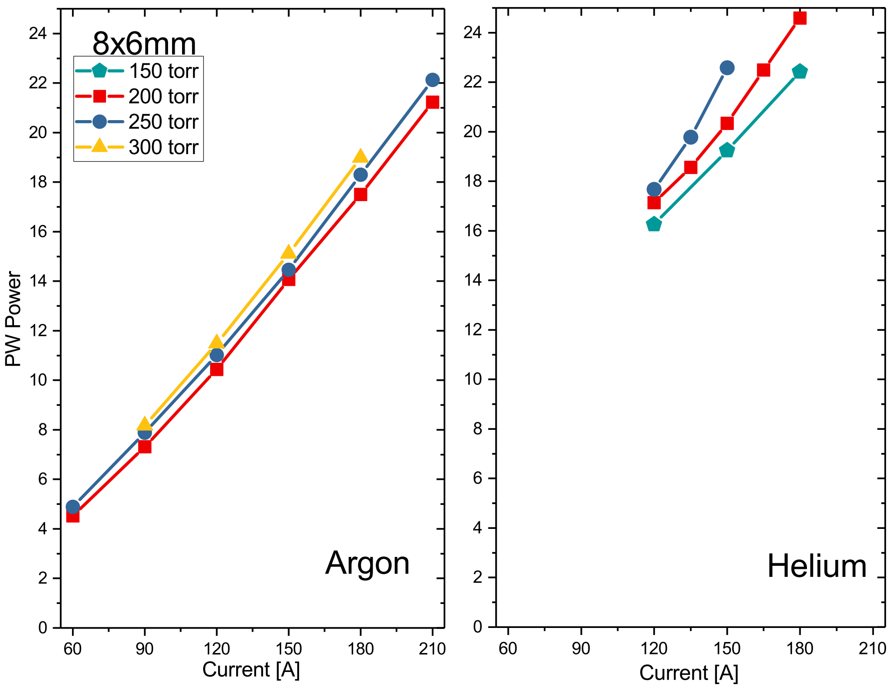

Figure 4.47: Arc power for various arc currents GCS pressures in the PW configuration of 8x6mm.

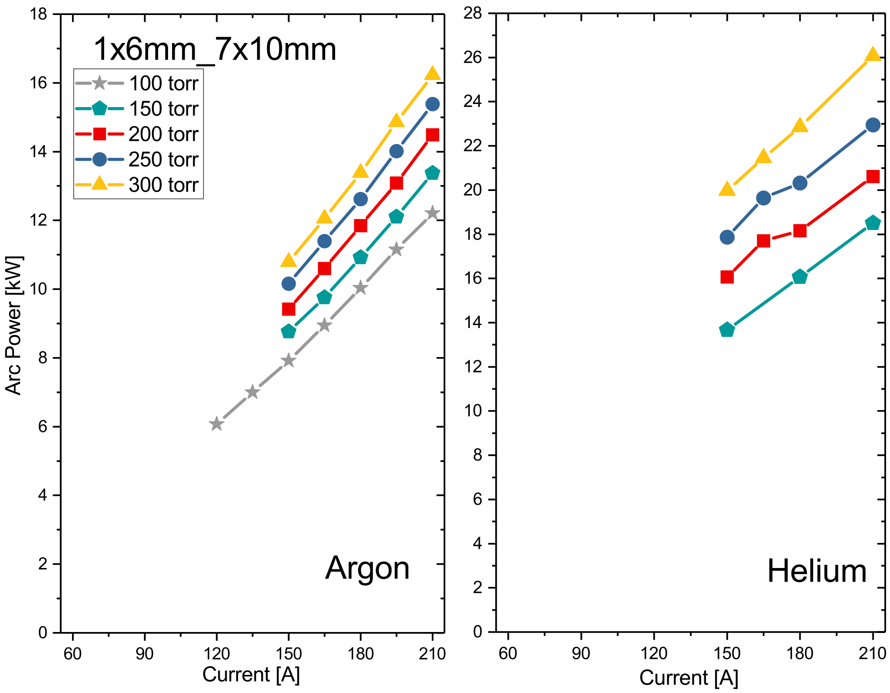

Figure 4.48: Arc power for various arc currents GCS pressures in the PW configuration of 1x6mm˙7x10mm.

value for utilizing this on an ion beam), at 150 A or above, the overall power consumption in helium can easily exceed 40 kW (in argon for all else equal, it's somewhat lower), and the coolant supply MUST be able to cope with at least this amount of power, especially for when the system is to be operated continuously for a two-week period.

4.4.5 Charge Stripper Gas Species Choice

Here will be provided a set of pros and cons for choosing either argon or helium as a possible charge stripping gas for an ion beam.

Equilibrium Charge State

Studies on the equilibrium charge state of heavy ion beams being stripped by gases have been carried out in e.g. Refs. [2, 22, 23, 31]. In these studies, specifically for an incoming ion beam of $^{238}U^{35+}$ at 11 MeV/nuc, it was found that the equilibrium charge state (post-

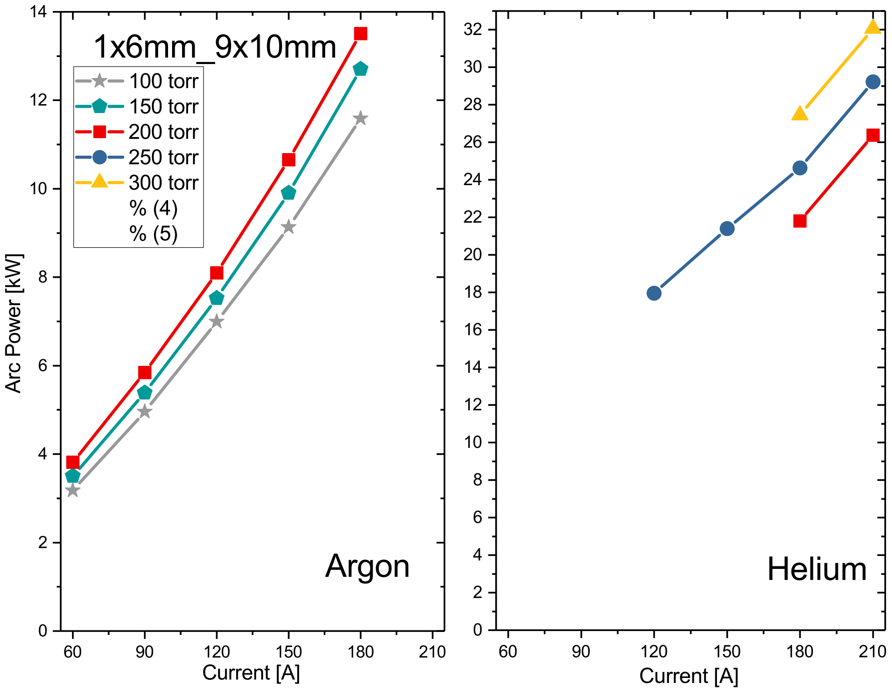

Figure 4.49: Arc power for various arc currents GCS pressures in the PW configuration of 1x6mm˙9x10mm.

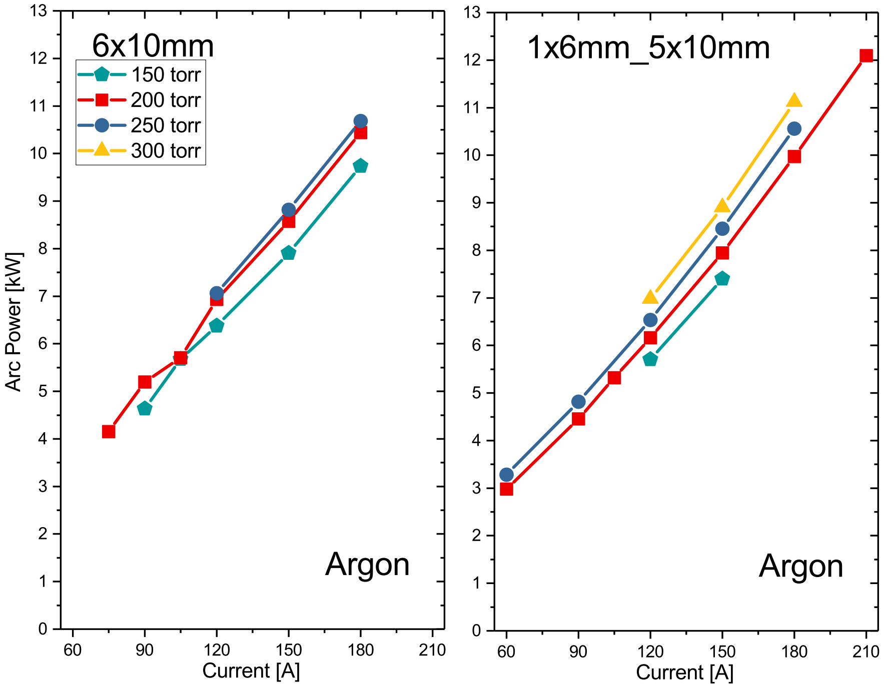

Figure 4.50: Arc power for various arc currents GCS pressures for two the PW configurations, both of which are for argon arc. The left plot is for 6x10mm configuration and the right plot is for 1x6mm˙5x10mm.

stripping) in helium gas was 66+ and in argon gas was 56.6+ which were compared to the equilibrium charge state through a solid carbon foil of 72+. So, helium tends to provide higher charge states as a stripping gas of heavy ions such as uranium.

Stability

As has been discussed both in Section 2.3 and Section 4.4.3, the helium arc frequently suffers from instability which can cause the arc to collapse entirely. When this happens, GCS pressure drops precipitously because it no longer has the flow rate reduction of the arc, so the instability in the helium arc absolutely must be addressed for the PW to be useful with a helium charge stripper. The root cause(s) and potential solutions of this instability remain somewhat elusive but it is likely that it originates at the cathode side, perhaps as a momentary repositioning of the arc spot on the cathode surface. Alternative cathode designs described in Section 4.4.2 could possibly reduce the frequency of this happening and therefore increase stability. The argon arc did not seem to suffer such instability, likely partly attributed to it having a much lower ionization degree, so any arc attachment repositioning that happens doesn't suppress the production of ions and electrons from gas that sustains the arc.

Lifetime

On the topic of cathode lifetime, it is not as yet known how the long term performance of thoriated tungsten cathodes in argon compares with that in helium. A thorough study on the long term performance of these cathodes should be the next topic of investigation related to the PW in the context of a gas charge stripper.

Flow Rate and Flow Reduction Factor

The figures which convey flow rate and flow reduction factors (FRF) in various operating conditions and geometries are Figs 4.34, 4.35, 4.1, and 4.2. From these figures we see that for equal GCS pressure and arc current, argon exhibits substantially lower flow rate and greater FRF than those in helium.

Arc Power

As seen in Figs. 4.46 - 4.50, the arc power into the argon arc is substantially less than that into the helium arc, at equivalent GCS pressure and arc currents. Ultimately the entirety of this power must be cooled, in addition to the other components not directly part of the arc but still require cooling, such as the pumps and resistors, as mentioned in Section 2.1.2 The results in these figures can be used as a guide for a future PW to assess what amount of cooling power will need to be provided throughout the PW region.

4.5 Empirical Scaling Behaviors

One goal of this project was to attempt to determine the scaling behavior of flow rate as a function of the various controllable parameters of arc current, GCS pressure, geometry, and gas species. Examining each scaling independently ultimately allowed an overall empirical scaling relation to be obtained, such that the flow rate is linearly related to an overall empirical scaling function (denoted ESF). This is presented in Fig. 4.51, for argon and helium separately. This empirical scale function ESF is defined as:

$$ESF \propto \frac{P^{5/3}}{I^{2/3}\bar{Y}^2}\,, \tag{4.5}$$

where $\bar{Y}$ is calculated if there is a two-radius (or more) PW channel as:

$$\bar{Y} = \frac{\sum L_i^{1/2}/D_i^4}{\sum L_i^{1/4}/D_i^2}\,, \tag{4.6}$$

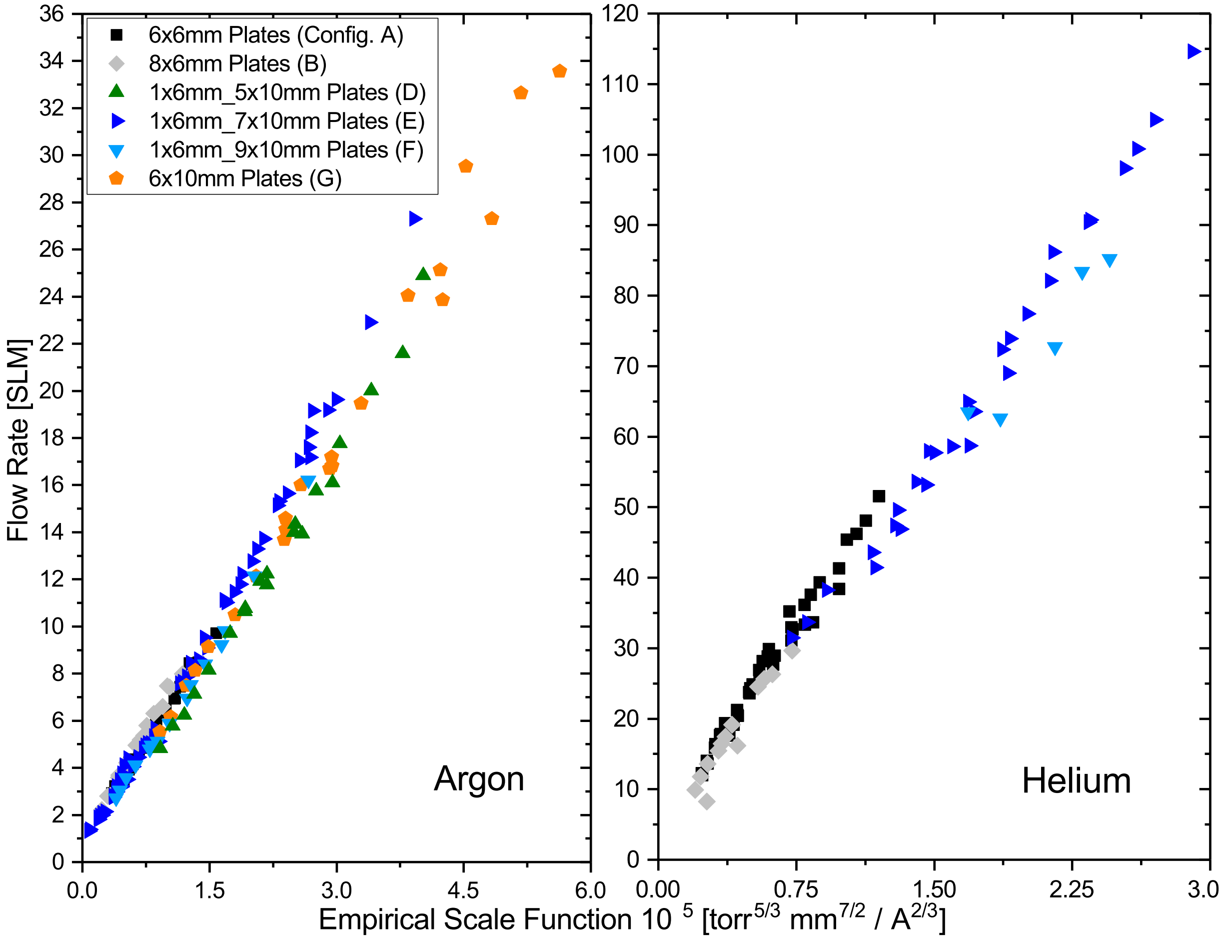

Figure 4.51: An empirical scaling relationship between operating conditions and flow rate. Each PW configuration shown includes the multitude of operating conditions explored within that configuration.

in which the subscript i denotes the channel portion, which has its own length L and diameter D, both in units of mm here. The pressure P is the GCS pressure and is here in units of torr and the arc current I is in units of amps. The relationship is plotted across a multitude of operating conditions (varied pressures and currents). It should be stressed that this relationship is phenomenological, and there may be finer adjustments to the powers of the properties to bring about a collectively better fit to a straight line. This is particularly true for the geometric factor $\bar{Y}$.

It is worth mentioning that there likely are several caveats to the utilization of this scaling law to consider before treating it as a universal scaling relation. In the PW, an areal expansion just downstream of the anode results in a choked flow condition. We know this because of a simple test in which the booster pump was turned off during PW arc operation, resulting in a pressure rise of the expansion chamber downstream of the PW, but crucially did not impact any pressure, flow, or other plasma properties within the PW channel itself. The only explanation is the establishment of a choked flow condition at the expansion location after the PW. Thus we consider a requirement to use the scaling law of Eq. (4.5) and Fig. 4.51 is that there exists a choked flow condition, i.e. the pumping speed is sufficiently great.

Chapter 5

Conclusions

As heavy ion accelerator facilities push for greater beam intensity with greater beam particle count, the solid charge strippers that have traditionally been used to remove further electrons from the ion beam are less viable options due to their short lifetimes at such intensities. In light of this, an alternative in the form of a gas charge stripper (GCS) is a promising avenue, but is challenging to implement because it requires a large pressure and aperture, yet also necessary is a low gas leakage rate from the GCS to the surrounding beamline. The plasma window (PW) is a device which can meet these challenges by substantially reducing that gas leakage rate, all else being equal.

Flow Reduction Mechanisms

One goal of this study was to ascertain what characteristics about the plasma most contribute to the observed flow rate reduction. A detailed characterization of the plasma within was carried out, particularly for the focused case of a 6x6mm PW configuration (6 plates, each of 6 mm aperture). In this PW configuration, the flow rate could be reduced by up to a factor of 24 in argon and 15 in helium from what it would be without the presence of the arc.

A 2D PW arc model was developed using PLASIMO and used to investigate an array of plasma properties and compare to measurements, in an effort to assess if this tool would be useful in gaining further insight into the flow reduction mechanisms, as well as in predicting and understanding the behavior of the next generation plasma window. While the models generally produced results that matched reasonably well with experimental ones, one must start off with a clear idea of what the cathode-side and anode-side pressures are to use as boundary conditions. This can be more easily done in a single-radius PW such as the 6x6mm configuration studied in this work, by extrapolating from the pressure measurements obtained and presented in this thesis in Fig. 3.8. A two-radius (or more) PW such as the 1x6mm_5x10mm configuration further requires input of the voltages at the positions of cathodes, the expansion location, and anode. However, one issue with using this modelling software for these two-radius systems is that it cannot treat the total arc current as a constant value over the channel, so the 6 mm and 10 mm aperture portions can have non-identical currents, which doesn't conform to the reality of the PW.

An expression that indicates for mass flow was obtained in Section 3.3, and an examination into which properties most heavily influence it was conducted. In Section 4.2.6 it was shown by thorough examination of PLASIMO modeled properties that what has most often been cited as the flow-limiting attribute of the PW, the large viscosity that it generates, is indeed not a substantial factor. Far more important is a heavy density factor, $\sqrt{-\frac{n_h'}{n_h^2}}$ which the mass flow is proportional to. For a given plasma pressure P_p, the heavy particle density n_h is reduced with increasing electron density n_e, electron temperature T_e, heavy particle (gas and ion) temperature T_h, and heavy particle axial rate of change n_h'. Greater presence of electrons means they more rapidly heat the gas. As a result, all of the parameters mentioned above increase with increasing arc current, matching the observation that measured flow rates are lower for higher arc currents. The conclusion is that what is most important in establishing the flow rate reduction is substantial ionization of the flowing gas which enables greater and quicker heating.

Plasma Window Outlook

Although the PW was successfully operated in helium for 6 days under continuous gas recirculation, there is still much room for improvement. Some considerations and recommendations were summarized in Section 4.4. Employing at least some of these should help PW maintain better stability, lifetime, or both. In the same section, many other potential improvements to the PW system are also presented, and this author strongly recommends at least some of these features be implemented for a next generation PW for isolating a high pressure gas target. The long-term behavior of the cathodes in both argon and helium in particular demands further study, as does the impact of the shape of the cathode(s) used since it is likely alternative designs to the three needle-cathode arrangement used in this thesis could reduce the surface current density and extend operating lifetime.

A number of conclusions have been reached regarding considerations in optimizing the PW geometry for the purpose of gas charge stripping of ion beams. Based on the results described in this thesis, it is recommended that a next generation PW employ a plate configuration akin to a 2-radius PW (e.g. the 1x6mm_5x10mm configuration) because this provides both a modest flow reduction degree (between that of a 6x6mm and a 6x10mm configuration), but also is composed of a wide aperture channel - with the exception of the single 6 mm aperture cathode-side plate - to permit un-scraped beam passage. Additionally, it was found that extending the overall arc length (e.g. the 6x6mm configuration to 8x6mm configuration) confers a slightly further flow rate reduction, and does so at the expense of a greater arc power which must be cooled. To help provide some ability to predict the flow rate through the PW for some desired operating conditions (GCS pressure, arc current, gas species, and PW geometry), an empirical scaling relation was developed. This was demonstrated in Fig. 4.51.

While helium can afford higher equilibrium charge states for the outgoing ion beam, it is generally far more difficult to maintain. For equivalent GCS pressure and arc current, compared to with argon, for helium the gas flow rate escaping from the GCS is significantly higher, the power deposition is much greater, and it suffers from greater arc instability and thus more prone to unexpected and undesired shutoffs. It is not clear which gas would experience the greater lifetime of the thoriated tungsten needle cathodes. In order to make use of the plasma window with a gas charge stripper, there must be more investigation into the root causes and possible solutions to the helium arc instability, as well as the likely related problem of the cathode lifetime. Previous studies (mentioned in Section 2.3) have successfully operated in argon gas for up to 1500 hours thoriated tungsten cathodes, the same as those used in this thesis, though in this current work, nowhere near that operating duration was observed. Furthermore, to this author's knowledge there have been no such studies for very long term cathode operation in a helium arc. It is likely that in order to achieve the desired longevity of two weeks continuous operation for a heavy ion accelerator facility, a different cathode structure would be necessary. Some alternatives to the three-needles structure used in the present work were laid out in Section 4.4.2. Testing such alternative cathode structures should be another next step to take in studying the plasma window in the context of a gas charge stripper. It is this author's belief that the goal of a two week uninterrupted and stable operation of the plasma window is attainable provided some attention is given to the challenges mentioned above,and the suggested design changes are implemented. In general, the plasma window is a promising device with the capability of greatly benefiting a gas charge stripper system for future high intensity ion accelerators.

BIBLIOGRAPHY

BIBLIOGRAPHY

[1] F. Marti. private communication.

[2] H. Okuno, N. Fukunishi, A. Goto, H. Hasebe, H. Imao, O. Kamigaito, M. Kase, H. Kuboki, Y. Yano, S. Yokouchi, and A. Hershcovitch. Low-Z gas stripper as an alternative to carbon foils for the acceleration of high-power uranium beams. *Physical Review Special Topics - Accelerators and Beams*, 14(3), 3 2011.

[3] J.A. Nolen and F. Marti. Charge strippers of heavy ions for high intensity accelerators. *Rev. Accel. Sci. and Tech.*, 6:221–236, 2013.

[4] H. Imao, H. Okuno, H. Kuboki, S. Yokouchi, N. Fukunishi, O. Kamigaito, H. Hasebe, T. Watanabe, Y. Watanabe, M. Kase, and Y. Yano. Charge stripping of ^{238}U ion beam by helium gas stripper. *Phys. Rev. Special Topics - Accel. and Beams*, 15, 2012.

[5] M. A. Lieberman and A. J. Lichtenberg. *Principles of Plasma Discharges and Materials Processing*. John Wiley Sons, Inc., 1st edition, 1994.

[6] J. A. Bittencourt. *Fundamentals of Plasma Physics*. Wiley-Interscience. Springer-Verlag New York, Inc., 3rd edition, 2004.

[7] A. P. Thorne. *Spectrophysics*. Chapman and Hall Ltd., 2nd edition, 1988.

[8] C. F. Hooper Jr. Electric microfield distributions in plasmas. *Physical Review*, 149(1):77–91, 1966.

[9] J. A. Sillero, D. Ortega, E. Muñoz Serrano, and E. Casado. An experimental study of thoriated tungsten cathodes operating at different current intensities in an atmospheric-pressure plasma torch. *Journal of Physics D: Applied Physics*, 43, 2010.

[10] P. Tsantrizos and W. H. Gauvin. Cathode erosion phenomena in a transferred-arc plasma reactor. *Plas. Chem. and Plas. Processing*, 12:17–33, 1992.

[11] A. A. Sadek, M. Ushio, and F. Matsuda. Effect of rare earth metal oxide additions to tungsten electrodes. *Metallurgical Transactions A*, 21A:3221–3236, 1990.

[12] G. Leichtfried, I. Wesemann, W. Spielmann, and T. Walde. Metallurgical Mechanisms for HID Lamp Electrodes. In *International Symposium on the Science and Technology of Light Sources*, number IL08, pages 177–191, 2007.

[13] A B Murphy and C J Arundell. Transport Coefficients of Argon, Nitrogen, Oxygen, Argon-Nitrogen, and Argon-Oxygen Plasmas. *Plasma Chemistry and Plasma Processing*, 14(4), 1994.

[14] M Goto. Collisional-radiative model for neutral helium in plasma revisited. *Quant. Spectr. Radial. Transfer*, 76:331–344, 2003.

[15] T. Fujimoto. A Collisional-radiative Model for Helium and its Application to a Discharge Plasma. *Quant. Spectr. Radial. Transfer*, 21, 1979.

[16] H. D. Betz and L. Grodzins. Charge states and excitation of fast heavy ions passing through solids: a new model for the density effect. *Physical Review Letters*, 25(4):211–214, 1970.

[17] H. D. Betz. Review of stripping of heavy ions. In *Proceedings of Particle Accelerator Conference*, volume 18, pages 1110–1114, 1971.

[18] A. T. M. Wilbers, G. M. W. Kroesen, C. J. Timmermans, and D C Sci-Iram. Characteristic Quantitities of a Cascade Arc used as Light Source for Spectroscopic Techniques. *J. Quant. Spectrosc. Radiat. Transfer*, 45(1):1–10, 1991.

[19] F. Marti, P. Guetschow, Y. Momozaki, J. A. Nolen, C. B. Reed, A. Hershcovitch, and P. Thieberger. Charge Stripper Development for FRIB. In *6th International Particle Accelerator Conference*.

[20] Y. Momozaki, J. Nolen, C. Reed, V. Novick, and J. Specht. Development of a Liquid Lithium Thin Film for use as a Heavy Ion Beam Stripper. *Journal of Instrumentation*, 4, 2009.

[21] T. Kanemura, J. Gao, M. LaVere, R. Madendorp, F. Marti, and Y. Momozaki. Progress of Liquid Lithium Stripper for FRIB. In *North American Particle Accelerator Conference*, Nov. 2019.

[22] H. Kuboki, H. Okuno, S. Yokouchi, H. Hasebe, T. Kishida, N. Fukunishi, O. Kamigaito, A. Goto, M. Kase, and Y. Yano. Charge-state distribution measurements using gas charge stripper toward 238U and 136Xe acceleration at RIKEN RIBF. In *Nuclear Instruments and Methods in Physics Research, Section A: Accelerators, Spectrometers, Detectors and Associated Equipment*, volume 655, pages 17–20, 11 2011.

[23] H. Okuno, H. Kuboki, O. Kamigaito, H. Hasebe, N. Fukunishi, Y. Watanabe, M. Fujimaki, T. Maie, T. Dantsuka, K. Kumagai, K. Yamada, T. Watanabe, M. Kase, and Y. Yano. Electron Stripping of High-intensity ^{238}U Ion Beam with Recirculating He Gas. In *Proceedings of International Particle Accelerator Conference*, number THPWO038, pages 3851–3853, 2013.

[24] V. P. Shevelko, P. Scharrer, Ch E. Düllmann, W. Barth, J. Khuyagbaatar, I. Yu Tolstikhina, N. Winckler, and A. Yakushev. Charge-state dynamics of 1.4- and 11-MeV/u uranium ions penetrating H2 and He gas targets. *Nuclear Instruments and*

Methods in Physics Research, Section B: Beam Interactions with Materials and Atoms, 428:56–64, 8 2018.

[25] P. Scharrer, Ch E. Düllmann, W. Barth, J. Khuyagbaatar, A. Yakushev, M. Bevcic, P. Gerhard, L. Groening, K. P. Horn, E. Jäger, J. Krier, and H. Vormann. Measurements of charge state distributions of 0.74 and 1.4 MeV/u heavy ions passing through dilute gases. *Physical Review Accelerators and Beams*, 20(4), 4 2017.

[26] P. Scharrer, W. Barth, M. Bevcic, Ch E. Düllmann, P. Gerhard, L. Groening, K. P. Horn, E. Jäger, J. Khuyagbaatar, J. Krier, H. Vormann, and A. Yakushev. Applications of the pulsed gas stripper technique at the GSI UNILAC. *Nuclear Instruments and Methods in Physics Research, Section A: Accelerators, Spectrometers, Detectors and Associated Equipment*, 863:20–25, 8 2017.

[27] E. Pozdeyev, J. Brandon, N. Bultman, K. Davidson, P. Gibson, L. Hodges, K. Holland, M. Konrad, S. Lidia, G. Machicoane, H. Maniar, T. Maruta, D. Morris, P. Morrison, C. Morton, P. Ostroumov, A. Platsun, H. Ren, T. Russo, J. Wei, Y. Yamazaki, T. Yashimoto, Q. Zhao, S. Zhao, S. Prestemon, D. Arbelaez, and Q. Z. Xing. FRIB front end construction and commissioning. In *Proceedings of International Particle Accelerator Conference*, number MOZGBF1, pages 58–62, 2018.

[28] Y. Raizer. *Gas Discharge Physics*. Springer-Verlag Berlin Heidelberg, 1st edition, 1991.

[29] H. Maecker et al. *The Electric Arc*. H. Popp Matlab GmbH, 1st edition, 2009.

[30] A. Hershcovitch. High-pressure arcs as vacuum-atmosphere interface and plasma lens. *J. Appl. Phys.*, 78(9):5283–5288, 1995.

[31] H. Kuboki, H. Okuno, A. Hershcovitch, T. Dantsuka, H. Hasebe, K. Ikegami, H. Imao, O. Kamigaito, M. Kase, T. Maie, T. Nakagawa, and Y. Yano. Development of Plasma Window for gas charge stripper at RIKEN RIBF. *Journal of Radioanalytical and Nuclear Chemistry*, 299:1030–1034, 2014.

[32] S. Huang, K. Zhu, Y. R. Lu, S. Z. Wang, A. Hershcovitch, L. Yang, and X. Y. Zhang. Quantitative characterization of arc discharge as vacuum interface. *Physics of Plasmas*, 21, 2014.

[33] Y. E. Krasik, S. Gleizer, V. Gurovich, I. Kronhaus, A. Hershcovitch, P. Nozar, and C. Taliani. Plasma window characterization. *J. Appl. Phys.*, 101, 2007.

[34] S. Huang, K. Zhu, B. L. Shi, Y. R. Lu, A. Hershcovitch, L. Yang, X. Y. Zhang, and G. D. Wei. Numerical simulation study on fluid dynamics of plasma window using argon. *Physics of Plasmas*, 20, 2013.

[35] A Hershcovitch. A plasma window for transmission of particle beams and radiation from vacuum to atmosphere for various applications. *Physics of Plasmas*, 5(5):2130–2136, 5 1998.

[36] W. Gerber, R. C. Lanza, A. Hershcovitch, P. Stefan, C. Castle, and E. Johnson. The plasma porthole: a windowless vacuum-pressure interface with various accelerator applications. *AIP Conference Proceedings*, 475:932–935, 1999.

[37] B.-L. Shi, S. Huang, K. Zhu, and Y.-R. Lu. Experimental study of the plasma window. *Chinese Physics C*, 38(1), 2014.

[38] I. H. Hutchinson. *Principles of Plasma Diagnostics*. Cambridge University Press, 2 edition, 2002.

[39] S. I. Braginskii. *Transport Processes in a Plasma*, pages 205–311. Consultants Bureau, 1st edition, 1965.

[40] V. V. Aristov. *Direct Methods for Solving the Boltzmann Equation and Study of Nonequilibrium Flows*, volume 60 of *Fluid Mechanics and its Applications*. Springer Netherlands, 2001.

[41] G. M. W. Kroesen, D. C. Schram, and J. C. M. de Haas. Description of a flowing cascade arc plasma. *Plasma Chemistry and Plasma Processing*, 10:531–551, 1990.

[42] C. H. Chang and J. D. Ramshaw. Numerical simulation of nonequilibrium effects in an argon plasma jet. *Physics of Plasmas*, 1(11):3698–3708, 1994.

[43] M. Mitchner and C. H. Kruger Jr. *Partially Ionized Gases*. Wiley-Interscience. John Wiley & Sons, Inc., 1st edition, 1973.

[44] J. A. M. van der Mullen. Excitation equilibria in plasmas; a classification. *Physics Reports*, (2), 1990.

[45] R. C. Hilborn. Einstein coefficients, cross sections, f values, dipole moments, and all that. *American Journal of Physics*, 50:982–986, 1982.

[46] U. Fantz. Basics of Plasma Spectroscopy. *Plasma Sources Sci. Technol.*, 15:S137–S147, 2006.

[47] J. Cooper. Plasma spectroscopy. *Rep. Prog. Phys.*, 29:35–130, 1966.

[48] A. T. M. Wilbers, G. M. W. Kroesen, C. J. Timmermans, and D. C. Schram. The Continuum Emission of an Arc Plasma. *J. Quant. Spectrosc. Radiat. Transfer*, 45:1–10, 1991.

[49] A. M. Gomés. Criteria for partial LTE in an argon thermal discharge at atmospheric pressure; validity of the spectroscopically measured electronic temperature. *J. Phys. D: Appl. Phys.*, 16:357–378, 1986.

[50] H. R. Griem. Validity of local thermal equilibrium in plasma spectroscopy. *Physical Review*, 131:1170–1176, 1963.

[51] A. LaJoie, J. Gao, and F. Marti. Study of High-Flow Argon Through Cascaded Arc for Use as a Gas Target Isolator. *IEEE Transactions on Plasma Science*, 47(5):2752–2758, 5 2019.

[52] H. R. Griem. *Principles of Plasma Spectroscopy.* Cambridge University Press, 1st edition, 1997.

[53] P. Schef, A. Derkatch, P. Lundin, S. Mannervik, L.-O. Norlin, D. Rostohar, P. Royen, and E. Biémont. Lifetimes of metastable levels in ar ii. *Eur. Phys. J. D*, 29:195–199, 2004.

[54] S. F. Biagi. Magboltz v7.1, 2004. www.lxcat.net, Retrieved on 8/1/2020.

[55] A. J. Dixon, F. A. Harrison, and A. C. H. Smith. A measurement of the electron impact ionization cross section of helium atoms in metastable states. *Journal of Physics B: Atomic and Molecular Physics J. Phys. B: Atom. Molec. Phys*, 9(15), 1976.

[56] F. F. Chen. *Plasma Diagnostic Techniques*, chapter Electric Probes. In Huddlestone and Leonard [62], 1st edition, 1965.

[57] R. A. Alpher and D. R. White. *Plasma Diagnostic Techniques*, chapter Optical Interferometry. In Huddlestone and Leonard [62], 1st edition, 1965.

[58] E. Carbone and S. Nujdam. Thomson scattering on non-equilibrium low density plasmas: principles, practice, and challenges. *Plasma Phys. Control. Fusion*, 57, 2015.

[59] K. Muraoka and A. Kono. Laser Thomson scattering for low-temperature plasmas. *J. Phys. D: Appl. Phys.*, 44, 2011.

[60] A. A. Ovysannikov and M. F. Zhukov. *Plasma Diagnostics.* Cambridge International Science Publishing, 1st edition, 2000.

[61] H. M. Mott-Smith and I. Langmuir. The theory of collectors in gaseous discharges. *Physical Review*, 28:727–763, 1926.

[62] R. H. Huddlestone and S. L. Leonard, editors. *Plasma Diagnostic Techniques.* Academic Press Inc., 1st edition, 1965.

[63] S. Hübner, J. S. Sousa, J. van der Mullen, and W. G. Graham. Thomson scattering on non-thermal atmospheric pressure plasma jets. *Plasma Sources Sci. Technol.*, 24, 2015.

[64] N. Konjevic. Plasma broadening and shifting of non-hydrogenic spectral lines: Present status and applications. *Phys. Reports*, 316:339–401, 1999.

[65] C. Yubero, M. S. Dimitrijević, M. C. García, and M. D. Calzada. Using the van der Waals broadening of the spectral atomic lines to measure the gas temperature of an argon microwave plasma at atmospheric pressure. *Spectrochimica Acta Part B*, 62:169–176, 2007.

[66] H. R. Griem. *Spectral Line Broadening by Plasmas.* Academic Press, Inc., 1st edition, 1974.

[67] A. V. Demura. Physical Models of Plasma Microfield. *International Journal of Spectroscopy*, 2010:1–42, 10 2010.

[68] M Baranger and B Mozer. Electric Field Distributions in an Ionized Gas. *Phys. Rev.*, pages 521–525, 1959.

[69] M. A. Gigosos. Stark broadening models for plasma diagnostics. *J. Phys. D: Appl. Phys.*, 47, 2014.

[70] C. F. Hooper, Jr. Low-Frequency Component Electric Microfield Distributions in Plasmas. *Physical Review*, 165:215–222, 1968.

[71] S. Beirle, J. Lampel, C. Lerot, H. Sihler, and T. Wagner. Parameterizing the Instrumental Spectral Response Function and its Changes by a super-Gaussian and its Derivatives. *Atmos. Meas. Tech.*, 10:581–598, 2017.

[72] J. A. Valenti, R. P. Butler, and G. W. Marcy. Determining Spectrometer Instrumental Profiles Using FTS Reference Spectra. *Astronomical Society of the Pacific*, 107(716), 1995.

[73] J. M. Lerner and A. Thevenon. The Optics of Spectroscopy, 2002. https://web.mit.edu/8.13/8.13d/manuals/Hydrogenic/jy-theory-optics-spectroscopy.pdf.

[74] U. Platt and J. Stutz. *Differential Optical Absorption Spectroscopy.* Physics of Earth and Space Environments. Springer-Verlag Berlin Heidelberg, 1st edition, 2008.

[75] Hans R Griem. Calculated Electron and Ion Stark Broadening of the Allowed and Forbidden 2 ^{3}P-4 ^{3}P, ^{3}D, ^{3}F Transitions in Neutral Helium. *The Astrophysical Journal*, 154, 1968.

[76] M. A. Gigosos and M. Á. González. Stark broadening tables for the helium i 447.1 line. *Astronomy and Astrophysics*, 503:293–299, 2009.

[77] Manuel A. González, Milivoje Ivković, Marco A. Gigosos, Sonja Jovićević, Natividad Lara, and Nikola Konjević. Plasma diagnostics using the He I 447.1 nm line at high and low densities. *Journal of Physics D: Applied Physics*, 44(19), 5 2011.

[78] C. Fleurier, G. Coulaud, and J. Chapelle. Study of ion dynamic effects at low electron densities on the lines He I 447.1 and 492.2 nm. *Physica B+C*, 100(1):127–134, 1980.

[79] M. Ivković, M. A. Gonzalez, N. Lara, M. A. Gigosos, and N. Konjević. Stark broadening of the He I 492.2nm line with forbidden components in dense low-temperature plasma. *Journal of Quantitative Spectroscopy and Radiative Transfer*, 127:82–89, 9 2013.

[80] N. I. Uzelac and N. Konjevic. Stark broadening of the He I 4471 Åline and its forbidden component in dense cool plasma. *Physical Review A*, 33(2), 1986.

[81] C. J. Timmermans, R. J. Rosado, and D. C. Schram. An investigation of non-equilibrium effects in thermal argon plasmas. *Zeitschrift für Naturforschung*, 40a:810–825, 1985.

[82] C. A. Bye and A Scheeline. Saha-Boltzmann Statistics for Determination of Electron Temperature and Density in Spark Discharges Using an Echelle/CCD System. *Applied Spectroscopy*, 47:2022–2030, 1993.

[83] National Institute of Standards and Technology. Atomic spectra database, 2019.

[84] W. C. Martin and W. L. Wiese. Atomic spectroscopy: A compendium of basic ideas, notation, data, and formulas, 2002.

[85] T. Fujimoto and R. W. P. McWhirter. Validity criteria for local thermodynamic equilibrium in plasma spectroscopy. *Physical Review A*, 42(11):6588–6601, 1990.

[86] J. Jonkers and J. A. M. Van Der Mullen. The Excitation Temperature in (Helium) Plasmas. *J. Quant. Spectrosc. Radiat. ransfer*, 61(5):703–709, 1999.

[87] H. W. Drawin. Validity conditions for local thermodynamic equilibrium. *Z. Physik*, 227:99–119, 1969.

[88] J. Jonkers, M. van de Sande, A. Sola, A. Gamero, and J. van der Mullen. On the differences between ionizing helium and argon plasmas at atmospheric pressure. *Plas. Sources Sci. and Technol.*, 12:30–38, 2003.

[89] A. C. G. Mitchell and M. W. Zemansky. *1961.* Cambridge University Press, 2 edition, 1961.

[90] R. W. P. McWhirter. *Plasma Diagnostic Techniques*, chapter Spectral Intensities. In Huddlestone and Leonard [62], 1st edition, 1965.

[91] G M W Kroesen. Plasma deposition: investigations on a new approach.

[92] M. Tanaka, M. Ushio, M. Ikeuchi, and Y. Kagebayashi. *In situ* measurements of electrode work functions in free-burning arcs during operation at atmospheric pressure. *J. Phys. D: Appl. Phys.*, 38:29–35, 2004.

[93] V. A. Nemchinsky. Life time of a refractory cathode doped with a work-function-lowering dopant. *Journal of Physics D:Applied Physics*, 29:2417–2422, 1996.

[94] L. Dabringhausen, D. Nandelstädt, J. Luhmann, and J. Mentel. Determination of HID electrode falls in a model lamp I: Pyrometric measurements. *J. Phys. D.: Appl. Phys.*, 35:1621–1630, 2002.

[95] E. Casado and V. Colomer. The Numerical Modelling of Joule Heating Effects in Thoriated Tungsten Cathodes of High-current Plasma Arcs. *Journal of Physics D: Applied Physics*, 33:1342–1347, 2000.

[96] V. Nemchinsky. Cathode erosion rate in high-pressure arcs: Influence of swirling gas flow. *IEEE Transactions on Plasma Science*, 30(6), 2002.

[97] T. Hoebing, P. Hermanns, A. Bergner, C. Ruhrmann, H. Traxler, I. Wesemann, W. Knabl, J. Mentel, and P. Awakowicz. Investigation of the flickering of La_2O_3 and ThO_2 doped tungsten cathodes. *J. Appl. Phys.*, 118, 2015.

[98] J. Haidar and A. J. D. Farmer. Surface temperature measurements for tungsten-based cathodes of high-current free-burning arcs. *J. Phys. D: Appl. Phys.*, 28:2089–2094, 1995.

[99] S. K. Nam and J. P. Verboncoeur. Effect of electron energy distribution function on the global model for high power microwave breakdown at high pressures. *Appl. Phys. Letters*, 92, 2008.

[100] I. Hutchinson and J. Freidberg. Lecture notes on collisions in plasmas, 2003. https://ocw.mit.edu/courses/nuclear-engineering/22-611j-introduction-to-plasma-physics-i-fall-2006/readings/chap3.pdf.

[101] G. J. M. Hagelaar and L. C. Pitchford. Solving the Boltzmann Equation to Obtain Electron Transport Coefficients and Rate Coefficients for Fluid Models. *Plasma Sources Sci. Tehcnol.*, 14:722–733, 2005.

[102] M. Allan, O. Zatsarinny, and K. Bartschat. Near-threshold absolute angle-differential cross sections for electron-impact excitation of argon and xenon. *Phys. Rev. A*, 75, 2006.

[103] O. Zatsarinny and K. Bartschat. B-spline BreitPauli R-matrix calculations for electron collisions with argon atoms. *J. Phys. B: At. Mol. Opt. Phys.*, 37:4693–4706, 2004.

[104] G. J. M. Hagelaar and L. C. Pitchford. Solving the Boltzmann equation to obtain electron transport coefficients and rate coefficients for fluid models. *Plasma Sources Science and Technology*, 14(4):722–733, 11 2005.

[105] D. R. Bates, A. E. Kingston, and R. W. P. McWhirter. Recombination between electrons and atomic ions I. Optically Thin Plasmas. *Proceedings of the Royal Society A*, 267:298–312, 1962.

[106] M. Goto. private communication.

[107] J. C. M. de Haas. *Non-equilibrium in flowing atmospheric plasmas.* PhD thesis, Eindhoven University of Technology, Jan. 1986.

[108] P. Gueye, Y. Cressault, V. Rohani, and L. Fulcheri. A simplified model for the determination of current-voltage characteristics of a high pressure hydrogen plasma arc. *Journal of Applied Physics*, 121(7), 2 2017.

[109] J. J. Beulens, D. Milojevic, D. C. Schram, and P. M. Vallinga. A two-dimensional nonequilibrium model of cascaded arc plasma flows. *Phys Fluids B*, 3:2548–2557, 1991.

[110] Charles H. Kruger. Nonequilibrium in confined-arc plasmas. *Physics of Fluids*, 13(7):1737–1746, 1970.

[111] Janssen, G. M. and van Dijk, J. and Benoy, D. A. and Tas, M. A. and Burm, K. T. A. L. and Goedheer, W. J. and van der Mullen, J. A. M. and Schram, D. C. PLASIMO, a general model: I. Applied to an argon cascaded arc plasma. *Plasma Sources Sci. Technol.*, 8:1–14, 1999.

[112] J. O. Hirschfelder, C. F. Curtiss, and R. B. Bird. *Molecular theory of gases and liquids.* Cambridge University Press, 1964.

[113] A. V. Phelps, C. H. Greene, and J. P. Burke Jr˙ Collision Cross Sections for Argon Atoms with Argon Atoms for Energies from 0.01 eV to 10 keV. *J. Phys. B: At. Mol. Opt. Phys.*, 33:2965–2981, 2000.

[114] A. V. Phelps. Collision cross sections for identical and non-identical rare-gas atom pairs for energies from 0.01 ev to 10 kev, 2004.

[115] A. B. Murphy. Transport Coefficients of Helium and Argon-Helium Plasmas. *IEEE Transactions on Plasma Science*, 25(5):809, 1997.

[116] J. van Dijk, K. Peerenboom, M. Jimenez, D. Mihailova, and J. van der Mullen. The plasma modelling toolkit PLASIMO. *J. Phys. D: Appl. Phys.*, 42, 2009.

[117] K. S. C. Peerenboom, W. J. Goedheer, J. van Dijk, and J. J. A. M. van der Mullen. Integral simulation of the creation and expansion of a transonic argon plasma. *Plas. Sources Sci. and Tech.*, 19, 2010.

[118] J. van der Mullen and J. Jonkers. Fundamental comparison between non-equilibrium aspects of ICP and MIP discharges. *Spectrochimica Acta Part B*, 54:1017–1044, 1999.

[119] S.-J. Oh, H.-C. Lee, and C.-W. Chung. Global model including multipstep ionizations in helium plasmas. *Phys. of Plasmas*, 23, 2016.

[120] J. Janssen. private communication.

[121] L. S. Frost. Conductivity of seeded atmospheric pressure plasmas. *Journal of Applied Physics*, 32(10):2029–2036, 1961.

[122] R. S. Devoto. Simplified expressions for the transport properties of ionized monatomic gases. *Physics of Fluids*, 10(10):2105–2112, 1967.

[123] J. F. J. Janssen. *Equilibrium and Transport in molecular Plasmas.* PhD thesis, Eindhoven University of Technology, Sept. 2016.

[124] A. J. Shirvan and I. Choquet. A Review of Cathode-Arc Coupling Modeling in GTAW. *Weld World*, 60:821–835, 2016.